

THREE-PHASE EROSION TESTING AND VIBRATION ANALYSIS OF
AN ELECTRICAL SUBMERSIBLE PUMP

A Thesis

by

DEZHI ZHENG

Submitted to the Office of Graduate and Professional Studies of
Texas A&M University
in partial fulfillment of the requirements for the degree of

MASTER OF SCIENCE

Chair of Committee, Gerald L. Morrison
Committee Members, Devesh Ranjan
Robert E. Randall

Head of Department, Andreas A. Polycarpou

December 2013

Major Subject: Mechanical Engineering

Copyright 2013 Dezhi Zheng

ABSTRACT

Electrical Submersible Pump (ESP) has been recognized as an excellent artificial lifting method in industry due to its high liquid flow rate in both onshore and offshore applications. As oil exploration goes deep into water, ESP equipment is facing a crucial problem of slurry erosion which may affect life and cost significantly. The wear caused by slurry erosion may bring the issue such as unbalanced side loads, severe vibration and decreased pressure head. Eventually, this phenomenon will lead to a complete system failure.

In present work, a systematic study on the erosion wear has been carried out in order to give better understanding. The WJE-1000 ESP pump manufactured by Baker Hughes has been employed in this study. During the whole procedure, 117 hours two-phase (water-sand) testing has been performed and is followed by 68 hours three-phase (water-sand-air) testing. A combined analysis by combining components erosion wear measurement, pump performance testing and vibration signal process has clearly indicated the trend of erosion process on each component. Furthermore, the correlation between vibration signals collected by proximity probe and remote 3D accelerometer provided a future direction for monitoring inaccessible downhole equipment. Finally, the conclusion that air could further accelerate ESP erosion has been found by comparing the erosion rate and vibration signals in two-phase test and three-phase test.

DEDICATION

To my dear wife, parents — for their support of all that I do

ACKNOWLEDGEMENTS

For those people who have supported the creation of this work, it is difficult for me to choose the words that can truly and accurately express my heartfelt gratitude and appreciation. Words cannot express all of my feelings. Nevertheless, I would like to start by thanking Dr. Gerald Morrison for acting as supervisor and giving valuable guidance during the course of this study. His enormous knowledge, intelligence and expertise always helped me unconditionally to solve various problems.

Also, I would like to thank my committee members, Dr. Devesh Ranjan and Dr. Robert E. Randall, for their guidance and support throughout the course of this research.

Thanks to Dr. Stuart Scott and Eng. Hector Casillas at Shell Exploration & Production for their continuous inputs and review about the progress of projects. Thanks also go to my friends Sahand Prouzpaneh, Ramy Saleh, Joey Marchetti, Sujan Reddy, Abhay Patil, Daniel Steck, Chase Williams, and Klayton Kirkland for making my time at Texas A&M University a great experience.

Finally, thanks to my mother and father for their encouragement and to my wife for her patience and love.

NOMENCLATURE

<i>ESP</i>	Electrical Submersible Pump
<i>BPD</i>	Barrels per Day
<i>H</i>	Pump Head
<i>BHP</i>	Break Horse Power
ΔP_s	Stage Differential Pressure
η	Efficiency
<i>GPM</i>	Gallons per Minute
<i>rpm</i>	Rotations per Minute
<i>g</i>	Gravity Acceleration Constant
ρ	Density
μ	Dynamic viscosity
<i>sH</i>	Specific Head
<i>sP</i>	Specific Power
<i>sQ</i>	Specific Capacity
ν	Kinetic viscosity
<i>Q</i>	Flow Rate
P_e	Power Electric
s_g	Specific Gravity
<i>NPSH</i>	Net Positive Suction Head
<i>HP</i>	Horse Power

ΔP_t	Total Differential Pressure
PSI	Pressure Square Inch
$PSIG$	Pressure Square Inch Gauge
$PSIA$	Pressure Square Inch Absolute
h_d	Total Head Pressure
h_s	Total Suction Pressure
H_2O	Water
V	Volt
Vdc	Volt Direct Current
mA	Milli-Amper Current
pk	Velocity Inch / Second
Hz	Frequency Hertz
oz	Ounce
PT	Pressure Transducer
OFM	Orifice Flow Meter
CFM	Coriolis Flow Meter
S/s	Sampling Rate / Second
PID	Proportional-Integral Derivative
VFD	Variable Frequency Drive

TABLE OF CONTENTS

	Page
ABSTRACT	ii
DEDICATION	iii
ACKNOWLEDGEMENTS	iv
NOMENCLATURE.....	v
TABLE OF CONTENTS	vii
LIST OF FIGURES.....	ix
LIST OF TABLES	xxv
CHAPTER I INTRODUCTION	1
CHAPTER II OBJECTIVES	8
CHAPTER III LITERATURE REVIEW	10
3.1. Electrical Submersible Pumps.....	10
3.2. Erosion Study of ESP	21
CHAPTER IV EXPERIMENTAL SETUP.....	48
4.1. Flow Loop	48
4.2. Electrical Submersible Pump (ESP).....	51
4.3. ESP Driven Motor	56
4.4. Auxiliary Pump	57
4.5. Sand Auger System	59
4.6. Tank and Sand Separator.....	60
4.7. Mechanical Seal	61
CHAPTER V INSTRUMENTATION.....	63
5.1. Instrument List	63
5.2. Accelerometers.....	64
5.3. Proximity Probe.....	65
5.4. Orifice Flow Meter.....	66

5.5.	Coriolis Flow Meter	68
5.6.	Turbine Flow Meter	71
5.7.	Pressure Transducer	73
5.8.	Thermocouple.....	74
5.9.	Data Acquisition.....	74
CHAPTER VI RESULTS AND DISCUSSION		78
6.1.	ESP Performance Degradation.....	79
6.2.	Component Wear Analysis.....	83
6.2.1.	Components Wear Pattern.....	83
6.2.2.	Component Measurement Analysis	103
6.3.	Vibration Analysis.....	117
6.3.1.	Shaft and Impeller Orbit.....	118
6.3.2.	Frequency Spectrum.....	122
CHAPTER VII CONCLUSION		140
REFERENCES.....		144
APPENDIX A WJE-1000 CONFIGURATION		148
APPENDIX B PUMP PERFORMANCE.....		154
APPENDIX C PUMP COMPONENT WEAR MEASUREMENT		163
APPENDIX D VIBRATION SIGNATURE.....		167
D.1.	0 Hours	167
D.2.	8 Hours	174
D.3.	24 Hours	187
D.4.	52 Hours	201
D.5.	117 Hours	215
D.6.	185 Hours	229
D.7.	FFT vs Time	243
D.8.	Vibration Signature vs GVF.....	251
D.9.	Vibration Signature vs Flow Rate Spectrum at 15% GVF.....	262

LIST OF FIGURES

	Page
Figure 1. Artificial Lifting Method Distribution Worldwide [2]	2
Figure 2. Conventional ESP System [3].....	3
Figure 3. ESP Pump Assembly [5].....	4
Figure 4. WJE-1000 ESP Assembly	6
Figure 5. Nomenclature of Impeller and Diffuser [6]	12
Figure 6. Configuration of Radial Flow Pump and Mixed Flow Pump[6]	13
Figure 7. Derivation of Pump H-Q Curve [6]	15
Figure 8. Power Conditions in ESP Stages [6].....	16
Figure 9. Distribution of Axial Forces in a Mixed Flow Impeller [6]	19
Figure 10. Sand Problem Area in Fixed Impeller ESP [6].....	22
Figure 11. Construction of a Resilient Radial Bearing [6].....	24
Figure 12. Particle Impact Erosion Due to the Deviation of the Particle [15]	25
Figure 13. Comparison of Impact Wear Rate Parameter with Different Flow Rate [15]	26
Figure 14. Comparison of Impact Wear Rate with Different Pump Speed [15]	27
Figure 15. Comparison of Impact Wear Rate with Different Particle Size [15]	27
Figure 16. Inclined and Perpendicular Impact Tester [16].....	29
Figure 17. Wear Rates of Impact Test [16].....	29
Figure 18. Impeller and Diffuser Dimensions in CFD Simulation [16].....	30
Figure 19. Effect of Particle Sizes on Erosion Rate of Impeller [16]	31
Figure 20. Effect of Particle Sized on Erosion Rate of Diffuser [16]	31

Figure 21. Particle Trajectories in Impeller and Diffuser [16].....	33
Figure 22. Erosion Rates for the Impeller with Different Coatings [16]	34
Figure 23. Erosion Rates for the Diffuser with Different Coatings [16].....	34
Figure 24. Pump Test Curve Showing Radial Wear [17].....	35
Figure 25. Pump Test Curve Showing Lost Compression [17]	36
Figure 26. Pump Test Curve Showing Downthrust Wear [17]	37
Figure 27. Pump Test Curve Showing Plastic Stages Heated and Melted [17]	37
Figure 28. ESP Installation with Gas Separator [6]	39
Figure 29. Gas Separator Configuration [6].....	40
Figure 30. Types of Multiphase Pumps [19].....	41
Figure 31. Schematic Diagram of Oil Aerator for Lubricant Supply [21]	45
Figure 32. Test Rig for Oil Aeration Effect [21].....	44
Figure 33. Pipe and Instrumentation Diagram (P&ID).....	48
Figure 34. Experimental Setup Diagram.....	50
Figure 35. Impeller Suction View [24]	52
Figure 36. Impeller Detailed Dimension.....	53
Figure 37. Diffuser Discharge View [24].....	52
Figure 38. Diffuser Detailed Dimension	53
Figure 39. Catalog Performance Curve for Three Stages of ESP under 3600 RPM [24]	54
Figure 40. Catalog Head Flow Rate Curves for Different Pump Speeds [24]	55
Figure 41. Motor Efficiency Curve	57
Figure 42. Motor Located at Top of Derrick.....	56

Figure 43. Feed Pump Assembly	58
Figure 44. Slurry Pump Assembly	58
Figure 45. Sand Auger Configuration	59
Figure 46. Tank and Separator Assembly	60
Figure 47. Combination of Plan 32 and Plan 11	61
Figure 48. Combination of Plan 11 and Plan 13	62
Figure 49. Mechanical Seal Test Results without Seal Flush Plan	62
Figure 50. Accelerometer Location on the Casing.....	65
Figure 51. Probes Location on the Casing	66
Figure 52. Orifice Flow Meter [24].....	68
Figure 53. Phase Shift between Different Coils [25]	69
Figure 54. Coriolis Flow Meter.....	71
Figure 55. Air Supply Setup.....	72
Figure 56. WJE-1000 Performance Monitor Panel	76
Figure 57. WJE-1000 Vibration Monitor Panel	77
Figure 58. Data Trigger Panel	77
Figure 59. General Test Procedure.....	78
Figure 60. Pump Performance Curve with Pure Water at 0-117-185 Hrs	80
Figure 61. Performance Degradation with Pure Water	80
Figure 62. Pump Performance Curve with 15% GVF at 117&185 Hrs.....	82
Figure 63. Performance Degradation with 15% GVF.....	83
Figure 64. WJE-1000 Detailed Configuration	84

Figure 65. Three Body Abrasive Wear	86
Figure 66. Journal Bearings Status after 185 Hours.....	87
Figure 67. Bearing Status after Two-phase Test at 117 Hours	87
Figure 68. Bearing 20&21 Status at Target Time Point.....	88
Figure 69. Secondary Flow Direction in Bearing Clearance	90
Figure 70. Scoring Wear and Hair Crack	91
Figure 71. Wear Pattern on Each Pairs of Bearings	92
Figure 72. Wear Mark between Two Bearings	93
Figure 73. Surface and Interior Material	93
Figure 74. WJE-1000 Impeller Configuration	94
Figure 75. Wear Mark on Leading Edges	95
Figure 76. Wear Marks on Different Stages	96
Figure 77. Horseshoe Shape Wear Mark	97
Figure 78. Secondary Flow Path around Impeller.....	97
Figure 79. Trailing Edge Wear Mark	98
Figure 80. Wear Mark on Impeller Labyrinth Seal	99
Figure 81. WJE-1000 Diffuser Configuration.....	99
Figure 82. Wear Mark on Leading Edges	100
Figure 83. Wear Mark on Diffuser Shroud	101
Figure 84. Contact Surface of Impeller Intake Labyrinth	102
Figure 85. Contact Surface of Impeller Discharge Labyrinth.....	102
Figure 86. Wear Mark on Upthrust Plate	103

Figure 87. Bearing and Bushing Mating Surface	104
Figure 88. Journal Bearing and Bushing Diameter Tracking.....	105
Figure 89. Journal Bearing Clearance Tracking.....	106
Figure 90. Bearing Wear Mode in Two-phase Test (0-117 Hours)	107
Figure 91. Bearing Wear Mode for Three-phase Test (117-185 Hours).....	107
Figure 92. Bearing Wear Mode for the Whole Test (0-185 Hours).....	108
Figure 93. Impeller Intake Labyrinth Seal	109
Figure 94. Impeller Discharge Labyrinth Seal	110
Figure 95. Labyrinth Seal Wear Mode in Two-phase Test (0-117 Hours)	110
Figure 96. Labyrinth Seal Wear Mode in Three-phase Test (117-185 Hours)	111
Figure 97. Labyrinth Seal Wear Mode in the Whole Test (0-185 Hours)	111
Figure 98. Tapered Edges on Bearing	112
Figure 99. Tapered Edges on Labyrinth.....	113
Figure 100. Erosion Rate Comparison between Bearing and Labyrinth Seal.....	115
Figure 101. Weight Track for Impeller	116
Figure 102. Weight Track for Diffuser	117
Figure 103. Shaft and Impeller Orbit Plot Comparison at Target Time Point	119
Figure 104. Orbit Increment after Two-phase Test and Three-phase Test	119
Figure 105. Orbit Mode Comparison	120
Figure 106. Orbit Comparison between 0% GVF and 15% GVF.....	121
Figure 107. Position for Proximity Probes and Accelerometer	122
Figure 108. PP1 Shaft Waterfall at 24 Hours.....	124

Figure 109. PP1 Shaft Waterfall at 52 Hours	124
Figure 110. PP1 Shaft Waterfall at 117 Hours	125
Figure 111. PP1 Shaft Waterfall at 185 Hours	125
Figure 112. PP1 Shaft Waterfall Plot at Different Hour	126
Figure 113. Third Stage Impeller Waterfall at 24 Hours	127
Figure 114. Third Stage Impeller Waterfall at 52 Hours	127
Figure 115. Third Stage Impeller Waterfall at 117 Hours	128
Figure 116. Third Stage Impeller Waterfall at 185 Hours	128
Figure 117. Third Stage Impeller Waterfall Plot at Different Hour	129
Figure 118. 3D Accelerometer FFT	131
Figure 119. Radial Direction Accelerometer Waterfall at 24 Hours	132
Figure 120. Radial Direction Accelerometer Waterfall at 52 Hours	132
Figure 121. Radial Direction Accelerometer Waterfall at 117 Hours	133
Figure 122. Radial Direction Accelerometer Waterfall at 185 Hours	133
Figure 123. FFT vs GVF Spectrum from Proximity Probe	134
Figure 124. FFT vs GVF Spectrum from Accelerometer	134
Figure 125. FFT vs Flow Rate at 15% GVF of Proximity Probe	136
Figure 126. FFT vs Flow Rate at 15% GVF of Accelerometer	137
Figure 127. Comparison between Vibration Data and Physical Wear	137
Figure 128. Correlation between Accelerometer and Bearing Clearance	139
Figure 129. WJE-1000 Configuration	150
Figure 130. Numbered Item on the Shaft	151

Figure 131. Impeller Configuration	152
Figure 132. Diffuser Configuration.....	153
Figure 133. WJE-1000 Pump Curve (Baker Hughes).....	154
Figure 134. 3600 RPM Performance Curve at 0 Hours	154
Figure 135. 3600 RPM Performance Curve at 16 Hours	155
Figure 136. 3600 RPM Performance Curve at 24 Hours	155
Figure 137. 3600 Pump Performance Curve at 32 Hours	156
Figure 138. 3600 RPM Performance Curve at 40 Hours	156
Figure 139. 3600 RPM Performance Curve at 48 Hours	157
Figure 140. 3600 RPM Performance Curve at 56 Hours	157
Figure 141. 3600 RPM Performance Curve at 64 Hours	158
Figure 142. 3600 RPM Performance Curve at 72 Hours	158
Figure 143. 3600 RPM Performance Curve at 88 Hours	159
Figure 144. 3600 RPM Performance Curve at 104 Hours	159
Figure 145. 3600 RPM Performance Curve at (0-117-185) Hours with 0% GVF	160
Figure 146. 3600 RPM Performance Curve at (0-117-185) Hours with 15% GVF	160
Figure 147. Pump Performance Degradation for 0% GVF	161
Figure 148. Pump Performance Degradation for 15% GVF.....	161
Figure 149. Orbit at 90 RPM – 0 Hours	167
Figure 150. Orbit at 3600 RPM – 0 Hours	168
Figure 151. Shaft 1 Ramp Up Orbit – 0 Hours	169
Figure 152. Impeller 2 Ramp Up Orbit – 0 Hours	169

Figure 153. Shaft 2 Ramp Up Orbit – 0 Hours	170
Figure 154. Impeller 3 Ramp Up Orbit – 0 Hours	170
Figure 155. Shaft 3 Ramp Up Orbit – 0 Hours	171
Figure 156. Shaft FFT – 0 Hours	171
Figure 157. Impeller FFT – 0 Hours	172
Figure 158. Inlet Accelerometer FFT – 0 Hours	172
Figure 159. Outlet Accelerometer FFT – 0 Hours	173
Figure 160. Shaft Waterfall Spectrum – 0 Hours	173
Figure 161. Impeller Waterfall Spectrum – 0 Hours	174
Figure 162. Orbit at 90 RPM – 8 Hours	174
Figure 163. Orbit at 3600 RPM – 8 Hours	175
Figure 164. Shaft 1 Ramp Up Orbit – 8 Hours	176
Figure 165. Shaft 2 Ramp Up Orbit – 8 Hours	176
Figure 166. Shaft 3 Ramp Up Orbit – 8 Hours	177
Figure 167. Shaft FFT – 8 Hours	177
Figure 168. Impeller FFT – 8 Hours	178
Figure 169. Inlet Accelerometer FFT – 8 Hours	178
Figure 170. Outlet Accelerometer FFT – 8 Hours	179
Figure 171. PP1 Waterfall Spectrum – 8 Hours	179
Figure 172. PP2 Waterfall Spectrum – 8 Hours	180
Figure 173. PP3 Waterfall Spectrum – 8 Hours	180
Figure 174. PP4 Waterfall Spectrum – 8 Hours	181

Figure 175. PP5 Waterfall Spectrum – 8 Hours	181
Figure 176. PP6 Waterfall Spectrum – 8 Hours	182
Figure 177. PP7 Waterfall Spectrum – 8 Hours	182
Figure 178. PP8 Waterfall Spectrum – 8 Hours	183
Figure 179. PP9 Waterfall Spectrum – 8 Hours	183
Figure 180. PP10 Waterfall Spectrum – 8 Hours	184
Figure 181. Inlet Accelerometer Radial Waterfall Spectrum – 8 Hours	184
Figure 182. Inlet Accelerometer Tangential Waterfall Spectrum – 8 Hours	185
Figure 183. Inlet Accelerometer Axial Waterfall Spectrum – 8 Hours	185
Figure 184. Outlet Accelerometer Radial Waterfall Spectrum – 8 Hours	186
Figure 185. Outlet Accelerometer Tangential Waterfall Spectrum – 8 Hours	186
Figure 186. Outlet Accelerometer Axial Waterfall Spectrum – 8 Hours	187
Figure 187. Orbit at 90 RPM – 24 Hours	187
Figure 188. Orbit at 3600 RPM – 24 Hours	188
Figure 189. Shaft 1 Ramp Up Orbit – 24 Hours	188
Figure 190. Impeller 2 Ramp Up Orbit – 24 Hours	189
Figure 191. Shaft 2 Ramp Up Orbit – 24 Hours	189
Figure 192. Impeller 2 Ramp Up Orbit – 24 Hours	190
Figure 193. Shaft 3 Ramp Up Orbit – 24 Hours	190
Figure 194. Shaft FFT – 24 Hours	191
Figure 195. Impeller FFT – 24 Hours	191
Figure 196. Inlet Accelerometer FFT – 24 Hours	192

Figure 197. Outlet Accelerometer FFT – 24 Hours	192
Figure 198. PP1 Waterfall Spectrum – 24 Hours.....	193
Figure 199. PP2 Waterfall Spectrum – 24 Hours.....	193
Figure 200. PP3 Waterfall Spectrum – 24 Hours.....	194
Figure 201. PP4 Waterfall Spectrum – 24 Hours.....	194
Figure 202. PP5 Waterfall Spectrum – 24 Hours.....	195
Figure 203. PP6 Waterfall Spectrum – 24 Hours.....	195
Figure 204. PP7 Waterfall Spectrum – 24 Hours.....	196
Figure 205. PP8 Waterfall Spectrum – 24 Hours.....	196
Figure 206. PP9 Waterfall Spectrum – 24 Hours.....	197
Figure 207. PP10 Waterfall Spectrum – 24 Hours.....	197
Figure 208. Inlet Accelerometer Radial Waterfall Spectrum – 24 Hours	198
Figure 209. Inlet Accelerometer Tangential Waterfall Spectrum – 24 Hours	198
Figure 210. Inlet Accelerometer Axial Waterfall Spectrum – 24 Hours.....	199
Figure 211. Outlet Accelerometer Radial Waterfall Spectrum – 24 Hours	199
Figure 212. Outlet Accelerometer Tangential Waterfall Spectrum – 24 Hours.....	200
Figure 213. Outlet Accelerometer Axial Waterfall Spectrum – 24 Hours.....	200
Figure 214. Orbit at 90 RPM – 52 Hours.....	201
Figure 215. Orbit at 3600 RPM – 52 Hours.....	202
Figure 216. Shaft 1 Ramp Up Orbit – 52 Hours	203
Figure 217. Impeller 2 Ramp Up Orbit – 52 Hours	203
Figure 218. Shaft 2 Ramp Up Orbit – 52 Hours	204

Figure 219. Impeller 3 Ramp Up Orbit – 52 Hours	204
Figure 220. Shaft 3 Ramp Up Orbit – 52 Hours	205
Figure 221. Shaft FFT – 52 Hours	205
Figure 222. Impeller FFT – 52 Hours	206
Figure 223. Inlet Accelerometer FFT – 52 Hours	206
Figure 224. Outlet Accelerometer FFT – 52 Hours	207
Figure 225. PP1 Waterfall Spectrum – 52 Hours.....	207
Figure 226. PP2 Waterfall Spectrum – 52 Hours.....	208
Figure 227. PP3 Waterfall Spectrum – 52 Hours.....	208
Figure 228. PP4 Waterfall Spectrum – 52 Hours.....	209
Figure 229. PP5 Waterfall Spectrum – 52 Hours.....	209
Figure 230. PP6 Waterfall Spectrum – 52 Hours.....	210
Figure 231. PP7 Waterfall Spectrum – 52 Hours.....	210
Figure 232. PP8 Waterfall Spectrum – 52 Hours.....	211
Figure 233. PP9 Waterfall Spectrum – 52 Hours.....	211
Figure 234. PP10 Waterfall Spectrum – 52 Hours.....	212
Figure 235. Inlet Accelerometer Radial Waterfall Spectrum – 52 Hours	212
Figure 236. Inlet Accelerometer Tangential Waterfall Spectrum – 52 Hours	213
Figure 237. Inlet Accelerometer Axial Waterfall Spectrum – 52 Hours.....	213
Figure 238. Outlet Accelerometer Radial Waterfall Spectrum – 52 Hours	214
Figure 239. Outlet Accelerometer Tangential Waterfall Spectrum – 52 Hours.....	214
Figure 240. Outlet Accelerometer Axial Waterfall Spectrum – 52 Hours.....	215

Figure 241. Orbit at 90 RPM – 117 Hours	215
Figure 242. Orbit at 3600 RPM – 117 Hours	216
Figure 243. Shaft 1 Ramp Up Orbit – 117 Hours	217
Figure 244. Impeller 2 Ramp Up Orbit – 117 Hours	217
Figure 245. Shaft 2 Ramp Up Orbit – 117 Hours	218
Figure 246. Impeller 3 Ramp Up Orbit – 117 Hours	218
Figure 247. Shaft 3 Ramp Up Orbit – 117 Hours	219
Figure 248. Shaft FFT – 117 Hours	219
Figure 249. Impeller FFT – 117 Hours	220
Figure 250. Inlet Accelerometer FFT – 117 Hours	220
Figure 251. Outlet Accelerometer FFT – 117 Hours	221
Figure 252. PP1 Waterfall Spectrum – 117 Hours	221
Figure 253. PP2 Waterfall Spectrum – 117 Hours	222
Figure 254. PP3 Waterfall Spectrum – 117 Hours	222
Figure 255. PP4 Waterfall Spectrum – 117 Hours	223
Figure 256. PP5 Waterfall Spectrum – 117 Hours	223
Figure 257. PP6 Waterfall Spectrum – 117 Hours	224
Figure 258. PP7 Waterfall Spectrum – 117 Hours	224
Figure 259. PP8 Waterfall Spectrum – 117 Hours	225
Figure 260. PP9 Waterfall Spectrum – 117 Hours	225
Figure 261. PP10 Waterfall Spectrum – 117 Hours	226
Figure 262. Inlet Accelerometer Radial Waterfall Spectrum – 117 Hours	226

Figure 263. Inlet Accelerometer Tangential Waterfall Spectrum – 117 Hours	227
Figure 264. Inlet Accelerometer Axial Waterfall Spectrum – 117 Hours.....	227
Figure 265. Outlet Accelerometer Radial Waterfall Spectrum – 117 Hours	228
Figure 266. Outlet Accelerometer Tangential Waterfall Spectrum – 117 Hours.....	228
Figure 267. Outlet Accelerometer Axial Waterfall Spectrum – 117 Hours.....	229
Figure 268. Orbit at 90 RPM – 185 Hours	229
Figure 269. Orbit at 3600 RPM – 185 Hours	230
Figure 270. Shaft 1 Ramp Up Orbit – 185 Hours	230
Figure 271. Impeller 2 Ramp Up Orbit – 185 Hours	231
Figure 272. Shaft 2 Ramp Up Orbit – 185 Hours	231
Figure 273. Impeller 3 Ramp Up Orbit – 185 Hours	232
Figure 274. Shaft 3 Ramp Up Orbit – 185 Hours	232
Figure 275. Shaft FFT – 185 Hours	233
Figure 276. Impeller FFT – 185 Hours	233
Figure 277. Inlet Accelerometer FFT – 185 Hours	234
Figure 278. Outlet Accelerometer FFT – 185 Hours	234
Figure 279. PP1 Waterfall Spectrum – 185 Hours.....	235
Figure 280. PP2 Waterfall Spectrum – 185 Hours.....	235
Figure 281. PP3 Waterfall Spectrum – 185 Hours.....	236
Figure 282. PP4 Waterfall Spectrum – 185 Hours.....	236
Figure 283. PP5 Waterfall Spectrum – 185 Hours.....	237
Figure 284. PP6 Waterfall Spectrum – 185 Hours.....	237

Figure 285. PP7 Waterfall Spectrum – 185 Hours	238
Figure 286. PP8 Waterfall Spectrum – 185 Hours	238
Figure 287. PP9 Waterfall Spectrum – 185 Hours	239
Figure 288. PP10 Waterfall Spectrum – 185 Hours	239
Figure 289. Inlet Accelerometer Radial Waterfall Spectrum – 185 Hours	240
Figure 290. Inlet Accelerometer Tangential Waterfall Spectrum – 185 Hours	240
Figure 291. Inlet Accelerometer Axial Waterfall Spectrum – 185 Hours	241
Figure 292. Outlet Accelerometer Radial Waterfall Spectrum – 185 Hours	241
Figure 293. Outlet Accelerometer Tangential Waterfall Spectrum – 185 Hours	242
Figure 294. Outlet Accelerometer Axial Waterfall Spectrum – 185 Hours	242
Figure 295. PP1 FFT vs Time Spectrum	243
Figure 296. PP2 FFT vs Time Spectrum	243
Figure 297. PP3 FFT vs Time Spectrum	244
Figure 298. PP4 FFT vs Time Spectrum	244
Figure 299. PP5 FFT vs Time Spectrum	245
Figure 300. PP6 FFT vs Time Spectrum	245
Figure 301. PP7 FFT vs Time Spectrum	246
Figure 302. PP8 FFT vs Time Spectrum	246
Figure 303. PP9 FFT vs Time Spectrum	247
Figure 304. PP10 FFT vs Time Spectrum	247
Figure 305. Inlet Radial FFT vs Time Spectrum	248
Figure 306. Inlet Tangential FFT vs Time Spectrum	248

Figure 307. Inlet Axial FFT vs Time Spectrum	249
Figure 308. Outlet Radial FFT vs Time Spectrum.....	249
Figure 309. Outlet Tangential FFT vs Time Spectrum	250
Figure 310. Outlet Axial FFT vs Time Spectrum	250
Figure 311. 0% GVF Orbit.....	251
Figure 312. 10% GVF Orbit.....	251
Figure 313. 15% GVF Orbit.....	252
Figure 314. Shaft FFT at 15% GVF.....	252
Figure 315. Impeller FFT at 15% GVF.....	253
Figure 316. Inlet Accelerometer FFT at 15% GVF	253
Figure 317. Outlet Accelerometer FFT at 15% GVF.....	254
Figure 318. PP1 FFT vs GVF Spectrum	254
Figure 319. PP2 FFT vs GVF Spectrum	255
Figure 320. PP3 FFT vs GVF Spectrum	255
Figure 321. PP4 FFT vs GVF Spectrum	256
Figure 322. PP5 FFT vs GVF Spectrum	256
Figure 323. PP6 FFT vs GVF Spectrum	257
Figure 324. PP7 FFT vs GVF Spectrum	257
Figure 325. PP8 FFT vs GVF Spectrum	258
Figure 326. PP9 FFT vs GVF Spectrum	258
Figure 327. PP10 FFT vs GVF Spectrum	259
Figure 328. Inlet Radial FFT vs GVF Spectrum.....	259

Figure 329. Inlet Tangential FFT vs GVF Spectrum	260
Figure 330. Inlet Axial FFT vs GVF Spectrum	260
Figure 331. Outlet Radial FFT vs GVF Spectrum	261
Figure 332. Outlet Tangential FFT vs GVF Spectrum.....	261
Figure 333. Outlet Axial FFT vs GVF Spectrum.....	262
Figure 334. PP1 FFT vs Flow Rate Spectrum.....	262
Figure 335. PP2 FFT vs Flow Rate Spectrum.....	263
Figure 336. PP3 FFT vs Flow Rate Spectrum.....	263
Figure 337. PP4 FFT vs Flow Rate Spectrum.....	264
Figure 338. PP5 FFT vs Flow Rate Spectrum.....	264
Figure 339. PP6 FFT vs Flow Rate Spectrum.....	265
Figure 340. PP7 FFT vs Flow Rate Spectrum.....	265
Figure 341. PP8 FFT vs Flow Rate Spectrum.....	266
Figure 342. PP9 FFT vs Flow Rate Spectrum.....	266
Figure 343. PP10 FFT vs Flow Rate Spectrum.....	267
Figure 344. Inlet Accelerometer Radial FFT vs Flow Rate Spectrum	267
Figure 345. Inlet Accelerometer Tangential FFT vs Flow Rate Spectrum	268
Figure 346. Inlet Accelerometer Axial FFT vs Flow Rate Spectrum	268
Figure 347. Outlet Accelerometer Radial FFT vs Flow Rate Spectrum	269
Figure 348. Outlet Accelerometer Tangential FFT vs Flow Rate Spectrum.....	269
Figure 349. Outlet Accelerometer Axial FFT vs Flow Rate Spectrum.....	270

LIST OF TABLES

	Page
Table 1. Sand Problem Level [6]	22
Table 2. Range of Vickers Microhardness Results of the Coated Specimens [16].....	28
Table 3. Common Reasons of ESP Failures [23].....	46
Table 4. Main Items Involved in the Flow Loop.....	50
Table 5. Instrument List and Description.....	63
Table 6. Pressure Transducer List	74
Table 7. Thermocouple List	74
Table 8. RMS Comparison among Various GVF	135
Table 9. Bill of Materials	148
Table 10. Pump Degradation Track	162
Table 11. Bushing ID Measurement	163
Table 12. Bearing OD Measurement.....	163
Table 13. Journal Bearing Clearance	164
Table 14. Sleeve Bearing Weight Track	164
Table 15. Spacer and Upthrust Plate Weight Track	165
Table 16. Impeller and Diffuser Weight Track.....	165
Table 17. Impeller Intake Labyrinth Diameter.....	166
Table 18. Impeller Discharge Labyrinth Diameter	166
Table 19. Diffuser Suction Labyrinth Diameter.....	166
Table 20. Diffuser Discharge Labyrinth Diameter.....	166

Table 21. Impeller Intake Labyrinth Clearance.....	166
Table 22. Impeller Discharge Labyrinth Clearance	166

CHAPTER I

INTRODUCTION

Electrical Submersible Pump (ESP) has been widely used in oil production as one of the efficient processes of artificial lift. Inside the ESP, liquid production will firstly be subjected to centrifugal forces generated by a high rotational speed impeller, and then its kinetic energy is converted to pressure in the diffuser. Multiple stages assembly of impeller and diffuser provide enough pressure rise for moving the well stream to the surface.

Since the Russian Armais Arutunoff invented ESP in the late 1910s, ESP equipment went through a continuous improvement during the long history [1]. Especially when mechanical seal, gas separator and variable frequency drive (VFD) were integrated in the ESP system. The life span of the ESP has increased considerably due to reduced amount of leakage, lower gas volume fraction and better accommodation to various wells.

Currently, as shown in Figure 1, ESP is second most commonly used oil production method, worldwide over 100,000 wells, particularly in Russia and US [2]. It is a great solution for high amount of total fluids production. Most ESP applied to the well in which natural flow stopped and pressure at the bottom is not sufficient to overcome total pressure losses along the flow path to the surface, so called dead well. Other than that, ESP has also been utilized in the flowing wells to increase the production rate.

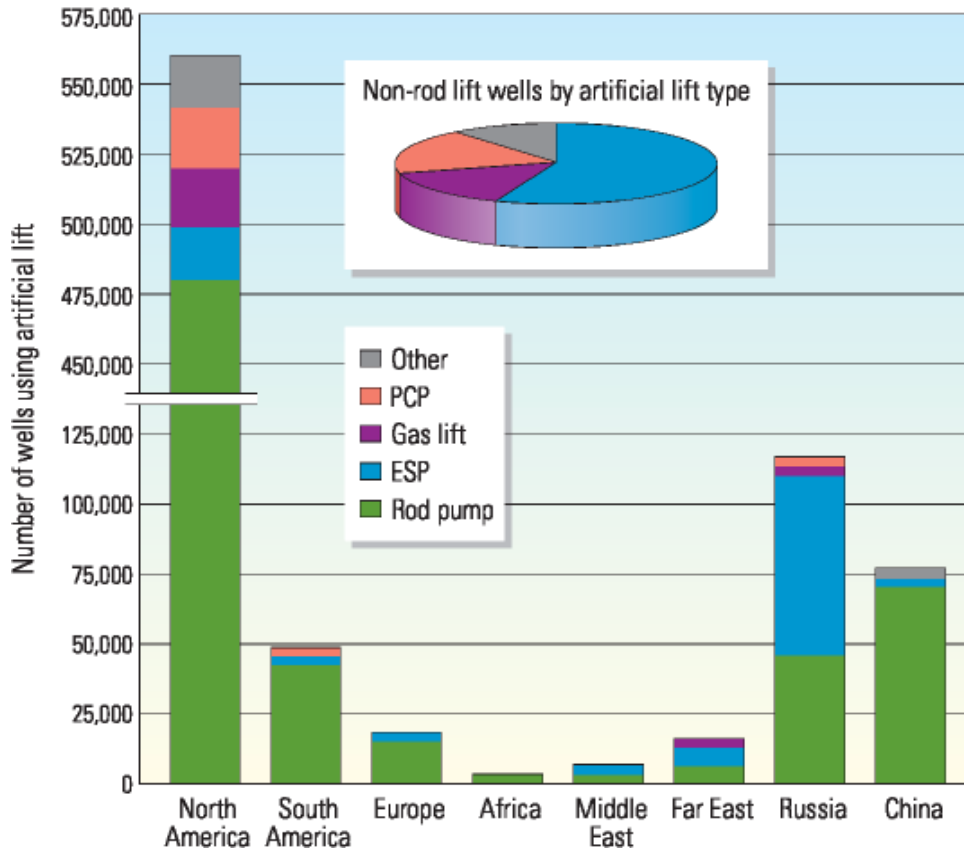


Figure 1. Artificial Lifting Method Distribution Worldwide [2]

A standard ESP system as shown below in Figure 2, includes both surface equipment and sub-surface equipment. Sub-surface key components such as multistage centrifugal pump, electrical motor, protector between motor and pump, gas separator and electrical cable extending from surface power supply to the motor. The whole assembly is submerged in the fluid to be pumped and cooled by the fluid as well. Surface equipment usually includes motor controller, surface cables and transformers.

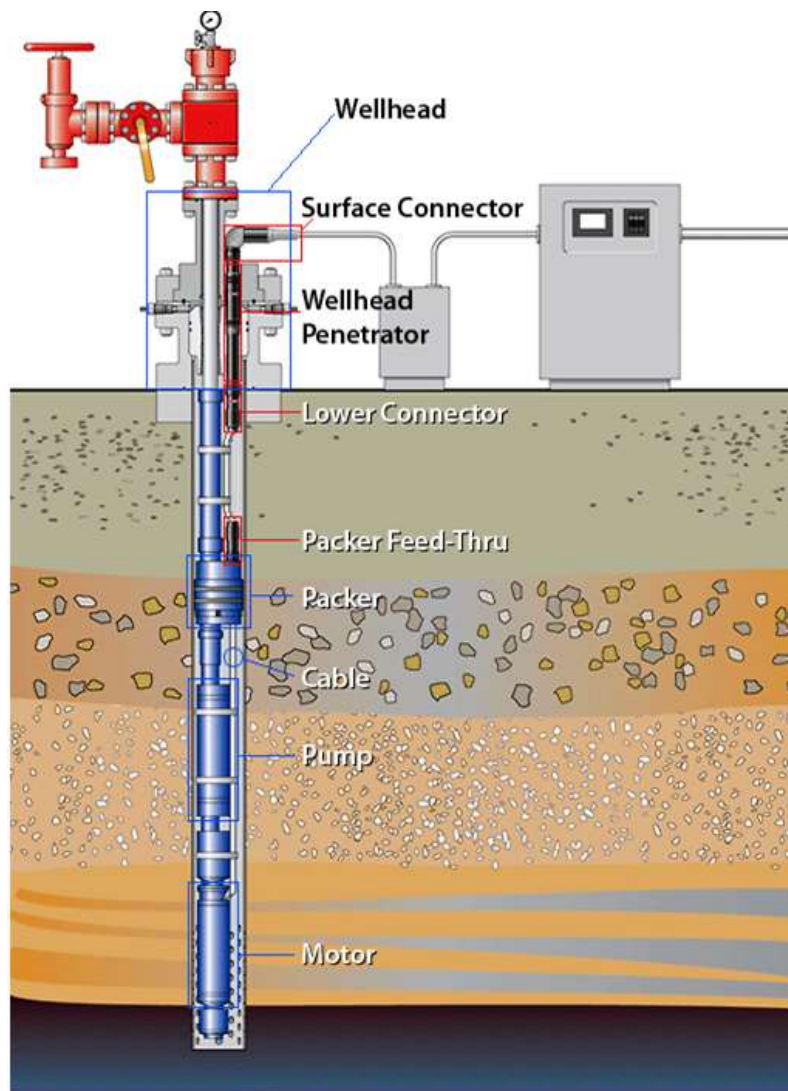


Figure 2. Conventional ESP System [3]

An ESP is built by stacking several stages of impeller and diffuser together in housing as Figure 3. Each stage includes an impeller which is rotates together with shaft and diffuser which converts the kinetic energy of production into potential energy, generates head which help lifting the fluid. Typically, there are two methods for impeller construction. The first one is called floating impeller. The bottom of impeller is touching top of diffuser at no flow condition while it can move freely during production lifting

process depending on the thrust applied on it. Although the construction is simpler, floating impeller has been limited by operating range and possibility to wear down thrust washers. The second method is compression configuration. The impellers are fixed axially to the shaft and load is transferred to the thrust bearings in the protectors. Hence, this configuration can safely operate below the recommended operating range. [4]



Figure 3. ESP Pump Assembly [5]

Generally, ESP system is an ideal artificial lift solution for extremely high liquid flow rate at medium depths and can be adjusted by deviated well conditions. In addition, since minimal surface space is required for installation, ESP can be used in the urban area and offshore environment. Meanwhile, engineers still face a series of challenges to make a more reliable ESP system in the harsh operating conditions. For example, in gassy wells, free gas present at suction inlet degrades pump efficiency and even stops liquid flow in severe operation condition. Sand or other abrasive particles in well fluids increases

erosion rate of pump components and shorten pump life span. Besides that, the extremely high cost of installation and uninstallation of ESP have to be considered ahead. Depending on the depth of well, the cost could go up to forth times the cost of a new pump when installed onshore. This amount can exceed 40 times the pump cost in subsea installations. Therefore, it is significant to emphasis on research which can help to approach a better understand of ESP and extend running life of ESP.

Current work describes the experimental facility designed and constructed to study sand and air effect on ESP. The WJE-1000 ESP as shown in Figure 4 which is manufactured by Baker Hughes has been involved in this study. It is a customized ESP especially for laboratory testing purpose. Three stages of impeller and diffuser are installed and hermetically sealed in a 10.25” diameter cylindrical casing. Fixed impeller and mixture flow design has been utilized on this pump. In order to study on the pump’s vibration, two accelerometers have been installed at the pump intake and discharge location and ten proximity probes have been inserted from the side of the casing to record shaft and impeller motion. Detailed setup will be given in the experimental test set up section. This pump is driven by a 250 HP three-phase two-pole induction motor and controlled by a VFD controller hooked up to the system.

Initially, 100 mesh sand has been injected to pump at concentration of 2 gram/L which is about ten times the severe running conditions in the field to ensure the testing can be finished in a proper time manner. ESP kept running up to 125 hours of two-phase testing

(water-sand) performed during testing, then is followed by a 65 hours three-phase (water-sand-air) testing. Sand concentration will maintain at 2 gram/L and air gas volume fraction (GVF) is 15%. Pump performance has been recorded and periodical disassemblies are also executed during the testing procedure to record measurement data on all critical components such as impeller, diffuser and bearings, etc.

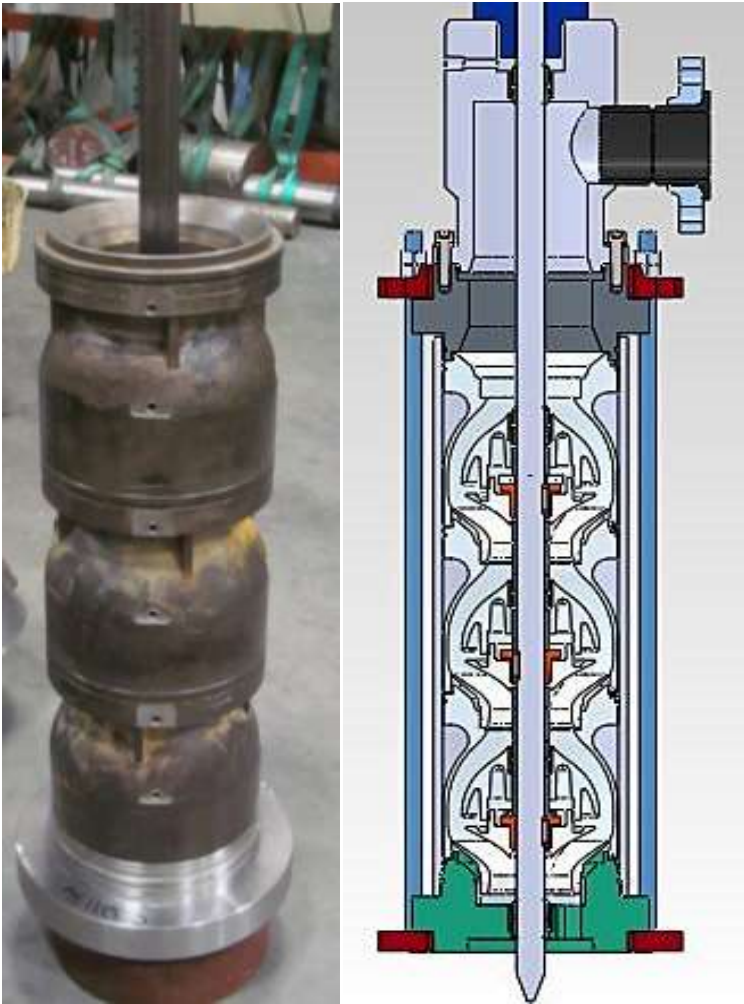


Figure 4. WJE-1000 ESP Assembly

A thorough and comprehensive analysis involving pump performance, component wear measurement and vibration signal has been performed in this experimental testing. The analysis is aiming to provide a clear clue as to how the sand and air affect the erosion progress on each component. Furthermore, the difference in erosion progress between two-phase erosion test and three-phase erosion test is compared after completion. Besides that, a correlation among proximity probe signal, accelerometer signal and physical bearing clearance growth could possibly work out a remote monitoring method on ESP. Generally, this work will help approach a better understand on ESP and propose design improvement to minimize failures possibility.

CHAPTER II

OBJECTIVES

This course of study aims to experimentally analyze the performance of an electrical submersible pump undergoing an erosive environment which includes both two-phase (water-sand) and three-phase (water-sand-air) conditions. A comprehensive analysis involving pump performance, components wear measurement and vibration signature is performed in order to provide an idea of air effect in the erosion process. During erosion testing, ESP has been scheduled for disassembly inspection, especially on the primary component such as impeller, diffuser, thrust plate and journal bearings. Periodically performance test and disassembly inspection at target time will benefit for finding out the reason of ESP degradation. By comparing the behavior of ESP in two-phase test and three-phase test, it is helpful to have a better understand on the effect of air in the degradation process when ESP is operating in an erosive environment. In oil & gas industry, there is a hypothesis that air usually has negative effect for the ESP system both on the performance wise and reliability wise. However, there is no enough evidence and clear explanations to prove this point at current time. This experiment will provide the fact which can either support or object to this hypothesis. Equally important, vibration analysis will be executed to find out pump performance behavior when air involved into the production line. Besides this, the vibration analysis also plays a role to explore a remote way to estimate downhole pump physical wear in the bearing system. In summary, this work will help approach a better understand on ESP and propose

design improvement to extend the lifespan of downhole ESP and minimize failures possibility when it is running in the harsh environment.

CHAPTER III

LITERATURE REVIEW

3.1. Electrical Submersible Pumps

In the early time of oil wells, the flow can reach surface naturally as so called flowing wells. The pressure of the well bottom is sufficient to overcome the total pressure losses along the flow path to the surface. When the pressure at bottom is not able to meet the criterion, flow will stop and natural flowing well becomes dead well. Artificial lifting mainly focuses on recovering flow from the dead well and increases the flow rate of the flowing well. Typically, a pump assembly is submerged below the oil level in the well to provide enough pressure rise in order to transport oil onto surface. Air lifting and jet lifting also belong to this category. [6]

The submersible pump of an ESP system includes multistage centrifugal pumps which are operating vertically. The development of construction and operation of the ESP system has went through a long history. However, the basic principle still keeps the same. The kinetic energy generated by the high rotating speed of the impeller converts to pressure energy in the diffuser. [6]

General advantages of using ESP units can be summed up as follows, based on [7-9] :

- Relatively high production rate
- Lifting depths are deeper than general application such as sucker rod pump
- Efficiency can maintain over 50%

- Suitable for different well and surrounding condition
- Low maintenance frequency
- Dominant less surface space
- Good corrosion resistance

General disadvantages are listed below [6]:

- Require a reliable source of high voltage electric power
- Need a proper installation design according to various well conditions
- Free gas present at suction side degrades the general efficiency of the ESP. An gas separator at extra cost is required to be installed when operating in a gassy well
- Sand or other solid particles increase the erosion rate and potentially cause system failures.
- Difficult to repair of ESP equipment in oilfield
- High well temperature limitation
- Not suitable for transportation of high viscosity oils

A typical centrifugal pump is a machine usually driven by a motor providing a rotary motion. It consists of two basic components, the rotor with multiple vanes and the stator which helps to convert kinetic energy to potential energy. The stationary part also called diffuser in the ESP system [6]. The basic nomenclature of diffuser and impeller can be found in Figure 5.

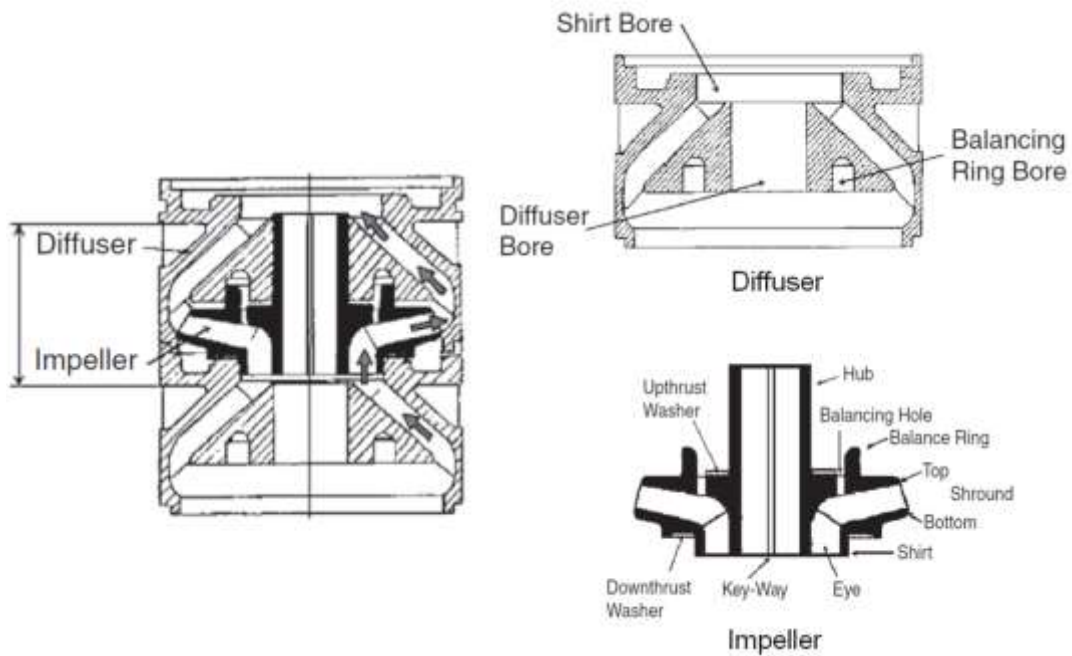


Figure 5. Nomenclature of Impeller and Diffuser [6]

Depending on the direction of impeller discharge, centrifugal pump can be classified in to three types, radial, axial and mixed. In liquid ESP, only radial flow and mixture flow are utilized. Comparing to mixture flow, radial flow usually applied in light production condition which is less than 3,000 bpd. A basic configuration comparison between radial flow pump and mixed flow pump can be found in Figure 6.

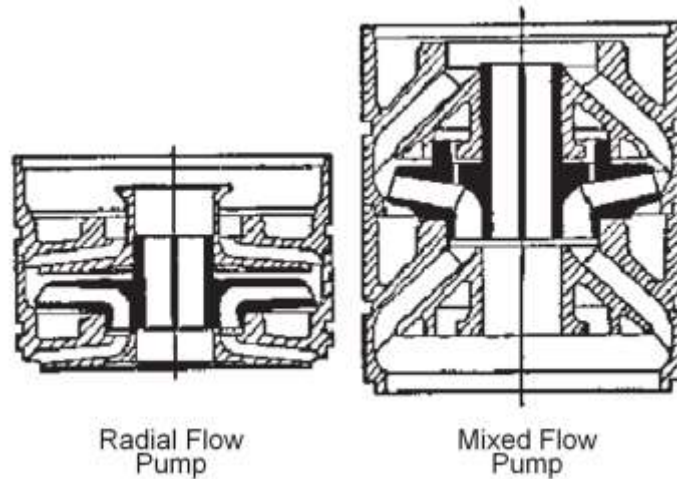


Figure 6. Configuration of Radial Flow Pump and Mixed Flow Pump[6]

The specific speed, N_s , is introduced in order to make different designs. It represents the required rotational speed (SPM) to generate a liquid flow rate of 1 gallon per minute for 1 ft of head within an impeller. All the pumps which apply this rule need have a similar geometry for investigation. The equation as following shows all parameters that are taken at the best efficiency point (BEP) of the pump. [6]

$$N_s = \frac{N\sqrt{Q}}{H^{0.75}} \quad (3.1)$$

where: N =pump speed, RPM,

Q =pumping rate, gpm,

H =head developed by one stage, ft.

Impeller design and specific speed are in close correlation. Due the various design of the pumps, the character value changes. Normally, the radial discharge pumps are suitable for the range of $500 < N_s < 1,800$. The maximum N_s of a mixed flow pumps can reach

up to 4,500. The purely radial impellers have relatively low N_s values and head generation is relied mostly on the centrifugal force. For mixed flow impeller, part of the head is produced from centrifugal force and the other part of head developed by the lifting force of the impellers. [6]

As we discussed before, centrifugal pump such as ESP transforms mechanical energy provided from motor driving to kinetic energy of liquid. Although the pressure rise of the pump varies due to different liquid density, the head will remain constant for a given pump at a certain flow rate. Therefore, it is convenient to discuss head in all performance calculations for all centrifugal pumps [6]. “The head developed by an impeller under ideal operating conditions (neglecting frictional and other losses) is calculated from the increase of centrifugal force acting on the liquid contained between two successive vanes, by assuming an infinite number of vanes” [10]. The ideal pump liquid flow rate from Euler equation shows a straight line in Figure 7. However, due the finite number of the vane and circulating flow as noticed usually, the actual head curve is lower than the theoretical line. [6]

Generally, as the liquid flow rate gradually increases, more hydraulic losses will present due to high level of fluid friction and diffusion losses in the impeller. Also, shock losses will show up if liquid flow rate is off from best efficiency point (BEP) or suddenly direction changes at suction or exit of impellers. Meanwhile, leakage losses will be noticed at any flow rate due to the liquid passing through the clearance between rotating

and stationary parts of the pump such as bearing clearance, labyrinth seal and balance hole. Increasing flow rate can reduce the amount of leakage losses.

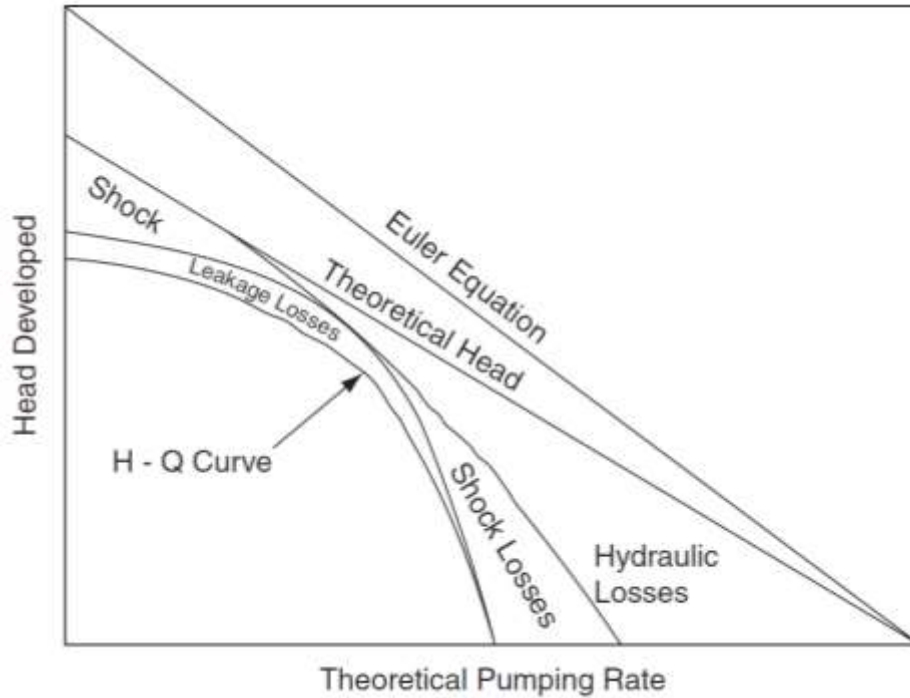


Figure 7. Derivation of Pump H-Q Curve [6]

Since ESP have several types of losses, the brake horsepower supply must overcome useful fluid power for the given flow rate plus all the energy losses. Fluid power is proportional to the liquid flow rate and the pressure rise of product. Therefore, it has two zero point at either flow rate is zero or pressure rise is zero as shown in Figure 8. At the low and high flow rates which are off BEP, turbulent losses are significant. As the flow rate moving towards the BEP, the turbulent loss diminishes. Frictional energy losses in the impeller passage increases proportionally with the production flow rate. Meanwhile,

liquid leakage, disk friction and bearing losses keep almost constant regardless the flow rate. [6]

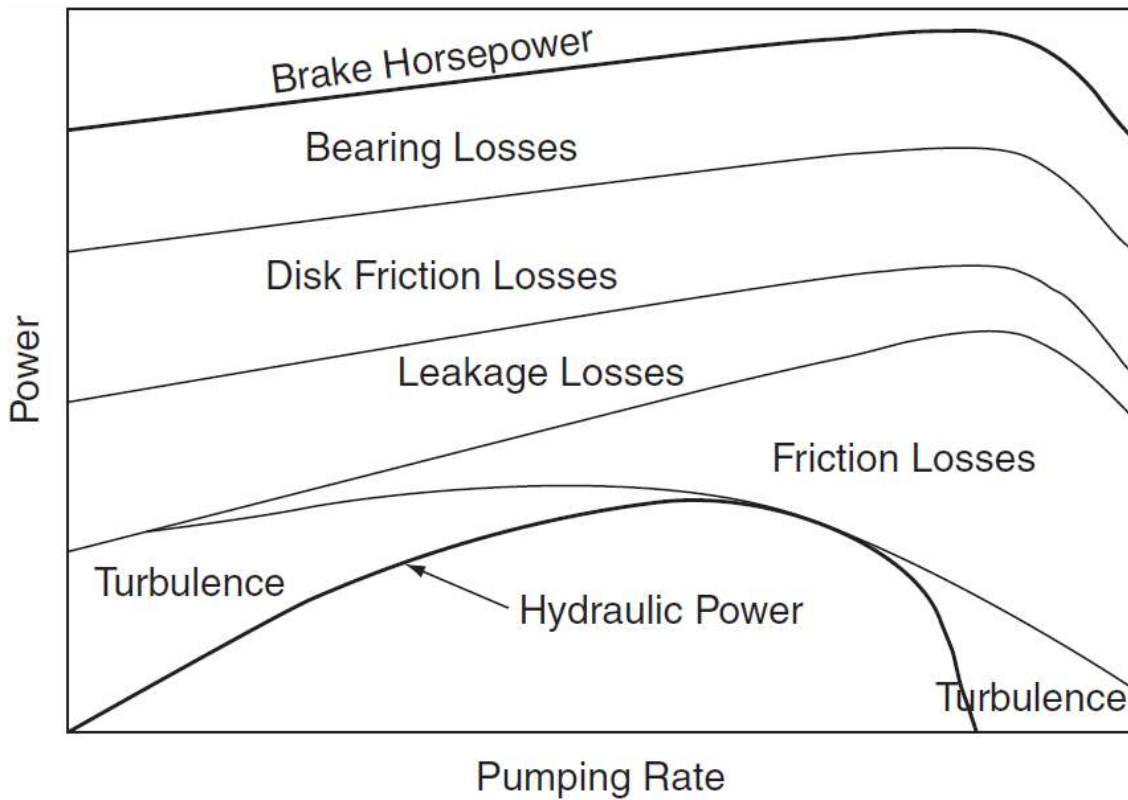


Figure 8. Power Conditions in ESP Stages [6]

As following equation, the efficiency of the ESP is decided by fluid power dividing by brake horsepower (BHP).

$$\eta_p = \frac{P_{fluid}}{BHP} \quad (3.2)$$

where: η_p = Efficiency of the ESP

P_{Fluid} = Fluid Power

BHP = Brake Horsepower

In order to evaluate the performance of the ESP, pump curve is introduced. A typical pump curve includes pressure rise, brake horsepower (BHP) and efficiency versus product flow rate. In addition to that, the number of stages has to be pointed out along with curve. ESP performance testing procedure usually starts by running it at a desired speed, then varying fluid flow rate by throttling the flow at pump discharges. During test, all key parameters such as flow rate, pressure at suction and discharge, temperature and brake horse power input need to be recorded at various flow rates. Normally, brake horsepower (BHP) can be monitored through Variable Frequency Drive (VFD) output or calculated through the following formula.

$$BHP = T * RPM \quad (3.3)$$

Where: BHP = Brake Horsepower

T = Torque on the haft

RPM = Rotational Velocity of the Shaft

Fluid horsepower (FHP) can be calculated by following the equation below.

$$FHP = Q * \Delta P \quad (3.4)$$

Where: FHP = Fluid Horsepower

Q = Fluid Flow Rate

ΔP = Pressure Rise

Since ESP is used mostly in pumping fluid, the pressure at any place inside the pump must be maintained above the saturated vapor pressure of the liquid at the operating

temperature. Otherwise, cavitation will occur. Small bubbles will start to form and be taken to location with higher pressure. Once pressure returns back above the saturated vapor again, bubbles will collapse suddenly. This phenomenon may lead to severely mechanical damage due to erosion on the metal part and significant drop on pump performance. According to this possible issue in the system, minimum pressure is required at suction conditions to avoid that. This is known as the net positive suction head (NPSH). This measured parameter of ESP is the difference between the absolute casing pressure available at the first stage impeller and the vapor pressure. NPSH has to remain higher than minimum NPSH value for a given pump. However, this is not a severe problem in the oil field since an adequate NPSH is always available length of liquid column above the pump intake. [6]

During the operation process, multiple types of unbalanced forces appear on the impeller and directly transmitted to the pump shaft. Generally speaking, there are mainly two types of forces, one is radial force and the other is axial force. Axial forces always include two elements which are static force and dynamic force. Static force comes from the weight of the pump part components such as impeller, diffuser, shaft and all the bearing sleeves. The direction of the static force is always downward. Dynamic forces are results of liquid pumping process.

Figure 9 shows conventional axial forces on the mixed flow impeller. “As shown, the hydraulic forces acting on the different surfaces of the top and bottom shrouds are

greater toward the periphery of the impeller because of the rotation of the fluid. Forces exerted by the discharge pressure are partially balanced because they oppose each other. Suction pressure, on the other hand, gives rise to an upward pointing force. As stated before, the sum of these forces gives a downward pointing net force. In addition to this, an inertial force arises due to the axial change in the momentum of the flowing fluid between the discharge and suction conditions. This upward pointing component increases the net axial forces. The sum of the previous forces gives the dynamic components of the impeller's axial thrust which, depending on the impeller design and the flow rate, can be zero (balanced state), can point upward (upthrust condition) or downward (downthrust condition). ESP are designed to be balanced near the best efficiency point (BEP)". [6]

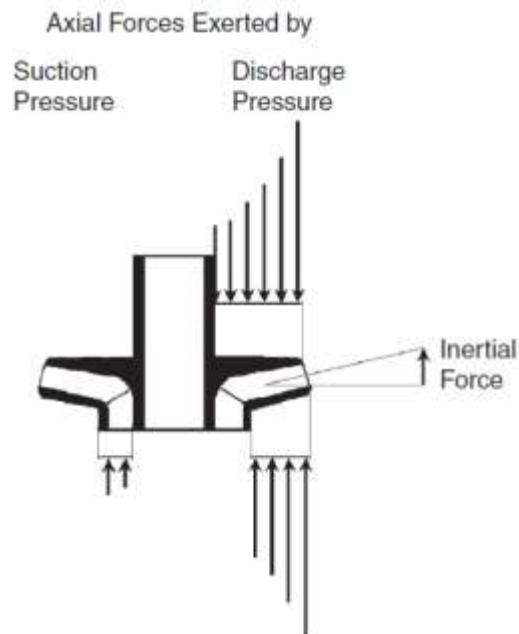


Figure 9. Distribution of Axial Forces in a Mixed Flow Impeller [6]

If the thrust bearing can't take the proper capacity of the axial force, this force components can induce the axial movement of rotating parts including the impeller and the shaft. This phenomenon may result in mechanical damage of the pump. Consequently, it is critical to balance the axial force components when installing tens or hundreds of stages of ESP. [6]

Initially, most centrifugal pumps operate at a constant speed because electrical motor is supplied with a constant frequency, no matter it is installed on the surface or downhole environment. However, the variable speed operation has been investigated and the basic rules have been investigated [11]. These rules are called affinity laws which include the relationships between the rotational speed of pump and performance parameters of the pump. The above rules can be expressed mathematically in following equations.

$$Q_2 = Q_1 \left(\frac{N_2}{N_1} \right) \quad (3.5)$$

$$H_2 = H_1 \left(\frac{N_2}{N_1} \right)^2 \quad (3.6)$$

$$BHP_2 = BHP_1 \left(\frac{N_2}{N_1} \right)^3 \quad (3.7)$$

where: N = Pump Rotational Speed

Q = Volume Flow Rate

H = Pump Head

BHP = Required Brake Horsepower

3.2. Erosion Study of ESP

Centrifugal pumps are widely used in transporting solid-liquid mixtures (slurries) with applications in oil & gas industry, chemical industry, coal industry and mining industry. One concern about slurry delivering through centrifugal pump is the erosion damage of the pump components. Erosion in slurry pumps occurs due to two mechanisms which are particle impact and sliding (scouring) action [12]. In dilute slurries, erosion is likely to be more due to particle impact. Dilute slurry flow in slurry transportation is of significance in handling sewage, silted waters and certain dredging and mining applications. In such situations, the absence of a protective sliding bed combined with appreciable deviations in the trajectories of the particles from the streamlines of the carrier phase facilitates wear by particle impact (known as impact wear). Particle impact could also be directional or random (due to turbulence). [13]

In Figure 10 of the fix impeller ESP, the possible locations which are suffered from sand have been pointed out. Normally, in the fixed impeller ESP, the wear location includes erosion in the pump stage, abrasive wear in the radial bearings and abrasive wear in the thrust washers. In industry, the severity of the sand problem has been defined base on the sand concentration like Table 1.

Table 1. Sand Problem Level [6]

concentration, mg/liter	definition
less than 10	light
11-50	moderate
51-200	heavy
more than 200	severe

Erosion in the ESP is caused by the abrasive solid particles impinging the metal surfaces as sandblasting process. The wear rate is greater for large and rough solid particles than for small and smooth ones. It has been found that wear is proportional to the square of flow velocity because the destructive potential of the solids is related to their kinetic energy. Although the significant erosion has been noticed on the pump stages, it rarely becomes the root reason of failures because pump usually failed for other reasons before the stages are worn out. [6]

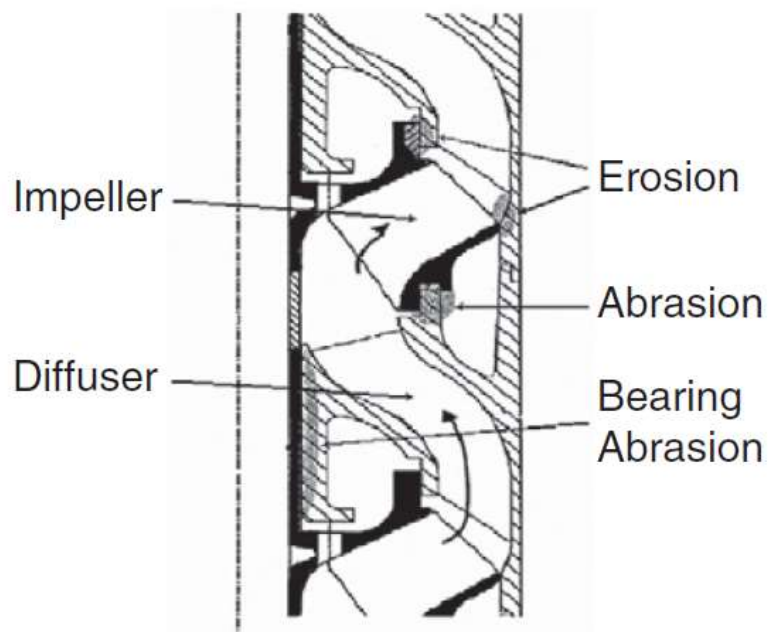


Figure 10. Sand Problem Area in Fixed Impeller ESP [6]

Radial wear happened in the tiny clearance of the pump such as bearing clearance and impeller seals. Normally, the same type of material is used to make journal and bearing. Although clearances are small, the fine sand particles are able to enter the clearance between the bearing and the journal. After entering the bearing clearance space, sand particles are crushed between the stationary and the rotating surfaces. Meanwhile, metal are removed from the bearing surfaces. Some small particles may be carried by the fluid flow without contacting the bearing surface. The wear rate in the bearing surface is highly depends on the liquid flow rate since the amount of particles entering the clearance changes as well. The growth of the bearing clearance brings about the radial instability and higher shaft eccentricity value. The excessive clearance will lead to severe vibration on the shaft and finally breakdown the system. [6]

According to Gabor Takacs [6], the severity of abrasive damage in ESP increases in the following order:

1. Erosion in impellers and diffusers
2. Axial wear in thrust bearings and up and downthrust washers in floater pumps
3. Radial wear in radial (journal) bearings

Also, some solutions to reduce radial wear have been mentioned in Gabor Takacs's ESP Manual. The earliest solution is coming from King et al [14]. As shown in Figure 11, a special resilient bushing (usually rubber) has been pressed into diffuser bore where shaft is rotating. On the contacting surface of bearing, the axial grooves have been

manufactured in order to continuously wash the particle through clearance by product. Another choice to reduce the wear is to harden the wearing surface materials by inserting the special material with great hardness such as silicon carbide, tungsten carbide and ceramics into diffuser and use the same hardness materials for bearing. The disadvantage is hard materials are very brittle and are easily fractured if loaded at one point or on a line.

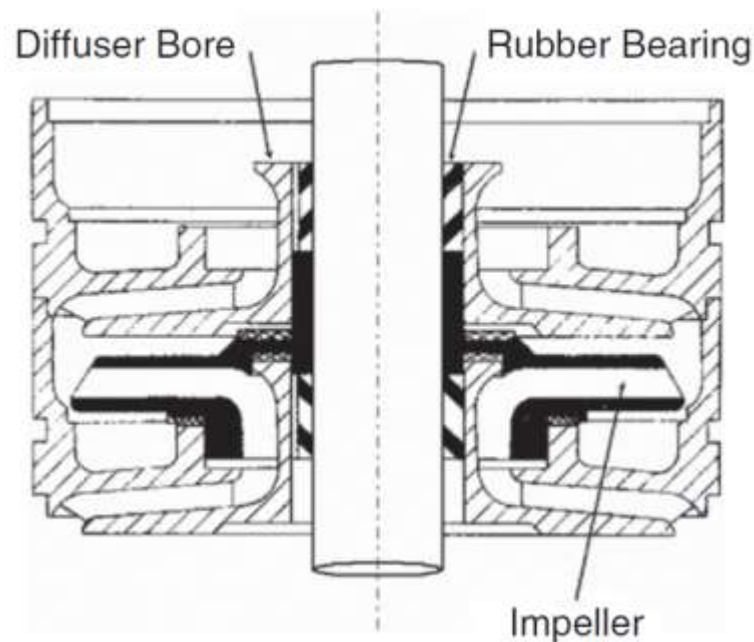


Figure 11. Construction of a Resilient Radial Bearing [6]

In ESP, the abrasive solid particles have great effect on the operation of the ESP pump since the particles may impinge the pump surface. Especially in the high velocity region, abrasive wear is one of the most critical effects on the stability of the pumps. [14]

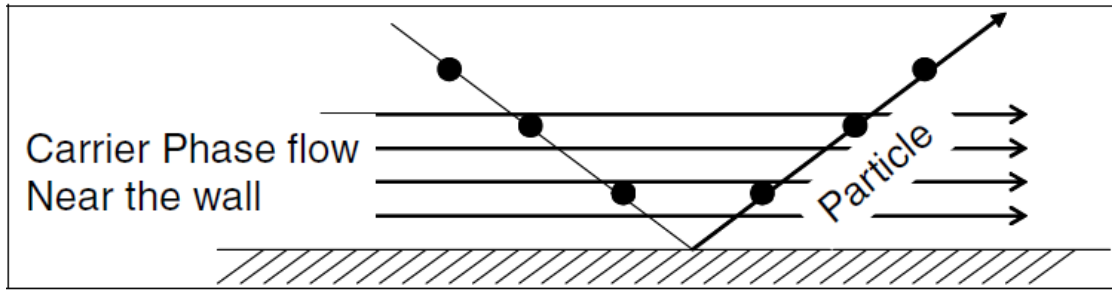


Figure 12. Particle Impact Erosion Due to the Deviation of the Particle [15]

Pagalthivarthi et al [15] performed a CFD (Computational Fluid Dynamics) prediction of erosion wear in centrifugal slurry pumps for dilute slurry flow as shown in Figure 12. A two-dimensional centrifugal pump model has been developed by using commercial code Fluent[®]. Erosion wear is calculated through wear mechanisms in which the flow properties of the slurry, slurry material and casing material are related together with certain empirical constants. Generally, the wear prediction comprises of two steps. First step is to compute the two-phase flow field in the centrifugal pump then followed by relating the computed flow field to the local wear rate through experimental results. The impact wear parameter given as $V_s^3 C_s$ represents the impact wear rate along the casing wall. Its variation is non-uniform along the casing wall and it monotonically increases from the tongue region to the belly region of the casing. Reduction in the peak value of the impact wear parameter and making it more uniform by applying several operational and geometry modifications is the goal for this study. Also, the different erosion rates with various operation conditions are compared. The impact wear parameter varies with different flow rates along the casing wall. The trends of variation can be seen in Figure 13 where with reduced flow rate, it is found that the magnitude of the impact wear

parameter reduces and it tends to even out along the casing wall. At the lowest RPM, the impact wear parameter is found to be minimum and at the highest RPM 1900 RPM, the normalized impact wear parameter peak value is maximum at 1 compared to a maximum of 0.76 at 1500 RPM in Figure 14. In addition, particle size is will affect the impact wear parameter. Four mono-size slurries with particle sizes of 100 μm , 200 μm , 500 μm and 1000 μm , respectively, are studied to determine the effect on impact wear parameter along the casing wall in Figure 15.

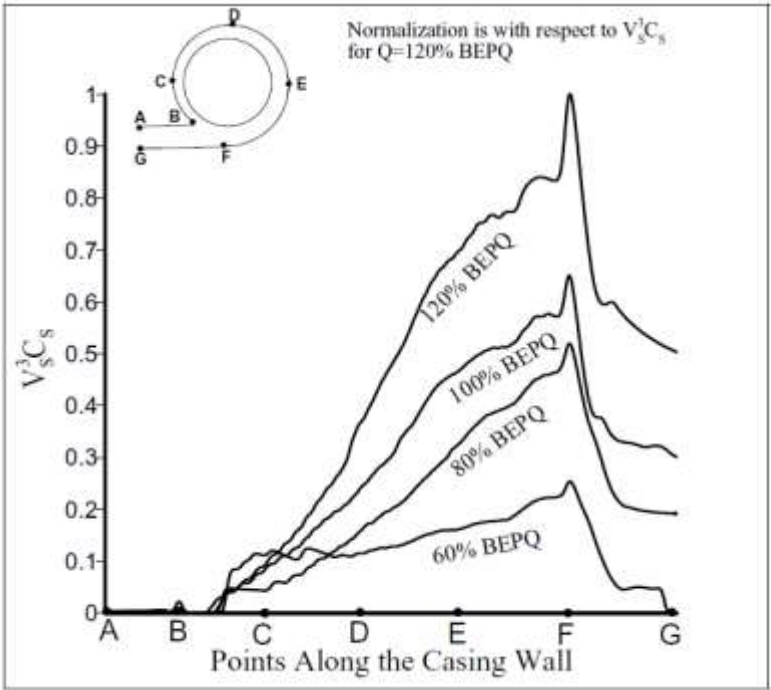


Figure 13. Comparison of Impact Wear Rate Parameter with Different Flow Rate [15]

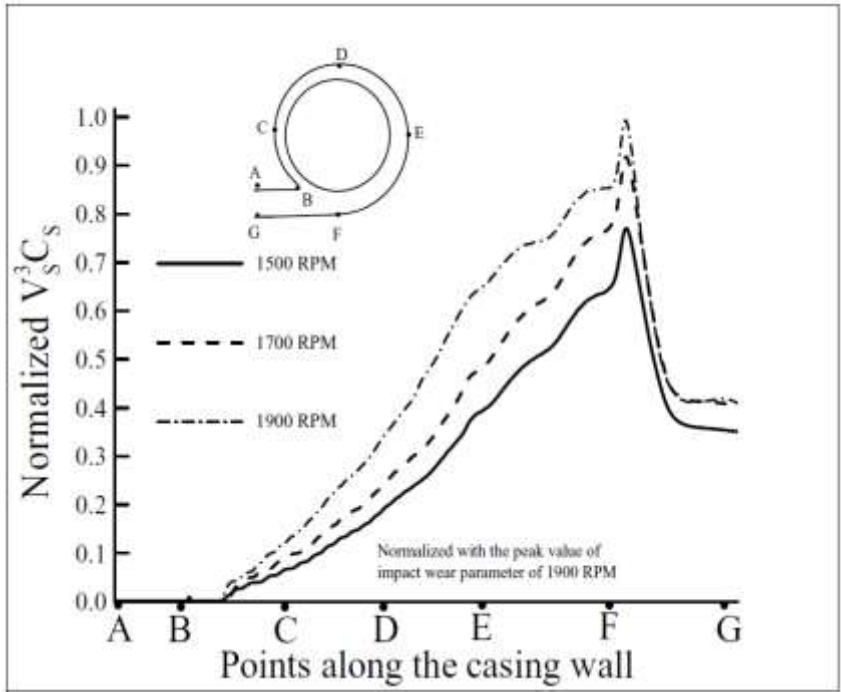


Figure 14. Comparison of Impact Wear Rate with Different Pump Speed [15]

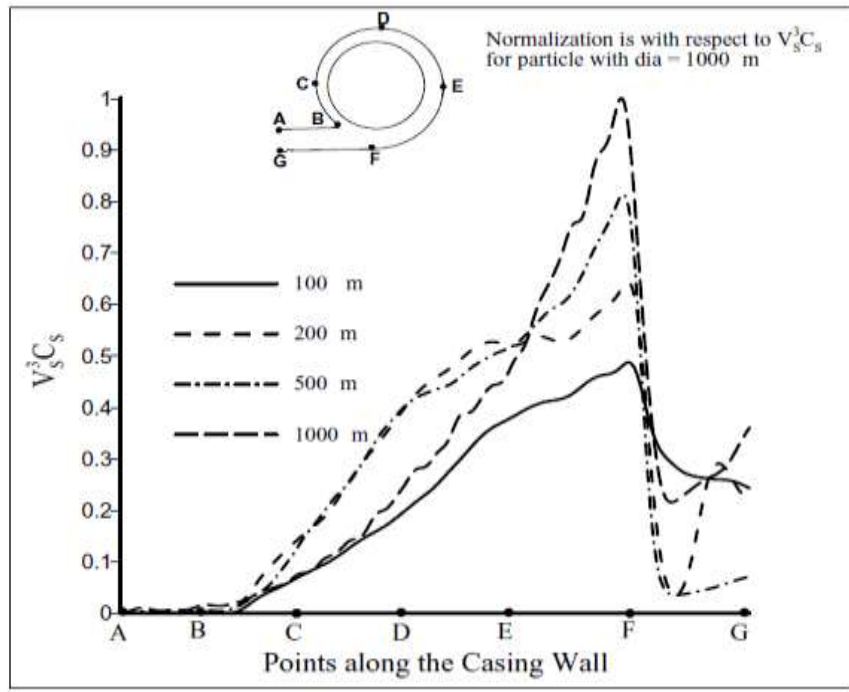


Figure 15. Comparison of Impact Wear Rate with Different Particle Size [15]

Hadjiyannis et al [16] conducted an erosion study of submersible pumps both on experimental testing and computational modeling in order to develop a methodology for selecting appropriate protective coatings. Initially, the study focused on selection of the most proper coatings using an experimental procedure which involves nano-indentations, impact tests and 3D-surface topography. The coatings studied were plasma and HVOF which is a cost effective solutions in the pump industry. According to the test results in Table 2 from microhardness tester with an applied load of 30g in 10 sec, coating HVOF SX314 and SX316 are hardest. SX115 is the softest from all three coatings. Then nano-indentations and FEM (Finite Element Method) has been utilized to analyze the mechanical elastic-plastic properties. The unit of hardness given by the test is known as the Vickers Pyramid Number (HV). The hardness number can be converted into units of Pascal. However, it is conceptually different with pressure because the area counted is the the surface of the indentation rather than the normal area to the force.

Table 2. Range of Vickers Microhardness Results of the Coated Specimens [16]

SX115 - B	SX316 - B	SX314 - B
470-580 HV	584-616 HV	584-716 HV

The next step is the determination of fatigue behavior by perpendicular and inclined impact tester in Figure 16. Impact tests combined with 3D surface topography were used for the determination of the geometric characteristics of the imprints that enabled the volume calculation of the removed material and hence the determination of the coating wear rate. The results shown in Figure 17 indicate that HVOF SX316, regardless of the fact that it does not have the best mechanical properties, it the most desirable coating

materials to prolong the life span of the pump which is operating in the erosive environment.

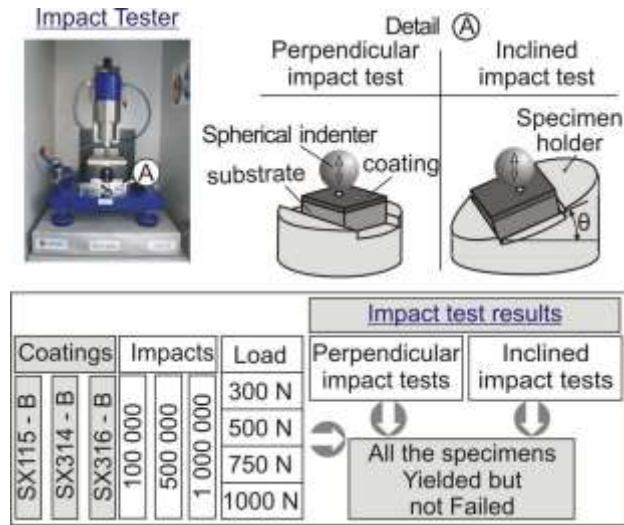


Figure 16. Inclined and Perpendicular Impact Tester [16]

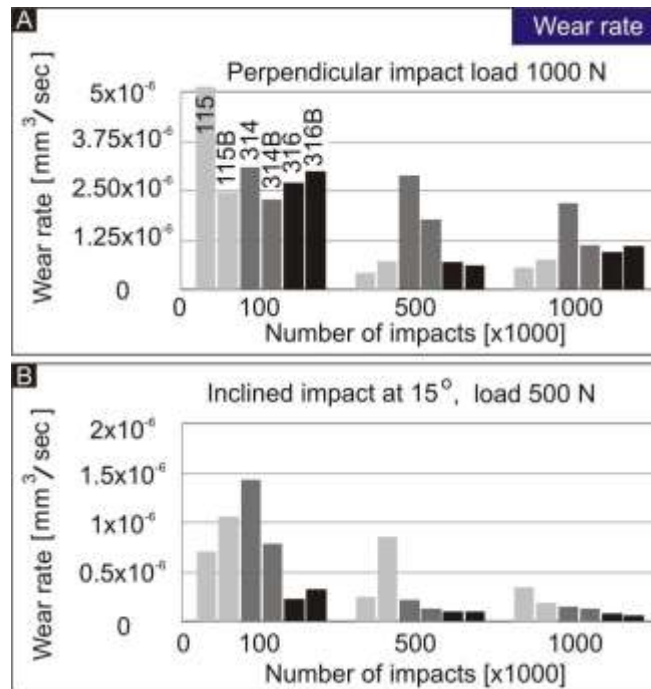


Figure 17. Wear Rates of Impact Test [16]

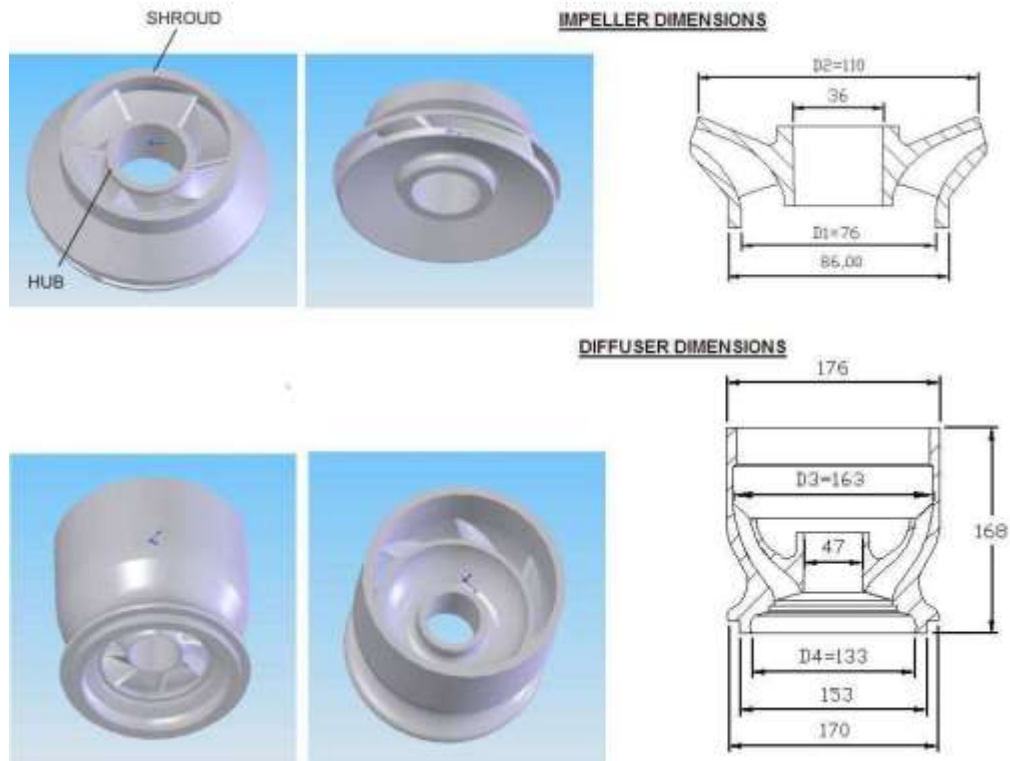


Figure 18. Impeller and Diffuser Dimensions in CFD Simulation [16]

Using CFD analysis and combined with the erosion model of Finnie the critical areas of impeller and diffuser were determined. The basic configuration and dimension is shown in the Figure 18. The CFD calculations were performed with different particle sizes without simulating the use of the protecting coating as shown in Figure 19 and Figure 20. Current step doesn't consider about the wall material, the purpose for simulation is to get the particle velocities for next step application which is going to relate computational results and experimental results together.

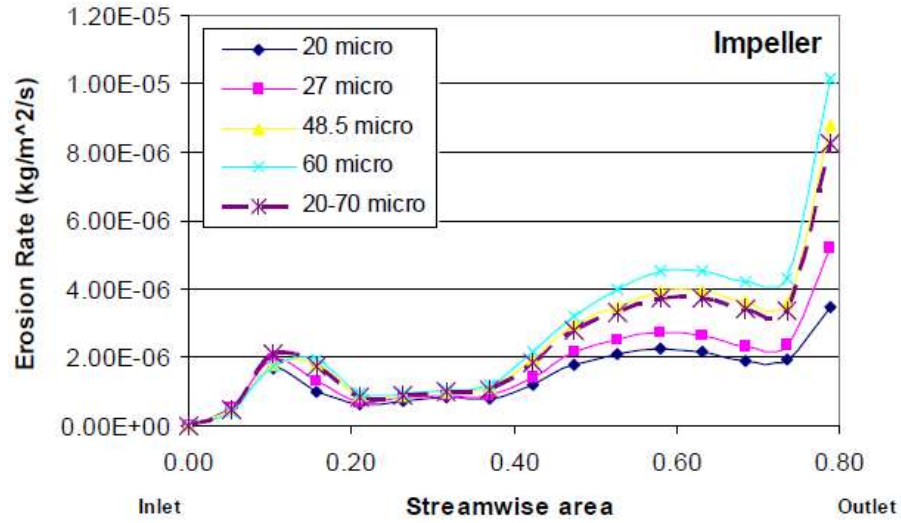


Figure 19. Effect of Particle Sizes on Erosion Rate of Impeller [16]

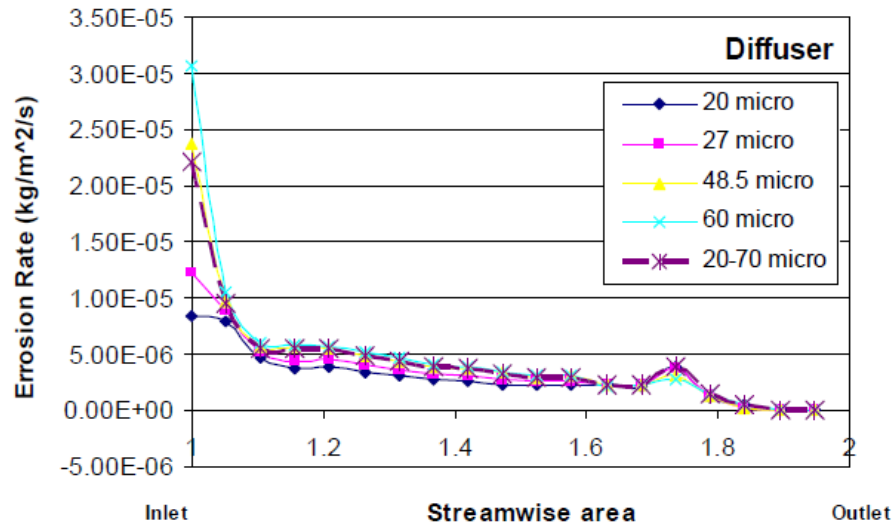


Figure 20. Effect of Particle Sized on Erosion Rate of Diffuser [16]

Using the experimental wear rates, the erosion factor k was calculated and used in the Finnie Erosion Model so as to computationally determine the erosion rates of the various coatings. According to Finnie Model, the important parameters are particles impact

velocity, the angle of the collision with the surface and wall properties where the particles are colliding. Based on the inclined impact test results, the k erosion factors depending on different materials are calculated. Computational analysis in Figure 21 shows most impact angles are dropped in the range between 15-25 °. The mathematical expression of Finnie Model is shown in the following equations.

$$E = kV_p^n f(\gamma) \quad (3.8)$$

$$f(\gamma) = \frac{1}{3} \cos^2 \gamma \quad \tan \gamma > \frac{1}{3} \quad (3.9)$$

$$f(\gamma) = \sin(2\gamma) - 3\sin^2 \gamma \quad \tan \gamma < \frac{1}{3} \quad (3.10)$$

where E = Non-dimensional Mass

k = Erosion Factor

V_p = Local Particle Velocity

γ = Impact Angle

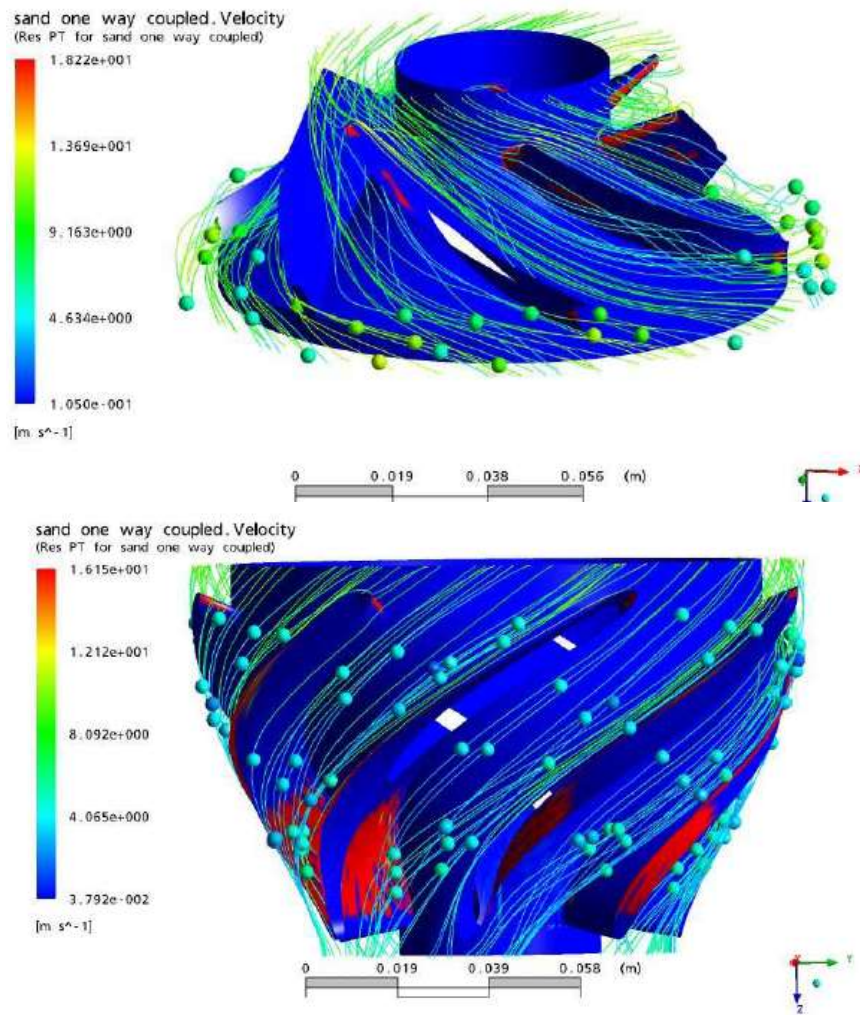


Figure 21. Particle Trajectories in Impeller and Diffuser [16]

The combination of impact test and CFD simulation finally points out the erosion factors vary with different coating materials. As shown in Figure 22 and Figure 23, the 314 coating is the hardest among all the six coatings, but is also the coating with the lower fatigue strength; therefore it is concluded that only surface hardness cannot always provide the wear resistance that is required. Results showed that the balanced combination of toughness and hardness is important for an optimum pump coating. The

abovementioned methodology was used to link the experimental and computational results in an effort to establish a computational methodology to evaluate pump coatings.

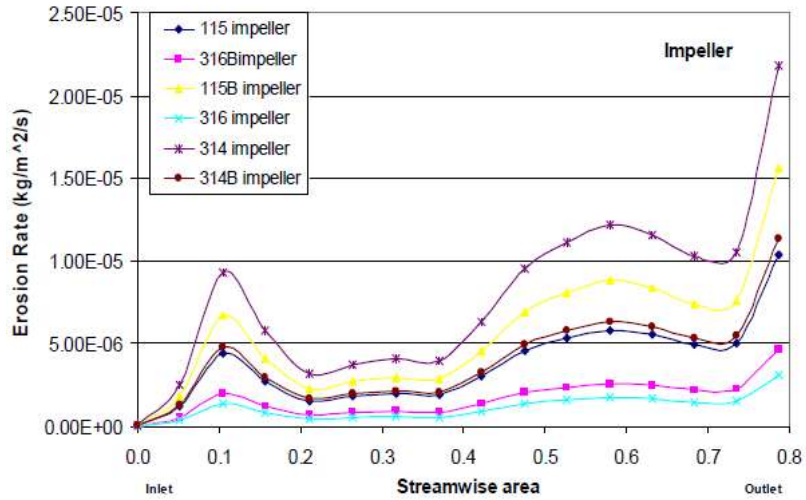


Figure 22. Erosion Rates for the Impeller with Different Coatings [16]

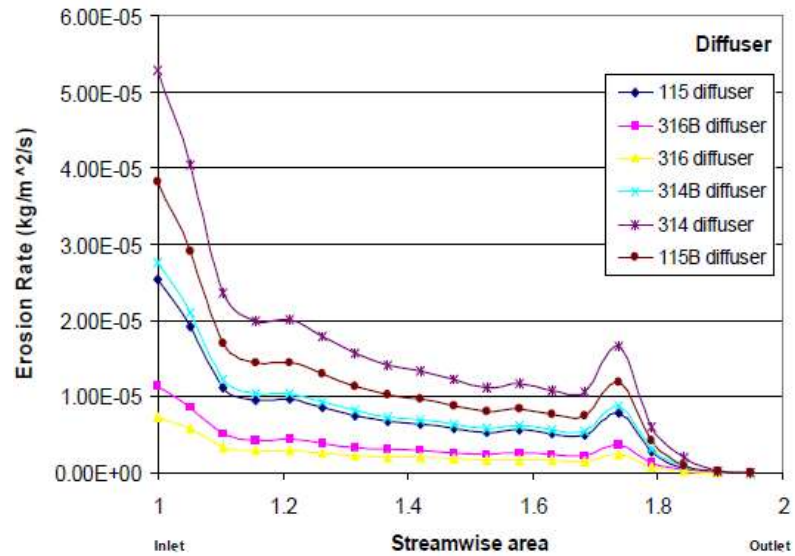


Figure 23. Erosion Rates for the Diffuser with Different Coatings [16]

Divine et al [17] studied a method to determine pump wear and remaining life by ESP pump test curve. The study shows different signatures on the pump curve associated with various types of wear which may happened during the pump operation such as radial wear, loss of compression on diffuser, upthrust wear, downthrust wear and impeller deformation.

According to their study, when radial wear appear in the operation, the clearance increases and higher leakage losses has been noticed all the way along H-q plot as shown in Figure 24. This pump which has suffered radial wear had a 15% head drop after 636 days operation at 1350 BPD. When the diffusers lost compression, a reduction at the H-q curve will look like a leakage loss. But this phenomenon will also cause a increase on the BHP curve and turns out a poor efficiency as shown in Figure 25.

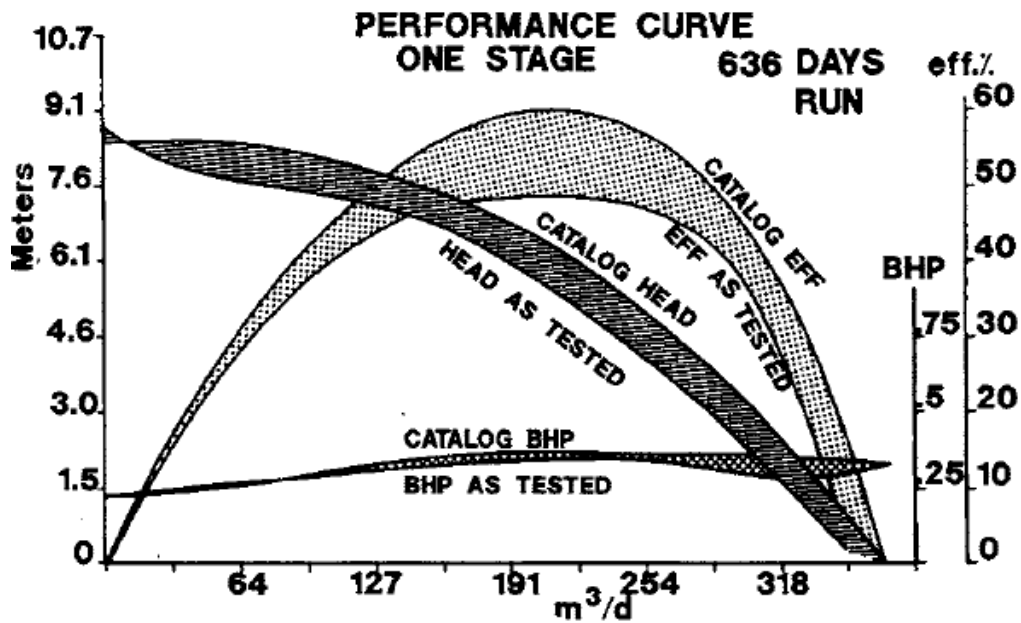


Figure 24. Pump Test Curve Showing Radial Wear [17]

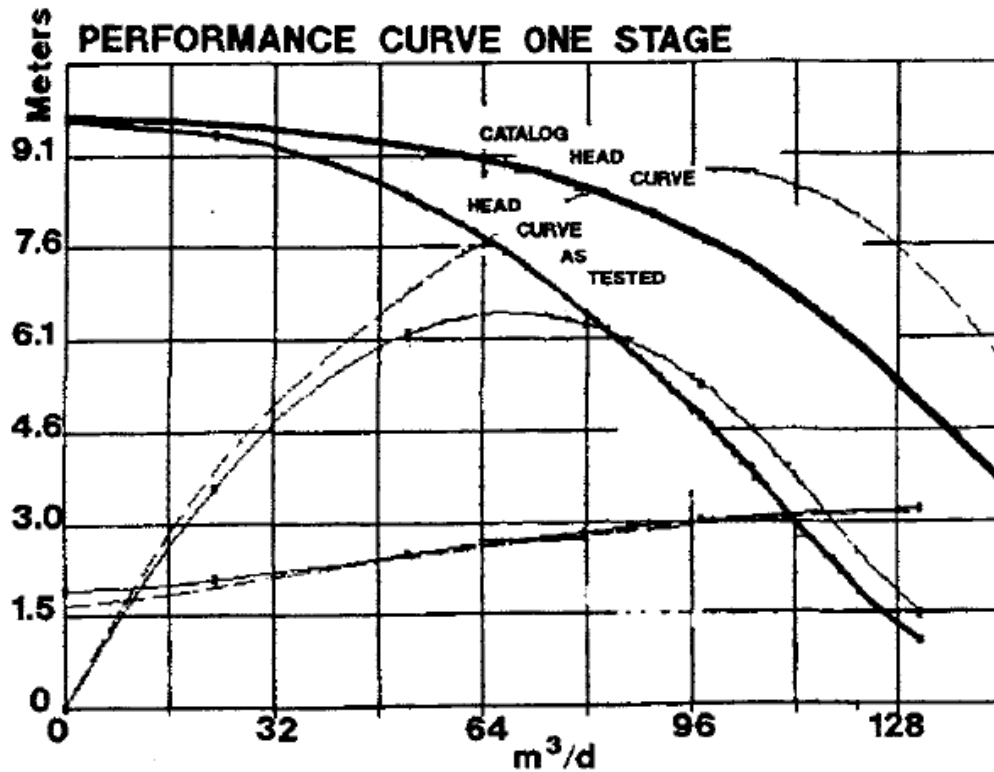


Figure 25. Pump Test Curve Showing Lost Compression [17]

Upthrust wear usually occurs when the stage is operated at flow rates located at the right side of best efficient point. The upthrust washer is the bearing surface for this force. Upthrust is not easily detectable with a test. On the other side, downthrust wear shows up when the pump is operated at the left side of best efficiency point. The ring and eye washers are the bearing surfaces for this force. As the wear on these surface increases, the bearing losses under the BHP curve in Figure 26 increase. The testing pump had 32% BHP above the catalog BHP curve.

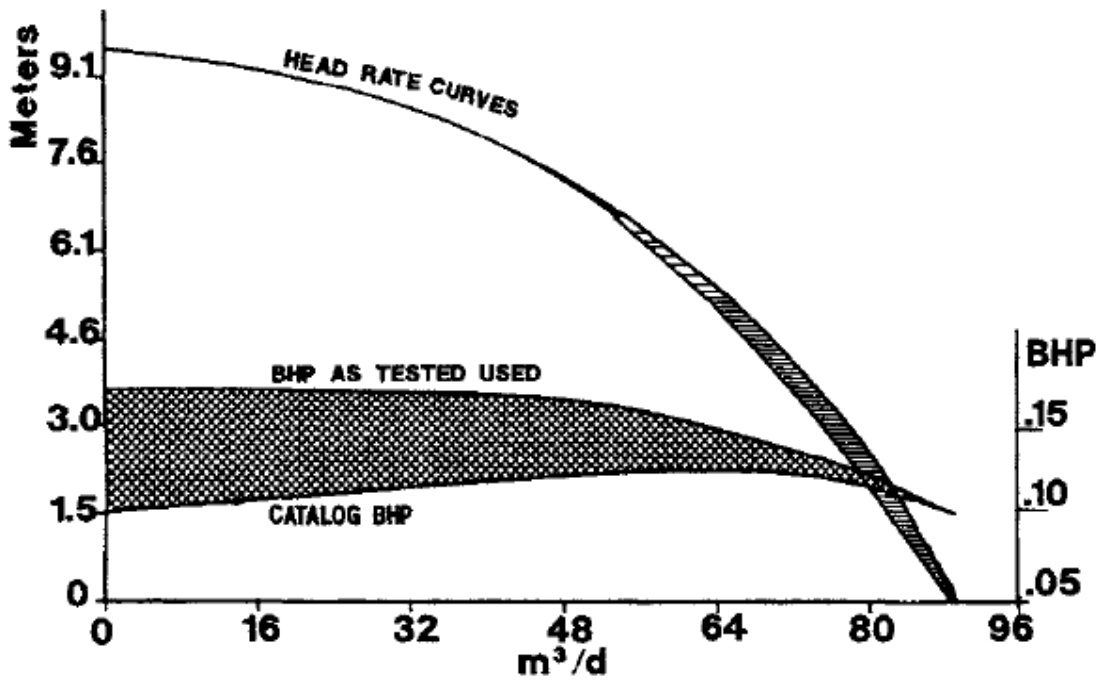


Figure 26. Pump Test Curve Showing Downthrust Wear [17]

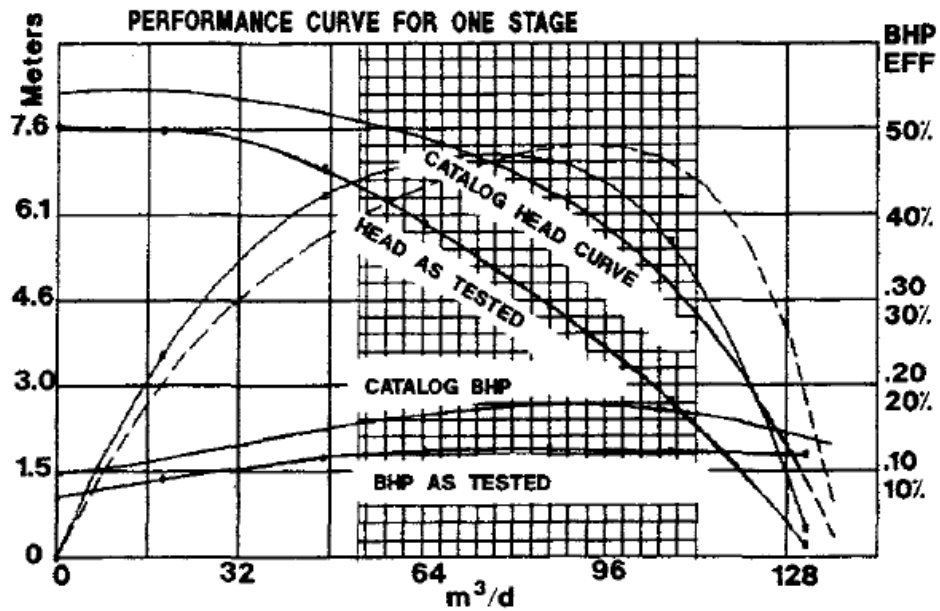


Figure 27. Pump Test Curve Showing Plastic Stages Heated and Melted [17]

Some manufacturers use plastic material for impeller designs. At elevated temperatures, which may occur during under load conditions, the impellers may deform, collapse, stick to the shaft or melt. When slightly heated, the head characteristics actually increase. The efficiency will maintain the same since BHP will increase as well. The signature of curve is shown in Figure 27.

Based on the principle of the centrifugal pumps, the presence of the free gas in the pump will degrade pump performance. The amount of kinetic energy passed on the fluid greatly depends on the fluid density. Liquid, with larger density, is able to receive more kinetic energy after conversion in the pump. On the other hand, gas cannot receive the same amount of pressure increase due to the smaller density. This principle leads to a conclusion that centrifugal pumps should always operating in a gas-free, single-phase liquid environment to ensure the reliability.

According to Gabor [6], it has been noticed that the existence of free gas will affects the operation of the ESP pump in several ways. The head developed by the pump decreased as compared to head generation with pure water. Also, the output of a pump producing gassy fluid fluctuates. In some extremely high gas volume flow (GVF) case, gas locking phenomenon may occur when no pumping action is done by the pump completely filled with gas. Usually, the solution for the gassy well is adding a gas separator between protector and pump as shown in Figure 28.

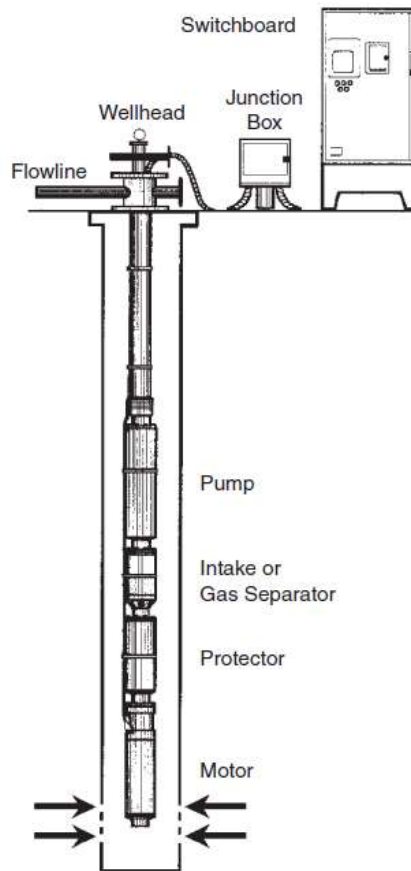


Figure 28. ESP Installation with Gas Separator [6]

As shown in Figure 29, the simplest separator which is still being used in the well is mainly suitable for low to moderate liquid and gas rates where the low separation efficiency achieved by this construction is sufficient. If the flow rate becomes high, the advanced separators with high efficiencies need to be used since liquid velocity is too high to be separated from free gas.

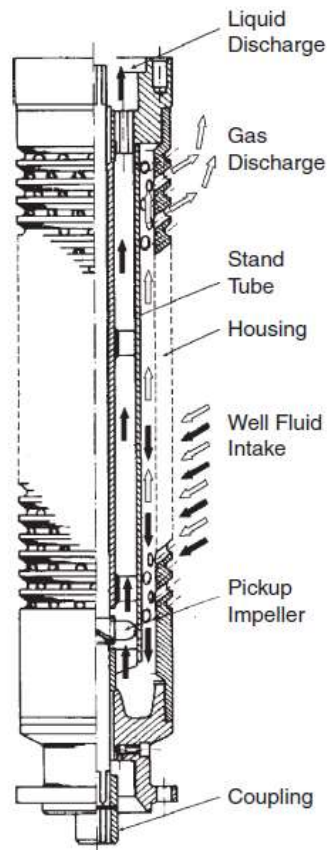


Figure 29. Gas Separator Configuration [6]

Except for adding a separator before pumping fluid, engineers also consider about self-improvement on the ESP itself. The multiple vane impellers have been invented for transporting the mixture of oil, water and gas. By using this multiphase production system, a significant cost reduce has been noticed compared to the conventional production operations in which free gas has to be filtered out before pumping and transportation. The cost of a multiphase pumping system only costs about 70% of the price for installing a conventional system. [18]

Shippen et al [19] did a study about multiphase pumping as an alternative to conventional separation. Based on the study results, the multiphase pumps are advantageous in not only reducing facilities, but also increase production rates by lower the backpressure on wells. Most types of multiphase pumps have been compared in this study. As shown in Figure 30, two kinds of multiphase pumps dropped into rotor dynamics range. One is helicon-axial pump, the other one is multi-stage centrifugal pump. However, on the down side, multiphase pumps do operate less efficiently (30-50%, depending on gas volume fraction and other factors) than conventional pumps (60-70%). However, a number of advantages abovementioned still make multiphase pumps a durable plan in oil production.

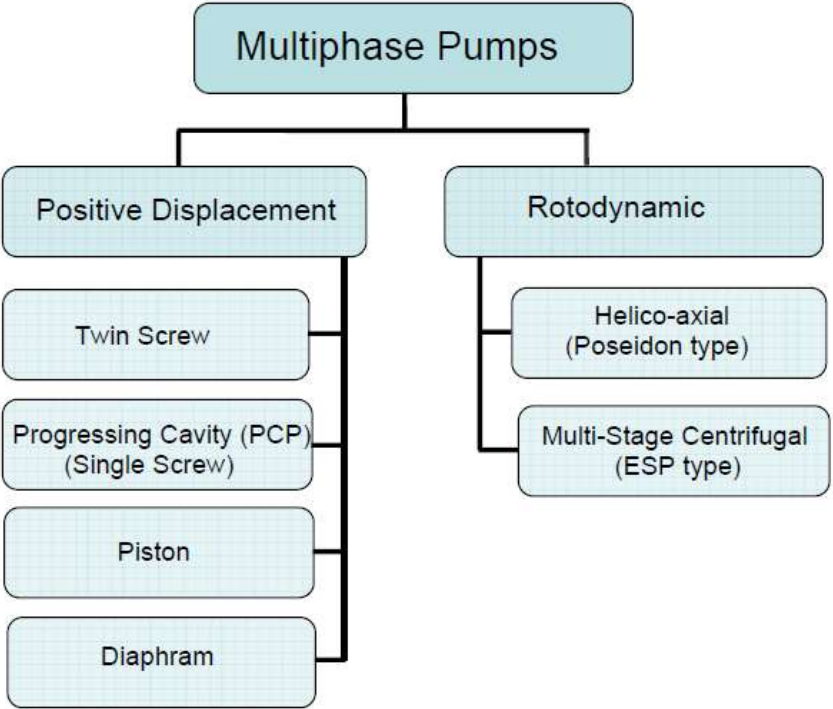


Figure 30. Types of Multiphase Pumps [19]

Hua et al [20] point out some challenges that still need to be overcome in pumping multiphase production streams. Normally, a specific model of pump is selected on the basis of the expected production which involves an estimation of bottomhole pressure, water cut, gas fraction and other reservoir parameters. For multiphase pump, the actual production may deviate from initial expectations, so the design of multiphase pump should be able to cope with various flow conditions which may happen during the life of the asset. In addition, multiphase pump must handle the GVF variation. During transient flow, continuous liquid flow along with gas pockets can be expected on a random basis. In some of the extreme cases, it can be 100% liquid followed by 100% gas. As a result of this, the load, torque of the shaft may experience a sharp fluctuation and pump operation time may be shortened as well. At last, multiphase pump design has to consider the gas compression effect. The free gas is compressed toward the discharge end. This phenomenon leads to a significant reduction in GVF and volumetric flow rate, as well as an increase in the mixture density. At this time, temperature increment may start due to the higher frequency of gas molecule collision.

The radial vibration is of prime importance in the design of ESP. The radial bearing, so-called journal bearing are located at several places along the shaft's length with certain distance. The rotational part of these bearings is keyed into the shaft and turns with shaft together, while the stationary part is mounted rigidly in the diffuser. Normally, journal bearings have identical materials both at rotational and stationary parts. Those bearings

running through the whole length of the shaft usually have the same clearance which is decided by the pump design and machining tolerances.

Another concern in the journal bearings are the presence of the free gas. Product lubricated journal bearing are widely used in the ESP. it widely assumed that the free gas entering the clearance is detrimental to the operation of the bearings. Therefore, manufacturers always make effort to remove any air bubbles before pumping, for example, adding gas separator before ESP. Goodwin et al [21] did an investigation of the effect of oil aeration on the load-carrying capacity of a hydrodynamic journal bearing. The bearing test rig in Figure 31 is established for this study. The rig was designed to enable operation close to the limit of stability so that more operation condition can be investigated. Experimental results therefore collected the data when the journal eccentricity ratios range from 0.1 to 0.9. Air and oil are mixed through the oil aerator and supplied to the bearing at an inlet port on the horizontal center line of the bearing.

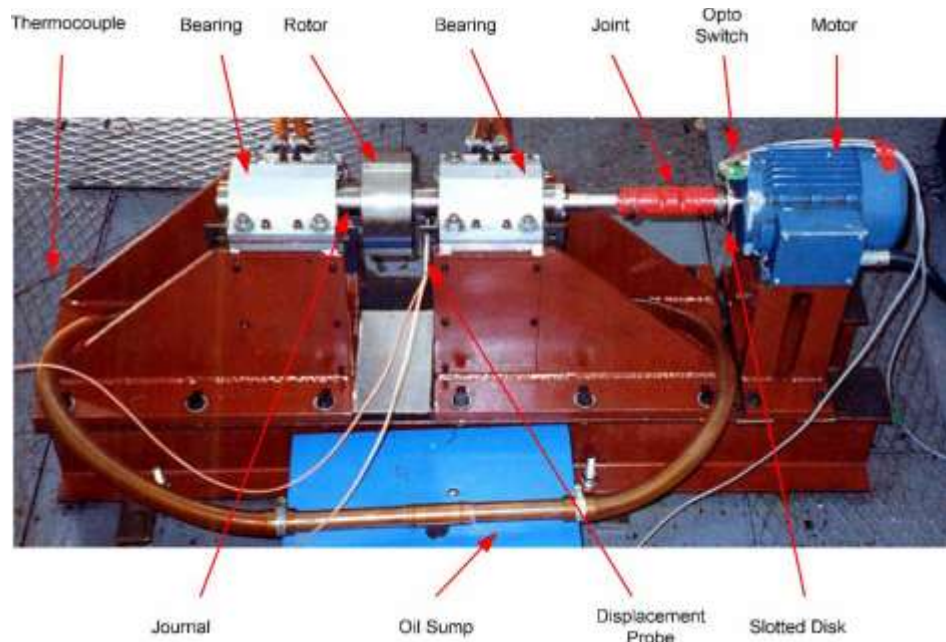


Figure 31. Test Rig for Oil Aeration Effect [21]

In the practical testing, both aerated and non-aerated oil case have been studied. The schematic drawing for the oil aeration system has been shown in Figure 32. “The lubricant aeration results in a negligible effect on the load-carrying capacity of plain journal bearings. For any given load and speed, aeration will cause either a slight increase in the eccentricity ratio when the nominal eccentricity ratio is in any instance small initially or no significant change at higher nominal eccentricity ratios.” [21]

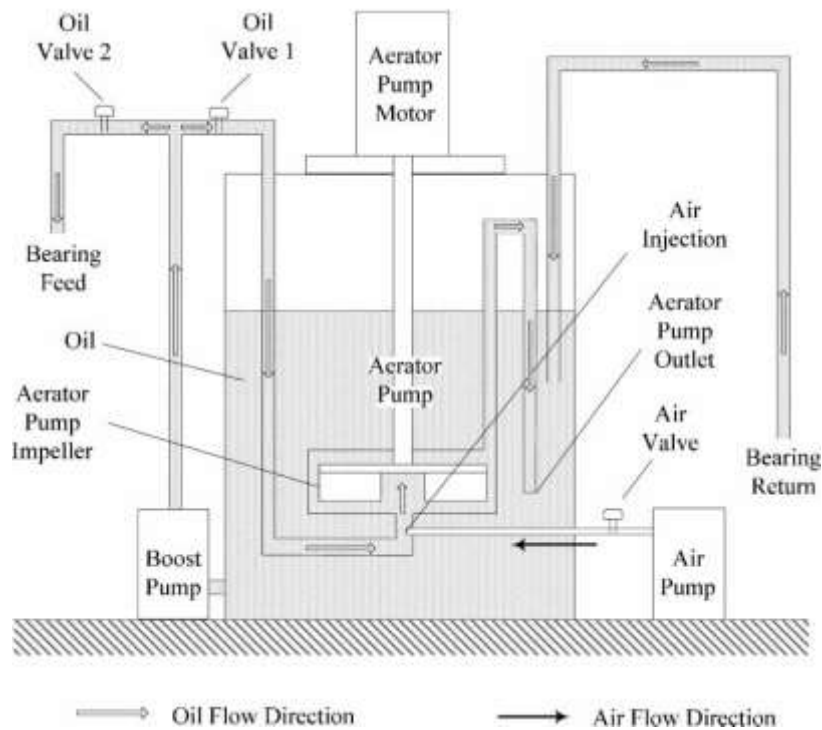


Figure 32. Schematic Diagram of Oil Aerator for Lubricant Supply [21]

Durham et al [22] reported an ESP failure analysis in 1990. According to them, ESP historically had a short run lives. Their failures usually were unexplained and accepted as norm. Industry average run times have improved from 300 days to more than 600 days at that time. The best performing systems have extended run lives of 7 to 10 years. However, there are some systems live still less than 30 days.

Mubarak et al [23] summarized the performance of ESPs in the Wafra field within the Divided Zone (DZ) Kuwait-Saudi Arabia and covered the period of 4 years started in January1998 to December 2001. Up to the end of 2001, the total number of ESPs

installed in the DZ was 251. Table 3 lists the common reasons of ESP failures and approximate percentages.

Table 3. Common Reasons of ESP Failures [23]

Failure Component	Percentage
Motor	40%
Pump	22%
Cable	26%
Others	12%

Three cases have been studied in this coursework. In the first case study, engineers are trying to set the pump close to the perforation so that the pump intake pressure increases. This allows ESP to operate smoothly and increased the production and life of the pump. Due to the modification on this, the mean time to failure of the pump is raised from 68 days to 223 days. The second case involves several ESPs with gas lock problem where the annulus (Casing & Tubing or Tubing & Pump) were full of gases. The stages keep running without fluid will lead to overheat of motor and pump. It could also burn the cable and motor. In this application, the shroud cover is place at pump intake, seal section and motor. The production liquid is directed from the perforations downwards along the OD of the shroud and is further routed to the pump intake through the annular space between motor OD and shroud ID. Then the gas accumulated in the annulus above the perforations will be vented through the casing valve. This helps to increase the average running time from 24 days to 371 days. The third case is dealing with severe sand production. Two solutions have been mentioned here. One of them is going to equip bearings with hardened abrasion resistance material (Tageston Carbide). The

second one is fixing the impeller with the shaft. This modification raised the average running time from 92 days to 422 days. [23]

CHAPTER IV
EXPERIMENTAL SETUP

4.1. Flow Loop

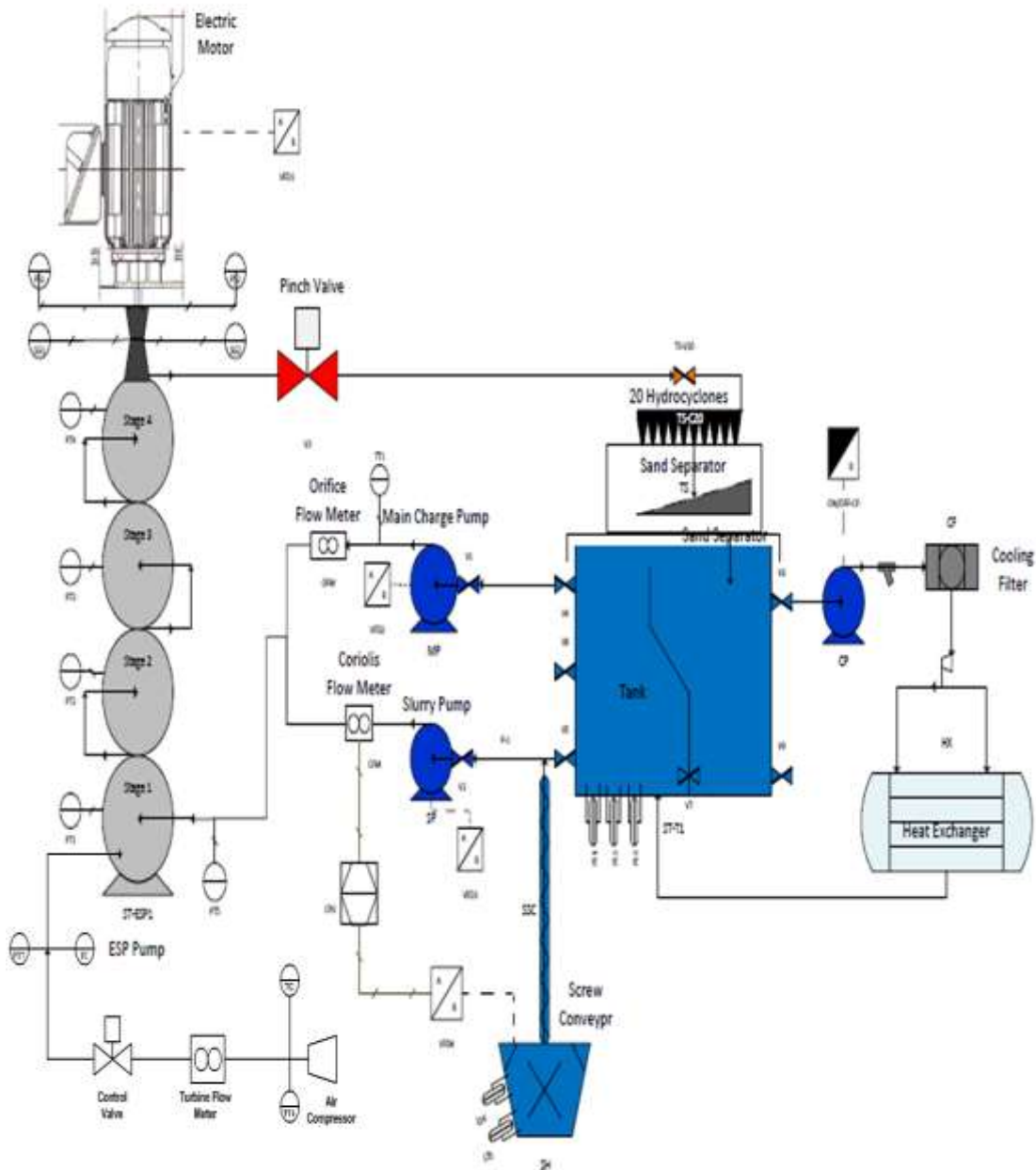


Figure 33. Pipe and Instrumentation Diagram (P&ID)

The three-phase (Water-Sand-Air) flow loop has been constructed for this test is shown in Figure 33. Figure 34 shows a systematical setup for this test and Table 4 lists the main items involved in the construction. Generally, this is an open flow loop with a 5,000 gallons tank which supplies the required water for the pump. Water is recycled through the tank, while sand and air are not. Sand is removed by the separator located at the top of the water tank which filters out the wet sand to collectors. Hence, the test can avoid uncontrolled sand particle size due to particle crush during the pumping operation. Air is vented through the discharge of the ESP. The separator consists of 20 hydro-cyclone separators and a screen shaker. Feed pump has been set in the main flow line to supply enough NPSH to prevent cavitation of the ESP. On the slurry line, a slurry pump is employed to provide sand water mixture into the ESP as well. Air is supplied via the air compressor at 110 psig before turbine flow meter (TFM). The two auxiliary pumps, feed pump and slurry pump, are controlled by Proportional Integral Derivative (PID) controllers to regulate the flow rate. Sand delivery speed is decided by the sand auger motor speed also using a PID controller in the control panel. Meanwhile, the cooling loop with heat exchanger is running all the time to maintain liquid at approximately constant temperature.

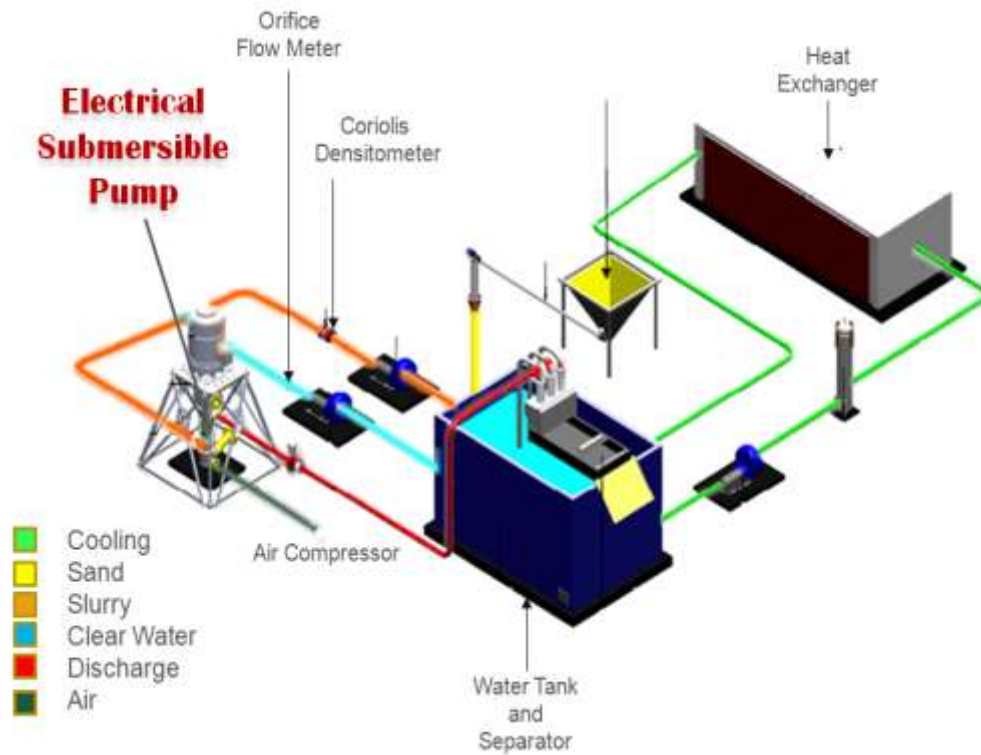


Figure 34. Experimental Setup Diagram

Table 4. Main Items Involved in the Flow Loop

No.	Item	No.	Item
1	ESP	10	Air Control Valve
2	ESP Drive Motor	11	Discharge Gate Valve
3	Derrick	12	Air Gate Valve
4	Feed Pump	13	Coriolis Flow Meter
5	Slurry Pump	14	Orifice Flow Meter
6	Cooling Pump	15	Turbine Flow Meter
7	Water Tank	16	Sand Hopper
8	Separator	17	Sand Auger
9	Discharge Pinch Valve	18	Heat Exchanger

The orifice flow meter (OFM) installed after the feed pump is used for monitoring volume flow rate of the feed pump while a coriolis flow meter (CFM) placed in slurry line measures the mass flow rate and density for the slurry mixture. A turbine flow meter

in the air line monitors the volume flow rate from the air compressor. The sum of the three volume flow rates is the flow rate of the ESP. Also, several pressure transducers and thermal couple are inserted in the flow loop for water density determination and ACFM conversion of the air supply.

Regarding to the motion monitor, 12 sets of proximity probe are placed to point on the shaft, rotor and coupling between motor and pump. Two probes facing the coupling also function as the alignment tools which ensure the offset and angularity between pump and motor maintain in the acceptable range. Two trial axial accelerometers attached to the casing at inlet and outlet position monitor the vibration level till the end of test.

4.2. Electrical Submersible Pump (ESP)

A three-stage WJE-1000 ESP mounted inside a 10.25" casing designed especially for the laboratory testing is cantilevered in the test rig exactly in vertical position which is very similar to the down-hole environment. As shown in Figure 35 and Figure 36, the impeller has five vanes and the diffuser has seven. Five balance holes are located in the impeller. Figure 37 and Figure 38 show the detailed dimensions for both impeller and diffuser. This ESP has relatively larger radius dimension among the normal ESPs with 9.24" diameter on the diffuser housing and 8.13" diameter on the impeller exterior shroud. Both weight and dimension of the impeller and diffuser are recorded during periodically disassembling.



Figure 35. Impeller Suction View [24]



Figure 36. Diffuser Discharge View [24]

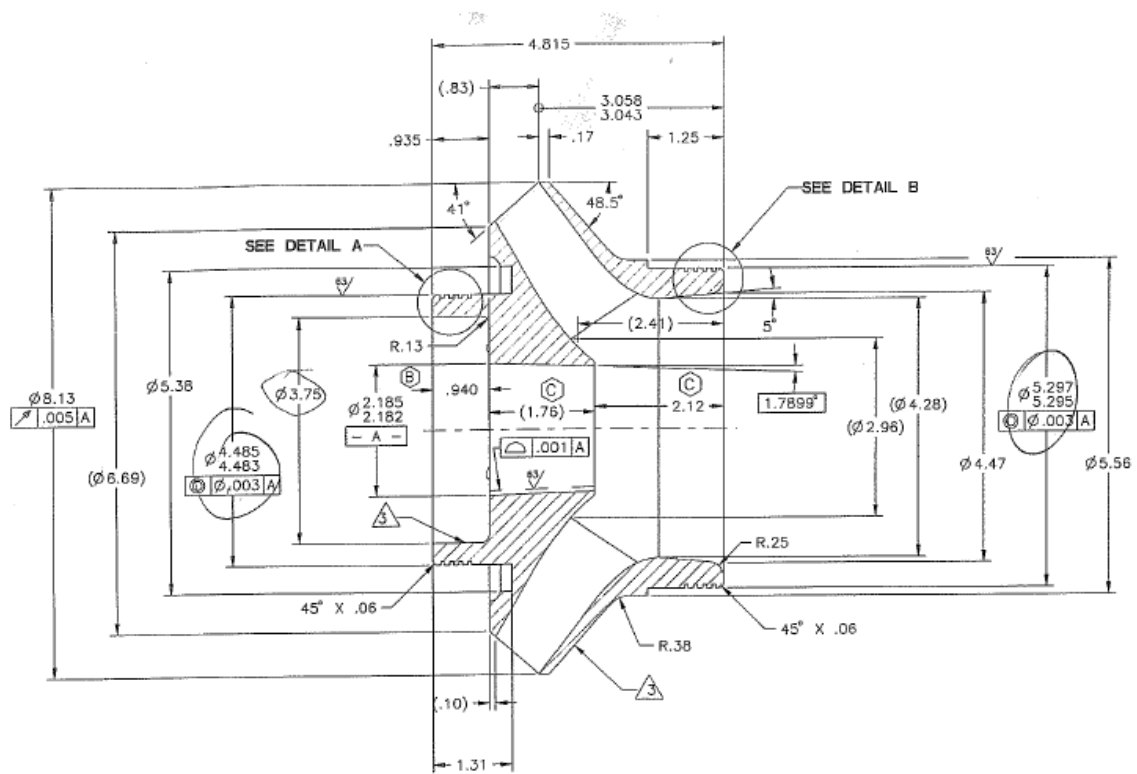


Figure 37. Impeller Detailed Dimension

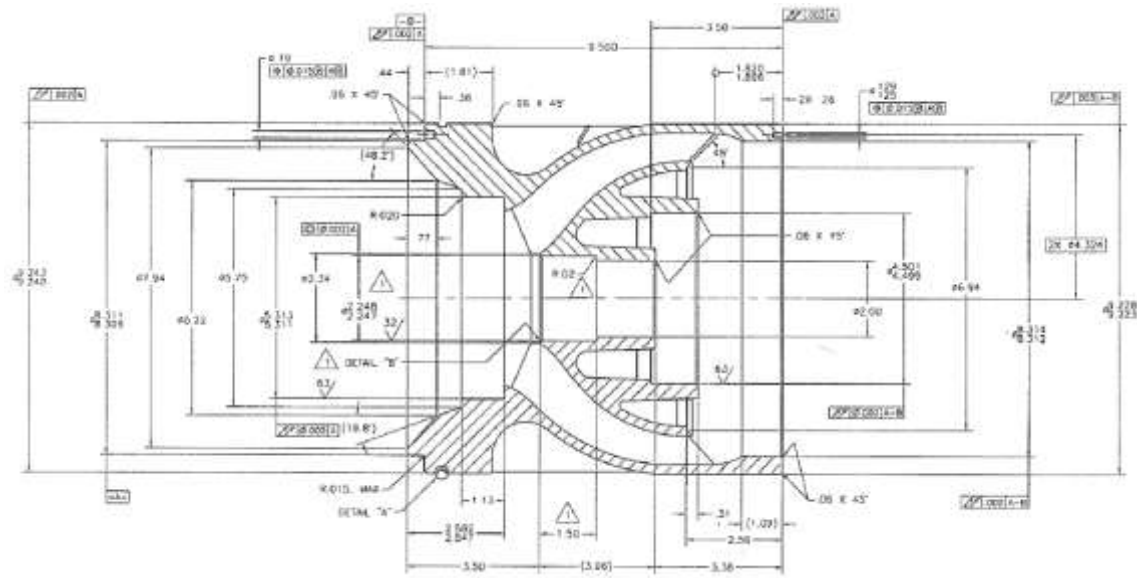


Figure 38. Diffuser Detailed Dimension

This three stage ESP is driven by a 250 hp three-phase induction motor which is mounted on the top of the test rig and controlled by a VFD. The pump curves from the manufacturer, Baker Hughes in Figure 39 show that each stage of the pump can generate a pressure rise of 51 psi at 1100 gpm flow rate for the best efficiency point 75%. The head-flow rate curve provided by manufacturer is shown in Figure 40.

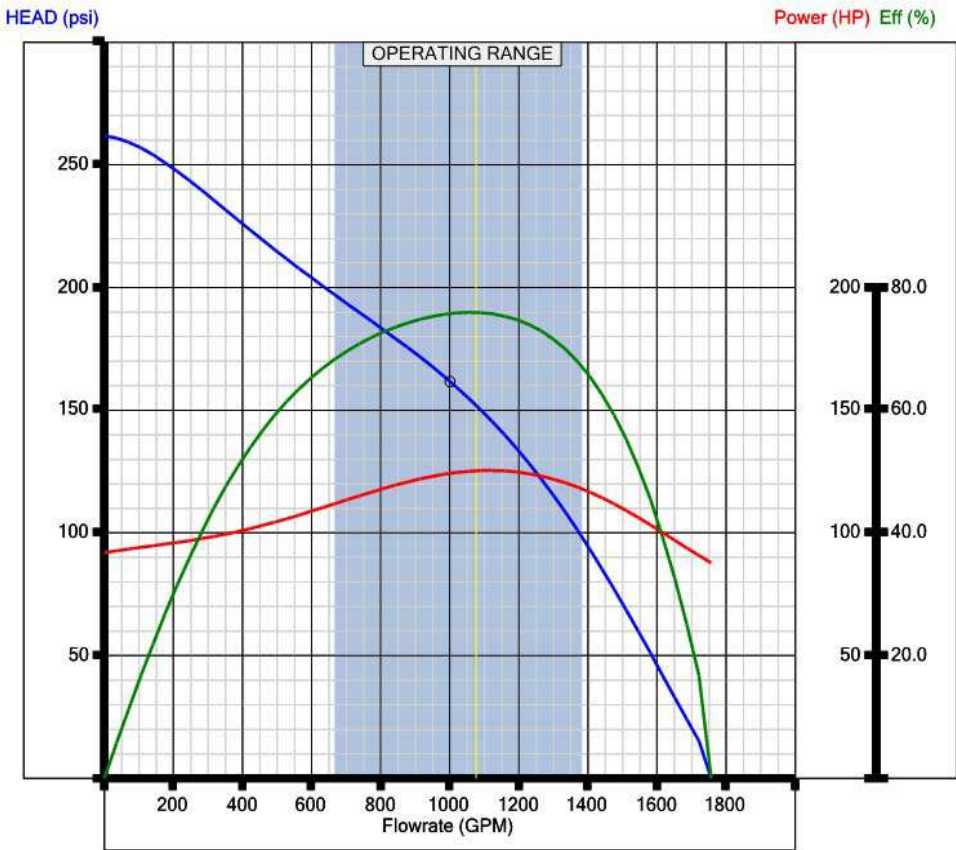


Figure 39. Catalog Performance Curve for Three Stages of ESP under 3600 RPM [24]



Baker Hughes Incorporated

HPump

(918) 341-9600 200W Stuart Rossa Dr. Claremore, OK 74017

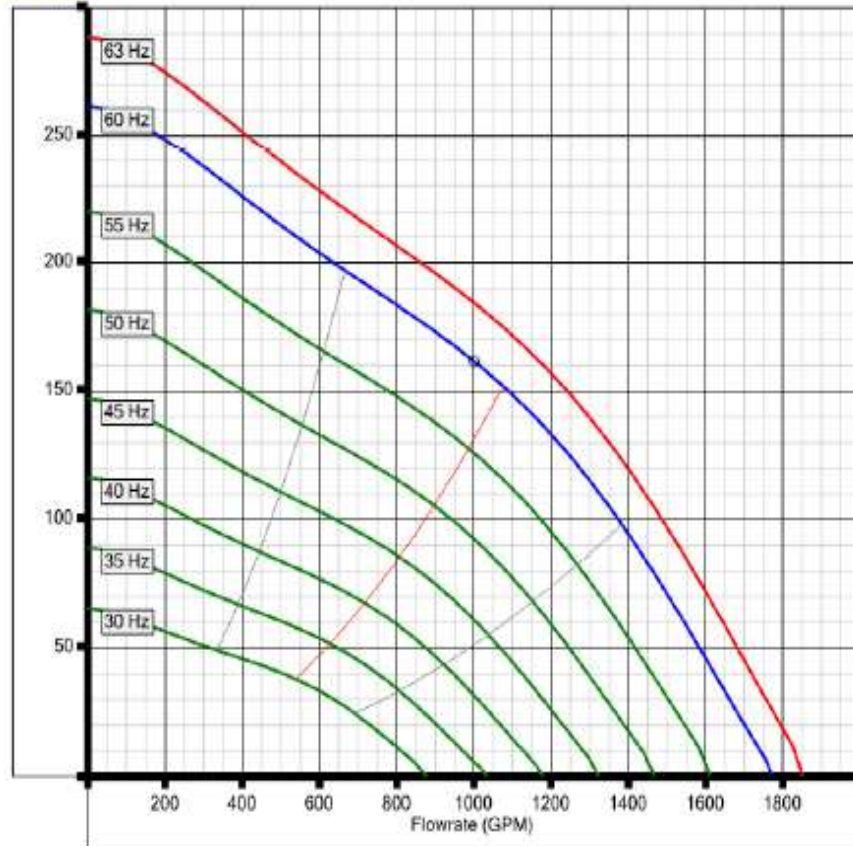
Project: WJE1000 Erosion Testing
Customer: Shell
Well: Texas A&M
Engineer: Jesse Gerber
NOTE: Motor ratings at 60Hz

Pump: 3-1025WJE1000
ThChmbr: 3.X HTC XM19
Motor: Siemens TEFC 200 HP 460 V 216 A
Controller: VSD 2150-VT 163kVA/ 480V/ 196A

Comments:
This extra line only shows on reports

3-1025WJE1000

HEAD (psi)



AutographPC™ V8.3 File:apcx.apcx
©Copyright 2012 Baker Hughes Inc. All Rights Reserved

Figure 40. Catalog Head Flow Rate Curves for Different Pump Speeds [24]

4.3. ESP Driven Motor

The ESP motor which is normally cooled by surrounding fluid, usually sits below the pump and other components. It is difficult to duplicate the original design in the lab testing loop. Instead, a two-pole, three-phase induction motor has been employed in the testing as shown in Figure 41. A VFD drives the motor to control the operating speed. The output of the motor is estimated by using the power output from the VFD multiplied by the efficiency on the curve given by the motor manufacturer in Figure 42.



Figure 41. Motor Located at Top of Derrick

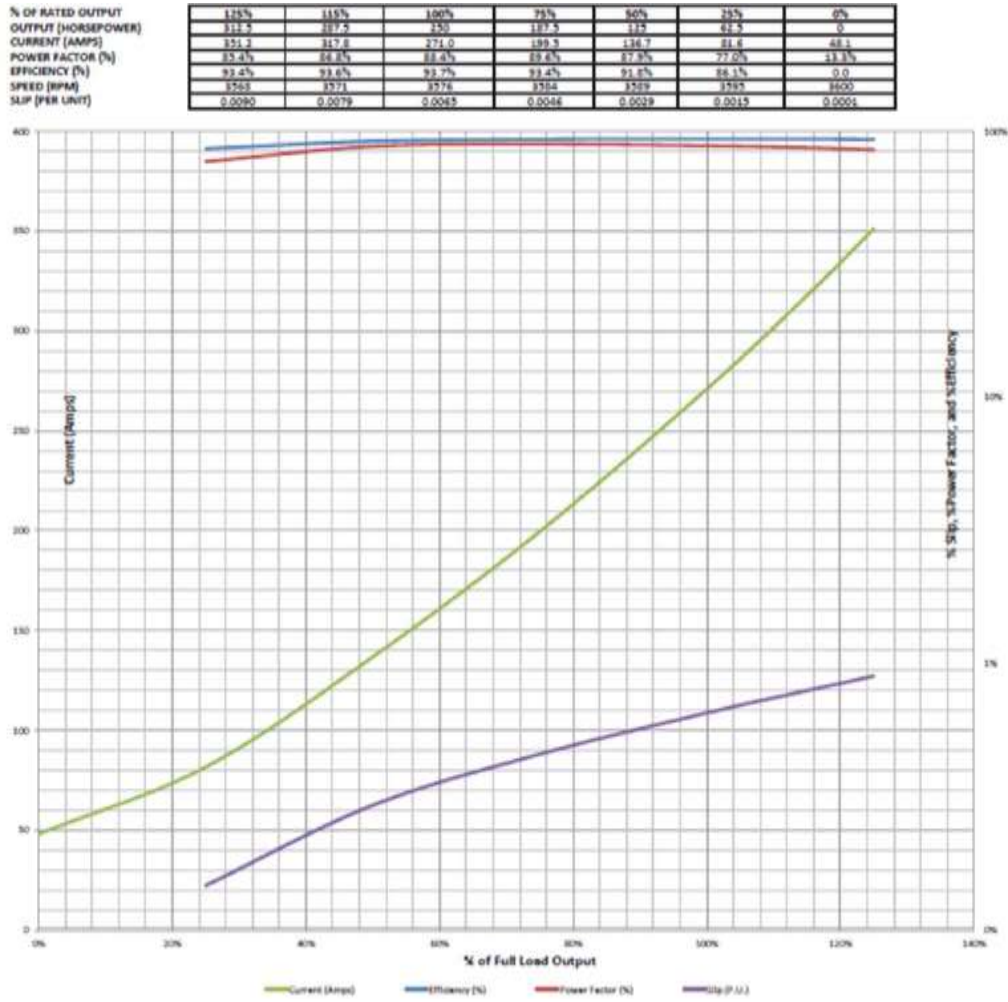


Figure 42. Motor Efficiency Curve

4.4. Auxiliary Pump

Two auxiliary centrifugal pumps, feed pump and slurry pump, have been installed in parallel position before the inlet of ESP. The main purpose of these pumps is to provide NPSH to avoid cavitation and concentrate water and sand mixture in a slipstream to measure flow rate accurately. The 75 hp feed pump in Figure 43 is responsible to provide a majority of the flow rate to the ESP while maintaining the inlet pressure above HPSHR which is the minimum pressure to prevent cavitation. Slurry pump in Figure 44

is a relatively small centrifugal pump with 20 hp. Sand and approximately 3% of water flow is mixed to obtain a desired density and mass flow rate. This allows accurate measurement of the sand flow rate. This flow is then mixed with the water flow from feed pump. In this way, the density measurement could be done accurately with condensed slurry flow by CFM which is installed right after slurry pump. After that, the sand concentration in the density is diluted to approximately 0.2%.



Figure 43. Feed Pump Assembly



Figure 44. Slurry Pump Assembly

4.5. Sand Auger System

The sand auger system consists of a hopper, a conveyor, and a gear motor drive assembly. The hopper is mounted on the floor and connected to the gear motor drive through the tube. A screw auger is located inside tube in order to deliver the dry sand from floor level in Figure 45 to the desired height on the other side of tube. A VFD controlled by a PID controller is responsible for controlling the speed of gear motor. Hence, the sand concentration can be adjusted according to the motor speed. Normally, running a sand auger without sand is not recommended since it would eliminate all damping on the system and will lead to severe damage.

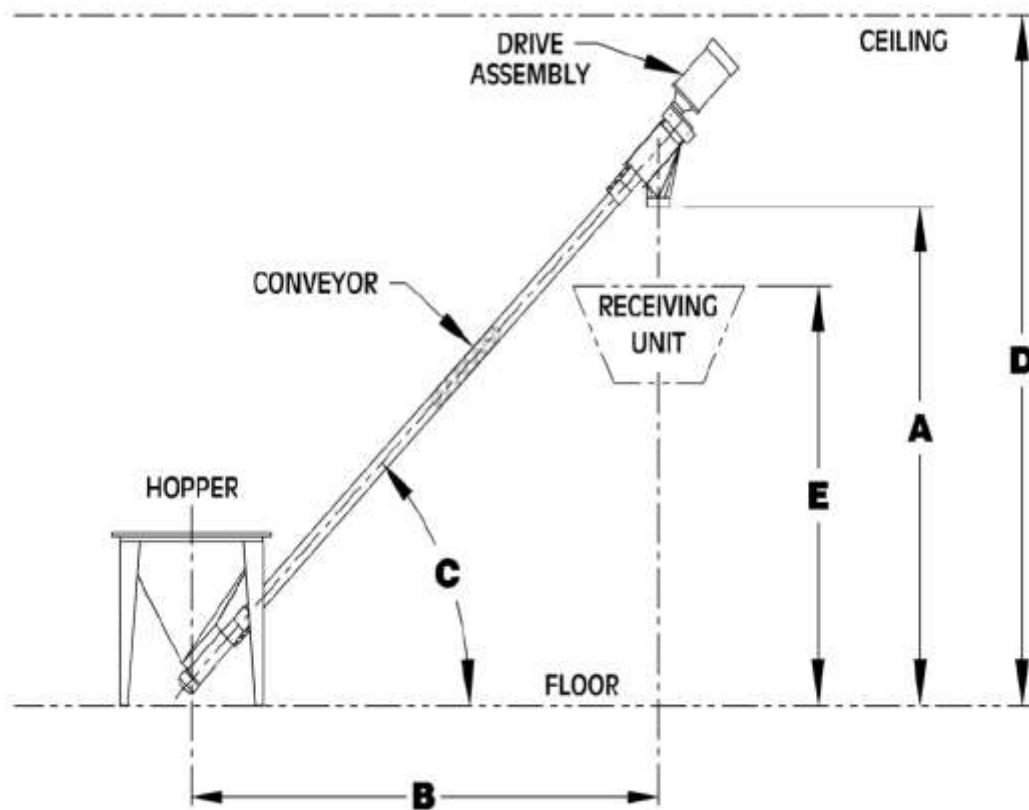


Figure 45. Sand Auger Configuration

4.6. Tank and Sand Separator

Figure 46 shows the sand separator located on the top of a 6000 gallon tank which has been divided into two sections. The separator itself contains 20 hydro-cyclones connected directly to the outlet of the ESP. Each cyclone has a 4" diameter and flow rate capacity of 65 gpm. The number of separators that should be open simply rely the formula $N=Q/65$. The operating pressure should be maintained around 25 psi when the correct number of cyclones is open. The hydro-cyclone sand separator creates a centrifugal action that moves the water toward the top of the body, throwing the sand and heavy materials to the outside of the cyclone. The heavy materials then fall into the underflow chamber to be collected. The sand out of chamber falls on the mesh screen shaker where additional water in the sand is recycled and returned to the tank.



Figure 46. Tank and Separator Assembly

4.7. Mechanical Seal

A mechanical face seal is required on the pump drive shaft. It requires a flow of water for cooling and lubrication, so called seal flush. Various selections are included for industrial plan. In this test, two plans have been used in the operation. First plan is the combination of plan 32 and plan 11 in Figure 47 where the seal flush is from an external clean source. A seal flush pump is necessary to pump clean water for seal chamber heat removal, solids removal and increasing the fluid vapor margin. However, it is relatively expensive on setting up external seal flush piping in the field.

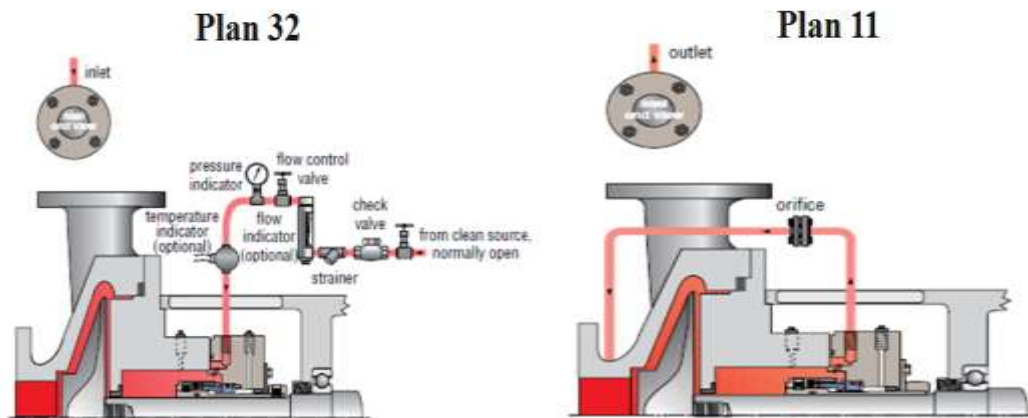


Figure 47. Combination of Plan 32 and Plan 11

Alternatively, a combination of plan 11 and plan 13 in Figure 48 is widely used in industry too. Seal flush itself is recirculated from the pump discharge through the mechanical seal then back to pump suction side. It is the standard flush plan on the vertical pumps. This plan provides an economic solution for the general vertical pump application without external seal flush resource.

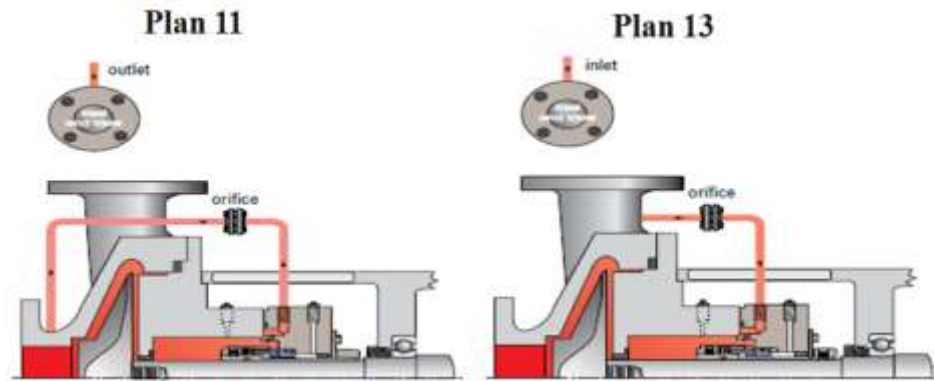


Figure 48. Combination of Plan 11 and Plan 13

The Eagleburgmann mechanical seal used in this test was operated without any seal flush plan so that the surface material between rotational part and stationary part of the seal can be examined. The results prove that this mechanical seal is robust and able to survive in the boundary lubrication and dry running conditions. As shown in Figure 49, the temperature starts at 73 °F as the same with test cell temperature, the maximum temperature 102 °F is reached in 20 minutes. Then the temperature retains at that range in the rest operating.

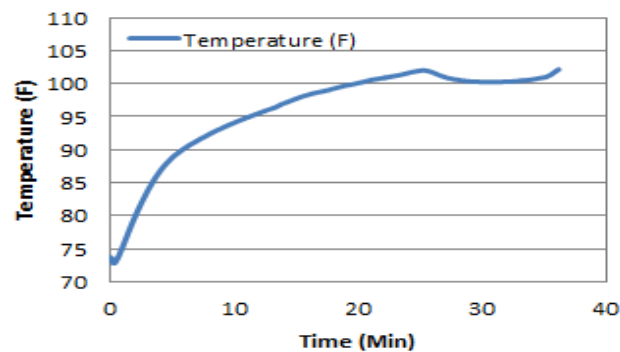


Figure 49. Mechanical Seal Test Results without Seal Flush Plan

CHAPTER V
INSTRUMENTATION

5.1. Instrument List

Table 5 shows the instrument nomenclature together with the description. With the help of this list and P&ID shows in Figure 33, the specific location of each instrumental item can be determined.

Table 5. Instrument List and Description

Item No.	Description	Manufacturer
A1	Inlet Accelerometer_Tangential	PCB
A2	Inlet Accelerometer_Radial	PCB
A3	Inlet Accelerometer_Axial	PCB
A4	Outlet Accelerometer_Tangential	PCB
A5	Outlet Accelerometer_Radial	PCB
A6	Outlet Accelerometer_Axial	PCB
PP1	Proximity Probe Shaft Stage 1 X	Bently Nevada
PP2	Proximity Probe Shaft Stage 1 Y	Bently Nevada
PP3	Proximity Probe Impeller Stage 2 X	Bently Nevada
PP4	Proximity Probe Impeller Stage 2 Y	Bently Nevada
PP5	Proximity Probe Shaft Stage 2 X	Bently Nevada
PP6	Proximity Probe Shaft Stage 2 Y	Bently Nevada
PP7	Proximity Probe Impeller Stage 3 X	Bently Nevada
PP8	Proximity Probe Impeller Stage 3 Y	Bently Nevada
PP9	Proximity Probe Shaft Stage 3 X	Bently Nevada
PP10	Proximity Probe Shaft Stage 3 Y	Bently Nevada
PP11	Proximity Probe Coupling X	Bently Nevada
PP12	Proximity Probe Shaft Coupling Y	Bently Nevada
OFM	Orifice Flow Meter	Lambda Square
CFM	Coriolis Flow Meter	Emerson
TFM	Turbine Flow Meter	Omega
LS1	Tank Level Sensor L	
LS2	Tank Level Sensor H	

Table 5. Continued

Item No.	Description	Manufacturer
LS3	Sand Level Sensor L	IFM
LS4	Sand Level Sensor M	IFM
PT1	Pressure Transducer ESP Inlet	Omega
PT2	Pressure Transducer ESP Outlet	Omega
PT3	Pressure Transducer Mechanical Seal	Omega
PT4	Pressure Transducer Air Resource	Omega
PT5	Pressure Transducer Separator	Omega
PT6	Pressure Transducer Heat Exchanger Filter	Omega
PT7	Pressure Transducer 2nd Stage	Omega
PT8	Pressure Transducer 3rd Stage	Omega
TC1	Thermal Couple ESP Inlet	Omega
TC2	Thermal Couple Air Resource	Omega
TC3	Thermal Couple Mechanical Seal	Omega
VFD1	VFD ESP Motro	Yaskawa
VFD2	VFD Feed Pump	Toshiba
VFD3	VFD Slurry Pump	Toshiba
VFD4	VFD Sand Auger	Altivar

5.2. Accelerometers

Two, three dimensional accelerometers are placed on the casing close to the ESP suction and discharge position as shown in Figure 50. These accelerometers are manufactured with three orthogonal internal sensing elements to enable simultaneous multi-axis measurements. The unit has a tapped hole in its base and secured with a screw passing through the object to aid in alignment. Accelerometers were mainly developed as a sensor for engine vibration, structural test, flight testing and oil & gas production monitor. Typically, the sensor is able to capture the accelerations up to 50 g and frequencies up to 50 Hz. The current two accelerometers have a factory-calibrated output of 500 mV/g.

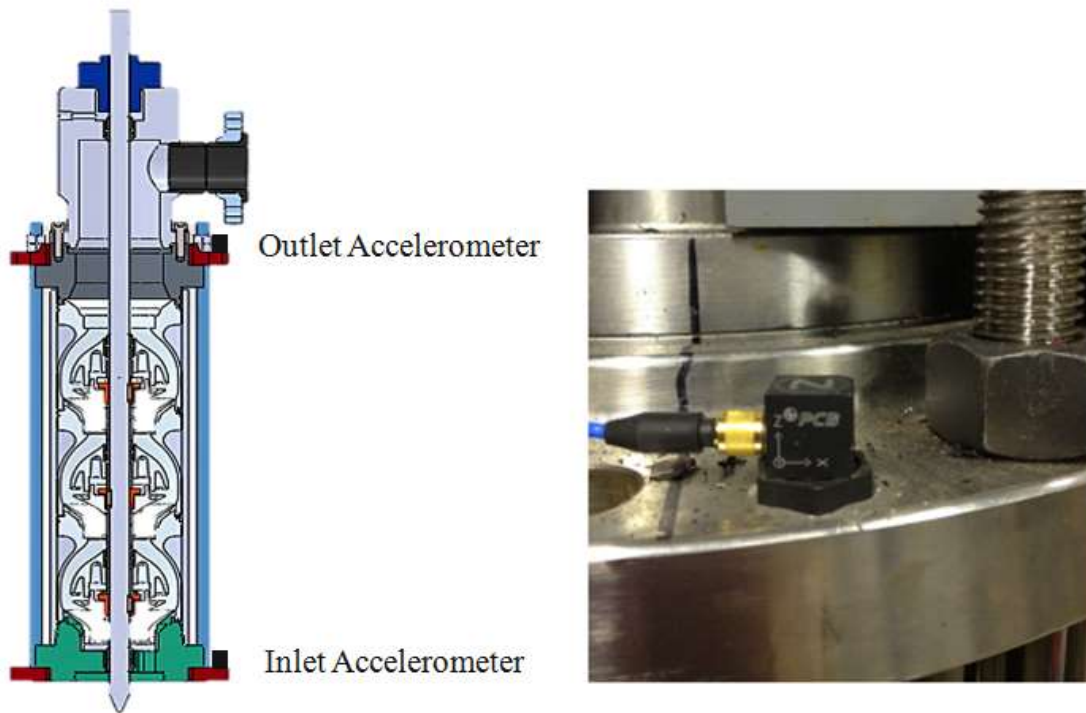


Figure 50. Accelerometer Location on the Casing

5.3. Proximity Probe

The proximity probe measurement system includes probe, extension cable and transducer. The system provides an output voltage which is proportional to the distance between probe tip and observed conductive objective. This method has been widely used in the fluid film bearing application, and it can be applied to keyphasor reference or rotating speed measurement. As shown in the Table 5 previously, twelve sets of proximity probe measurement system have been employed in this study. Six of them point at the shaft of each stage. Four of them are monitoring the rotor labyrinth seal at second and third stages. The last two are located at coupling which connects motor and pump together. Probes used in this study are 3300 XL 5mm and 3300 XL 8 mm. The

corresponding extension cable must be 4 meters long in order to keep a total length of 5 meters so that the factory calibration can be utilized. This type of proximity probe has a scale factor of 200 mV/mil and the measurement range is linear from 0 V to 20 V. In Figure 51, probes with odd number are in x direction and probes with even number are in Y direction.

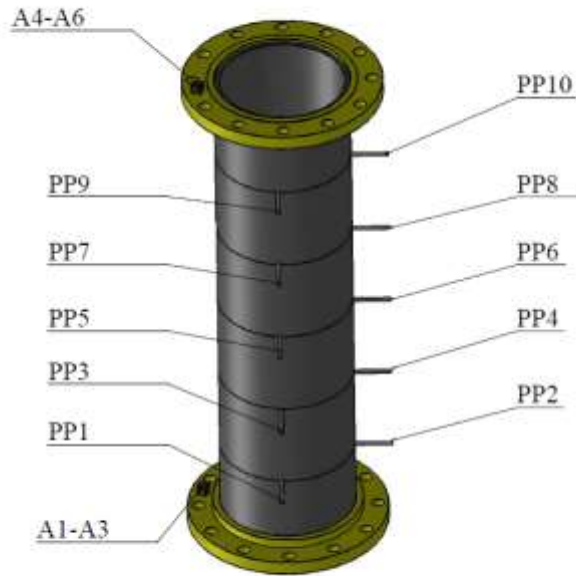


Figure 51. Probes Location on the Casing

5.4. Orifice Flow Meter

An orifice flow meter is a conduit which creates a pressure drop when fluid passes through. It uses the same principle as a Venturi nozzle which relates the pressure drop of the fluid to the velocity of the fluid. Usually, an orifice plate is a thin steel plate with a hole in the center. By measuring the difference in fluid pressure between the normal pipe

section and the point of maximum convergence downstream, the volumetric and mass flow rates can be obtained. Figure 52 shows the experimental setup on the primary flow pipe for the orifice flow meter. The volume flow rate is calculated by the following equations.

$$Q_{FP} = d^2 * K * \sqrt{\frac{\Delta P_{OFM}}{\rho_w}} \quad (5.1)$$

$$K = C * \frac{1}{\sqrt{1 - \beta^4}} \quad (5.2)$$

$$C = 0.5959 + 0.0312\beta^{2.1} - 0.1840\beta^8 + 91.71\beta^{2.5} \quad (5.3)$$

where Q_{FP} = feed pump flow rate

d = bore diameter

K = flow coefficient

ΔP_{OFM} = pressure difference

ρ_w = water density

C = discharge coefficient

β = beta ratio



Figure 52. Orifice Flow Meter [24]

5.5. Coriolis Flow Meter

Coriolis is one of the fastest growing technologies in the oil and gas market. This technology offers more value in two-phase mixture measurement. Since Coriolis measures the flowing mass of fluids and its accuracy is independent of fluid composition, flow pulsations and flow swirl, the meter is more accurate over a wide range of operation conditions. Meanwhile, the low cost for installation and maintenance makes this technology popular and competitive among various industrial fields.

Typically, a Coriolis flow meter contains two primary components, a sensor and a transmitter. Mass flow rate and density of mixture can be obtained by sensing the Coriolis force on the vibrating tubes. Sensing coils are located on the inlet and outlet sections of the tubes which oscillate in proportion to the sinusoidal vibration. When flow goes through the meter, the vibration causes a phase shift between the inlet coil and

outlet coil as shown in Figure 53. This shift is directly proportional to the mass flow rate and the vibration frequency is proportional to the flowing density of the fluid.

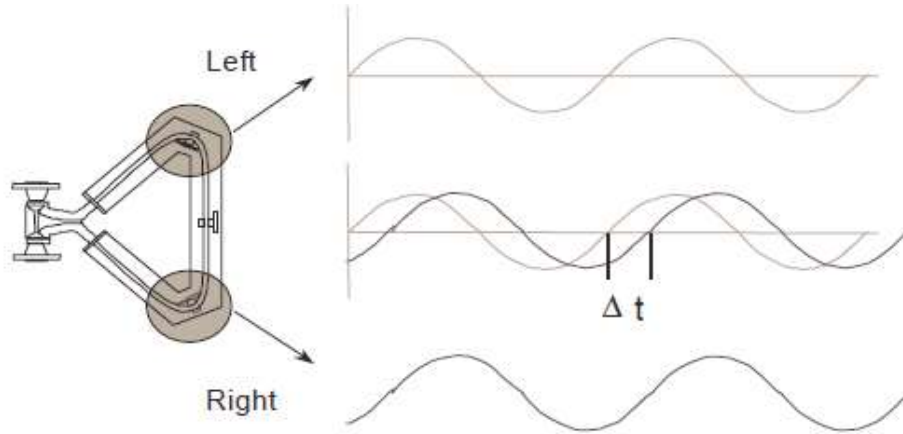


Figure 53. Phase Shift between Different Coils [25]

The Coriolis Flow Meter (CFM) in Figure 54 has been installed for slurry flow rate measurement after the exit of the slurry pump. The output mass flow rate and density of the slurry will be used to calculate the volume flow rate of the slurry and count as part of ESP flow rate. The mass flow rate of the mix and density can also be used to determine the concentration of sand in the mixture. The mass flow rate and concentration of sand can be found by using the following equations.

$$\dot{m}_s = \frac{\dot{m}_m - \frac{m_m}{\rho_m} \rho_w}{\left(1 - \frac{\rho_w}{\rho_s}\right)} \quad (5.4)$$

$$C_{two-phase} = \frac{\dot{m}_s}{Q_{FP} + \frac{(\dot{m}_m - \dot{m}_s)}{\rho_w}} \quad (5.5)$$

$$C_{three-phase} = \frac{\dot{m}_s}{Q_{FP} + \frac{(\dot{m}_m - \dot{m}_s)}{\rho_w} + Q_{Air}} \quad (5.6)$$

where \dot{m}_s = sand mass flow rate

\dot{m}_m = mixture mass flow rate

m_m = mixture mass

ρ_w = density of water

ρ_s = density of sand

C = sand concentration

Q_{FP} = feed pump flow rate

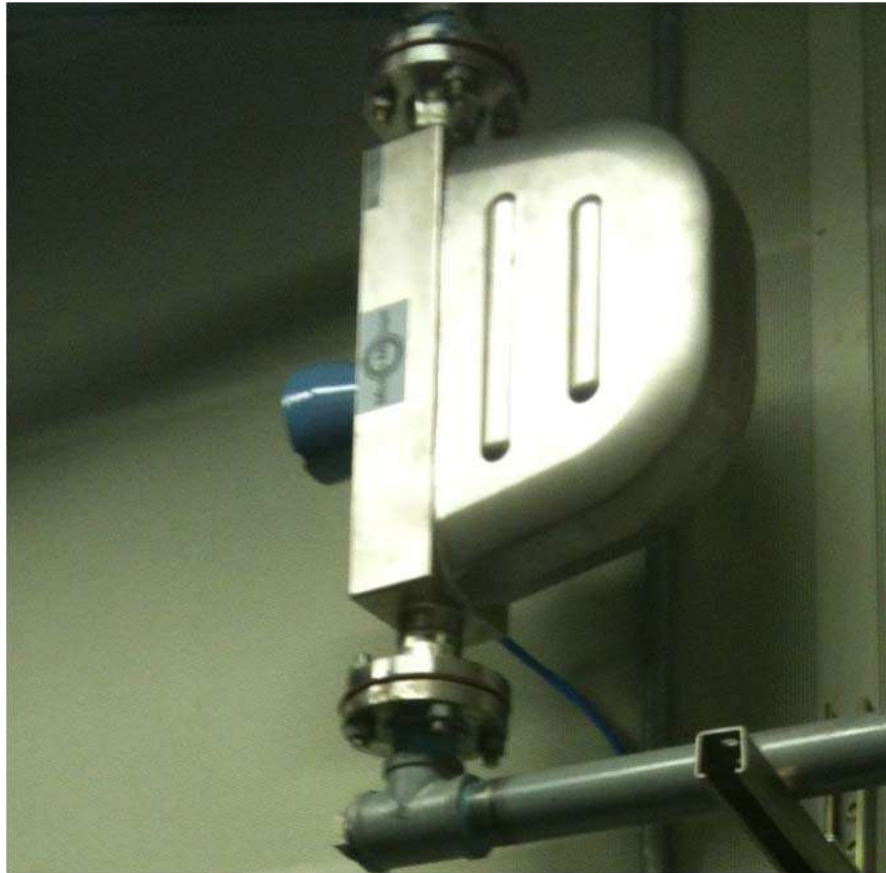


Figure 54. Coriolis Flow Meter

5.6. Turbine Flow Meter

Turbine flow meter has been available in market for many years and has proven itself to be a very precise measurement tools for liquid and gas flow in various applications.

There are two types of turbine flow meter, inline meter and insertion meter. The inline turbine meter is the most popular one and applied in this course study. Theoretically, turbine meters are inferential measurement devices which obtain the flow rate indirectly by sensing the natural kinetic energy of the flow as it passes through the angled blades of the turbine rotor. The frequency of pulses produced by each blade passage is directly

proportional to the volume flow rate. Pressure and temperature effects are critical for the accuracy of metering. Due to the relative incompressibility of liquids, pressure effect is not usually as important as temperature effect. However, both pressure and temperature will significantly change the volume flow rate of gas. Therefore, pressure and temperature sensor are usually used along with the flow meter. In general, at least 10 uninterrupted pipe diameters of straight pipe locate at upstream of metering point and 5 uninterrupted pipe diameters run downstream of metering point. [26]



Figure 55. Air Supply Setup

Figure 55 shows the air supply setup in current study. It ensures that 10 uninterrupted pipe diameter straightly located upstream and 5 uninterrupted pipe diameter downstream of turbine flow meter. Also, two thermocouples and two pressure sensors has been set ahead of flow meter and inlet of air injection separately. Normally, the air compressor will provide air at 110 psig and drop down to 40 psig at the ESP inlet. A control valve has been installed after the turbine flow meter for fine tuning of air flow rate. According to the temperature and pressure reading, the actual flow rate of air at inlet can be determined by the following equation.

$$Q_{Air} = \frac{Q_{TFM} * T_{Air} * P_{Comp}}{T_{Comp} * P_{Air}} \quad (5.7)$$

where Q_{Air} = actual flow rate of ESP

Q_{TFM} = actual flow rate of TFM

T_{Comp} = temperature of supplied compressed air

P_{Comp} = pressure of supplied compressed air

T_{Air} = air temperature at ESP inlet

P_{Air} = air pressure at ESP inlet

5.7. Pressure Transducer

Eight pressure transducers are used to monitor the operation and generate performance curves. The difference between pressures of the transducers at the inlet and outlet of the ESP are used to calculate the pressure rise of the pump. The pressure rise per stage can be determined either by dividing the total head developed by the pump by the number of stages or pressure difference between PT8 and PT7. Due to the compressibility of gas, pressure transducers are necessary in the air injection line to obtain the actual flow rate based on local condition. Also, pressure transducers installed on the separator, mechanical seal and heat exchanger filter ensure that all equipment is working under the desired conditions. Table 6 shows the description of each pressure transducer and location. Each pressure transducer was calibrated in the laboratory using a dead weight tester.

Table 6. Pressure Transducer List

Item No.	Description	Manufacturer
PT1	Pressure Transducer ESP Inlet	Omega
PT2	Pressure Transducer ESP Outlet	Omega
PT3	Pressure Transducer Mechanical Seal	Omega
PT4	Pressure Transducer Air Resource	Omega
PT5	Pressure Transducer Separator	Omega
PT6	Pressure Transducer Heat Exchanger Filter	Omega
PT7	Pressure Transducer 2nd Stage	Omega
PT8	Pressure Transducer 3rd Stage	Omega

5.8. Thermocouple

Three thermal couples have been placed in the ESP testing loop. They help to calculate the density of water and actual air flow rate into system. All thermocouples are factory calibrated and directly connected to data acquisition equipment. Table 7 lists the location of each thermal couple.

Table 7. Thermocouple List

Item No.	Description	Manufacturer
TC1	Thermal Couple ESP Inlet	Omega
TC2	Thermal Couple Air Resource	Omega
TC3	Thermal Couple Mechanical Seal	Omega

5.9. Data Acquisition

The hardware used for control signal output and data acquisition for all instruments that do not require a high frequency response and/or simultaneous measurements is a National Instrument cRIO chassis with multiple modules including NI 9205, NI 9265, NI 9213, NI 9215 and NI 9217. The 9205 module is a voltage-reading module able to read up to 32 single-ended channels, 16 differential input channels or a combination of both. Two 9265 modules with 4 output channels each are used for 0 to 20mA signal

outputs to control the VFDs, pinch valve and air control valve. NI 9215 with 4 simultaneously sampled analog inputs can reach maximum sampling rate at 100 kS/s. NI 9213 and NI9217 are temperature measurement modules for thermal couples (TC) and resistance temperature detectors (RTD).

To connect to the instruments, a special box was prepared with RS235 connectors for easy removal and modification. The box contains plugs for the instruments' cables where each instrument is connected, depending on the requirements of the instrument, to a power supply, 470 ohm resistance (to convert from 4-20 mA signal to the 0-10 V signal compatible with the A/D converter) and/or tied directly to another plug which connects to the A/D converter (if the instrument has its own power supply and a 0-10 V output). The RS235 connector coming out of the box and going to the instruments is connected using multi-pair, multi-shield cable to minimize noise from the equipment in the test cell. [24]

For the instruments that require high frequency responses and simultaneous measurements such as proximity probes and accelerometers, a 1616FS USB module from measurement computing has been used. 10 proximity probes and 6 accelerometer channels are connected to FS1616 in order to record data simultaneously for comparison. Since measurement range of the FS1616 is 0~10V, a voltage separator which contains two resistors in series reduce the proximity output 0~20V into the proper measurement range.

The software used to collect all the performance and vibration data is National Instruments Labview. The main program includes two parts, performance and vibration. The performance program in Figure 56 includes PID controller for auxiliary pumps, sand auger and air control valve and data collection from instruments which connected to NI cRio Chassis. Figure 57 is the vibration monitor panel which display acceleration and proximity probe amplitude. Also, root mean square (RMS) value and Fast Fourier Transform (FFT) plot are contained in the program for real time monitoring purpose. Since the FS1616 module does not have a built-in data trigger. A data trigger panel has been involved in the vibration program as shown in Figure 58. As long as the signal surpasses the configured threshold, program will record the data both before and after triggering. The sampling rate can be adjusted according to the actual need.

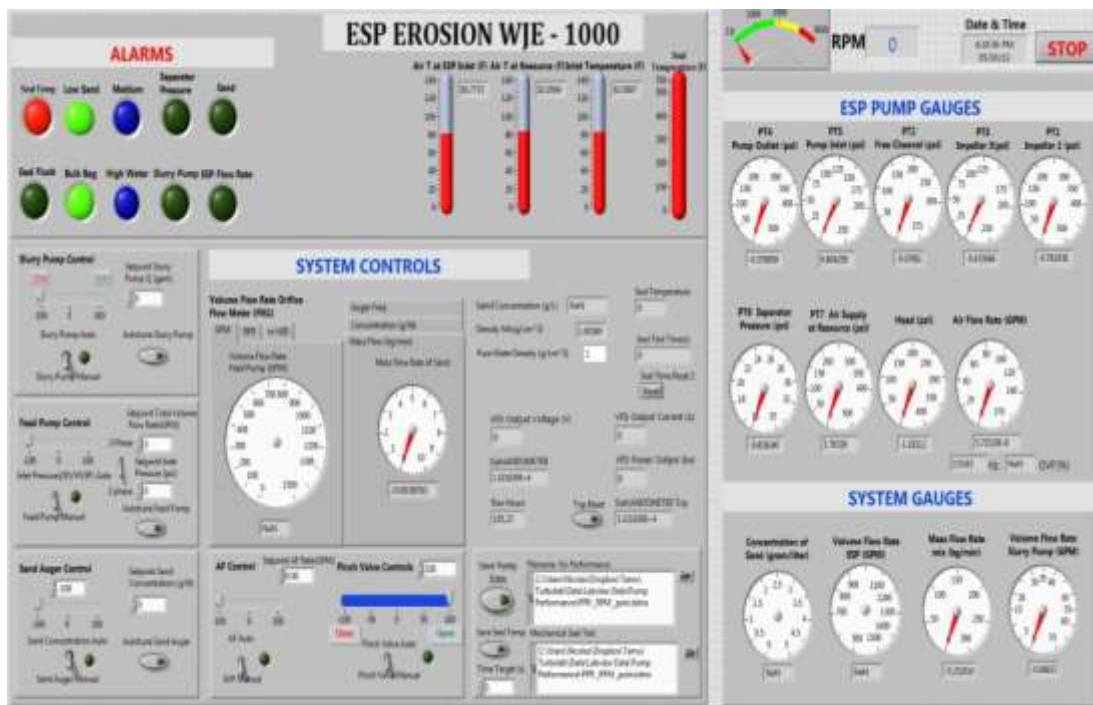


Figure 56. WJE-1000 Performance Monitor Panel

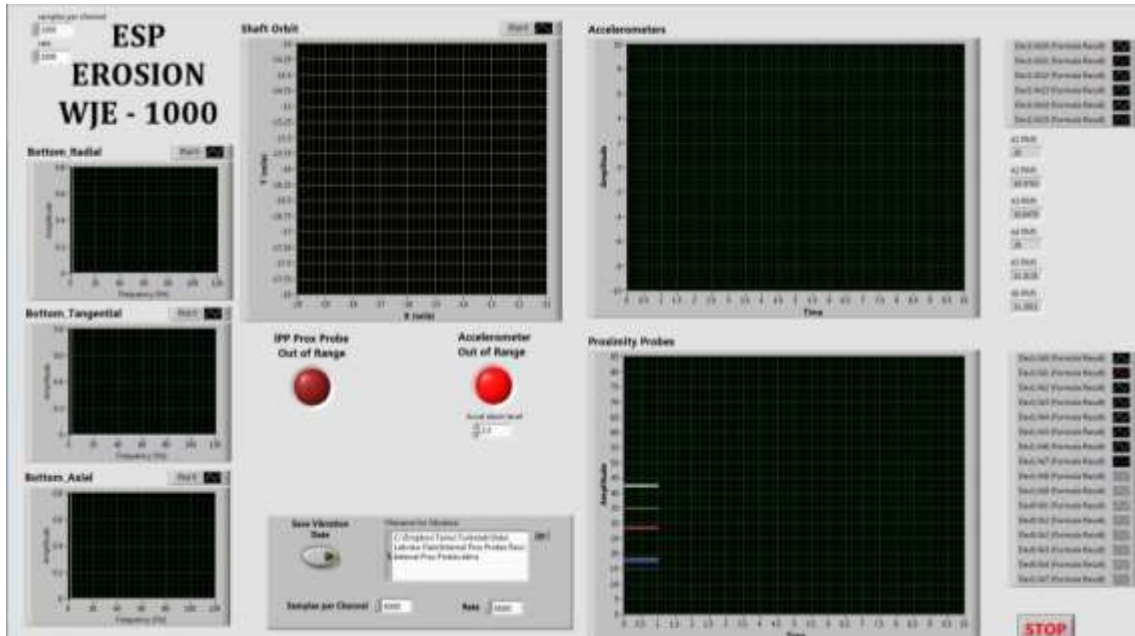


Figure 57. WJE-1000 Vibration Monitor Panel

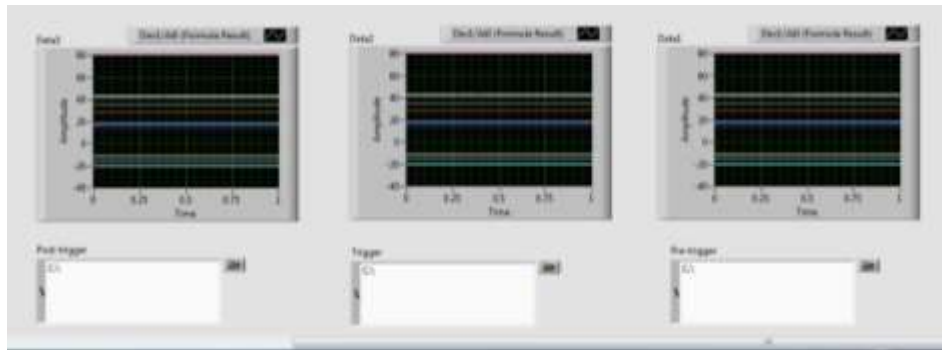


Figure 58. Data Trigger Panel

CHAPTER VI

RESULTS AND DISCUSSION

Results shown in this thesis cover initial 117 hours two-phase test with water and sand, then followed by 68 hours three-phase test which involves water, sand and air. Air is the only different factor between two-phase test and three-phase test. The goal is to estimate the effect of air in the ESP erosion test. Two-phase test maintains the consistent operating condition at BEP flow rate of 1100 GPM, 3600 RPM speed. Three-phase test is running at best efficiency point of 850 GPM liquid flow rate with 15% gas volume fraction (GVF) of air. 100 Mesh sand at 0.2% (2000 ppm) concentration by weight of sand and water is used for both two-phase test and three-phase test. Figure 59 presents the schedule during the erosion test. As mentioned before, periodic disassembles inspection were performed. Meanwhile, performance and vibration test are executed at targeted time intervals.

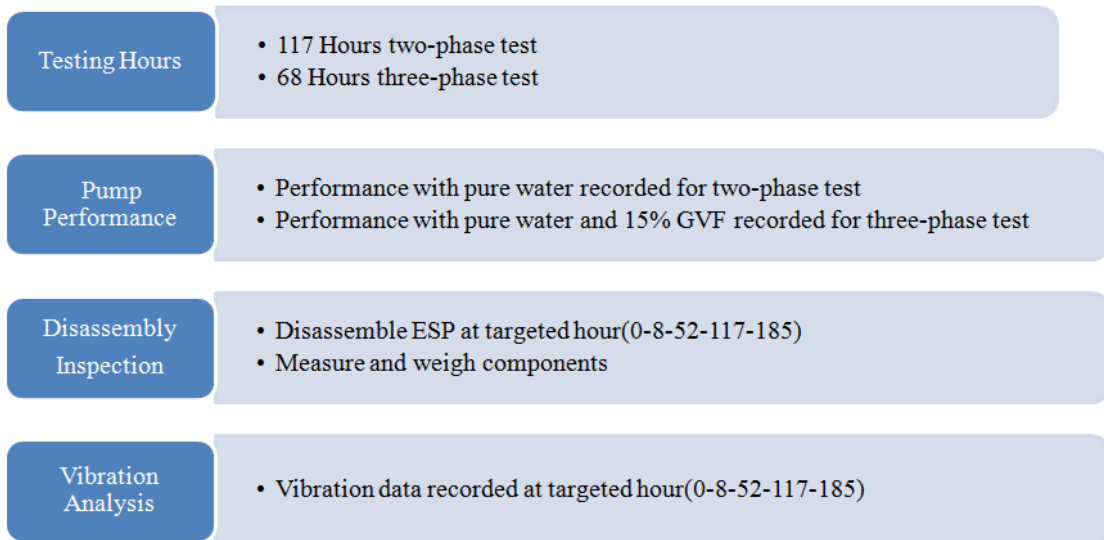


Figure 59. General Test Procedure

6.1. ESP Performance Degradation

ESP performance curves for clean water at 3600 RPM are recorded periodically during the erosion test. Data collected at each targeted hour has been compared with established baseline curve in order to track the degradation of the ESP. Three basic measurements, capacity, pressure rise and power requirement are involved in the test. All three factors are equally important to determine the pump efficiency. Figure 60 shows comparison among three important time points, baseline, the end of two-phase test (117 hrs) and the end of three-phase test (185 hrs). The BEP efficiency dropped from initial value 76% to 74% after 117 hours and 69% after 185 hours. When running the two-phase test, the pressure rise around BEP doesn't change much, only went down when it is off from BEP point. However, three-phase test shows decrement around BEP too.

In Figure 61, the mean efficiency fell down about 6.58% after 117 hours and 11.37% after 185 hours. The efficiency relies on two main factors which are pressure rise and power consumption. Most contribution is made by 5.52% decreasing on pressure rise after 117 hours and 11.37% decreasing on pressure rise after 185 hours. On the other side, the electrical power consumption only slight increases about 1.56% after 117 hours and 3.95% after 185 hours. Pump efficiency degradation rate is slow at the very beginning, and then speeds up at the second half of the two-phase test. The degradation rate is further increased when switching to three-phase test after 117 hours. From the slope of the trend line, it is easy to tell that three-phase test made a quicker degradation progress on pump performance.

WJE 1000 at 3600 RPM and 0% GVF

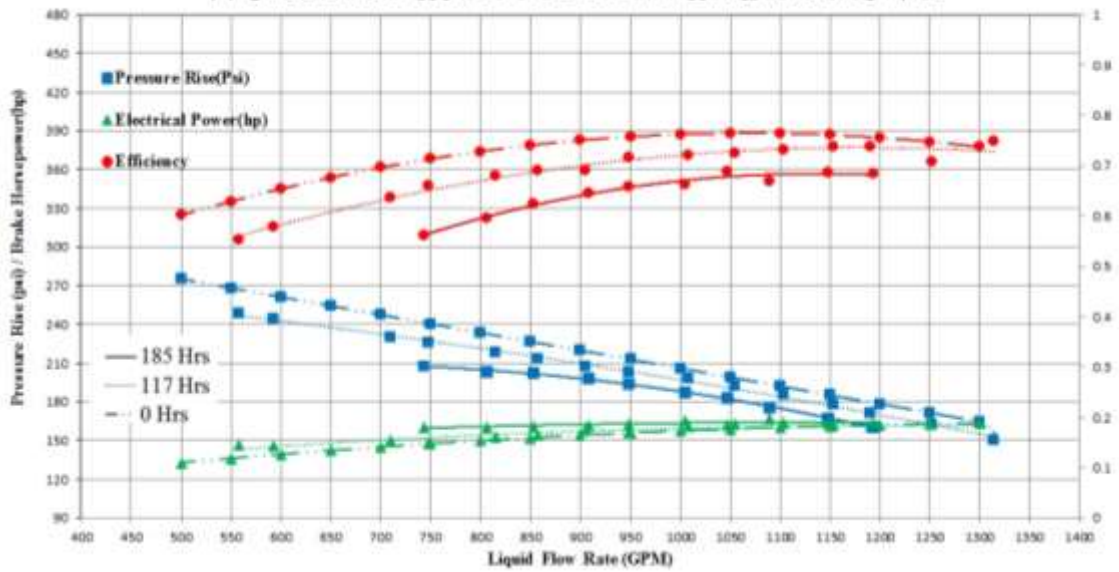


Figure 60. Pump Performance Curve with Pure Water at 0-117-185 Hrs

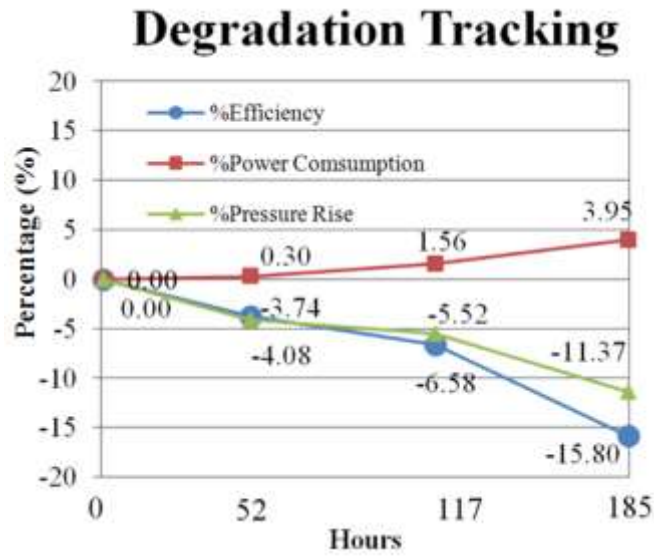


Figure 61. Performance Degradation with Pure Water

Also, the pump performance with 15% GVF was tracked during the three-phase test. Since the WJE-1000 ESP is not made for multiphase flow purpose, the maximum GVF it can reach is only 17% GVF. However, the pump performance at 17 GVF can only operate at a narrow flow rate range and surging is easily induced. Hence, 15% GVF was selected for the constant air fraction in the three-phase test.

Figure 62 compared the pump performance with 15% GVF at the beginning and the end of three-phase test. BEP with 15% GVF is about 850 GPM of liquid flow (1000 GPM for total flow rate). The 15% GVF data taken at 117 hours is treated as baseline data for the three-phase test. Air injection results in a significant decrease on both the pressure rise and power consumption. The efficiency at BEP which is only 60% initially falls down to 55% at the end. Unlike what happened on the pressure rise with pure water, degradation on pressure rise has the similar amount both close and off the BEP. After 68 hours operation, 9.18% reduction has been discovered for efficiency which is due to 7.46% decrement on the pressure rise and 2.60% augment of power consumption. From the trend line in Figure 63, the efficiency degradation rate remains relatively constant through the whole procedure of three-phase test.

During the whole test process, the leakage losses through secondary flow passage such as impeller labyrinth seal and bearing clearance increased. Also, the impeller and diffuser gradually obtained erosion wear mark on the blades, hub and shroud. The combination of these affects resulted in a continuous pump performance degradation.

Later on, air injection accelerated the erosion rate when the three-phase test was performed.

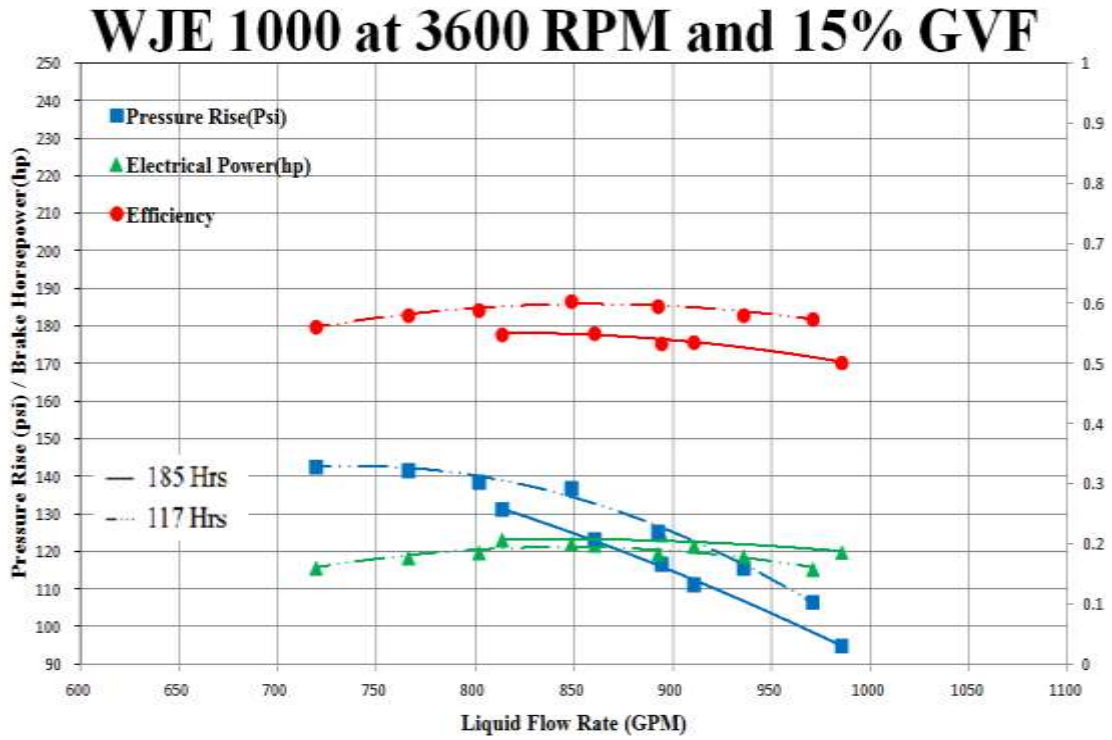


Figure 62. Pump Performance Curve with 15% GVF at 117&185 Hrs

Degradation Tracking

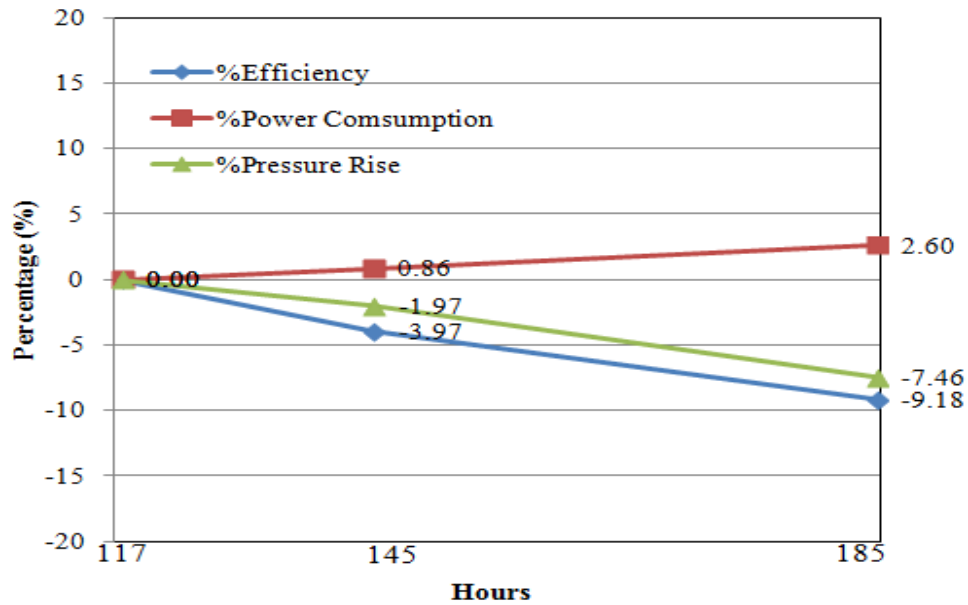


Figure 63. Performance Degradation with 15% GVF

6.2. Component Wear Analysis

As mentioned before, periodical disassembly inspections were performed to investigate components' physical degradation due to erosion. The critical dimensions and weight were recorded at each targeted time point. Then analysis will aim to study the effect of sand and air on the erosion process. In this section, the wear marks on each component will be displayed and the possible causes will be discussed as well. This part of research will provide critical erosion data measurement for the test and future simulation as well.

6.2.1. Components Wear Pattern

This portion of study focuses on the description of physical wear patterns. Figure 64 shows the detailed configuration including impeller, diffuser, bearing, spacer and thrust

plate. Also, the bearings and spacers have been numbered according to the location from top to bottom in order to track the wear progress in various locations. After disassembly inspection, components are reassembled at the same location.

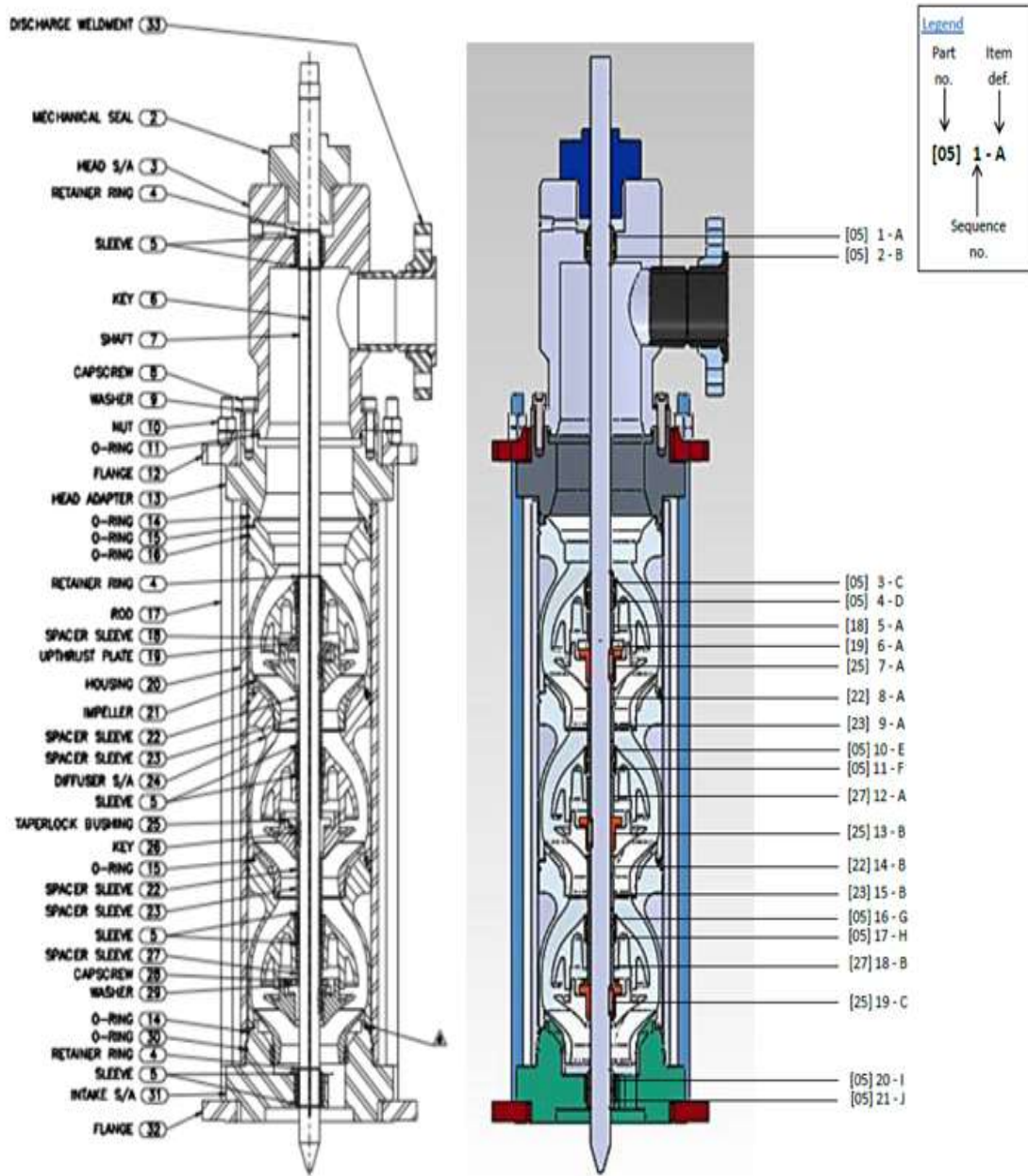


Figure 64. WJE-1000 Detailed Configuration

In these three stages of the WJE-1000 ESP, five pairs of one inch long tungsten carbide bearings are keyed on the shaft. Three of them are placed in the diffuser bore of each stage and the other two pairs sit in the inlet flange and discharge stuffing box. The stationary part of journal bearings, which are mounted rigidly in the pump body, are made of tungsten carbide as well. When the loose particle pass through the tiny clearance of journal bearing, the three body abrasive wear is going to happen as shown in Figure 65. In Figure 66, wear in tangential direction, so-called scoring wear has been noticed on each bearing after 185 Hours. Visible cracks are apparent on bearings 16, 17 and 20 at the keyway where stress is concentrated more than other places. This type of wear mark is due to the solid particles embedded in the bearing surface. When the hard particle is small enough to enter the bearing clearance at the side with maximum film thickness, the water starts to carry the particles into the clearance, and then the wear marks grooves continuous around the bearing circumference. This type of wear is also called three body abrasive wear. The particle in the middle may be either free or partially embedded into one side of the bearing surface. It is obvious that radiuses of the bearings have been reduced on the portion where are mating to the stationary part. The minimum film thickness in the clearance may reduce further after air injected because of the compressibility of air.

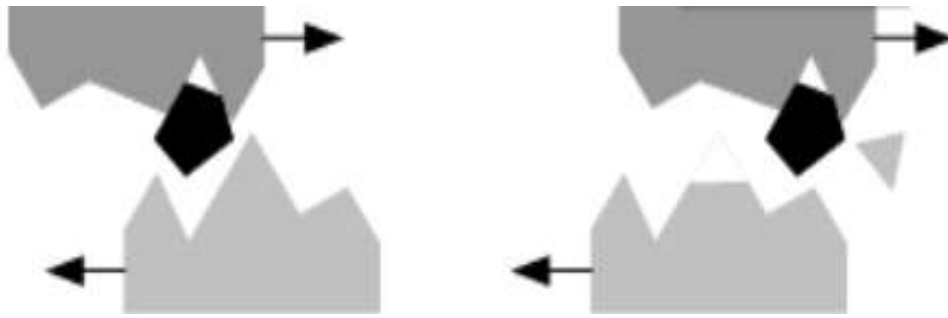


Figure 65. Three Body Abrasive Wear

Figure 67 shows bearing status after two-phase test at 117 hours for comparison purposes. Although scoring wear already existed on most of the bearing surfaces at that time, the number and depth of scoring grooves are much less than what observed at 185 hours. In summary, the last 68 hours of three-phase test had more to the scoring wear than the first 117 hours test with water and sand. The pump curve comparison also reflects the same trend. The leakage losses dragged the pressure rise down about 10% in last 68 hours but only 6% in the first 117 hours. Taking an example of bearing pair 20& 21 in Figure 68, the status at each target time point shows the general erosion process. Apparently, there is almost no change in the first 8 hour and most of the tangential scoring wear started after 117 hours.



Figure 66. Journal Bearings Status after 185 Hours



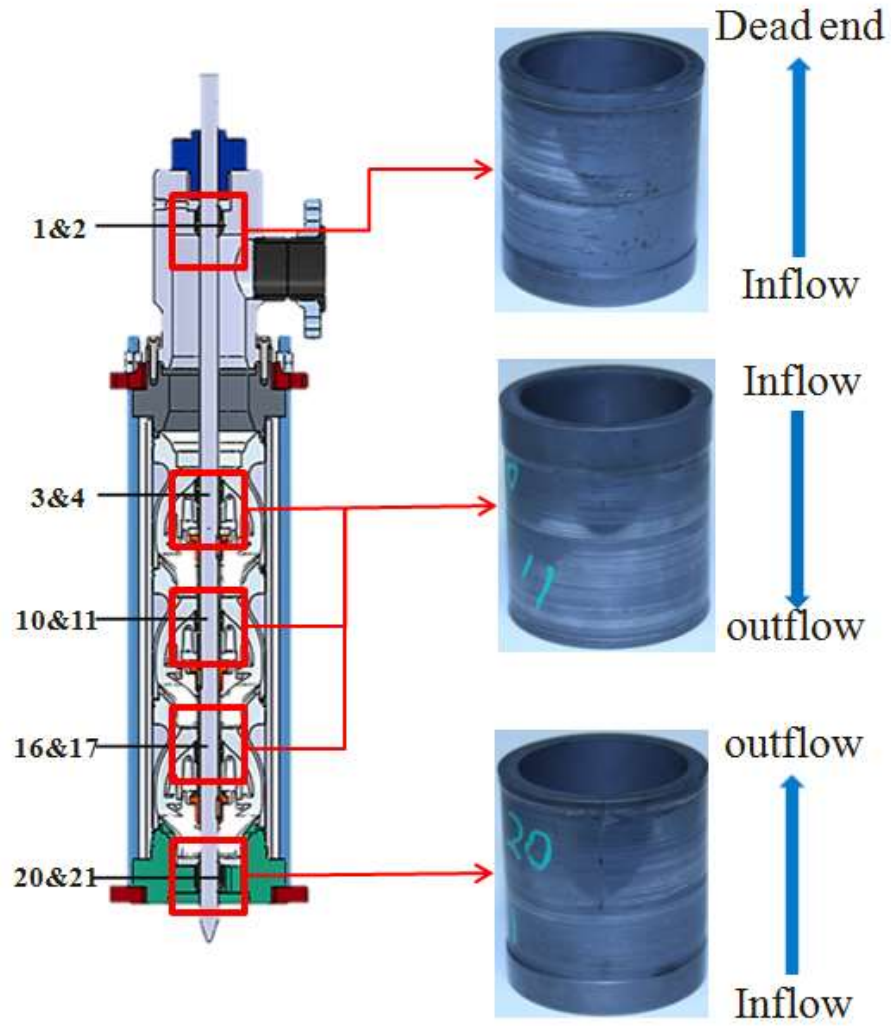
Figure 67. Bearing Status after Two-phase Test at 117 Hours



Figure 68. Bearing 20&21 Status at Target Time Point

Besides the abrasive wear on the tangential direction, the hair cracks with uniform distribution are also detected on the bearing surface. Abrasive wear grooves have the width similar to sand particle size because it is a result of sand particle rubbing. Hair cracks have smaller width than abrasive wear grooves and can be noticed under microscope only and are aligned in the axial direction. Since all the hair cracks showed up as a uniform pattern, it doesn't look like it is due to sand particle. The possible reason for this may be fatigue failure issue due to the direct contact of tungsten carbide. Figure 69 shows the secondary flow direction in the bearing clearance. The secondary flow direction in the three stages of the diffuser is top to bottom while the flow direction in the bearing 20&21 is bottom to top. The condition for bearing 1&2 is different with others since they are facing to a dead end where the flow stopped by the mechanical seal.

The reason to point out the secondary flow direction is that abrasive wear and hair cracks always appear in the same direction with secondary flow as shown in Figure 70. The tangential wear mark, whose groove width is similar to the particle size, appears at the inlet part of the bearing clearance and disappeared at bearing exit. Sand induced contact is the main reason for this phenomenon. The sand started to polish both size of bearing surface at the inlet side and gouged bearing surface. Then the sand particle was crashed while traveling in the bearing clearance. At the part of bearing clearance exit, the tangential grooves no longer existed. Instead, very uniform shape of hair crack due to fatigue failure started to show up. The reason is that sand induced shaft instability led the direct contact between the rotating and stationary surface at the exit part. Abrasive wear shows up first near the inflow place then followed by uniform hair cracks. In other way, bearing pairs of 3&4, 10&11 and 16&17 have abrasive wear at top and hair cracks at bottom. Bearing pair of 20&21 has hair cracks at top and abrasive wear at bottom as what is showed in Figure 71. For bearing 1&2, the abrasive wear and hair crack don't have an order like others because one side is dead end.



Secondary Flow Direction

Figure 69. Secondary Flow Direction in Bearing Clearance

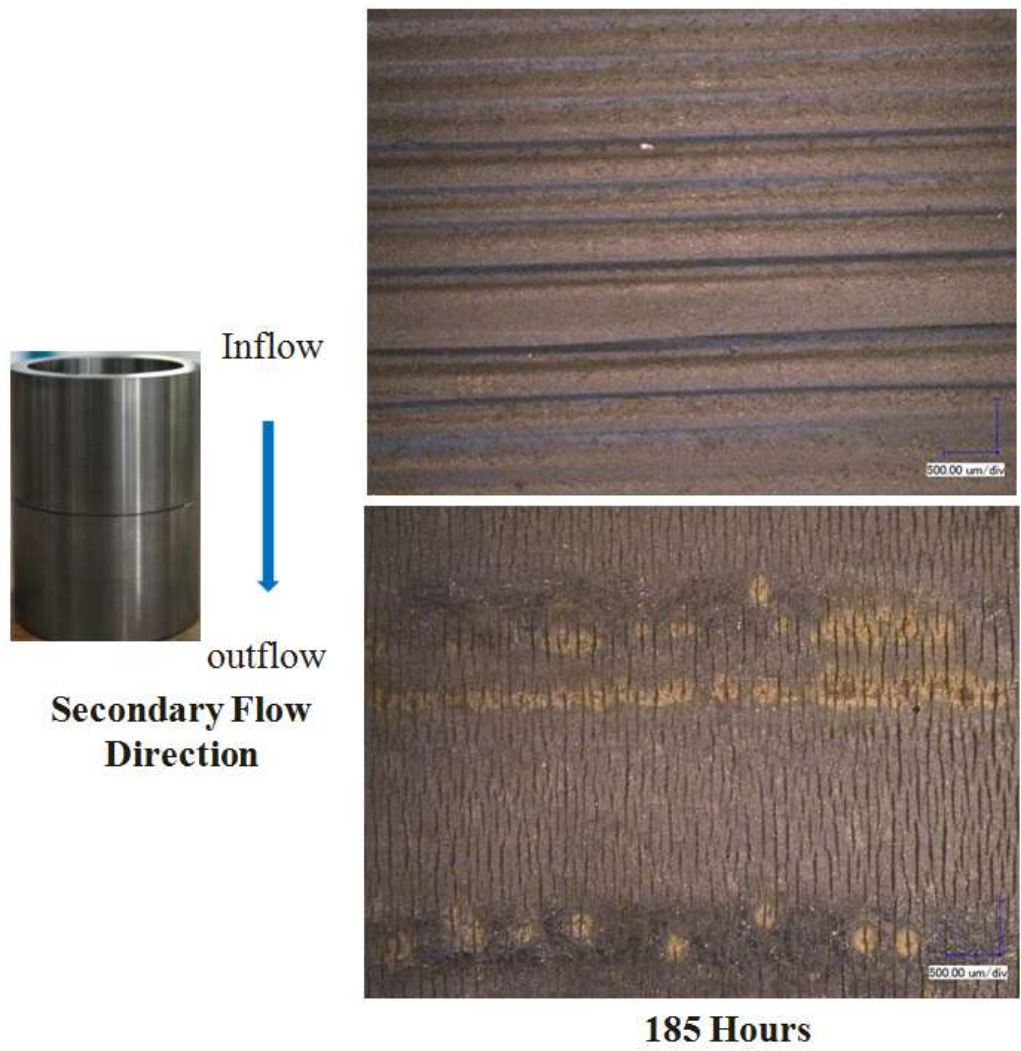


Figure 70. Scoring Wear and Hair Crack

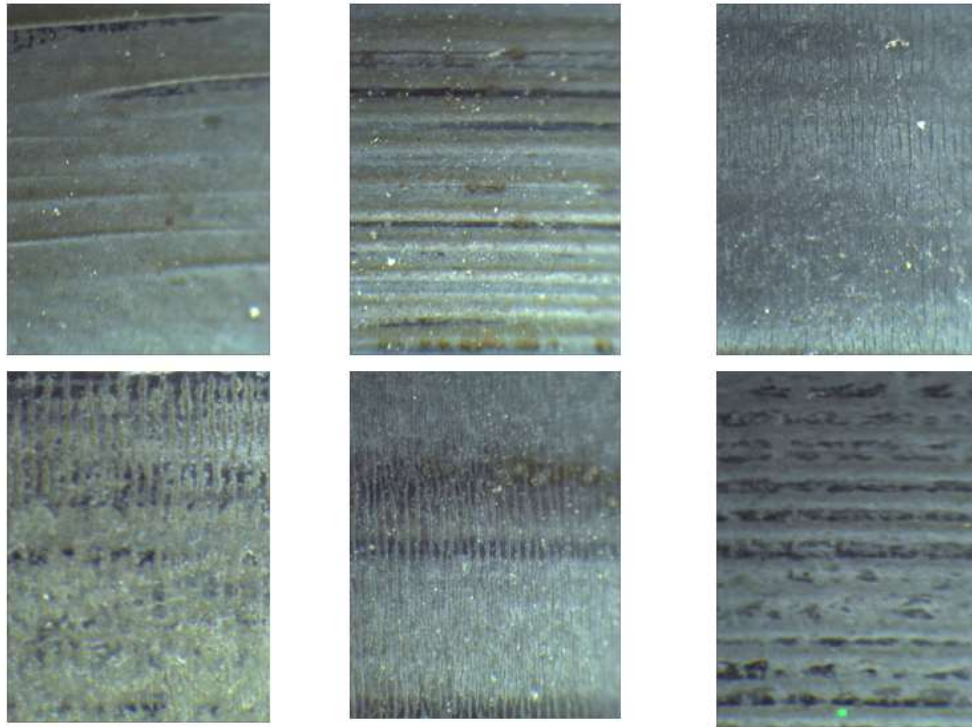


Figure 71. Wear Pattern on Each Pairs of Bearings

Except for the wear on the contact surface of bearings between rotational and stationary part, there are still some wear marks found in the circumference mating surface between two bearings as shown in Figure 72. The cracks start from the internal surface, and then spread out radially towards external surface. The width of the crack is a little bigger than the one on the vertical surface. In order to confirm abovementioned types of cracks are not original present in a brand new bearing due to a process issue, a brand new tungsten carbide bearing in Figure 73 is sliced by the depth of 0.04 inches which approximates to the worn surface. It is clear that no existing cracks are present on the bearing originally. However, there is not enough evidence to fully explain this phenomenon based on the current test. Further study is needed to continue on this subject.

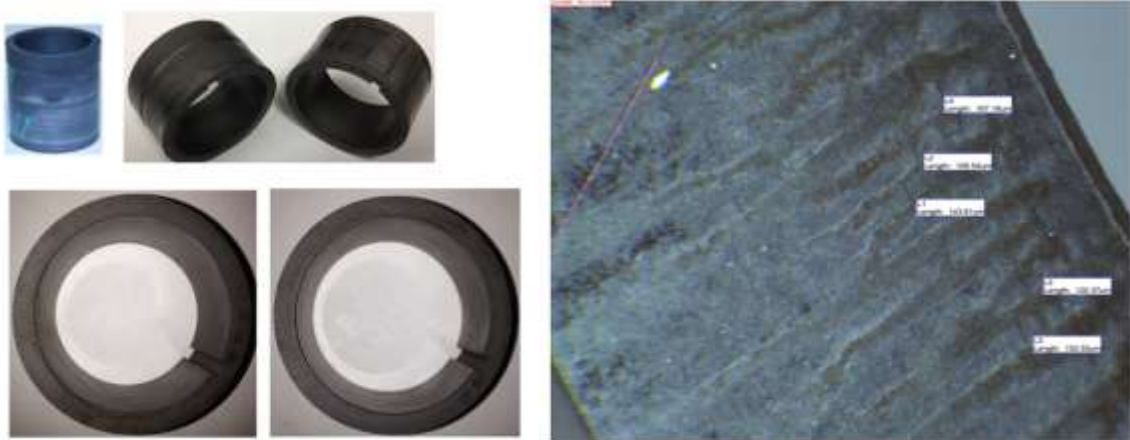


Figure 72. Wear Mark between Two Bearings



Figure 73. Surface and Interior Material

Besides the tungsten carbide bearings, the impeller is another critical rotating part in the ESP. A significant amount of wear marks are present on the impellers. As shown in Figure 74, two labyrinth seals are located at both the intake and the discharge sides of impellers. Five balance holes manufactured through impeller bores. A majority of the observed wear marks appeared at leading edges and trailing edges of blades, hub and shroud and labyrinth seal.

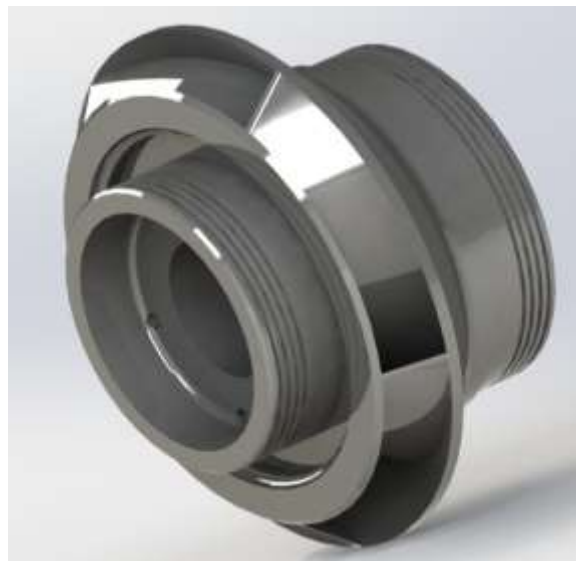


Figure 74. WJE-1000 Impeller Configuration

Figure 75 shows the wear mark growth process from beginning to the end of the test. The leading edge of the impeller blades is manufactured initially as a straight edge. The third disassembly inspection at 52 hour is the time point when distinct wear mark on the leading edge appears. Due to the flow separation and sand particle impingement happening near the edge, part of material on the leading edge is removed during the erosion test. Interestingly, the wear mark on the first stage has a different pattern

compared to the one on the other stages as shown in Figure 76. On the first stage, leading edge has greater erosion rate at the location which is close to impeller shroud while other stages have been eroded more on the interior hub side. This phenomenon may due to different flow and particle distribution between first stage and other stages. First stage wear pattern highly depends on the inlet flow loop setup. All impellers except the first stage have a diffuser connected right before its suction side. Seven flow passages in the diffuser make flow distribution evenly compared to inlet condition.



Figure 75. Wear Mark on Leading Edges



Figure 76. Wear Marks on Different Stages

Another type of wear noticed is a horseshoe shape wear which is resulted from flow separation as shown in Figure 77. On the leading edge of impeller, the flow is separated into pressure side and suction side and made the progress for the horseshoe shape wear on the hub and shroud where they join the blades. The horseshoe shape wear is also located around balance holes due to flow separation happened there as well. As shown in Figure 78, the direction of secondary flow from balance hole is opposite to the main flow direction. Then the main flow is forced to go around the balance hole. The wear mark around balance hole has one portion on the hub and the other portion on the blade. Meanwhile, it is worth to point out that stages suffered from different levels of horseshoe shape wear. The higher the stage is, the severer the wear is.

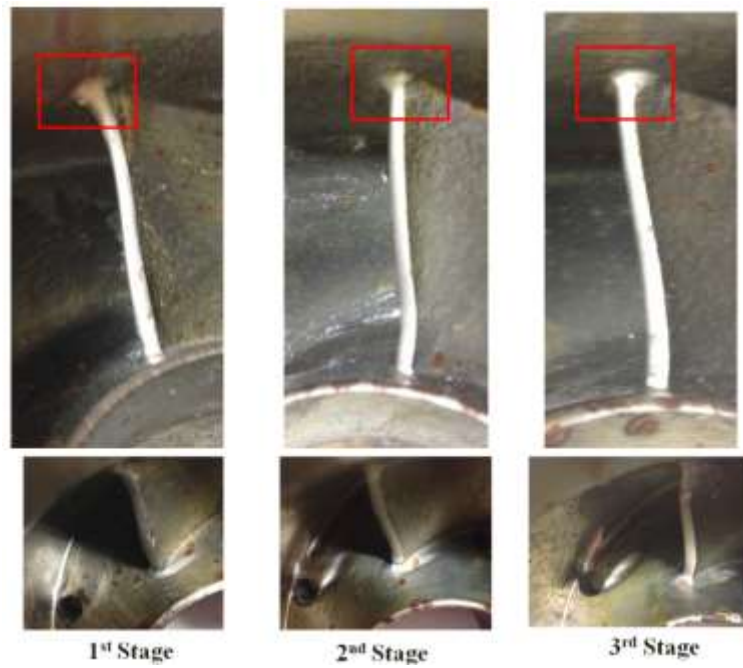


Figure 77. Horseshoe Shape Wear Mark

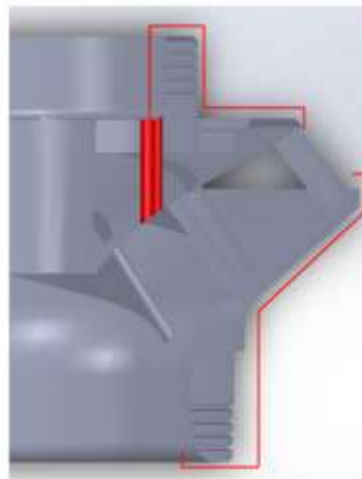


Figure 78. Secondary Flow Path around Impeller

Wear marks are also present at trailing edge of the impeller blades as shown in Figure 79. During the erosion process, all the trailing edges become slimmer and sharper

compared to the initial condition. Some blades start to have curved edge instead of straight one. On the suction side of trailing edge, there are wear marks on the shroud and hub as well.

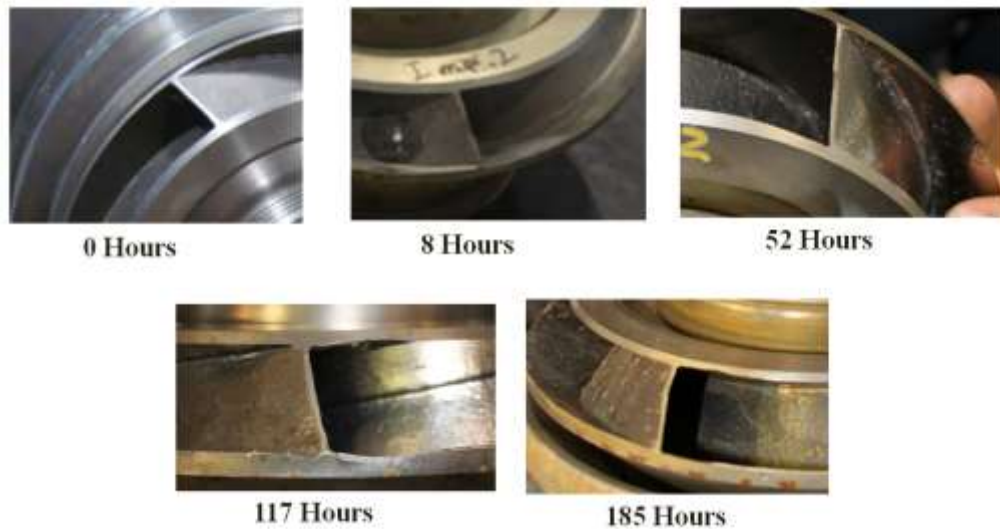


Figure 79. Trailing Edge Wear Mark

Each impeller has two labyrinth seals located at the suction and discharge side. The clearance of the seal is large enough to let the sand particle go through it. In Figure 80, the erosion progress of them from beginning to 185 hours has been provided. The photo of 0 hour shows the impeller with wear-resisting coating on the labyrinth seals and the coating still existed at 8 hour. Then all the coatings are gone on the seals after that. It is obvious that the diameter of labyrinth seals is reducing during the erosion test. The detailed measurement will be discussed in the next portion.



Figure 80. Wear Mark on Impeller Labyrinth Seal

The stationary diffuser in Figure 81 has less wear marks with respect to impeller. The locations suffering from erosion includes the leading edge of blades, the shroud and the contact surfaces with the impeller labyrinth seals. Most of wear is detected at the suction side of the diffuser housing where flow velocity is higher.



Figure 81. WJE-1000 Diffuser Configuration

Figure 82 shows wear marks on the leading edges of a diffuser blade. In order to identify the wear easily, the interior part of diffuser has been painted at very beginning. As the erosion process proceeds, the paint on the shroud and leading edges of blades disappeared and the sharp leading edge becomes blunt. The tip of blade that joints to shroud and hub has been eroded as well.

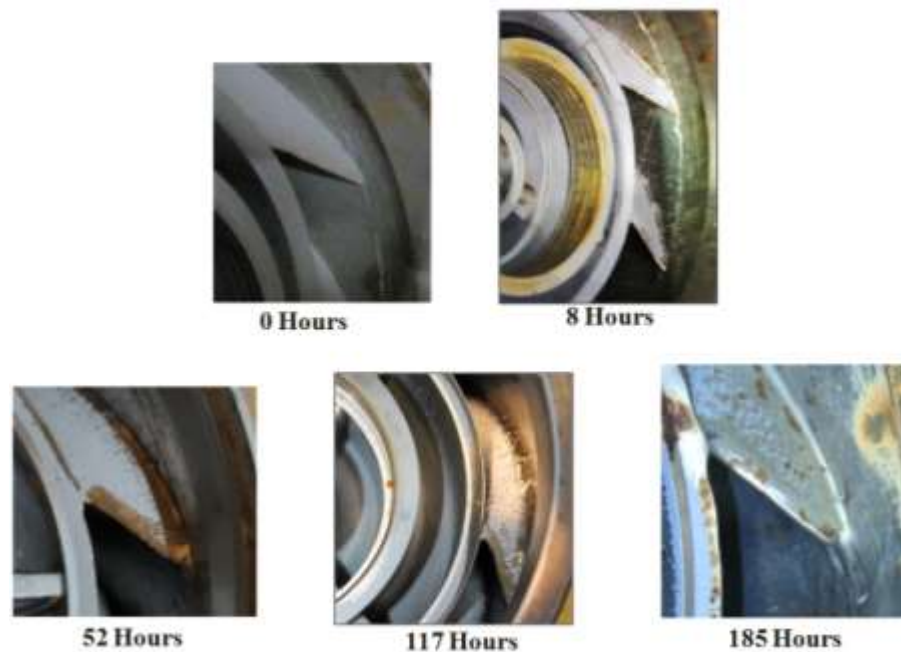


Figure 82. Wear Mark on Leading Edges

Another wear mark of the diffuser is shroud wear as shown in Figure 83. At the suction side of the diffuser, flow velocity is relatively higher and particle impingement is more likely to happen there. As we noticed, the wear made by particle impingement is more obvious on the shroud other than hub. It is possible that sand concentration may be higher at shroud due to the centrifugal force.

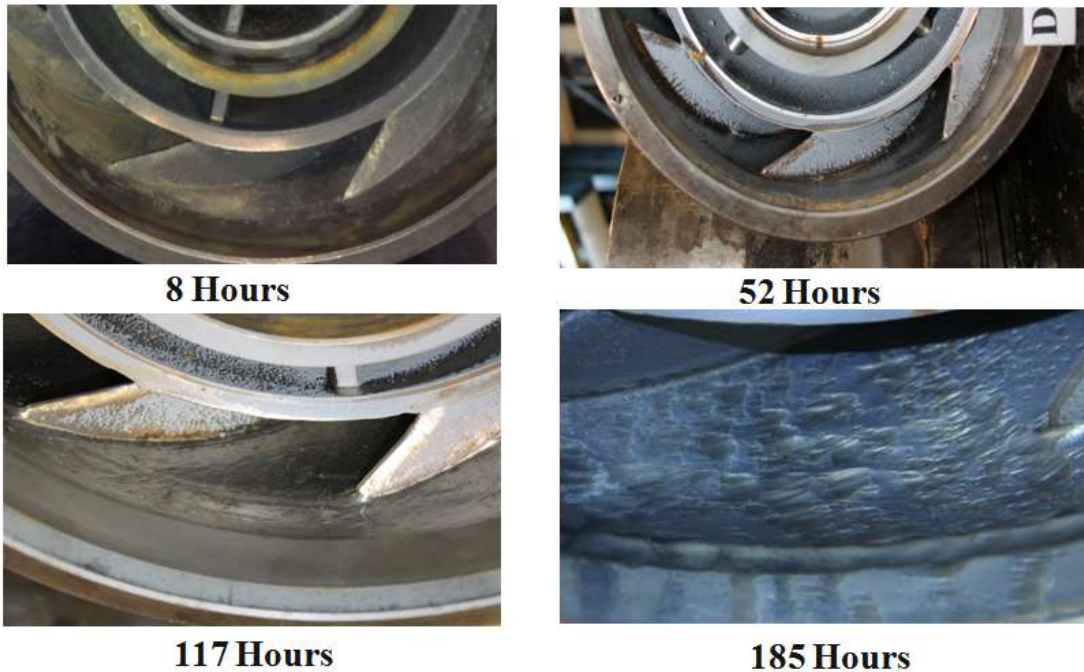


Figure 83. Wear Mark on Diffuser Shroud

The contact surface of the impeller labyrinth seal also showed wear as shown in Figure 84 and Figure 85. It is a flat surface on the circumference without any grooves originally. When sand particles went through the clearance in the labyrinth seal and embedded in the surface. The diffuser surface is gouged as shown by several grooves. The labyrinth seal and bearings are critical parts that can provide damping forces in the system. This wear makes the clearance larger in the labyrinth seal which may lead to disfunction when excessive clearance appears.



Figure 84. Contact Surface of Impeller Intake Labyrinth



Figure 85. Contact Surface of Impeller Discharge Labyrinth

In fixed impeller pumps, all axial forces are transmitted to the pump shaft and must be absorbed by using the thrust washer in the impeller. It is necessary in the ESP, especially for relatively large capacity. As shown in Figure 86, three slots located at top surface of plate and three screw holes have a little deformation after erosion test. However, the thickness of the upthrust plate has almost no change towards the end of the test.

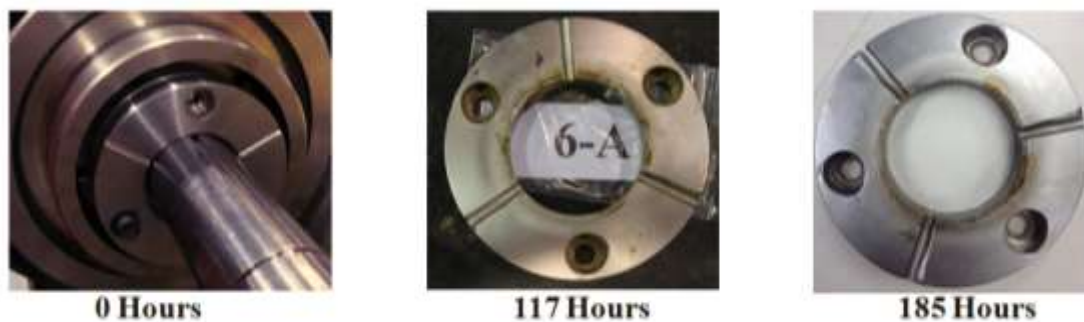


Figure 86. Wear Mark on Upthrust Plate

6.2.2. Component Measurement Analysis

During the erosion test process, all critical components of pump were inspected and measured periodically after pump disassemblies. The record of component wear progress indicates the degradation rate when two-phase test and three-phase test were performed. The wear progress of components, especially on bearing, impeller and diffuser, will be discussed in detail in this session. Figure 87 shows the mating part between bearing and bushing. Each location has two bearings of 1” length mated with a 1.58” long bushing which is mounted rigidly in the pump body. Three pair of bearings placed at diffuser stages, the other two pairs located at the bottom flange and stuffing box separately.



Figure 87. Bearing and Bushing Mating Surface

Figure 88 shows the bearing outer diameter (OD) and bushing inner diameter (ID) status from 0 hour to 185 hour. It is clear that both bearing and bushing have diameter changes. The only exception is the pair on the stuffing box whose bearing OD didn't change much during two-phase test in the first 117 hours. In the three-phase test after 117 hour, the erosion rate on all of bushings speeds up. On the other hand, only bearings on second stage, third stage and stuffing box increase the erosion rate. Bearings on bottom flange and first stage almost keep the same erosion rate when switching to three-phase test. Another noticed fact is that two bearings in the pair always stay at the similar diameters after being eroded.

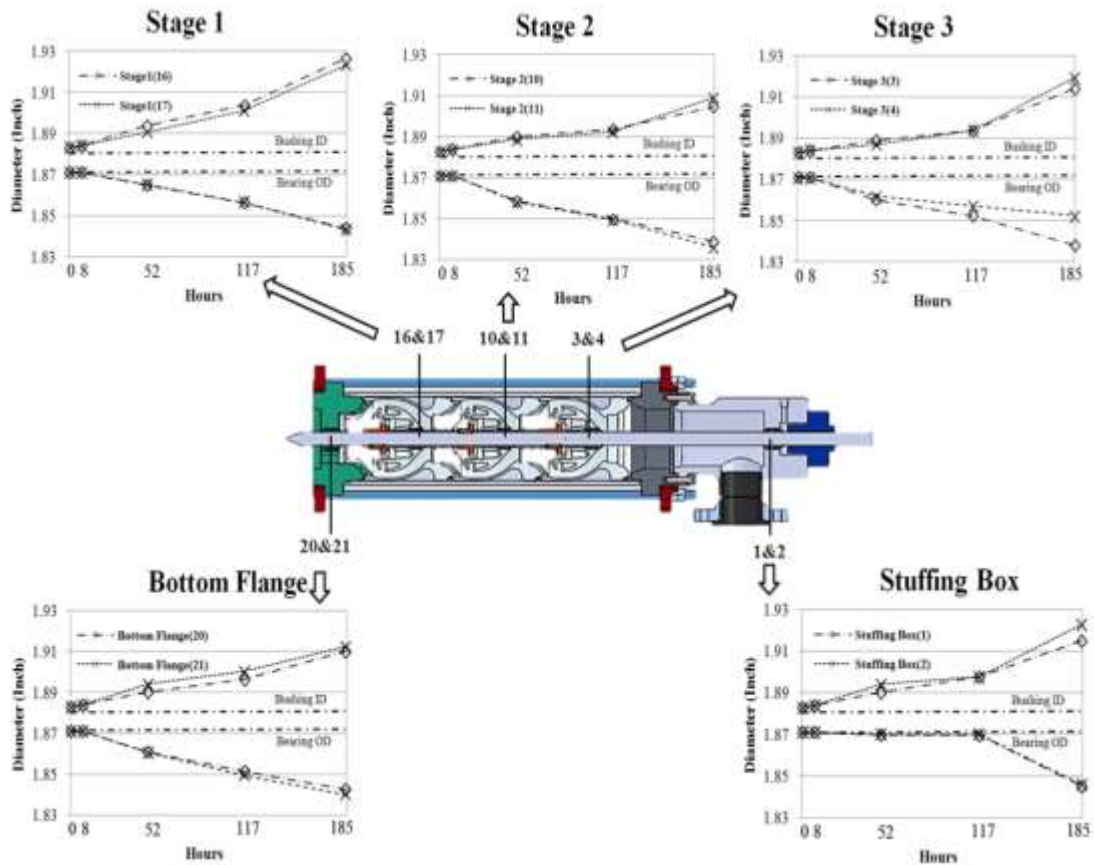


Figure 88. Journal Bearing and Bushing Diameter Tracking

Figure 89 tracks diametrical clearance that equals to bushing ID minus bearing OD from beginning to the end. Initially, radius clearance is 6 micro inches which barely allows 100 mesh size sand particle into the clearance. That is why bearing clearance almost has no change during the first 8 hours. After the clearance has opened up, more sand particles may go through the clearance and increase the erosion rate. When air is injected into system, erosion rate further increased due to the air compressibility. Aerated lubricant is less effective at preventing contacting between bearing and bushing so that the minimum lubricant film thickness decreased. This phenomenon will lead to higher possibility of surface contact. Also, since the surfaces of both bearing and bushing are

gouged as several grooves on the tangential direction, sand particle may be embedded into grooves and potentially accelerate the wear rate. After 185 hour test, the maximum diametrical clearance in the system is 0.0826" which is located in first stage.

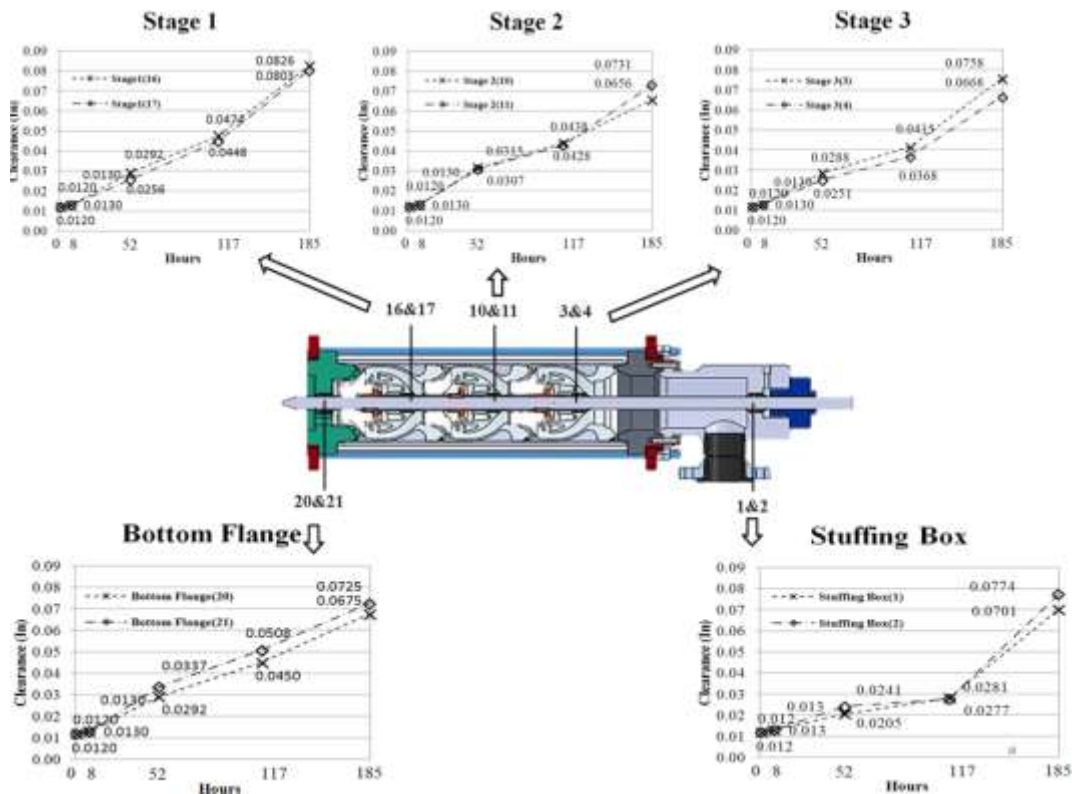


Figure 89. Journal Bearing Clearance Tracking

Figure 90 and Figure 91 compared the bearing wear mode in the two-phase test and three-phase test. Erosion rate is higher at bottom side in two-phase test. However, it is higher at top side during the three-phase test. It is clear that air changed the bearing wear mode. At the end, all bearings at different locations come to a similar clearance as shown in Figure 92. Meanwhile, it has been noticed that bearings and their corresponding bushings are usually eroding at different rates.

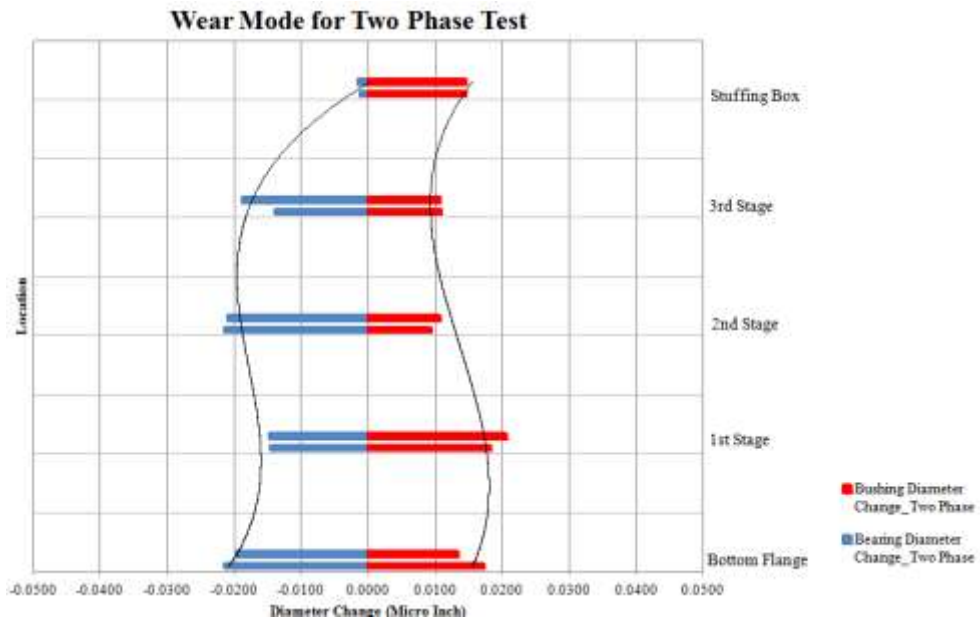


Figure 90. Bearing Wear Mode in Two-phase Test (0-117 Hours)

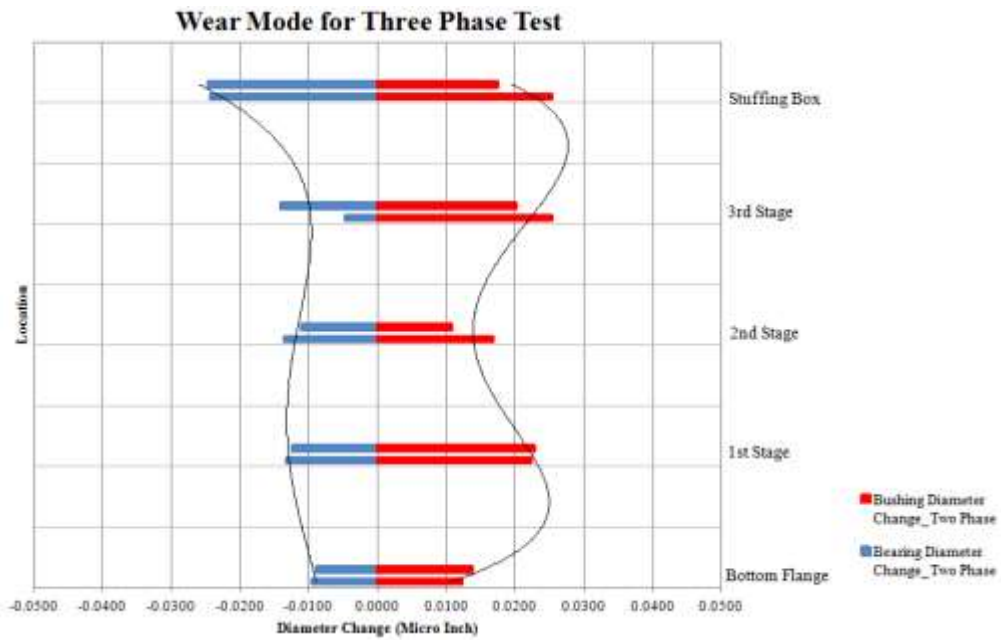


Figure 91. Bearing Wear Mode for Three-phase Test (117-185 Hours)

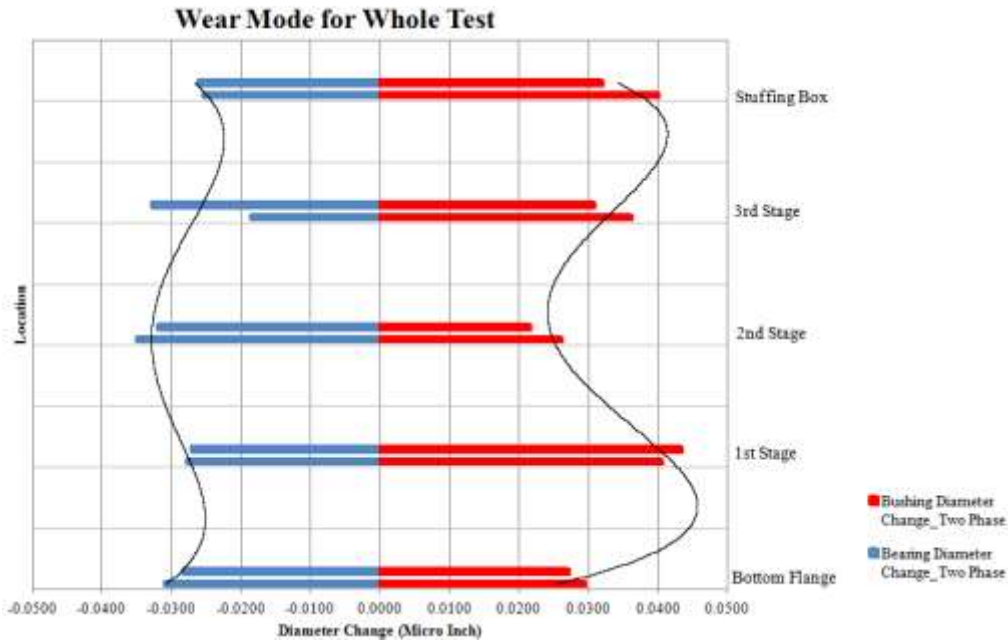


Figure 92. Bearing Wear Mode for the Whole Test (0-185 Hours)

Besides bearings, the impeller labyrinth seal is another critical part which can provide a damping effect in the system. As mentioned before, each impeller has two labyrinth seals at the suction and discharge sides. Figure 93 and Figure 94 monitored the labyrinth seal on the intake side and discharge side. The increasing clearance is contributed to by both the impeller and stator for the intake side and mainly on the impeller for discharge side. Unlike the bearings, the labyrinth seal initially has diametrical clearance of 0.017” which is large enough to pass 100 mesh sand particle. As a result of this, the labyrinth seal starts erosion at a relatively fast rate during the first 8 hours. Then the erosion rate decreases down a little in the next 44 hours. In the last half time of two-phase test, some labyrinth seals had almost no change in the clearance. However, it seems that air activated the erosion process again after 117 hours. All the labyrinth seals started to increase in clearance again.

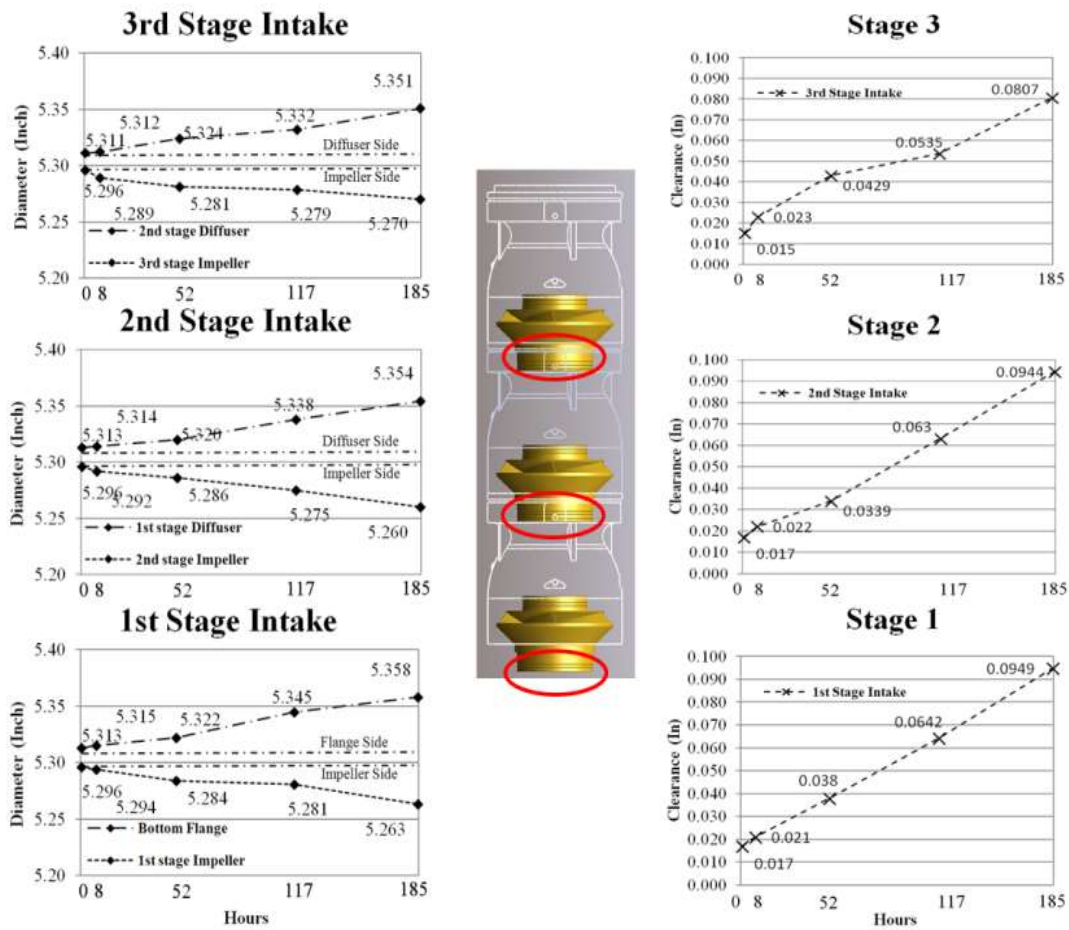


Figure 93. Impeller Intake Labyrinth Seal

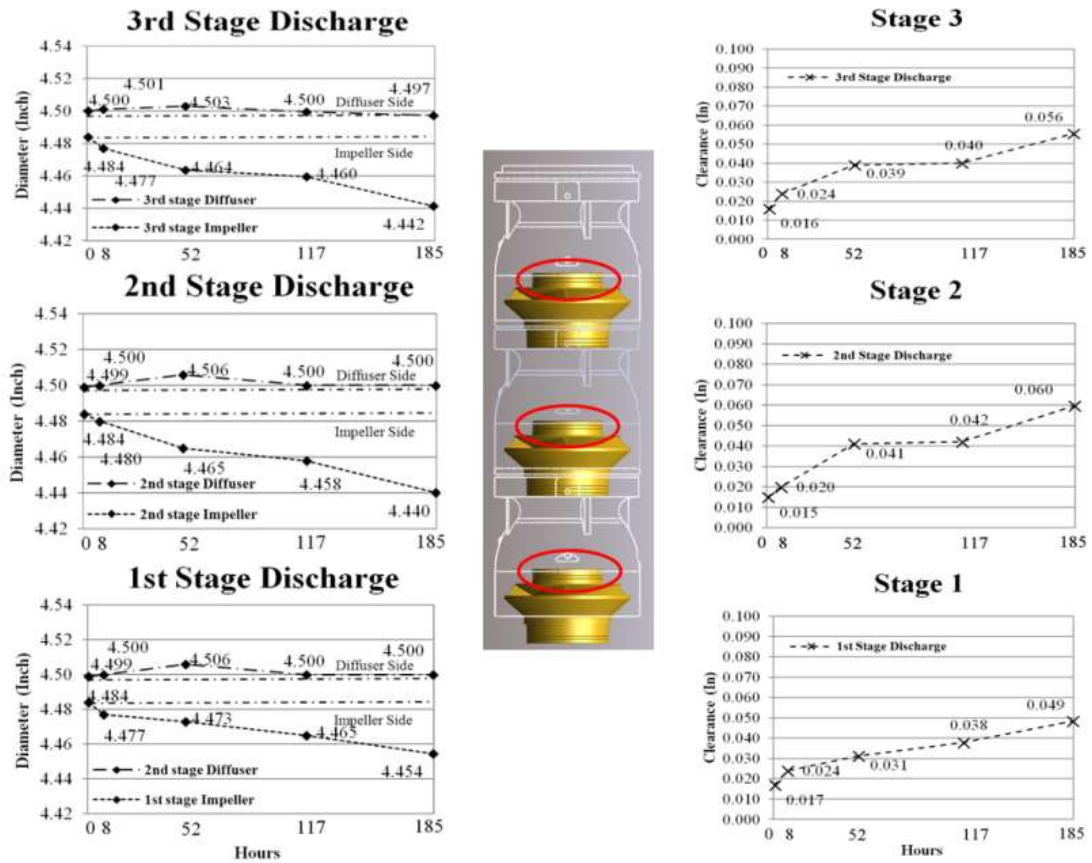


Figure 94. Impeller Discharge Labyrinth Seal

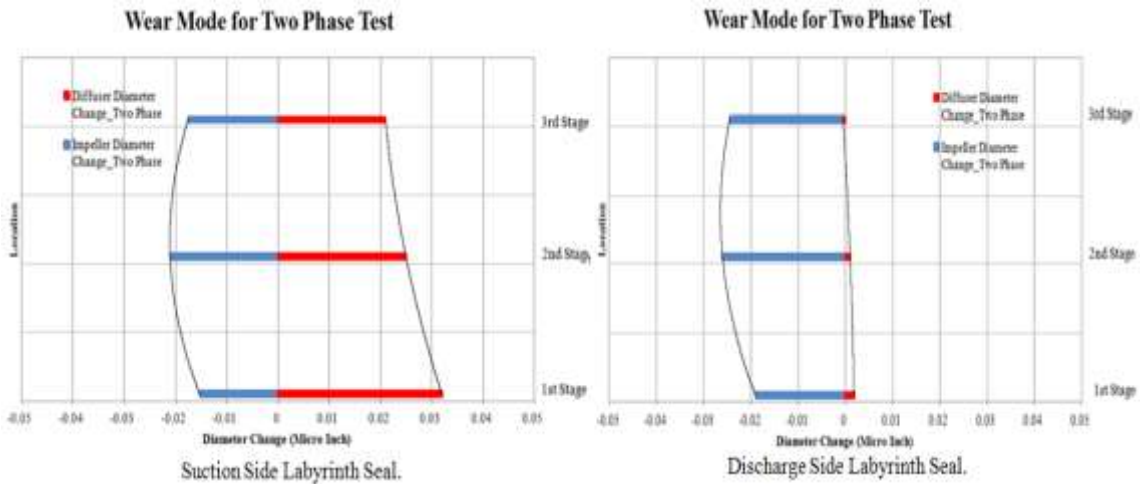


Figure 95. Labyrinth Seal Wear Mode in Two-phase Test (0-117 Hours)

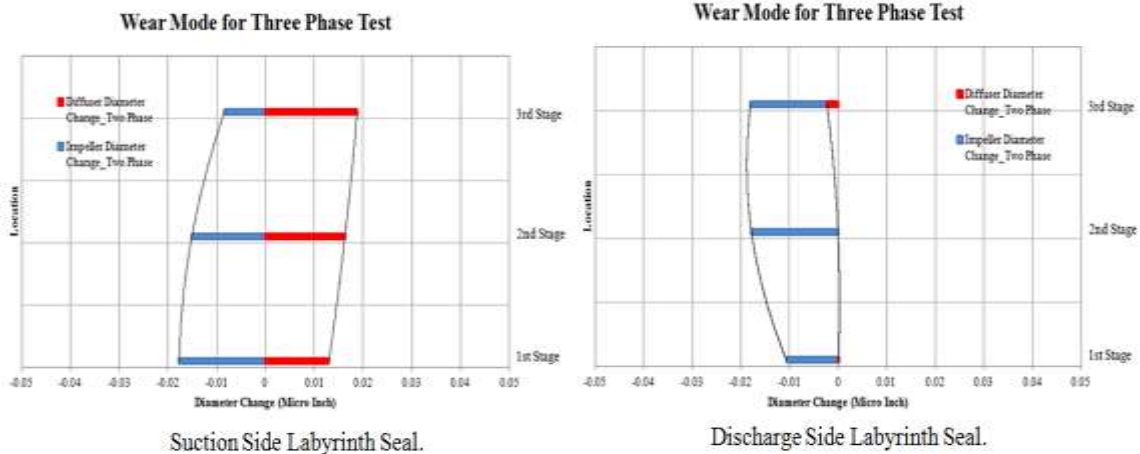


Figure 96. Labyrinth Seal Wear Mode in Three-phase Test (117-185 Hours)

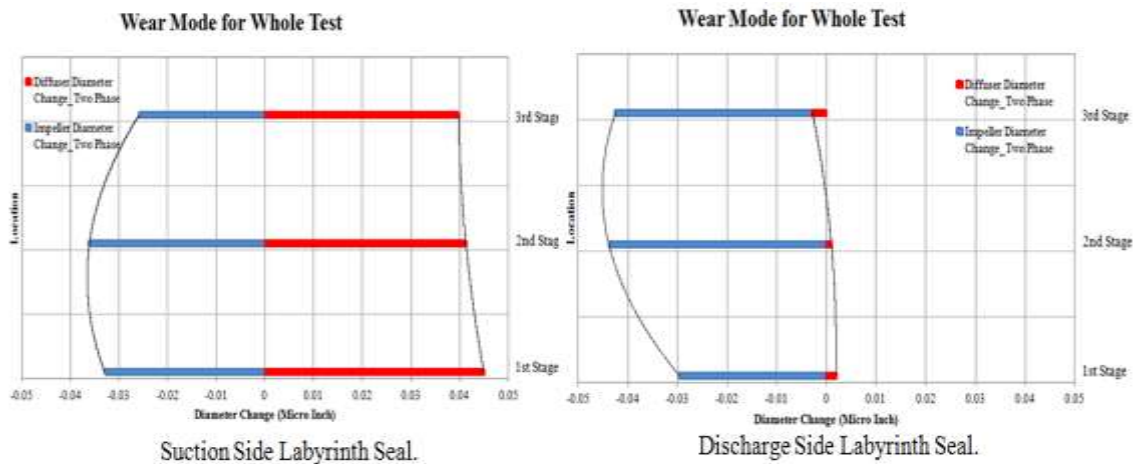


Figure 97. Labyrinth Seal Wear Mode in the Whole Test (0-185 Hours)

Figure 95, Figure 96 and Figure 97 showed the wear mode on the impeller labyrinth seals during the different time periods. It is obvious that wear modes are different between two-phase test and three-phase test. For the labyrinth seal on the suction side, clearances opened up mainly on the diffuser side at the bottom but on impeller side at top in two-phase test. However, there appears to be an opposite trend in the three-phase test. Consequently, at the end of the test, it seems that diameter changed a similar

amount on the impeller side and diffuser side. For the labyrinth seal on the discharge side, the increment of clearances was only contributed to by the impeller side. The wear mode of the discharge labyrinth seal doesn't have significant change during the two-phase test and the three-phase test.

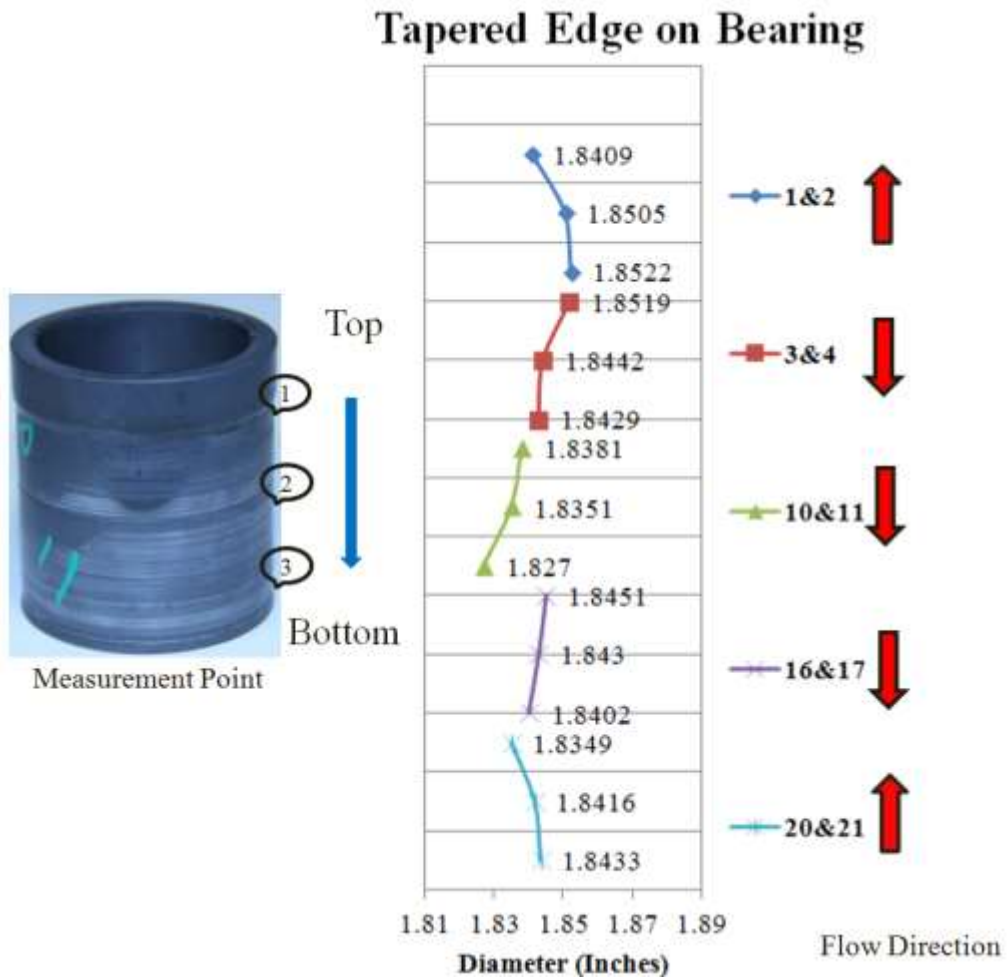


Figure 98. Tapered Edges on Bearing

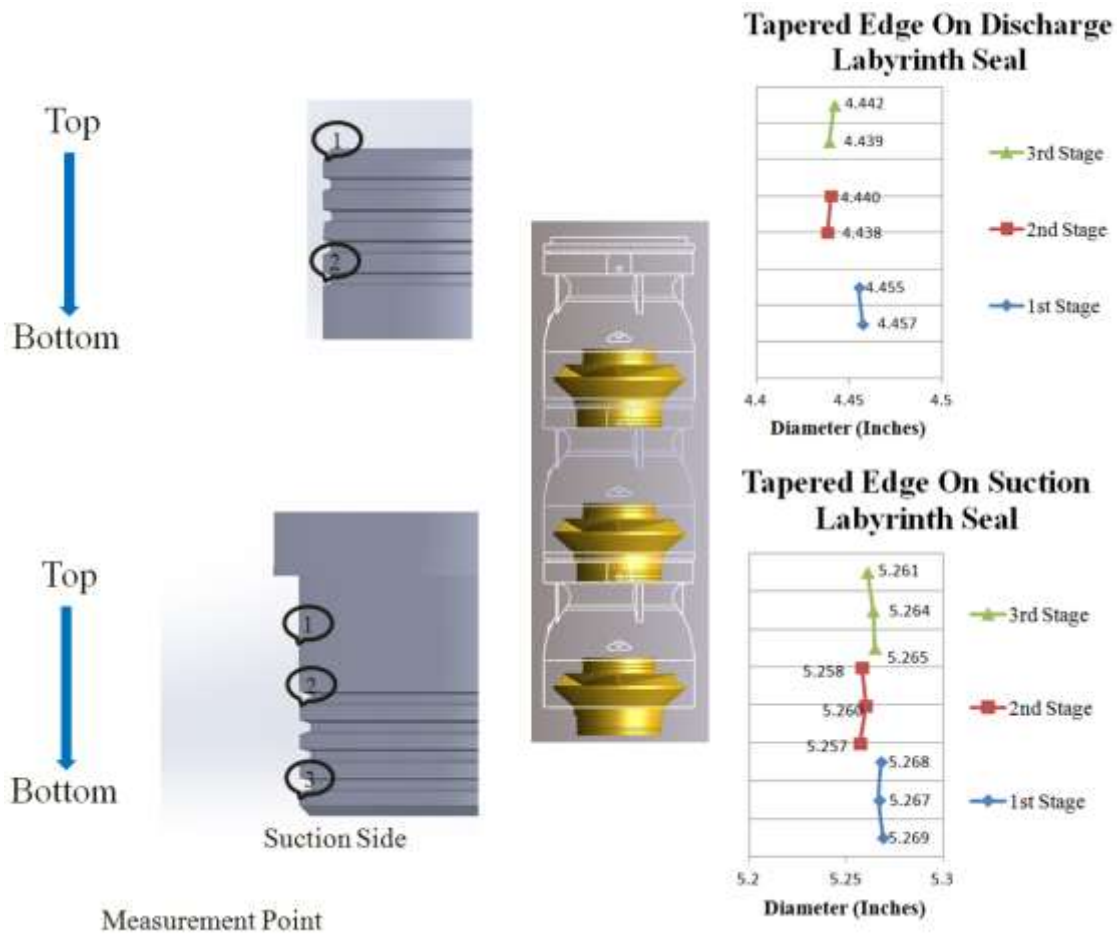


Figure 99. Tapered Edges on Labyrinth

As shown in Figure 98 and Figure 99, the originally straight edges on bearings and labyrinths have become tapered after 185 hours of erosion based on the diameter measurement on the various points along the edge. For the labyrinth, the diameter variations range from 1 to 4 micro inches. However, the bearings have a diameter difference from top to bottom of 10 micro inches. It is clear that the tapered shape on the bearing is related to the secondary flow direction. Diameter reduction on the outflow side is more than inflow side.

In this study, it is also interesting to observe the erosion rate relation between bearing and labyrinth seal as shown in Figure 100. Apparently, the impeller labyrinth seal starts erosion faster in the first 8 hours with a rate which is about ten times that of bearing erosion rate. Within next 44 hours, bearings start to be eroded very quickly while the labyrinth seal erosion rate drops down. Then this phenomenon is repeated in the rest of test. It is clear that clearance growth starts on the impeller. Bearings clearances open up when impeller clearance is much bigger. During the whole erosion test, they took turns to be the leader of clearance growth. However, they both increased in erosion rate when the test switched from two-phase to three-phase. It seems that air induced unbalance force on the impeller labyrinth seal and bearing clearance resulting in acceleration of the speed of erosion progress. In general, bearing erosion rate controls the erosion rate of the labyrinth seal since bearings are made by the stronger materials. Whirling of bearings grinds out the bearing surface and leads to the same grinding of the seal.

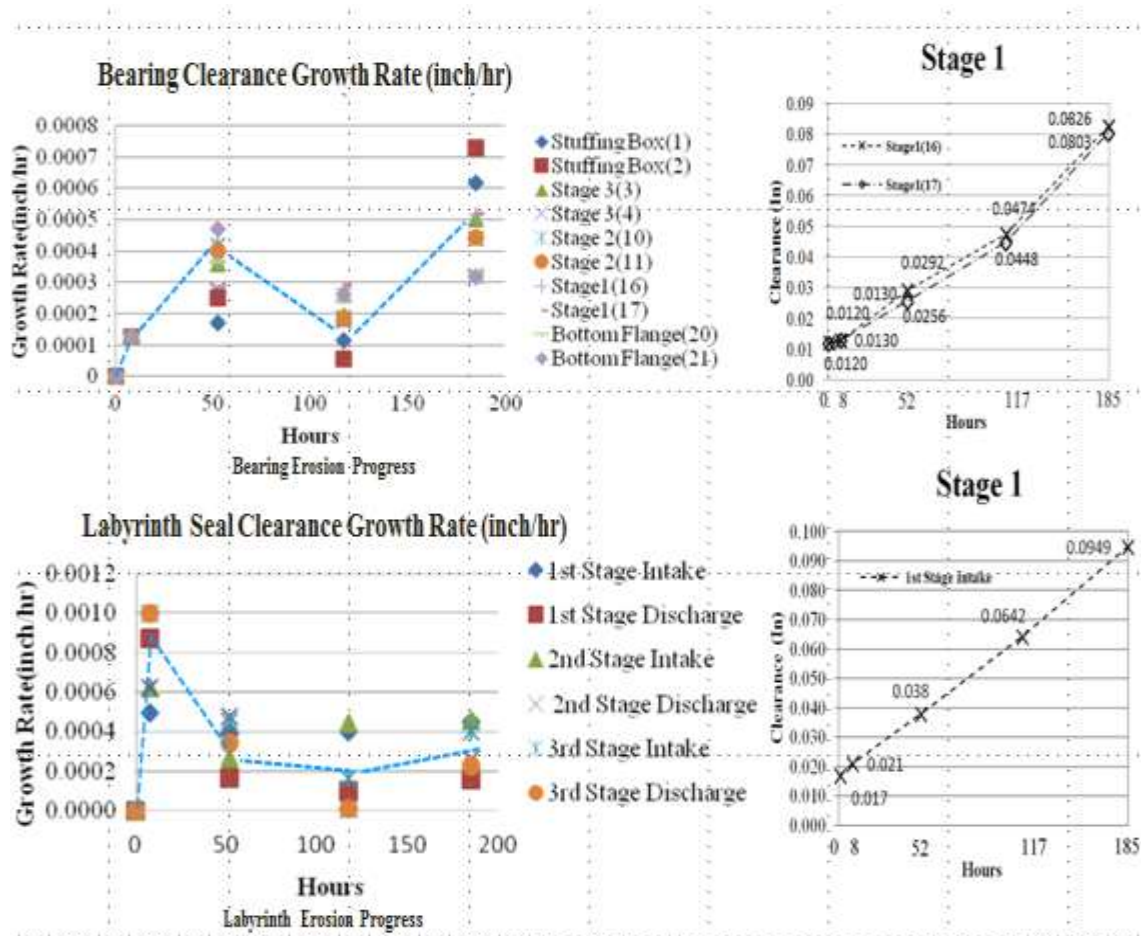


Figure 100. Erosion Rate Comparison between Bearing and Labyrinth Seal

Another critical factor to track erosion is weight measurement. In Figure 101 and Figure 102, impellers and diffusers are both weighed at each target time except the impeller on the first stage which needed to stay on the shaft to ensure the right position for next time disassembly. The trend lines of weight measurement are similar on the impeller and diffuser. This indicates that a majority of erosion may happen on the contact surface like labyrinth seals and the erosion process remove material on the impeller and the diffuser at same time. At the end of the two-phase erosion test, the rate of erosion reduced compared to what happened at beginning. After that, air activated the erosion procedure

again on both the impeller and the diffuser. By showing the clearance and weigh measurement, it is obvious to conclude that air accelerates erosion speed on impeller and diffuser.

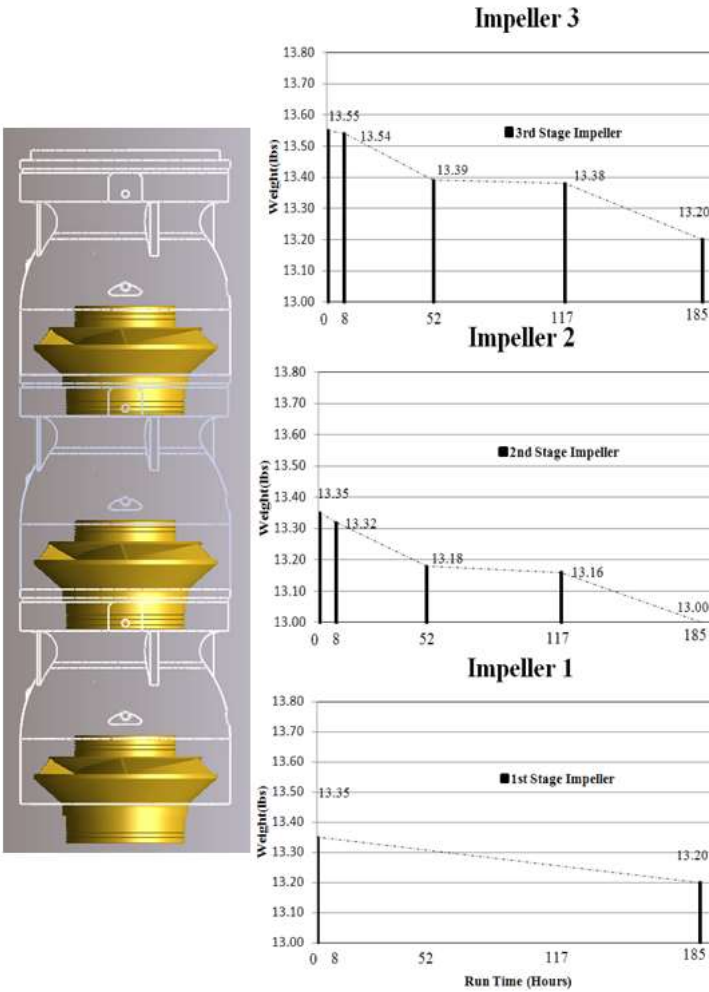


Figure 101. Weight Track for Impeller

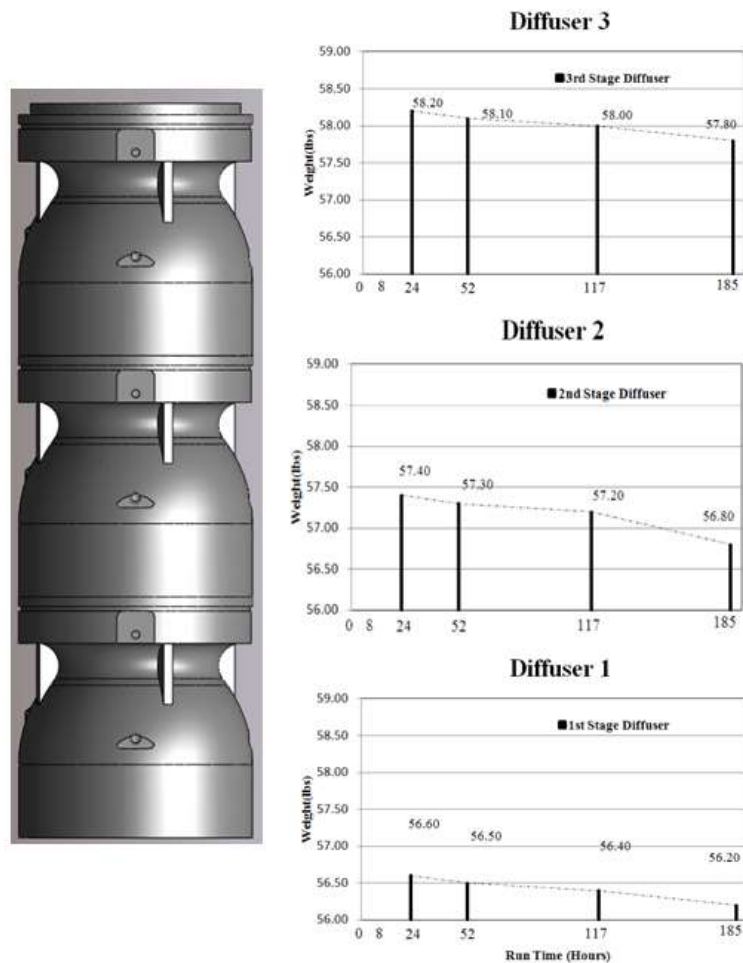


Figure 102. Weight Track for Diffuser

6.3. Vibration Analysis

Vibration analysis is one of the essential elements for monitoring rotating equipment. It has been widely used for detecting component failure in the industry. Basically, vibration from rotating equipment can provide a direct correlation between the mechanical conditions such as bearing clearance, labyrinth seal clearance and recorded vibration signals. Also, vibration signal is very helpful for monitoring specific degradation on the components, diagnosing imbalance or misalignment issue and

preventing serious damage. This portion of study will focus on vibration analysis of the WJE-1000 ESP. Vibration in the two-phase test and the three-phase test will be compared.

6.3.1. Shaft and Impeller Orbit

Five pairs of orthogonal proximity probes are mounted on the casing of the ESP to observe the complete motion of the shaft and impeller. The orbit represents the trajectory of the shaft centerline within the bearing clearance. Orbit size grows with increased bearing clearance during erosion test. Figure 103 shows the orbit development history from very beginning to the end of the test. Bearing orbit size starts at about 0.004 inches when diametrical clearance is 0.012 inches. The third stage impeller has an initial orbit size of 0.005 inches while diametrical clearance is 0.016 inches. The orbit size of the second stage impeller starts at a relatively bigger value of 0.012 inches with the same clearance of 0.016 inches. At 117 hours, distinct increase happened both on shaft and impeller and ecliptic shape orbit showed up on the second stage shaft. The next 68 hours of three-phase test also caused significant growth on the orbits as well, especially on impellers. Figure 104 shows orbit size after two-phase and three-phase test which compared to original orbit size. It is clear that orbit size grows more in the three-phase test even though the testing period is about half of the two-phase test. The injected air played a very important role in the erosion progress.

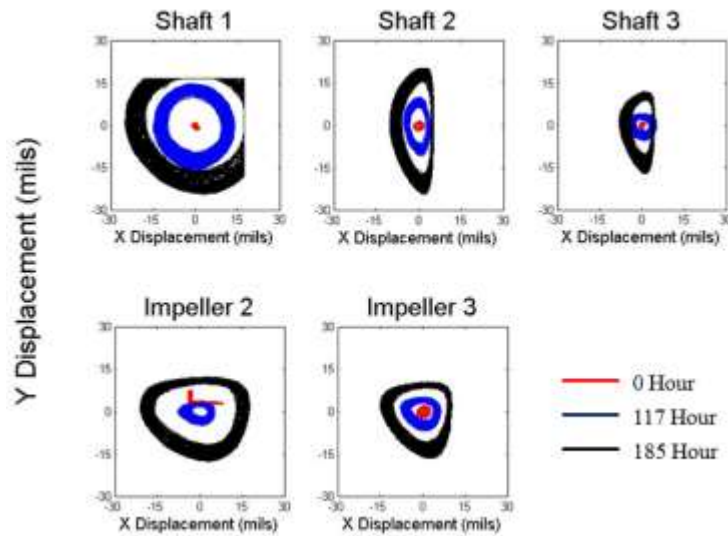


Figure 103. Shaft and Impeller Orbit Plot Comparison at Target Time Point

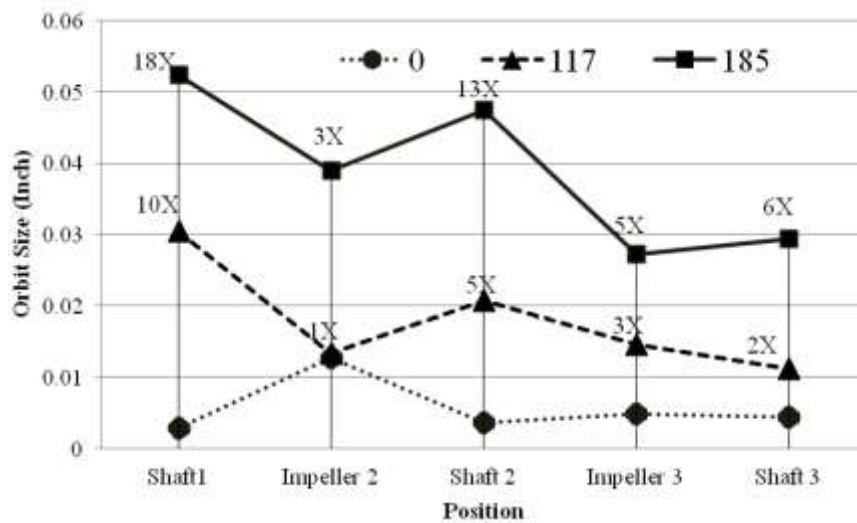


Figure 104. Orbit Increment after Two-phase Test and Three-phase Test

By putting all the orbit size together from top to bottom, the orbit mode can be shown as in Figure 105. Impeller 2 has relatively large orbit size from the beginning; however, it didn't grow a lot during two-phase test. Impeller 3 stopped at similar orbit size after 117 hours. It seems that sand and water can only enlarge the orbit of impeller to a certain

level and then the orbit growth almost stopped. In the three-phase test, air induced unbalance force activates erosion on the impeller and bearings and further increased the orbit size. This result also indicates that injected air may enlarge the eccentricity of the shaft and potentially increase the chance of rubbing between rotor and stator. Therefore, the erosion rate suddenly went up after air has been injected.

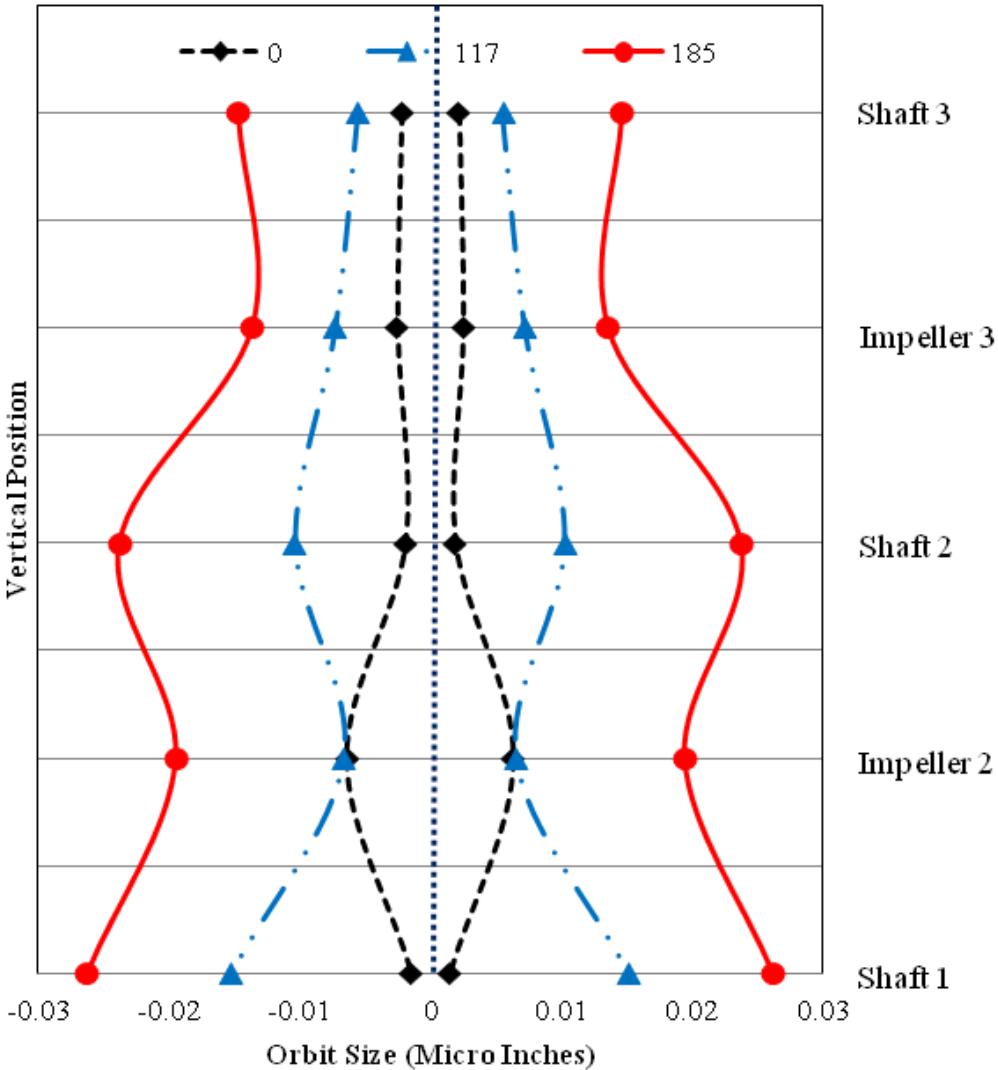


Figure 105. Orbit Mode Comparison

It is also interesting to compare the orbit difference between two-phase and three-phase flow conditions. The orbit comparison is made when pump is already eroded and the bearing clearance has been opened up. From Figure 106, the minor difference is noticed between pure water and water with 15% GVF. The orbit with 15% GVF is a little bigger than the orbit of pure water. However, this phenomenon is noticed on a worn out pump with excessive bearing clearance. In order to investigate the effect of air in the healthy pump, the similar test should be repeated on a brand new pump later. Then the combined results could provide a clue as to whether to study the air effect on the pump orbit.

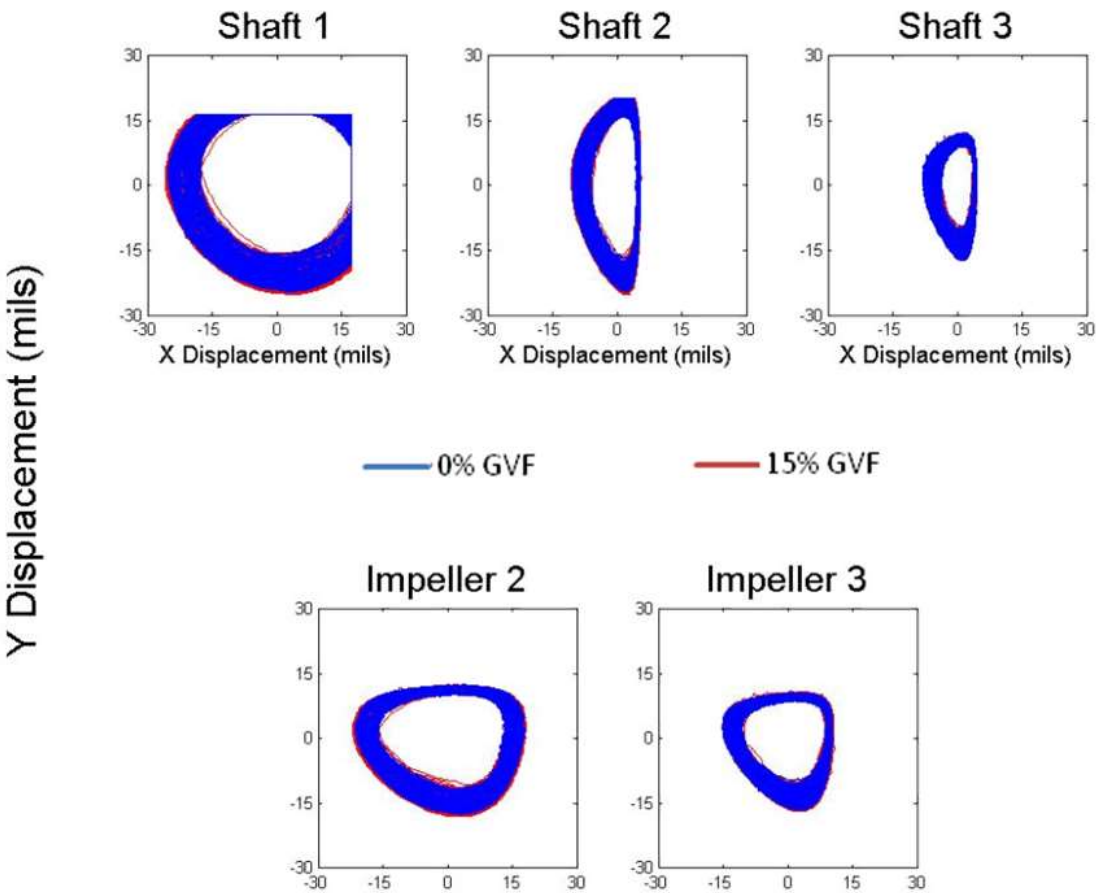


Figure 106. Orbit Comparison between 0% GVF and 15% GVF

6.3.2. Frequency Spectrum

In order to analyze frequency spectrum of the vibration, Fast Fourier Transform (FFT) has been performed on the data. It has become very popular in the oil production industry due to its simplicity for processing and capability to show interesting outcomes in the spectrum. Figure 107 shows the position for five pairs of proximity probe and two three dimensional accelerometers. Probes in X direction are labeled with odd number and Y direction probes are labeled with even number. The vibration analyze in this study aims to find an effective method to monitor the downhole ESP system and coupling the physical wear on the component with vibration signals. All the waterfall data is collected at BEP for both pure water and 15% GVF test.

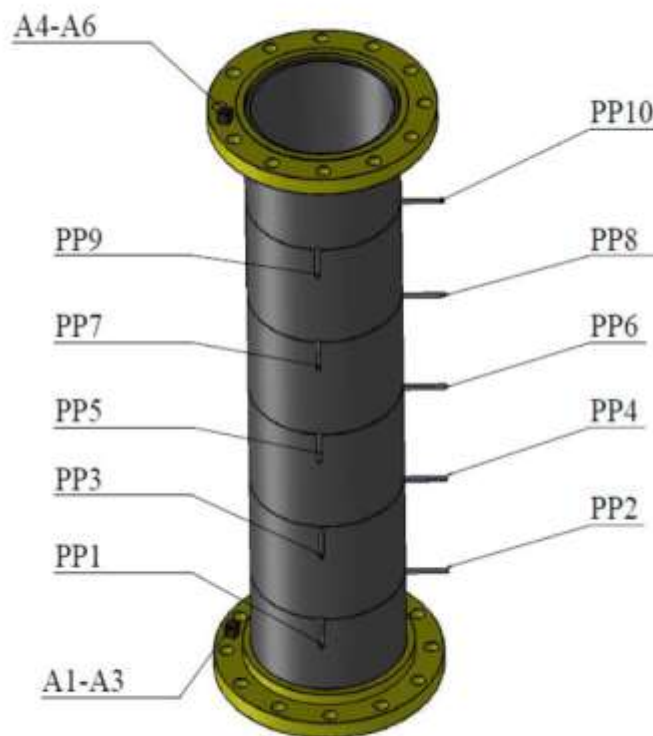


Figure 107. Position for Proximity Probes and Accelerometer

Figure 108, Figure 109, Figure 110 and Figure 111 show the 0% GVF shaft waterfall plot for increasing pump speeds at target times of 24, 52, 117 and 185 of the erosion test. The dominant peak at 24 hours appeared at 1X of running speeds. Meanwhile, minor subsynchronous oscillation at $2/3X$ has been noticed for the first time when running speed is close to 3600 RPM. At 52 hours, a clear peak of $2/3X$ has been established along all the tested speeds. However, the amplitude is much less compared to the 1X peak. $2/3X$ subsynchronous peak starts to become the dominant frequency at 117 hours. It is also important to point out that both the amplitudes at both $2/3X$ and 1X frequency have increased at this time. During this period, some peaks at other frequency such as $1/3X$, $4/3X$, $5/3X$ and 2X have been developed. After this, the test switched to the three-phase condition. At the end of 185 hours, the amplitude at $1/3X$, $2/3X$ and 1X significantly increased compared to the amplitudes of 117 hours. Also some supersynchronous frequency peaks have been noticed as well. Figure 112 combined waterfall plots of the first proximity probe at various time points together to show the peak grow process along the entire erosion test. Since there is no wear at severe level has been detected on the main flow region, the instability reflected by waterfall peak may be induced by excessive clearance on bearing and impeller labyrinth seal. The detailed waterfall plots for other proximity probes are listed in the Appendix D.

PP1 3600 RPM SHAFT WATERFALLS AFTER 24 HOURS

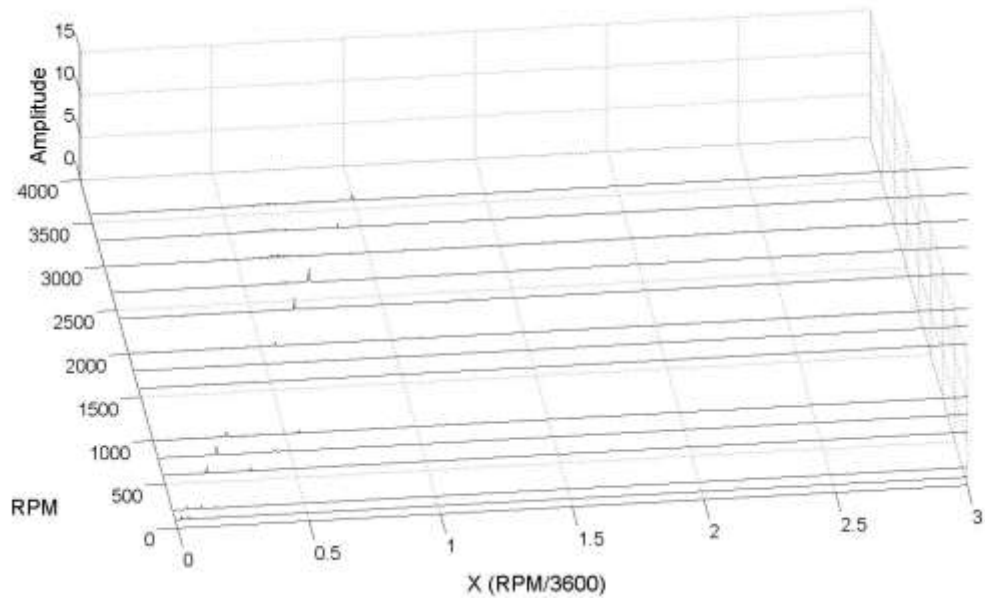


Figure 108. PP1 Shaft Waterfall at 24 Hours

PP1 3600 RPM SHAFT WATERFALLS AFTER 52 HOURS

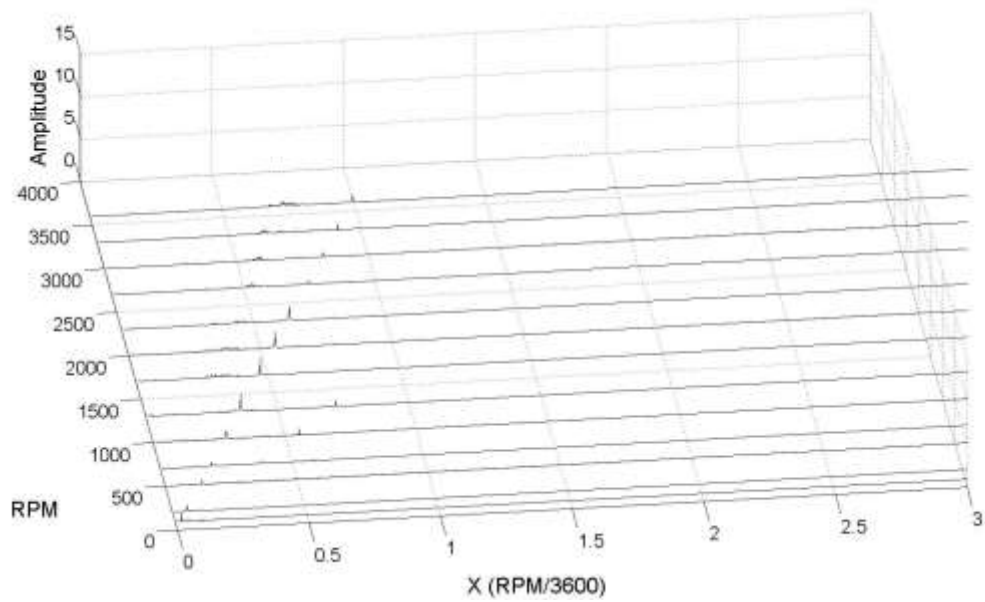


Figure 109. PP1 Shaft Waterfall at 52 Hours

PP1 3600 RPM SHAFT WATERFALLS AFTER 117 HOURS

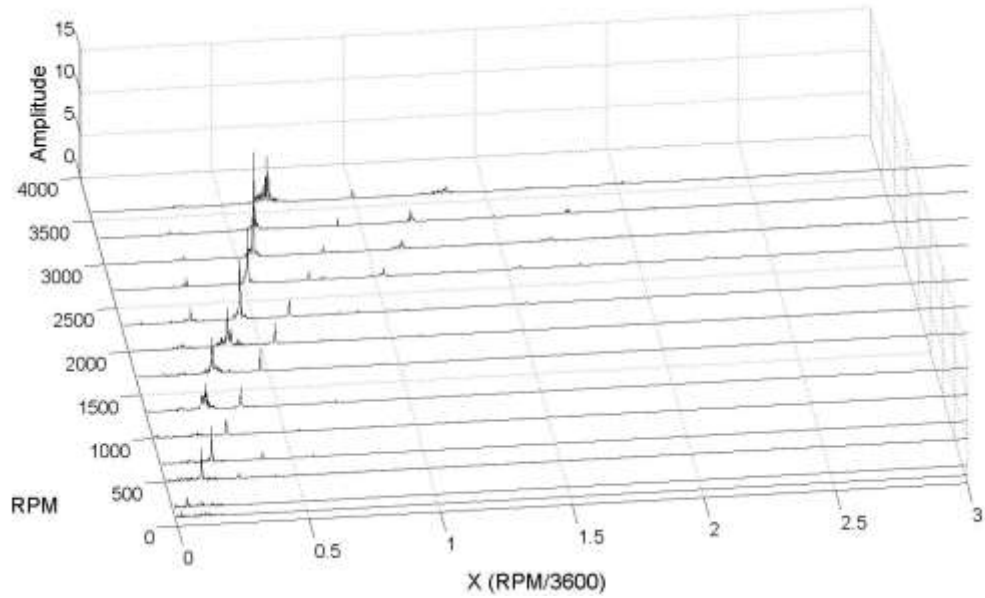


Figure 110. PP1 Shaft Waterfall at 117 Hours

PP1 3600 RPM SHAFT WATERFALLS AFTER 185 HOURS

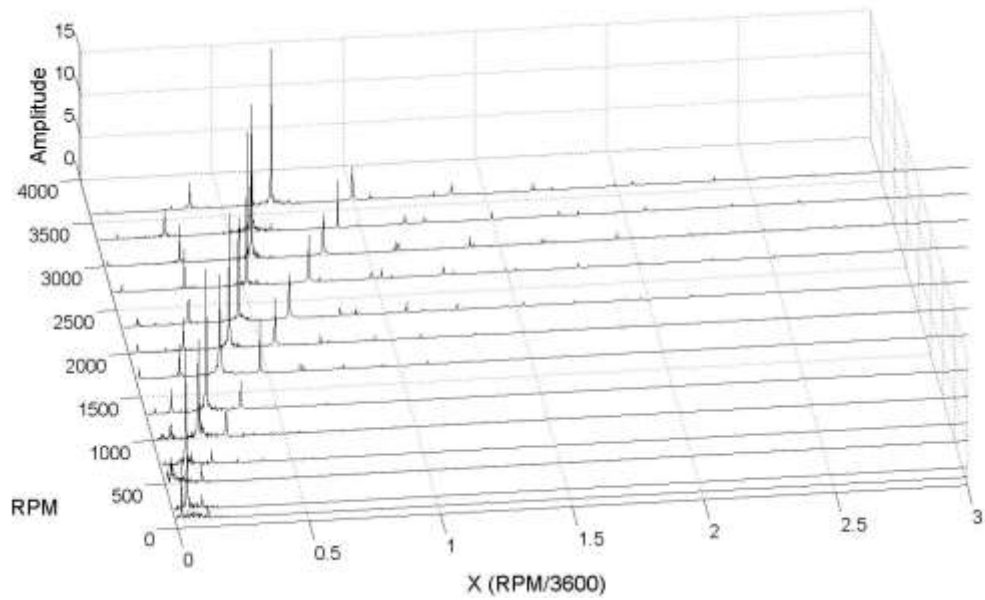


Figure 111. PP1 Shaft Waterfall at 185 Hours

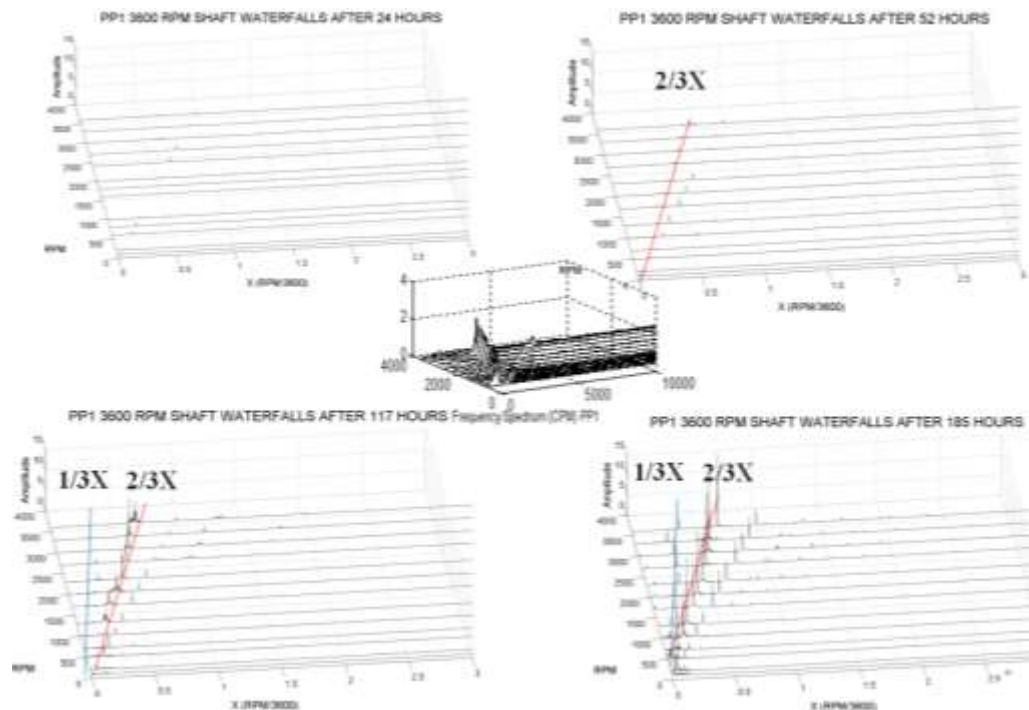


Figure 112. PP1 Shaft Waterfall Plot at Different Hour

Similarly, several sets of proximity probes have been mounted on the casing to collect vibration data for impellers as well. Figure 113, Figure 114, Figure 115 and Figure 116 show the 0% GVF waterfall plots for the third stage impeller at 24, 52, 117 and 185 hours. The synchronous peak is dominant at 24 and 52 hours while the $2/3X$ subsynchronous peak started at 24 hours and become obvious after 52 hours. The same as what happened on the shaft waterfall, $2/3X$ subsynchronous peak became the primary peak at 117 hours. After that, the peaks of $1/3X$, $2/3X$ and $1X$ kept growing in the amplitude and new frequency peaks started to appear. It is easy to see that proximity probes on the shaft and the impeller reveal almost the same information through waterfall plots. Therefore, it is not necessary to install multiple proximity probes to

monitor the pump performance. Figure 117 displays the waterfall plot growth along the entire erosion test.

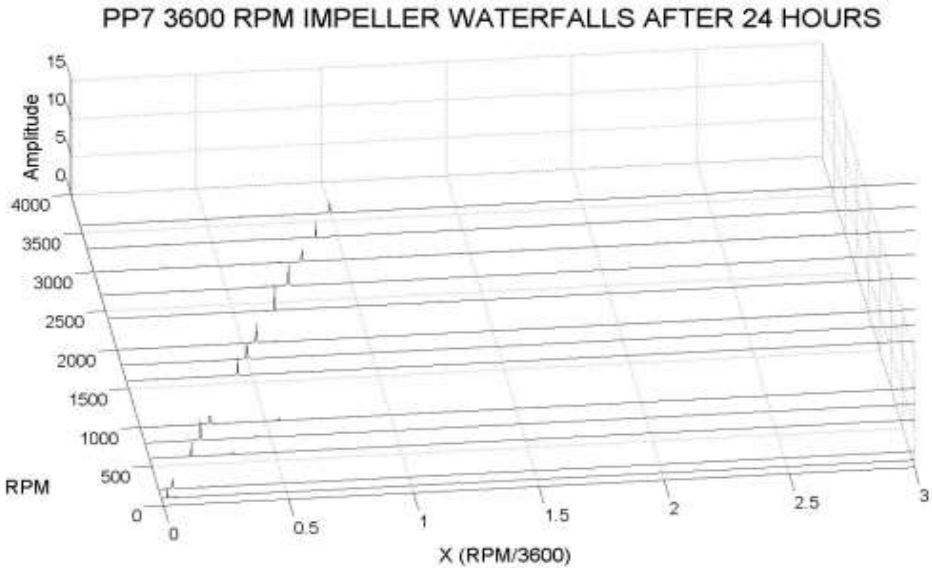


Figure 113. Third Stage Impeller Waterfall at 24 Hours

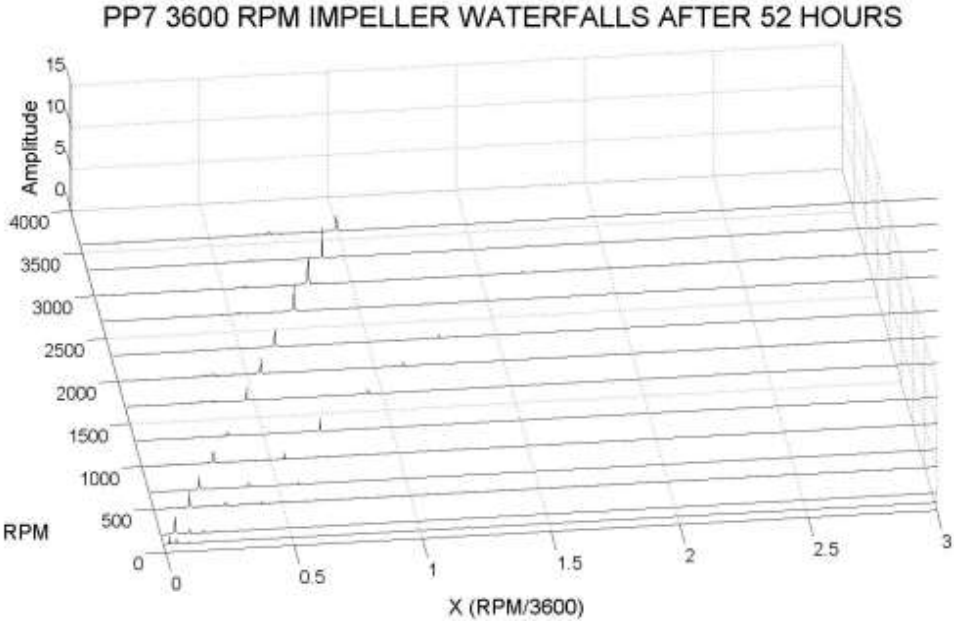


Figure 114. Third Stage Impeller Waterfall at 52 Hours

PP7 3600 RPM IMPELLER WATERFALLS AFTER 117 HOURS

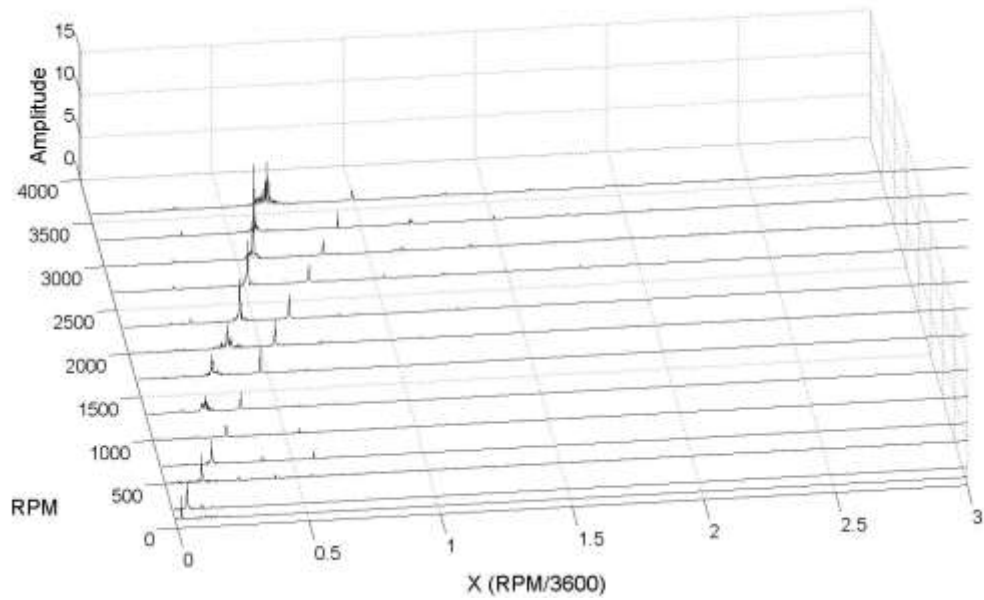


Figure 115. Third Stage Impeller Waterfall at 117 Hours

PP7 3600 RPM IMPELLER WATERFALLS AFTER 185 HOURS

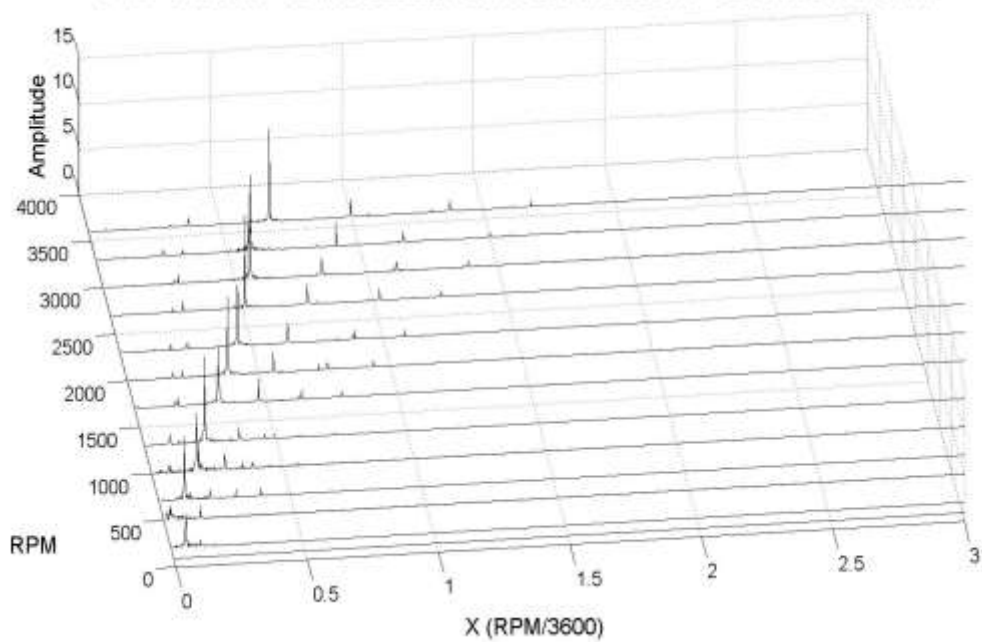


Figure 116. Third Stage Impeller Waterfall at 185 Hours

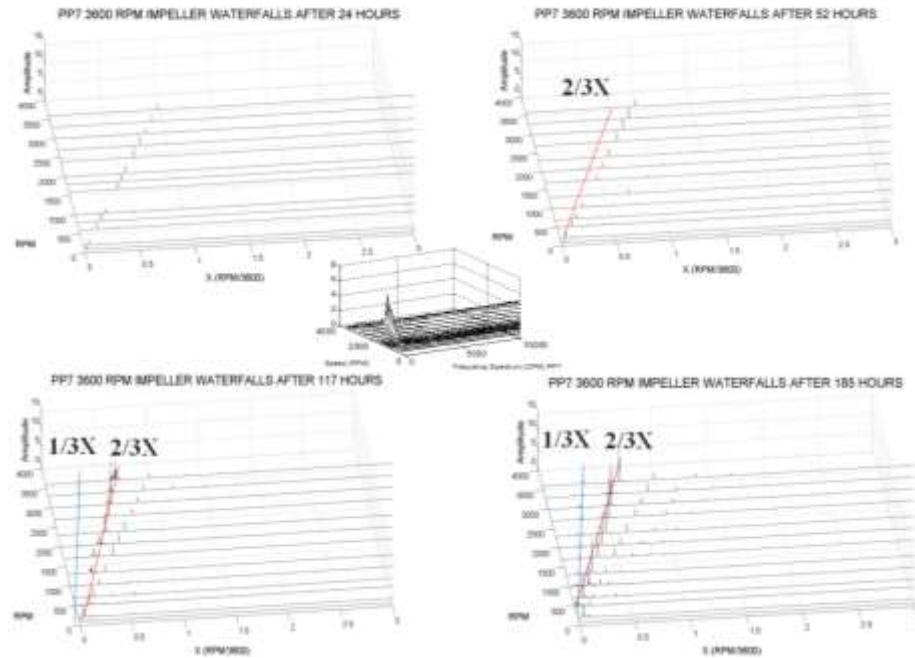


Figure 117. Third Stage Impeller Waterfall Plot at Different Hour

Although the proximity probe is able to provide pure motion data for any rotor, it is not easy to install in the downhole condition. The probe sensor is not able to survive in the sandy environment due to the weakness of erosion resistance. Currently, the established technology can only install accelerometers in the downhole environment. Therefore, the vibration data from accelerometer has been collected in order to determine any relationship with proximity probes. For vibration data of accelerometer, there are three directions such as radial, tangential and axial directions referred to the shaft. Radial sensor monitors the vibration along the radius. Tangential sensor monitors the vibration which is perpendicular to the shaft circle. Axial sensor monitors the vibration along the shaft direction. Figure 118 shows FFT plots for three directions. It is clear that radial direction plot is has the most close trend compared to the plot of proximity probes.

Radial direction plot then utilized for comparing purpose with proximity probe. Figure 119, Figure 120, Figure 121 and Figure 122 show the waterfall plots for the radial direction accelerometer at the pump intake. The result shows a good alignment with the proximity probe waterfall plots. However, when the vibration level is lower at low speed, the accelerometer didn't capture all the peaks which were observed on the proximity probe waterfall plots. It is possible that overwhelming vibration is coming from external resource such as test rig and piping system when the pump is running at a low speed. However, the accelerometer is still an excellent candidate to relate with proximity probe data since the vibration signal usually becomes strong enough to be captured by the accelerometer when the pump is out of healthy conditions. More discussion about correlating signal among accelerometer, proximity probe and physical wear will be discussed later in the next section.

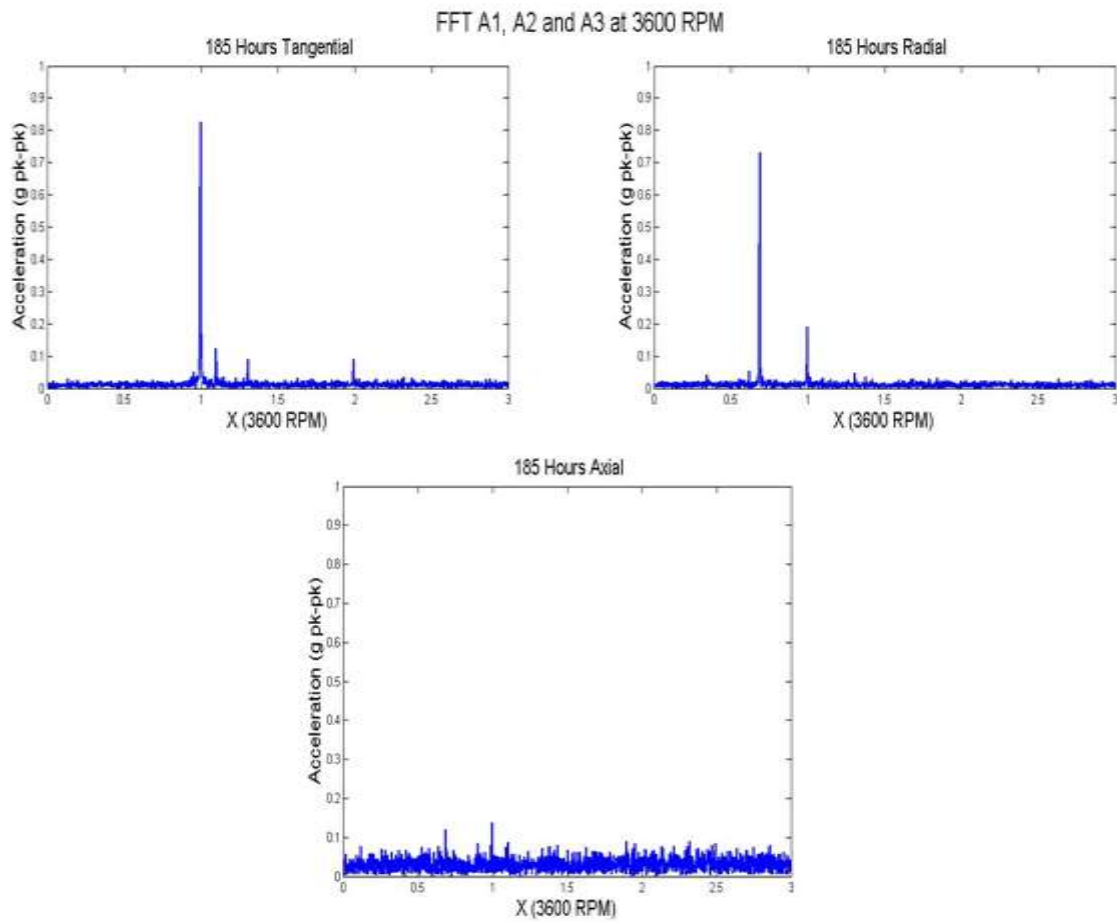


Figure 118. 3D Accelerometer FFT

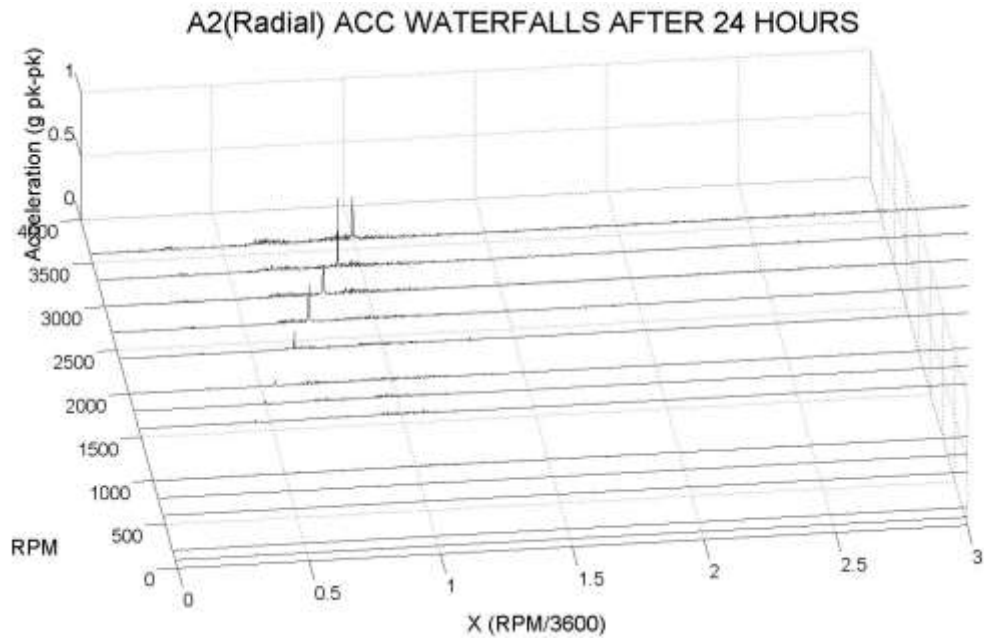


Figure 119. Radial Direction Accelerometer Waterfall at 24 Hours

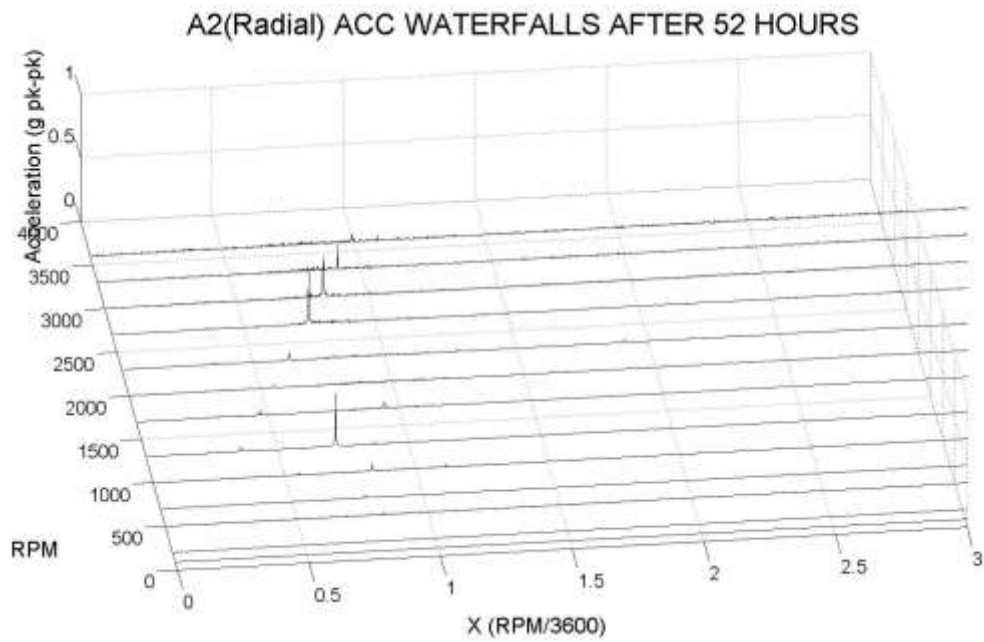


Figure 120. Radial Direction Accelerometer Waterfall at 52 Hours

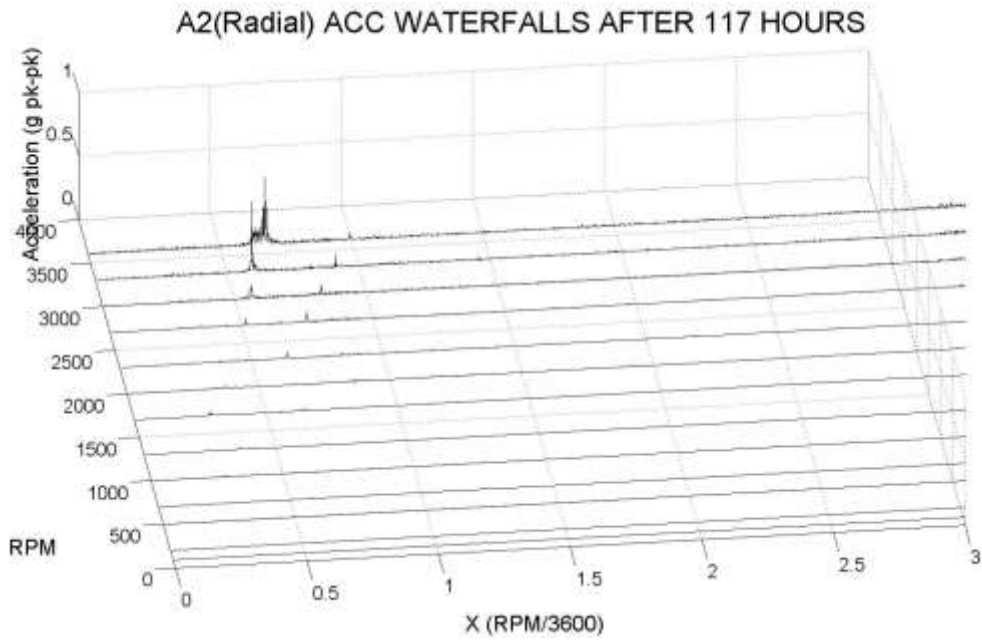


Figure 121. Radial Direction Accelerometer Waterfall at 117 Hours

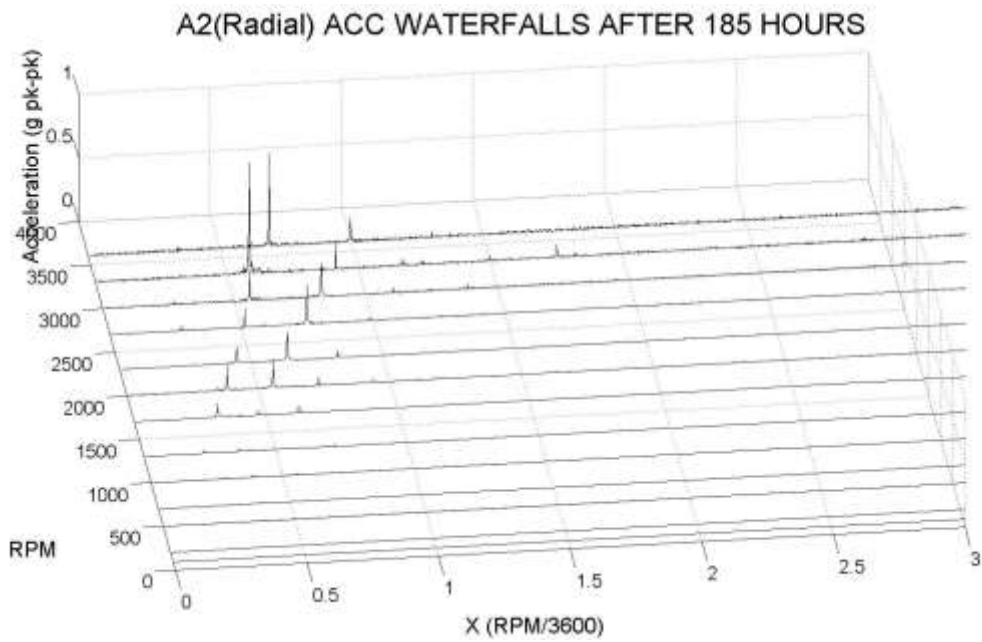


Figure 122. Radial Direction Accelerometer Waterfall at 185 Hours

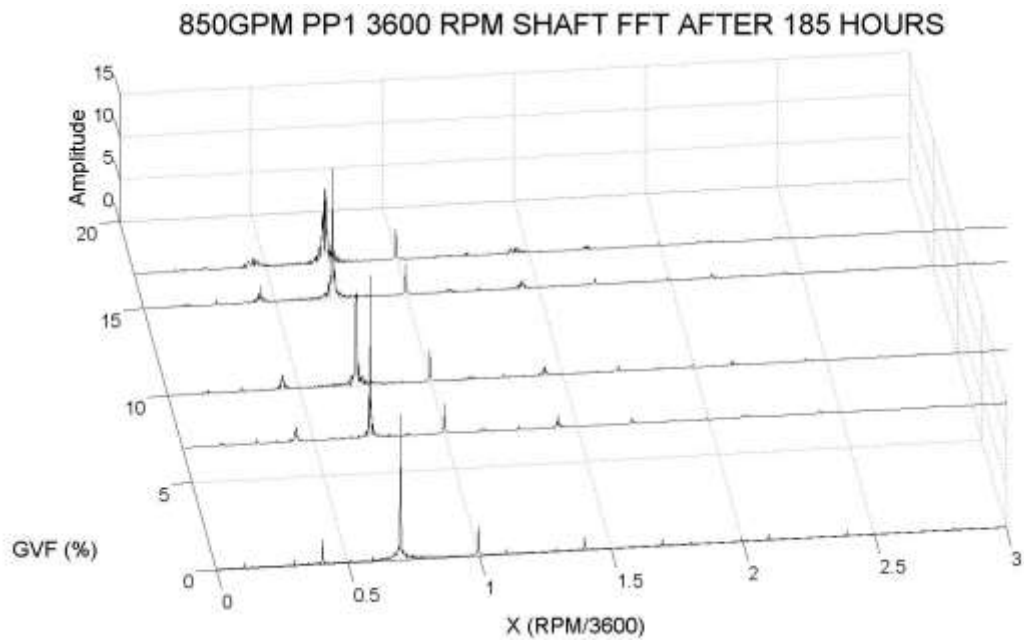


Figure 123. FFT vs GVF Spectrum from Proximity Probe

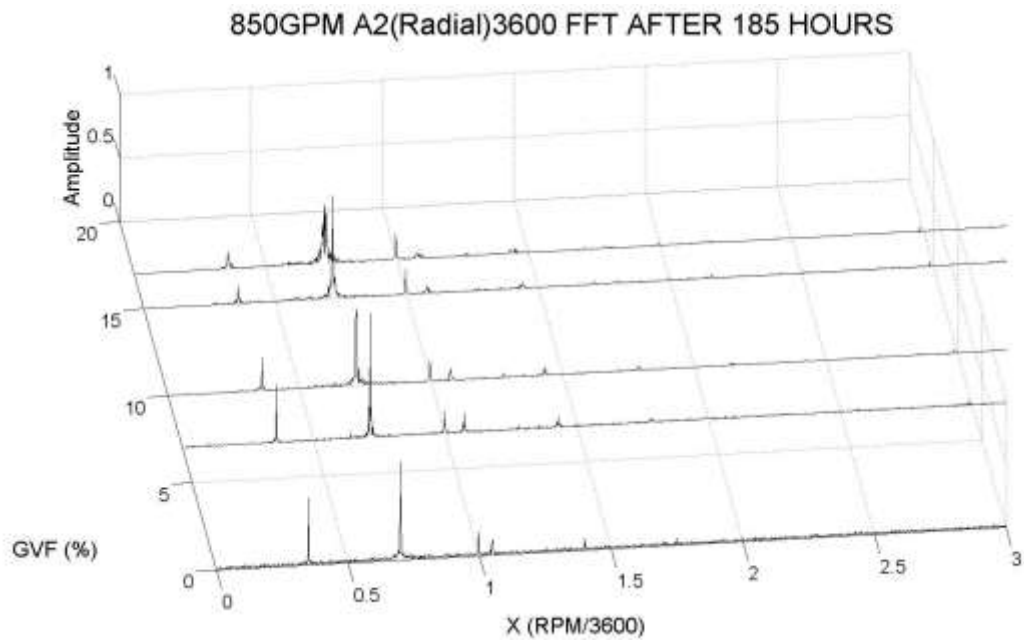


Figure 124. FFT vs GVF Spectrum from Accelerometer

In this test, it is also interesting to see the different vibration signatures when gas volume fraction (GVF) varies. Since the WJE-1000 ESP is not specially designed for a gassy well, the maximum GVF it can reach is only 17% at the NPSH available. The vibration power didn't change much as Table 8 shows the root mean square value for each case is approximately the same. From the vibration signatures in Figure 123 and Figure 124, the amplitude is different when GVF is changing. The peaks at 1/3X decreased their amplitude and spreaded around the peak when volume fraction of air is increasing. Due to the compressibility of air, we saw more damping effect when the GVF increased. However, the amplitude of the 2/3X and 1X peaks do not have a clear relationship with GVF. Since this test is performed with worn out bearings, the results may not be able to reflect the effect of GVF for a healthy pump accurately. Future study is needed for comparison.

Table 8. RMS Comparison among Various GVF

GVF (%)	RMS Value (Micro Inches)
0	29.7329
7	29.9437
10	29.937
15	29.9634
17	30.0128

Likewise, FFT with different flow rates have been performed as well. The vibration signatures are very similar among the different flow rates as shown in Figure 125 and Figure 126. When the flow rate increases, obvious damping characteristics have been discovered around the 1/3X and the 2/3X peaks. The phenomenon like this might be caused by more air entering into the bearing and labyrinth seal clearance. The

compressibility of air enhanced the damping effect in the fluid film of bearing and labyrinth. At the same time, the subsynchronous peaks at $1/3X$ and $2/3X$ and supersynchronous peaks at $1.5X$ and $1.75X$ have a trend to shift toward lower frequency. It is possible that fluid stiffness varied with flow rate, and then different vibration signature showed on the plot.

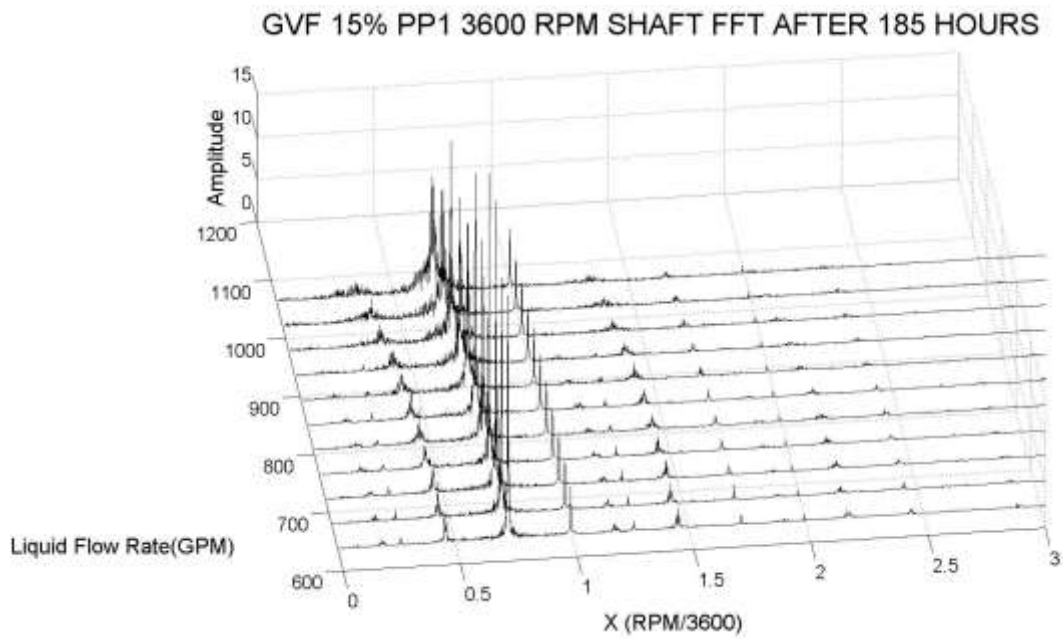


Figure 125. FFT vs Flow Rate at 15% GVF of Proximity Probe

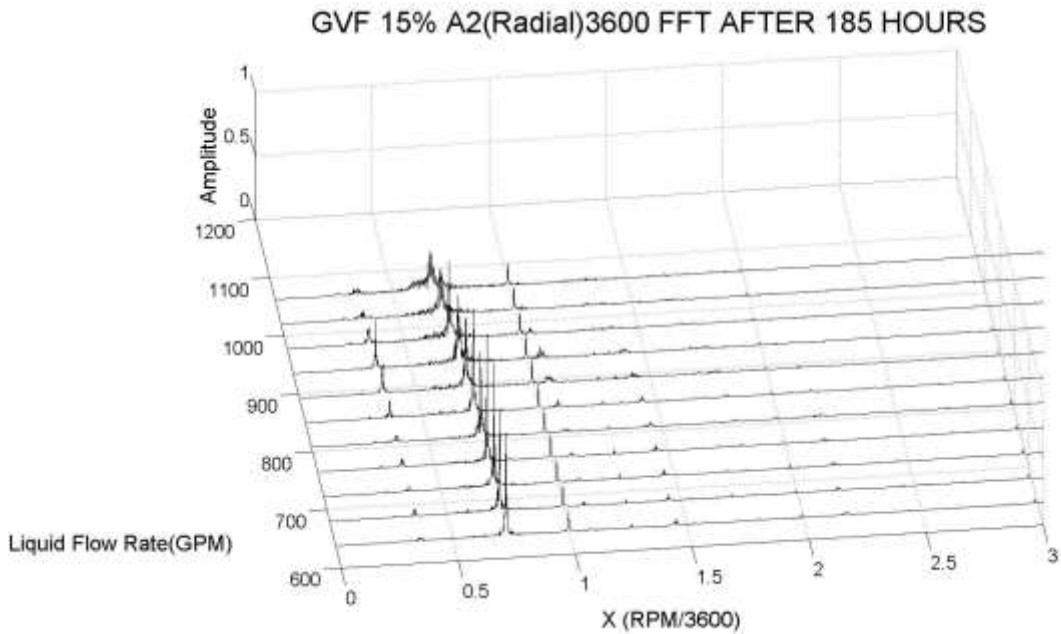


Figure 126. FFT vs Flow Rate at 15% GVF of Accelerometer

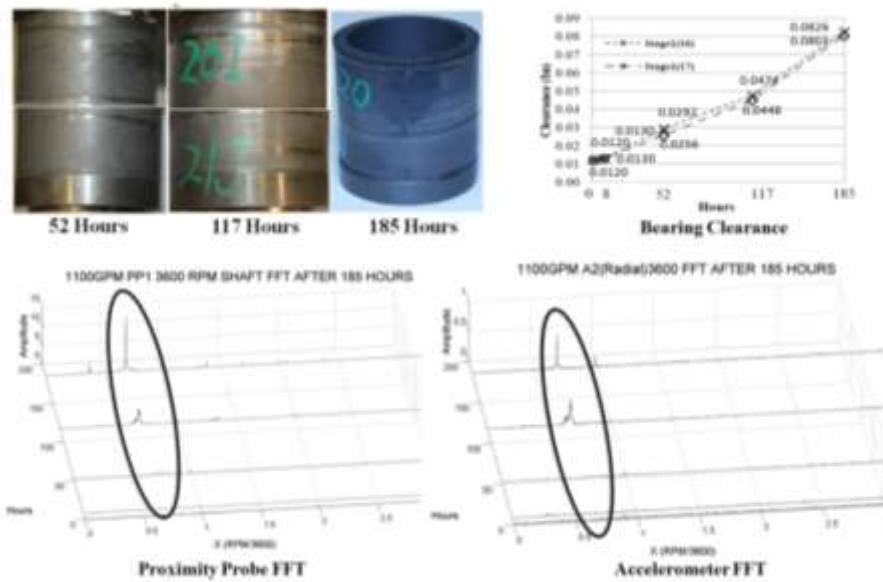


Figure 127. Comparison between Vibration Data and Physical Wear

In order to find an efficient and valid way to monitor the pump condition, it is necessary to couple the physical wear data and the vibration signature together with a function. In

this way, a remote monitoring method can be established. It is beneficial for industrial safety and time management. In this test, 2/3X subsynchronous peak has been noticed for a significant growth along with the erosion progress. Based on the experimental facts, this peak may be excited by the bearing induced unbalance force as shown in Figure 127. The following Equation 5.1 provides the relationship between the bearing clearance and acceleration peak. As we know, accelerometer usually captures the vibration signal from both interior and exterior of the pump. In order to generate the relationship between them, the stage number must be included. The stage which is close to the motor has been numbered as the first one. Then the rest will be numbered based on their order. Figure 128 shows the correlated results compared to the actual 2/3X peak and bearing clearance. The dash line in the chart is from the clearance predict equation as followed. However, this relationship may not be perfect to represent the bearing clearance as real because only two accelerometers have been involved in this study. It will be beneficial to have more accelerometers in the next study. Consequently, the effect of stage can be further studied. Also, this relationship is based on the current test rig and three stage of WJE-1000. It will be an interesting topic to find out whether this relation can be applied for more stages of ESP or another test rig in the future work.

$$C = \left\{ \frac{0.04A_n}{A_1(n-1)} \right\} * A + C_0 \quad (6.1)$$

where: C = Dimensionless Bearing Clearance

n = Stage No. Counts from Motor Side

A = Dimensionless 2/3X Acceleration Peak at Local Accelerometer

C_0 = Dimensionless Original Bearing Clearance

A_n = Dimensionless Acceleration Initial 2/3X Peak at n Accelerometer

A_1 = Dimensionless Acceleration Initial 2/3X Peak at 1 Accelerometer

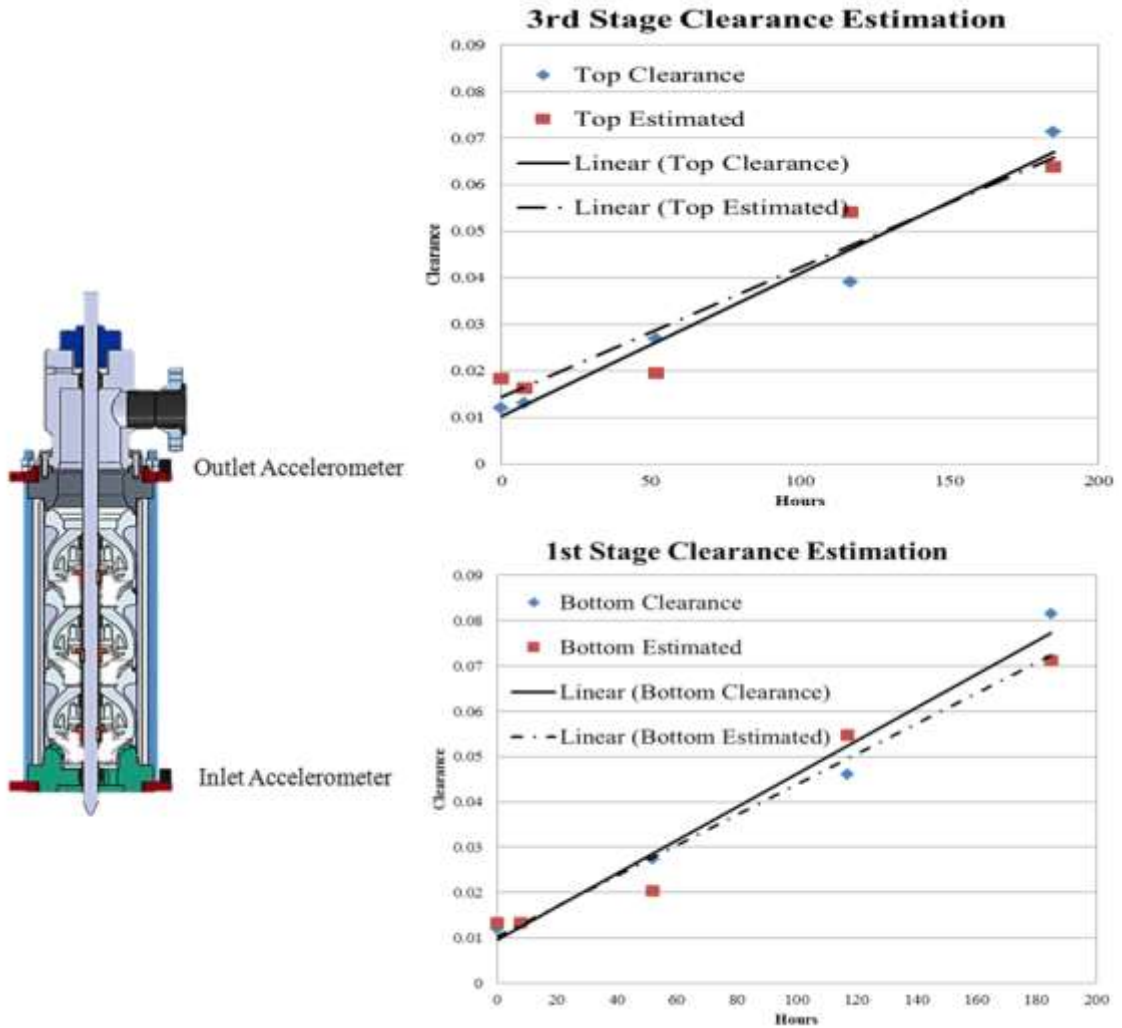


Figure 128. Correlation between Accelerometer and Bearing Clearance

CHAPTER VII

CONCLUSION

In the course of study, the WJE-1000 electrical submersible pump went through 117 hours of two-phase test and 68 hours of three-phase test. 100 mesh fracture sand maintained at the concentration of two grams per liter during entire test and the volume fraction of air is constant at 15% in the three-phase test. The three-stage ESP was operated at best efficiency point at a speed of 3600 RPM. Along the erosion test, significant component wear, increased vibration level and performance degradation has been documented. In addition, air effect was studied by comparing two-phase testing and three-phase testing.

First of all, component wear pattern due to abrasive erosion has been detected both on the main flow field and secondary flow field. In the main flow field, the wear is mainly caused by sand particle impingement. The area suffered from the type of wear includes hub, shroud, blades, balance holes of impeller and blades, shroud of diffuser. At the region such as the balance hole on the shroud or front tip of impeller blade, significant horseshoe shape wear has been noticed due to fluid separation. Equally important, each stage has different level of wear and largest wear is occurring in the third stage pump. The impeller has a curved shape on the leading edge and trailing edge has been sharpened. The first stage impeller has a different curved pattern on the leading edge compared to any of other two stage impellers. During three-phase testing, all component wear has become more obvious in only a short period, especially the horseshoe shape

wear on impellers. Another important component in this system is the upthrust plate. Since the tested pump is fixed impeller design, it doesn't generate the thrust as much as from float impeller design. Consequently, there is no significant wear either from thickness measurement or weight measurement.

Secondary flow field study usually contains the regions including bearing clearance and impeller labyrinth seal located both at suction and discharge side. The type of wear is caused by sand passing through the clearance between the rotor and the stator. One end of the pump is driven by the motor and the other end is free. Bearings have more wear on the free end. At the end of 185 hours, the maximum clearance on the bearing has reached to 0.09 inches which means components probably already loss the function as bearings and two pair of bearings had a crack along the keyway at the free end. All bearing surfaces have been gouged by sand particles. At the end of test, all bearings showed a uniform crack pattern on the axial direction. This is a possible sign of material fatigue. Comparing clearance growth rate between the two-phase test and the three-phase test, it is clear that injected air enhanced the erosion progress and all the bearings has a larger erosion rate when air is presenting in the pump. As air is mixed in the pumping fluid, the compressibility of air may further enlarge the eccentricity of the rotor motion and lead to a high possibility of rubbing.

On the performance side, efficiency dropped 6.58% after the two-phase test (117 hours) and 15.8% (185 hours) when we finish testing. Considering the relatively shorter period

for three-phase test, pump performance degraded significantly more when air is involved. The significant decrease in the total efficiency is mainly due to the lost pressure rise. There is a small difference for the input electrical power supply. This result is in good alignment with the physical wear measurement. The opened clearances on the bearing and labyrinth seal will definitely raise the leakage loss and pull the head curve down. At the same time, the friction loss increases when sand particle impinges the surface and makes it coarse.

On the rotor dynamic side, vibration signals go through a considerable change during the erosion test. Orbit size has a giant size growth due to increased bearing clearance. When air is injected in the pump, the orbit is slightly larger than the orbit for pure water. This is the phenomenon noticed on a worn out pump. It is not enough to make a conclusion for the air effect on the healthy pump yet. Meanwhile, since the current pump is not a special design for gassy well, the maximum GVF can only reach 15%. Therefore, a future study is needed to further investigate the effect of air for the orbit of rotor. The waterfall plots show the vibration signature at different time points changing in frequency and amplitude. Especially on the subsynchronous peak of $2/3X$, the trend of growth is similar to what happened on the bearing clearance. Therefore, the correlation between accelerometer and physical wear has been developed in order to find a new and reliable way to remote monitor the health of ESP system. The vibration signatures among different GVF and flow rate has been analyzed as well. Due to the compressibility of air, we saw more damping effect when the GVF went high. However,

the amplitude of $2/3X$ and $1X$ peaks doesn't have a clear relationship with GVF. The vibration signatures are very similar among different liquid flow rate. When the flow rate increased, more obvious damping characteristics were discovered around $1/3X$ and $2/3X$ peak.

In summary, WJE-1000 had serve wear on the secondary flow field, especially on the bearing clearance which is the main controlling factor for the degradation of pump. For the component in the main flow field, although the wear has been detected on all the components, it doesn't reach failure level yet. The comparison between two-phase and three-phase test represent a clear clue about the air effect in the pump. Generally, air accelerates erosion progress and performance degradation. Therefore, a future study should focus on optimizing of bearing design or adding equipment that can eliminate air into system.

REFERENCES

- [1] Carter, D., 1961, "History of Petroleum Engineering," American Petroleum Institute, Washington DC, pp. 83-124.
- [2] "Advanced Artificial Lift Methods," 2012,
https://www.google.com/url?sa=t&rct=j&q=&esrc=s&source=web&cd=1&ved=0CDcQFjAA&url=http%3A%2F%2Fwww.nmt.edu%2F~petro%2Ffaculty%2FNguyen%2FPE571%2FPresentation%2FC1%2F1_IntroductionToArtificialLiftMethods.ppt&ei=3a2UrTgMYqy2QWTloHQBg&usg=AFQjCNFFnF451OyMaeHgvR_NQIg8Sl_HtA&sig2=VDqEBPMa28DFA5bH6ENPLQ&bvm=bv.58187178,d.b2I&cad=rja.
- [3] "Black Gator® – Electric Feed-thru System," 2013,
<http://www.pftsys.com/products.php>.
- [4] "Electrical Submersible Pumps for Geothermal Applications," 2010,
http://www.slb.com/~media/Files/technical_papers/2010/2010_esp_geothermal_applications.pdf.
- [5] "ESP Pumping System," 2013,
http://www.ge-energy.com/products_and_services/products/electric_submersible_pumping_systems/.
- [6] Gabor, T., 2009, "Electrical Submersible Pumps Manual," Elsevier Science.

- [7] Clegg, J., Bucaram, S., and Hein, N., 1993, "Recommendations and Comparisons for Selecting Artificial Lift Methods (Includes Associated Papers 28645 and 29092)," *Journal of Petroleum Technology*, **45**(12) pp. 1128-1131, 1163-1167.
- [8] Brown, K.E., and Beggs, H.D., 1977, "The Technology of Artificial Lift Methods," PennWell Publishing Company, Tulsa, Oklahoma.
- [9] Neely, B., Gipson, F., Clegg, J., 1981, "Selection of Artificial Lift Method," SPE American Institute of Mining Engineers, San Antonio, Texas.
- [10] Stepanoff, A.J., 1957, "Centrifugal and Axial Flow Pumps," Wiley, New York.
- [11] Karassik, I.J., and McGuire, J., 1998, "Centrifugal Pumps," Chapman & Hall : International Thomson, New York.
- [12] Roco, M., Nair, P., Addie, G. R., 1984, "Erosion of Concentrated Slurries in Turbulent Flow." *Journal of Pipelines*, **4**(3) pp. 213-222.
- [13] Minemura, K., and Uchiyama, T., 1990, "Calculation of the Three-Dimensional Behaviour of Spherical Solid Particles Entrained in a Radial-Flow Impeller Pump," *Proceedings of the Institution of Mechanical Engineers, Part C: Journal of Mechanical Engineering Science*, **204**(3) pp. 159-168.
- [14] King, D., Traylor, F., and Stewart, R., 1983, "Abrasion Technology for Electric Submersible Pumps," SPE Annual Technical Conference and Exhibition, San Francisco, California.

[15] Pagalthivarthi, K. V., Gupta, P. K., Tyagi, V., 2011, "CFD Prediction of Erosion Wear in Centrifugal Slurry Pumps for Dilute Slurry Flows," *Journal of Computational Multiphase Flows*, **3**(4) pp. 225-246.

[16] Hadjiyannis,S., Charalambous,N., Tournlidakis,A., 2009, "An experimental and Computational Study of the Erosion in Submersible Pumps and the Development of A Methodology for Selecting Appropriate Protective Coatings," ASME Turbo Expo, Orlando, Florida.

[17] Divine, D., Lannom, R., and Johnson, R., 1993, "Determining Pump Wear and Remaining Life from Electric Submersible Pump Test Curves," *Old Production & Facilities*, **8**(3) pp. 217-221.

[18] DF, D., and Larson, L., 1996, "Multiphase Pump Field Trials Demonstrate Practical Applications for the Technology," *Old Production & Facilities*, **12**(3) pp. 159-164.

[19] Shippen,M., and Scott,S., 2002, "Multiphase Pumping as an Alternative to Conventional Separation, Pumping and Compression," PSIG Annual Meeting, Portland, Oregon.

[20] Hua,G., Falcone,G., Teodoriu,C., 2011, "Comparison of Multiphase Pumping Technologies for Subsea and Downhole Applications," SPE Annual Technical Conference and Exhibition, Denver, Colorado, USA.

[21] Goodwin, M., Dong, D., Yu, H., 2007, "Theoretical and Experimental Investigation of the Effect of Oil Aeration on the Load-Carrying Capacity of a Hydrodynamic Journal Bearing," Proceedings of the Institution of Mechanical Engineers, Part J: Journal of Engineering Tribology, **221**(7) pp. 779-786.

[22] Durham, M. O., Williams, J. H., and Goldman, D., 1990, "Effect of Vibration on Electric-Submersible Pump Failures," Journal of Petroleum Technology, **42**(2) pp. 186-190.

[23] Mubarak,H., Farooq,A., and Mehmet,M., 2003, "ESP Failures/Analysis/Solutions in Divided Zone-Case Study," Middle East Oil Show, Bahrain.

[24] Carvajal Diaz, N., 2012, "Effects of Sand on the Components and Performance of Electric Submersible Pump," Texas A & M University, College Station, Texas.

[25] "Coriolis Mass Flow Meters For Natural Gas Measurement,"
http://www.documentation.emersonprocess.com/groups/public_public_mmisami/documents/articles_articlesreprints/jds-030705naturalgas.pdf.

[26] "Fundamental Principles of Turbine Flow Meters," 2010,
<http://www.asgmt.com/default/papers/asgmt2010/docs/D4.pdf>.

APPENDIX A

WJE-1000 CONFIGURATION

Table 9. Bill of Materials

WJE-1000 3 Stage BOM			
no.	Item no.	Item Description	Quantity
1	2	Mechanical Seal	1 EA
2	3	HEAD S/A 1025P Series Pump	1 EA
3	4	Retainer Ring	5 EA
4	5	Sleeve Bearing 1.501 X 1.871 X 1.000	10 EA
5	6	Key 0.125 X 0.125	3 EA
6	7	1.5" Pump Shaft 1025P Series	1 EA
7	8	Capscrew 0.625-18 X 2.50"	12 EA
8	9	Lock Washer	12 EA
9	10	Nut Well Head 0.875-9NC	12 EA
10	11	O-Ring CL 180 7.484 X 0.139	1 EA
11	12	Flange 10" Slip-on Class 159	1 EA
12	13	Head Adapter 1025P Series Pump	1 EA
13	14	O-Ring CL 180 8.984 X 0.139	2 EA
14	15	O-Ring CL 180 8.237 X 0.083	5 EA
15	16	O-Ring Fluor 8.484 X 0.139	3 EA
16	17	Tension Rod 1025MVP Series Pump	6 EA

Table 9. Continued

WJE-1000 3 Stage BOM			
17	18	Sleeve Spacer 1.501 X 1.869 X 1.750	1 EA
18	19	Thrust Plate 1025	1 EA
19	20	Housing 1025P Series Pump	1 EA
20	21	Impeller WJ-1000	3 EA
21	22	Sleeve Spacer 1.501 X 1.869 X 1.188	4 EA
22	23	Sleeve Spacer 1.501 X 1.869 X 1.875	4 EA
23	24	Diffuser WJ-1000	3 EA
24	25	Taper Bushing 1.500	3 EA
25	26	Key 0.375 X 0.313 X 1.25	6 EA
26	27	Sleeve Spacer 1.501 X 1.869 X 2.313	4 EA
27	28	Capscrew 0.25-20 X 1.25"	9 EA
28	29	Lock Washer 0.25 Hi Collar	9 EA
29	30	O-Ring CL 180 9.234 X 0.139	1 EA
30	31	Intake S/A 1025P Series Pump	1 EA
31	32	Flange 1025 Test PMP	1 EA

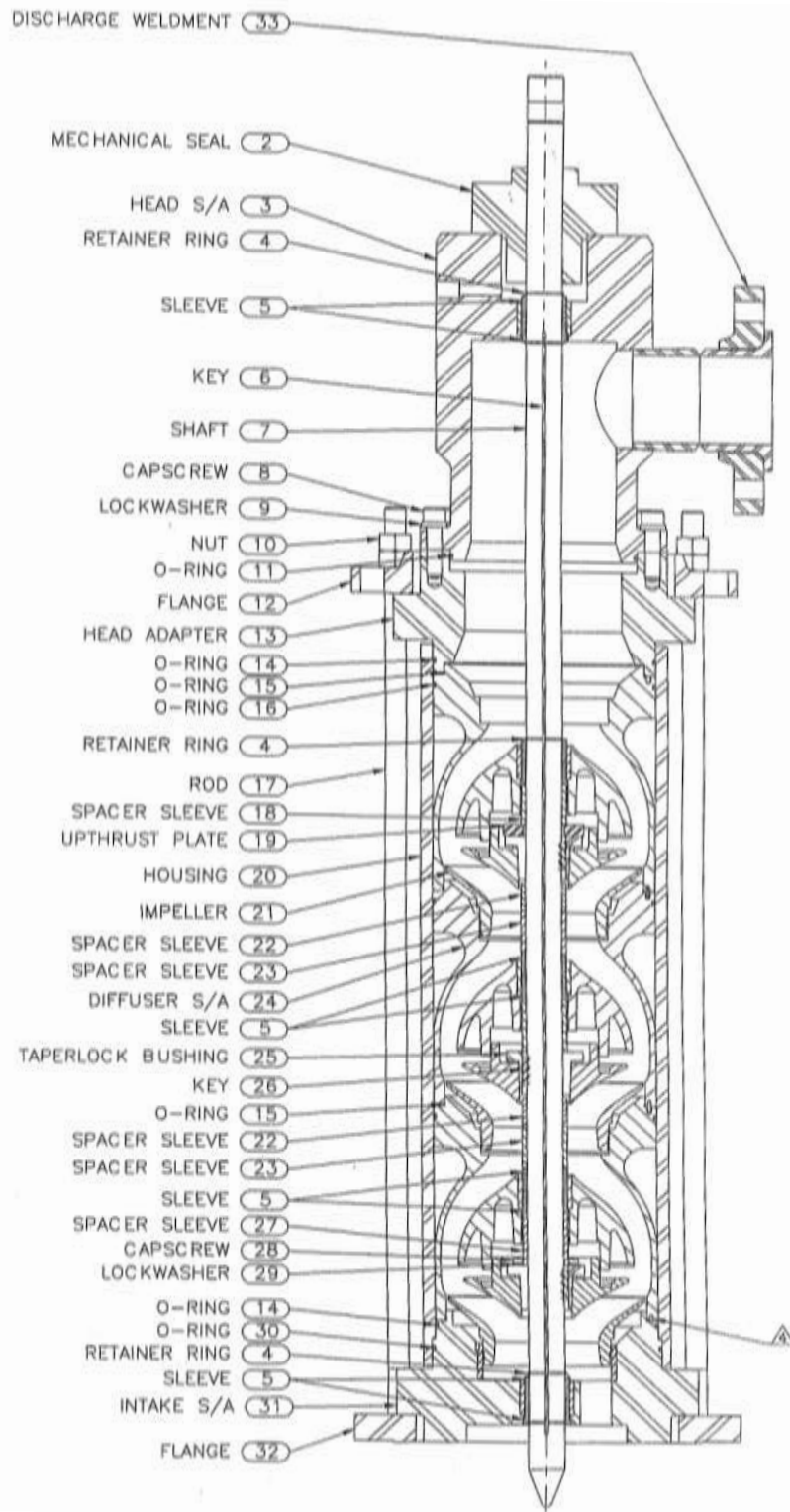


Figure 129. WJE-1000 Configuration

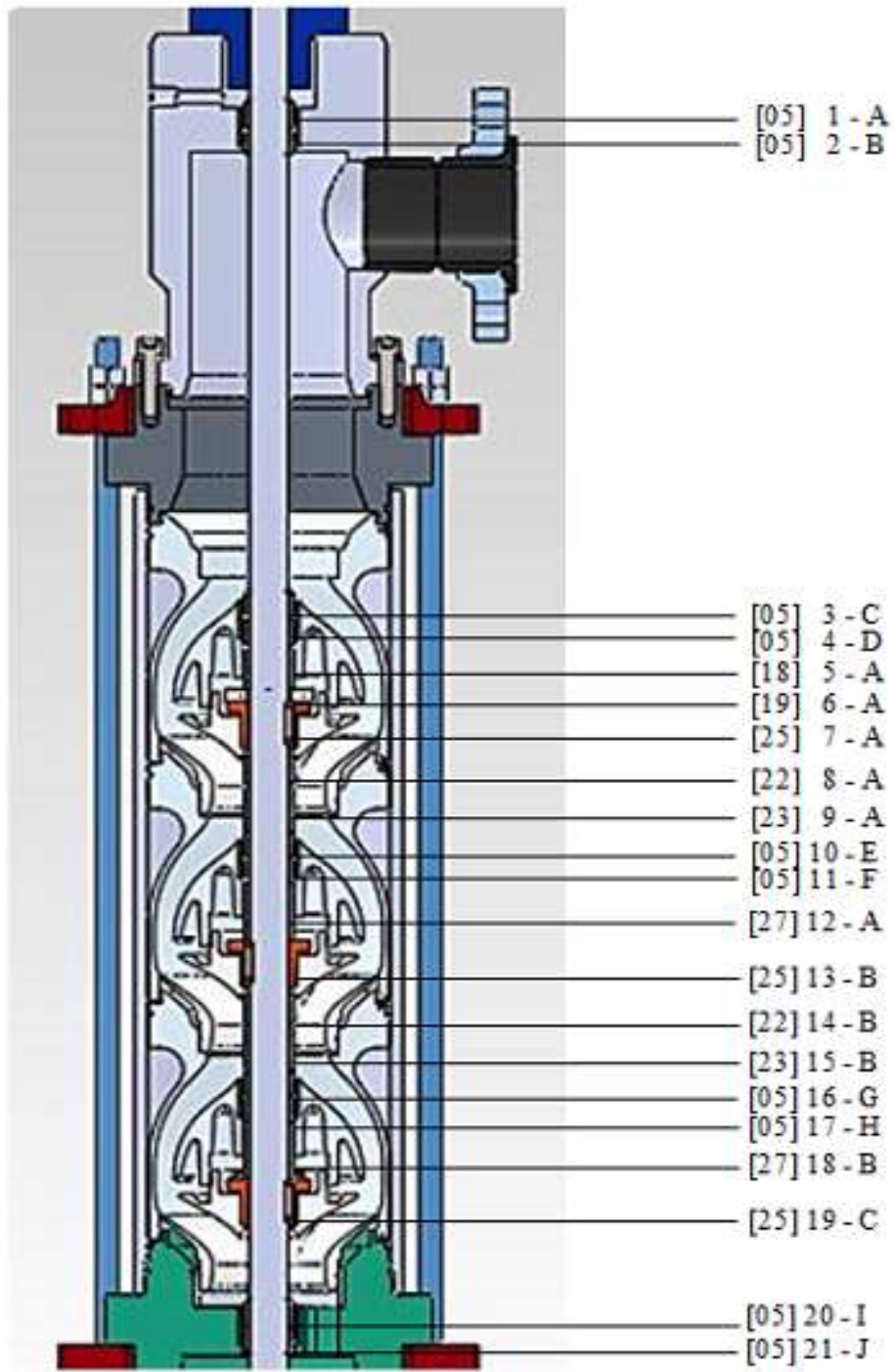


Figure 130. Numbered Item on the Shaft

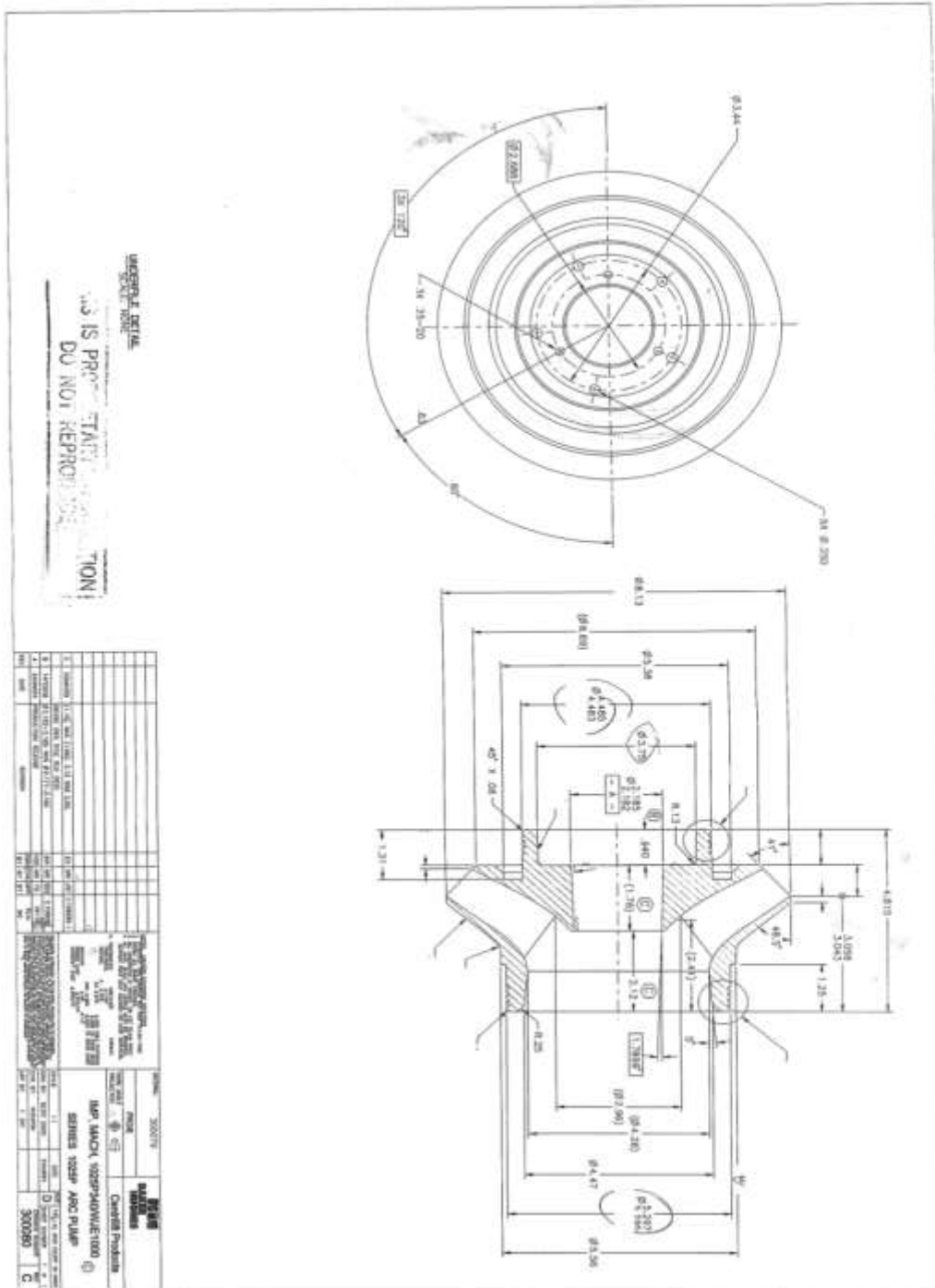


Figure 131. Impeller Configuration

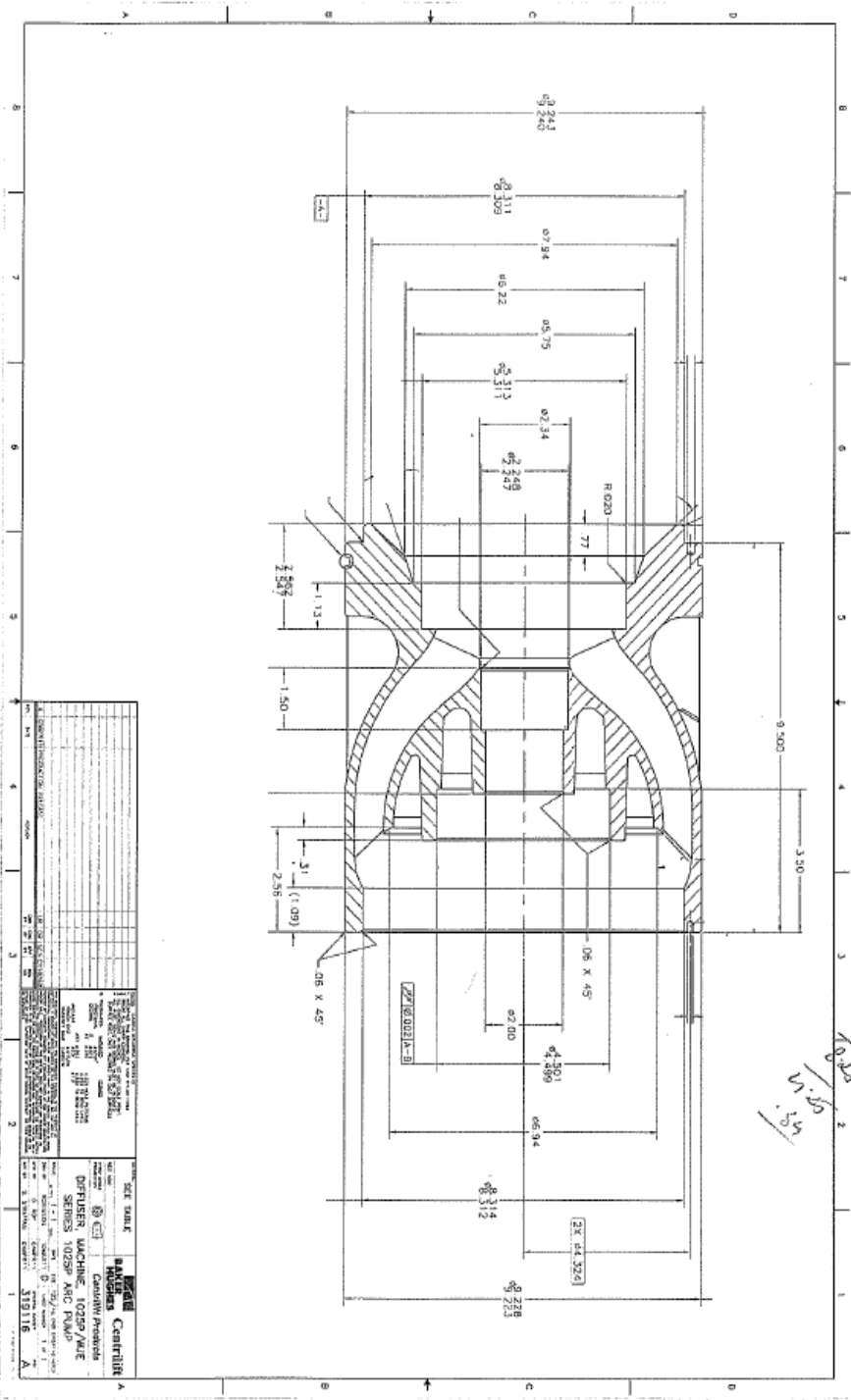


Figure 132. Diffuser Configuration

APPENDIX B
PUMP PERFORMANCE

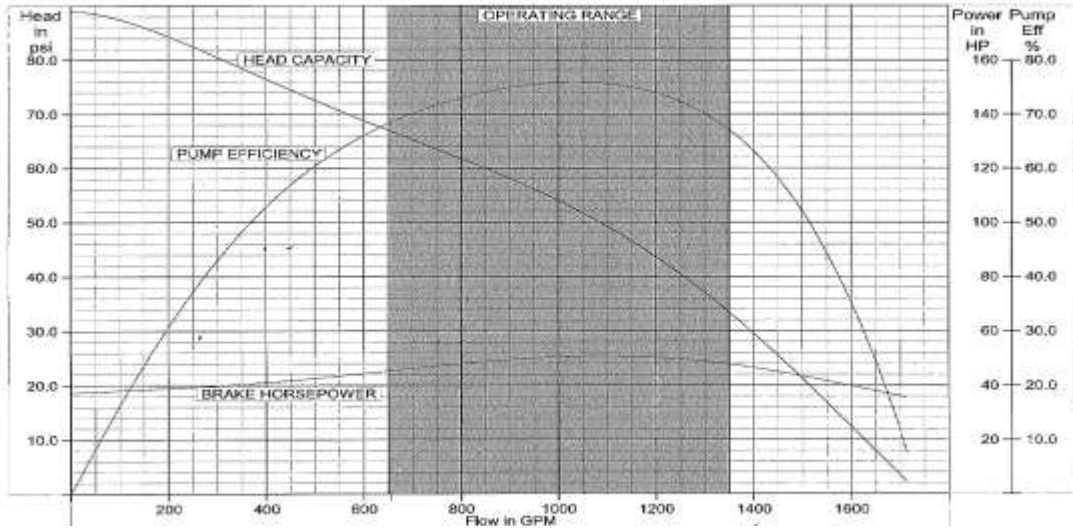


Figure 133. WJE-1000 Pump Curve (Baker Hughes)

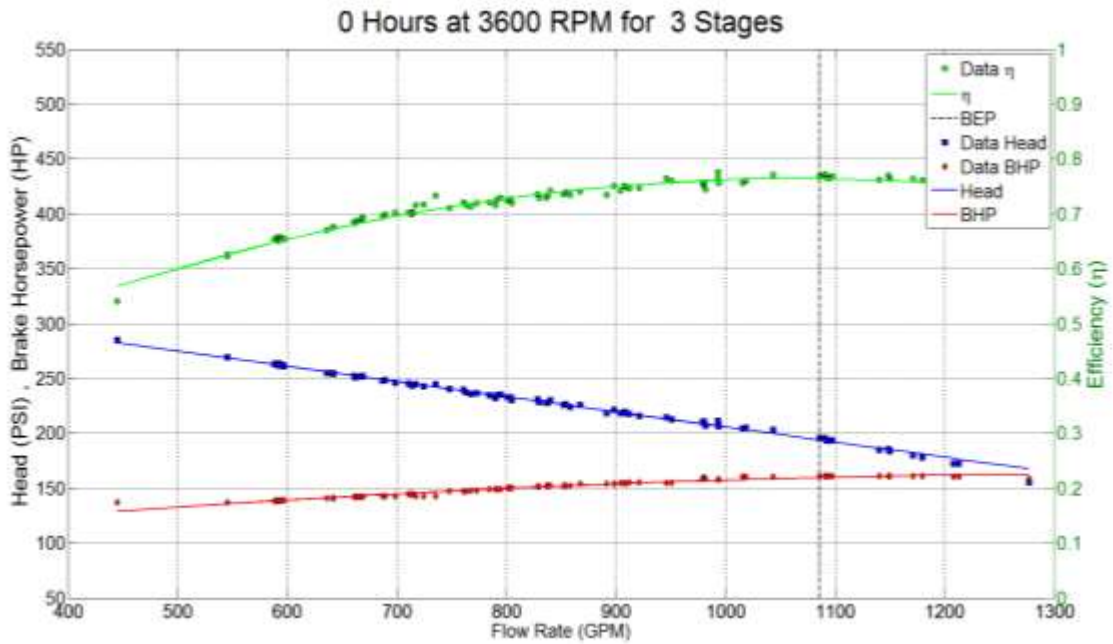


Figure 134. 3600 RPM Performance Curve at 0 Hours

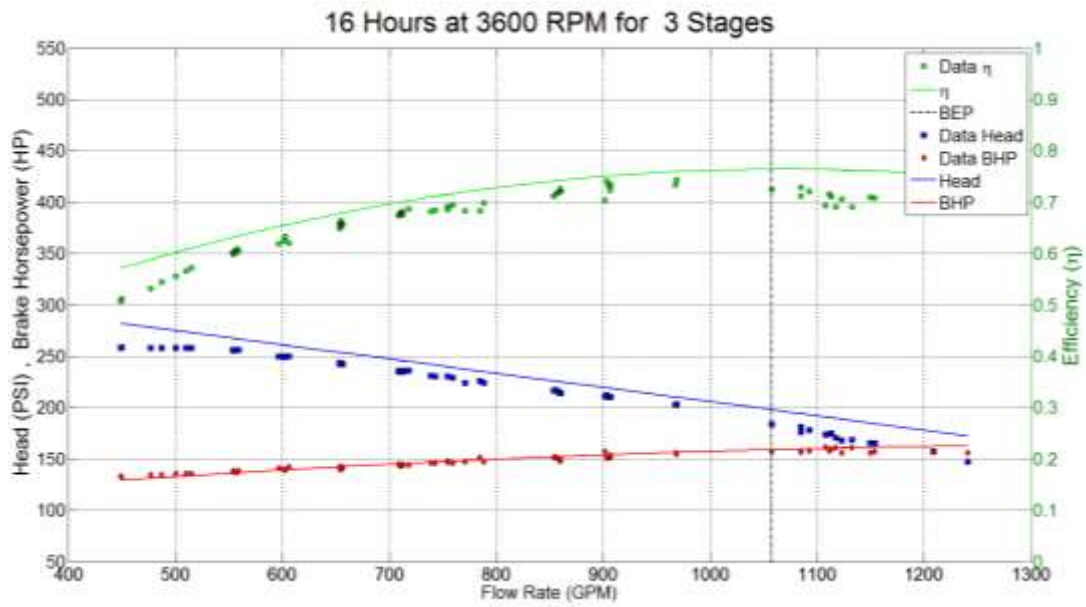


Figure 135. 3600 RPM Performance Curve at 16 Hours

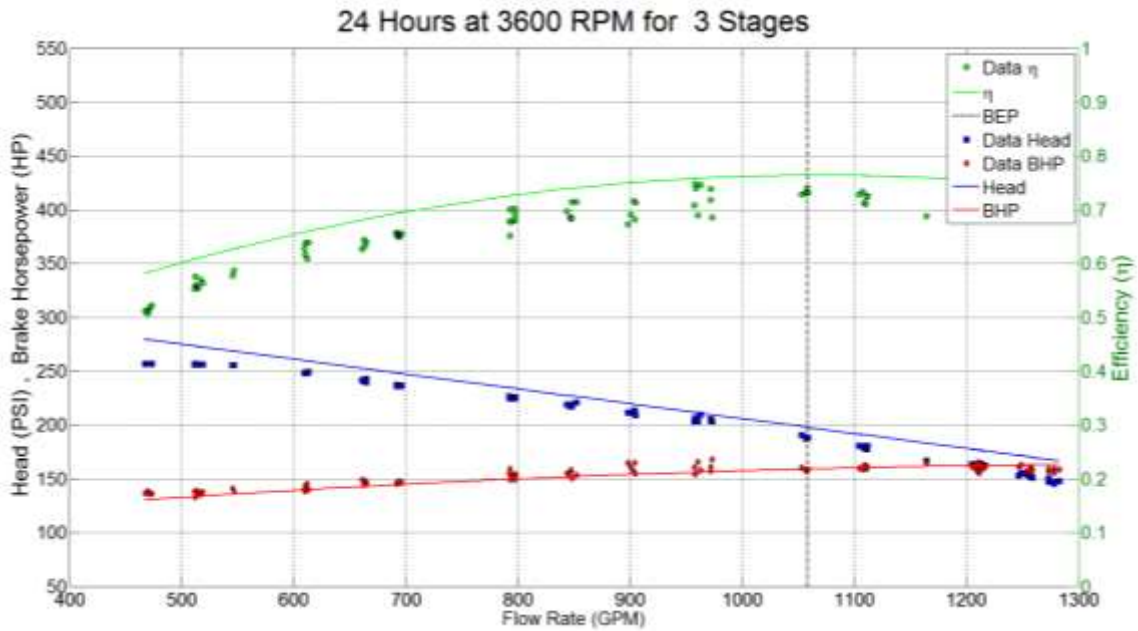


Figure 136. 3600 RPM Performance Curve at 24 Hours

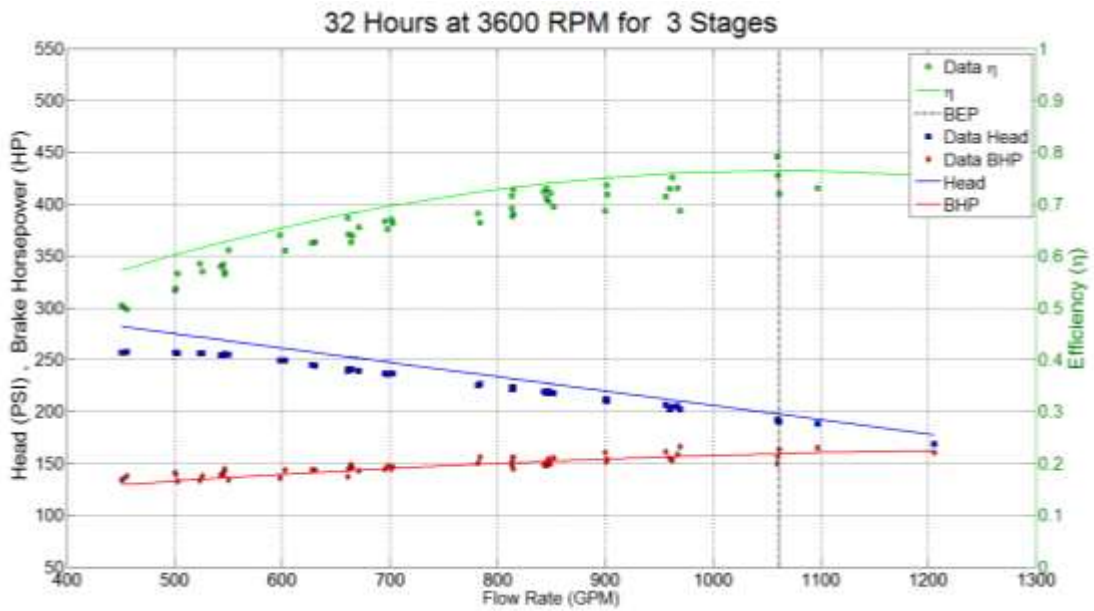


Figure 137. 3600 Pump Performance Curve at 32 Hours

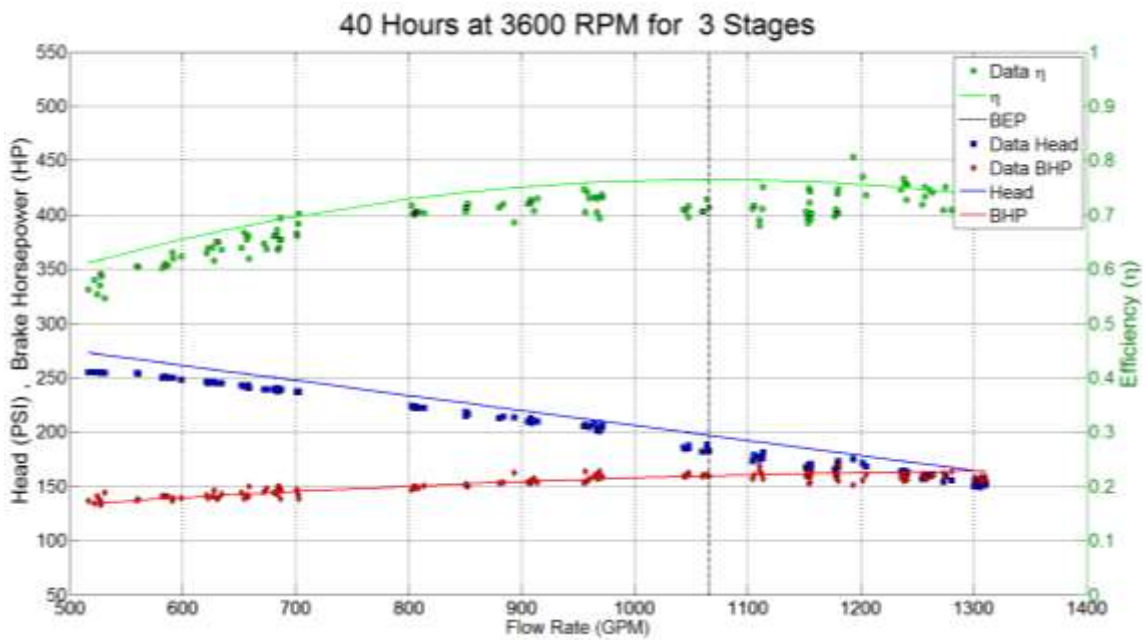


Figure 138. 3600 RPM Performance Curve at 40 Hours

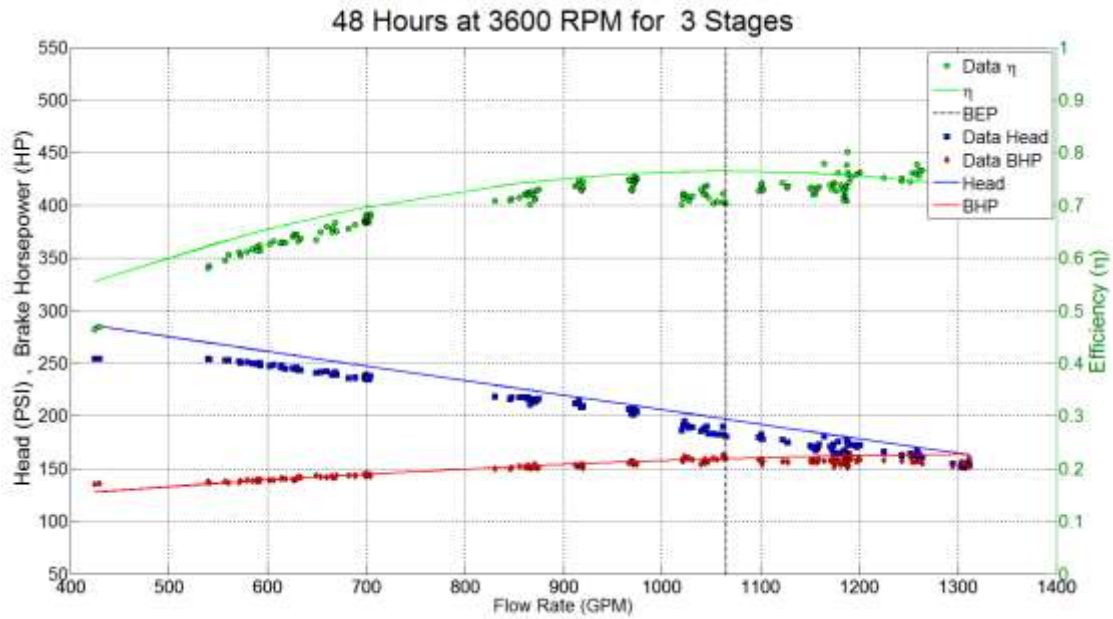


Figure 139. 3600 RPM Performance Curve at 48 Hours

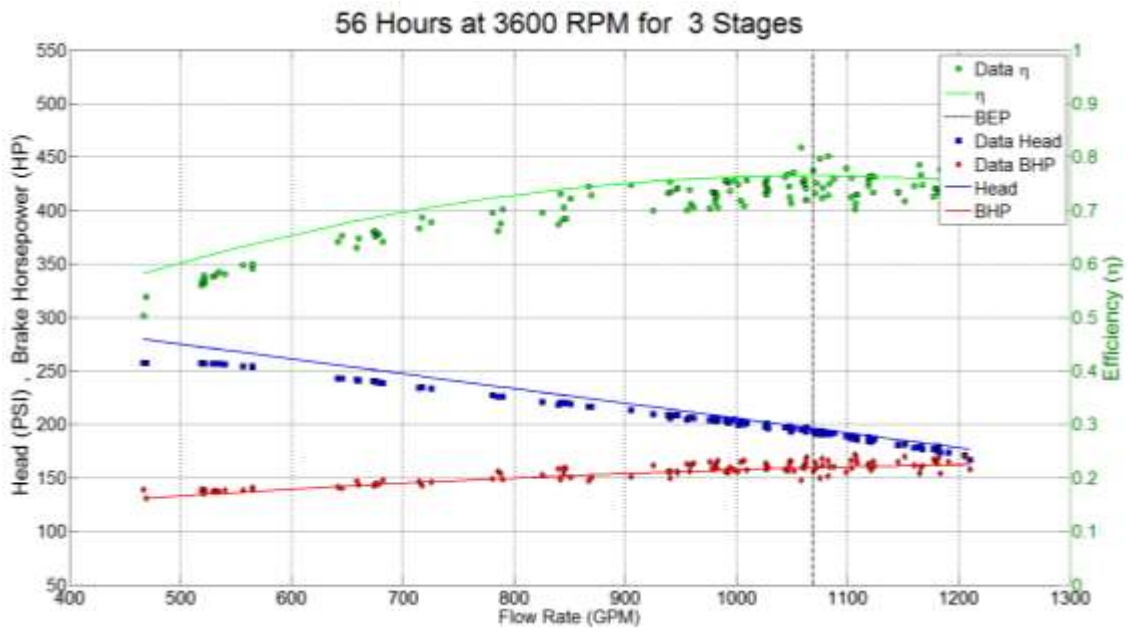


Figure 140. 3600 RPM Performance Curve at 56 Hours

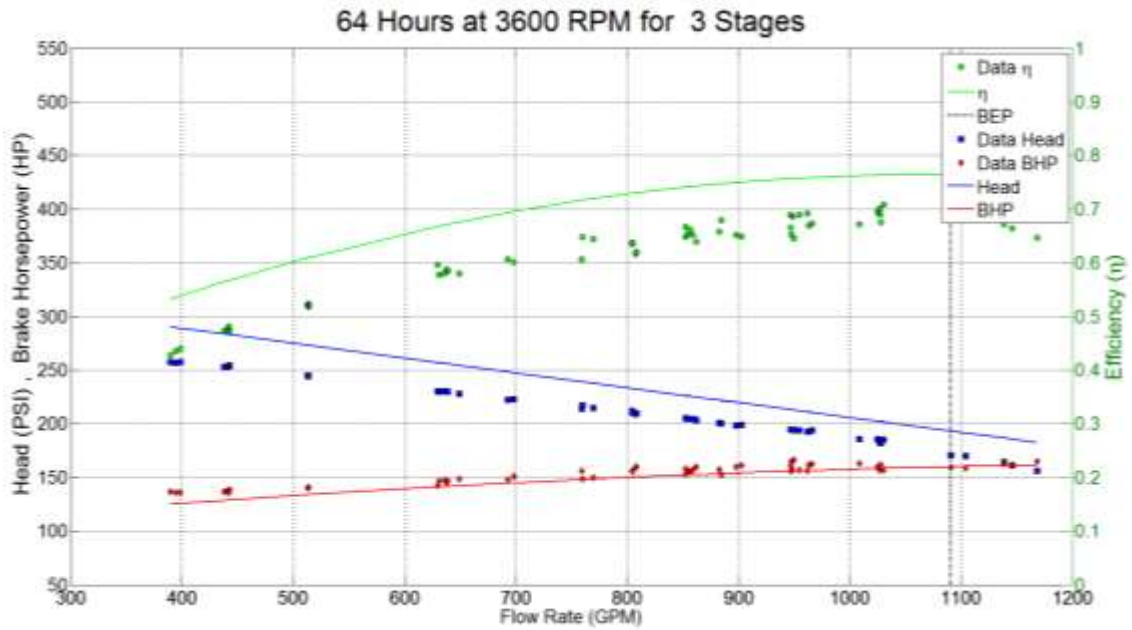


Figure 141. 3600 RPM Performance Curve at 64 Hours

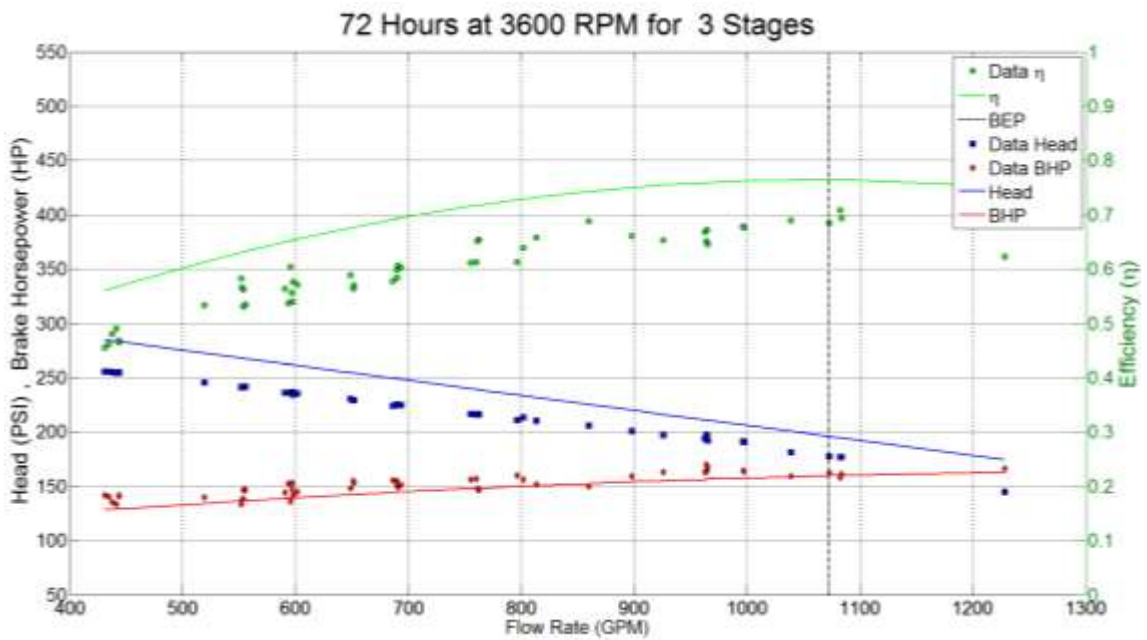


Figure 142. 3600 RPM Performance Curve at 72 Hours

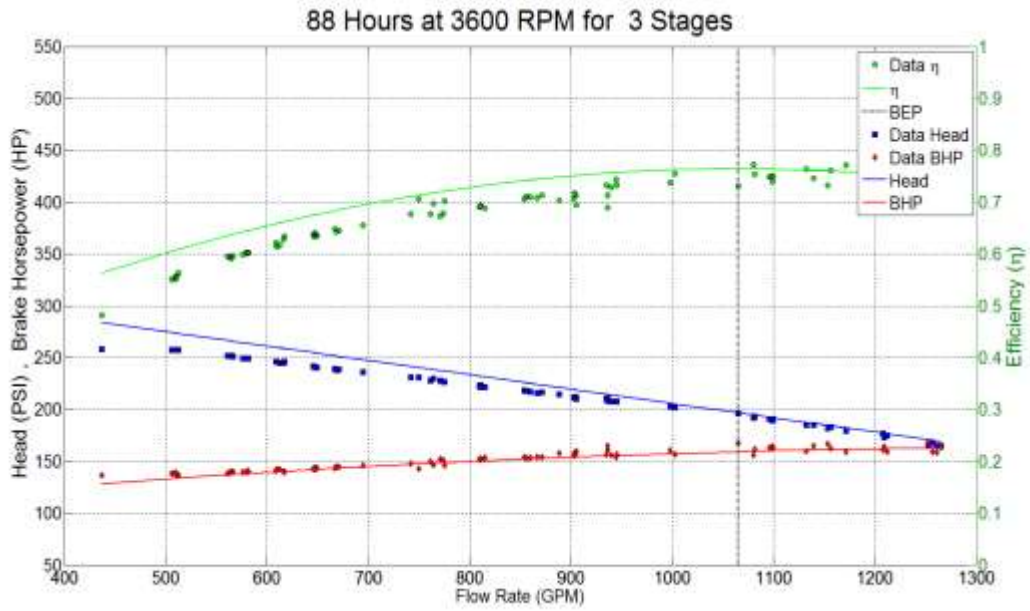


Figure 143. 3600 RPM Performance Curve at 88 Hours

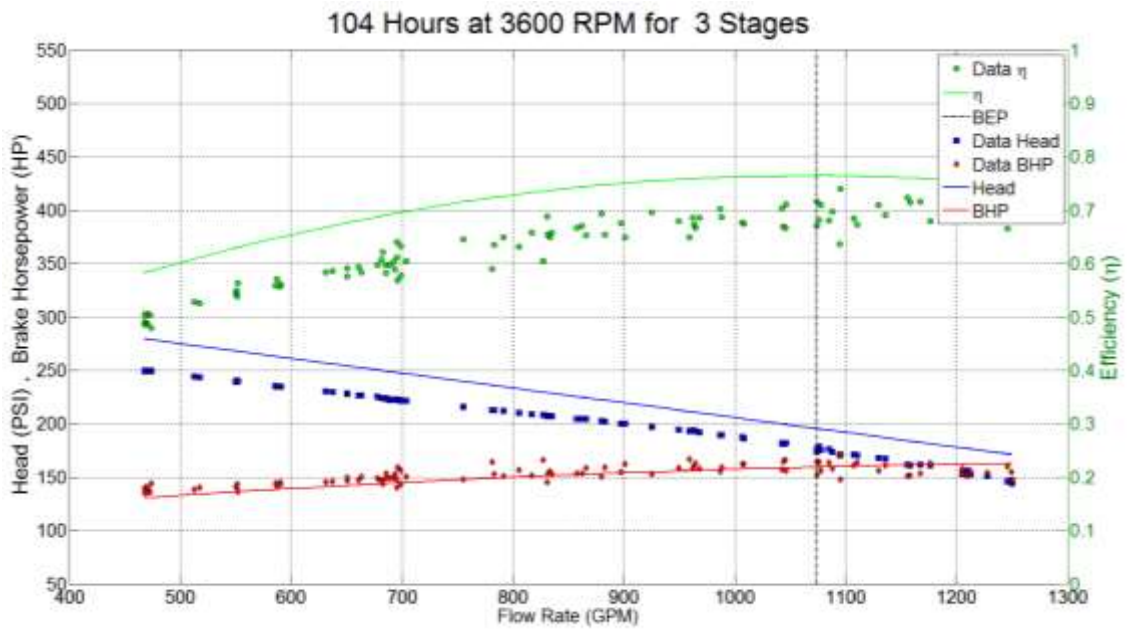


Figure 144. 3600 RPM Performance Curve at 104 Hours

WJE 1000 at 3600 RPM and 0% GVF

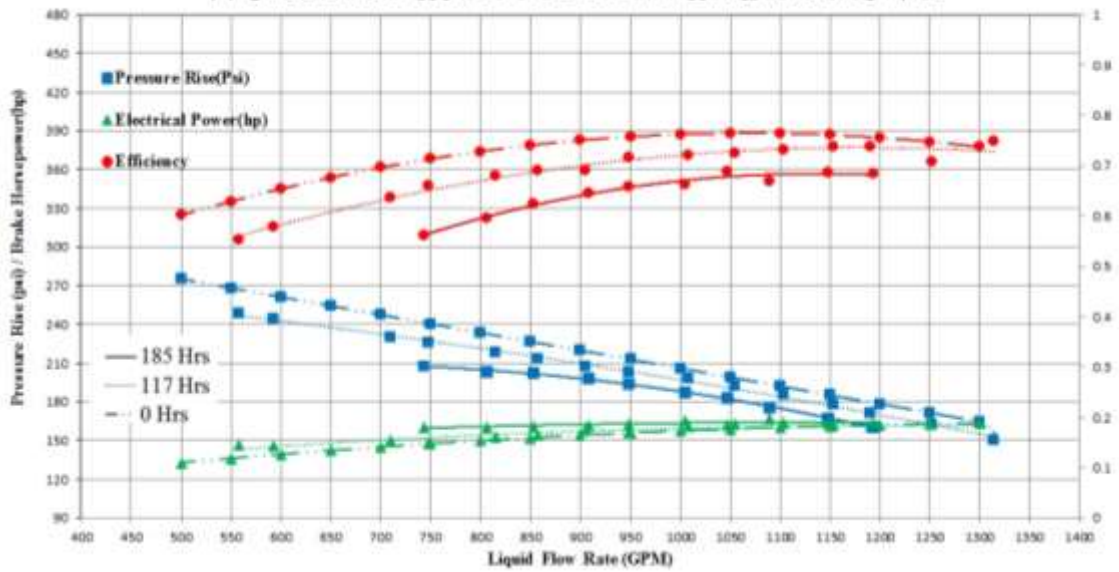


Figure 145. 3600 RPM Performance Curve at (0-117-185) Hours with 0% GVF

WJE 1000 at 3600 RPM and 15% GVF

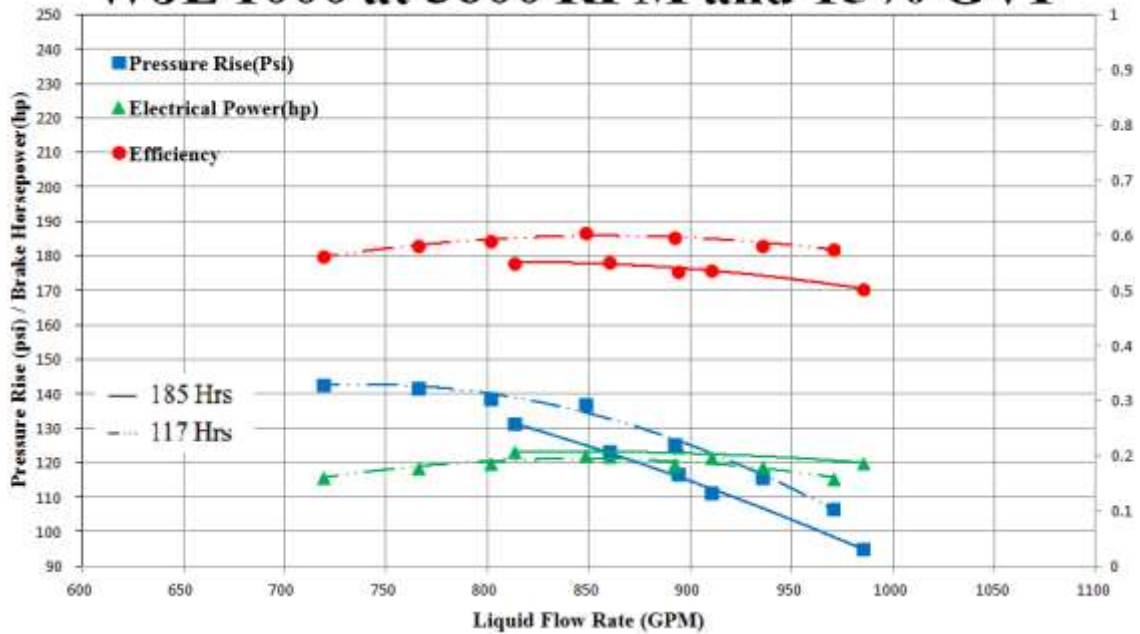


Figure 146. 3600 RPM Performance Curve at (0-117-185) Hours with 15% GVF

WJE 1000 at 3600 RPM and 0% GVF

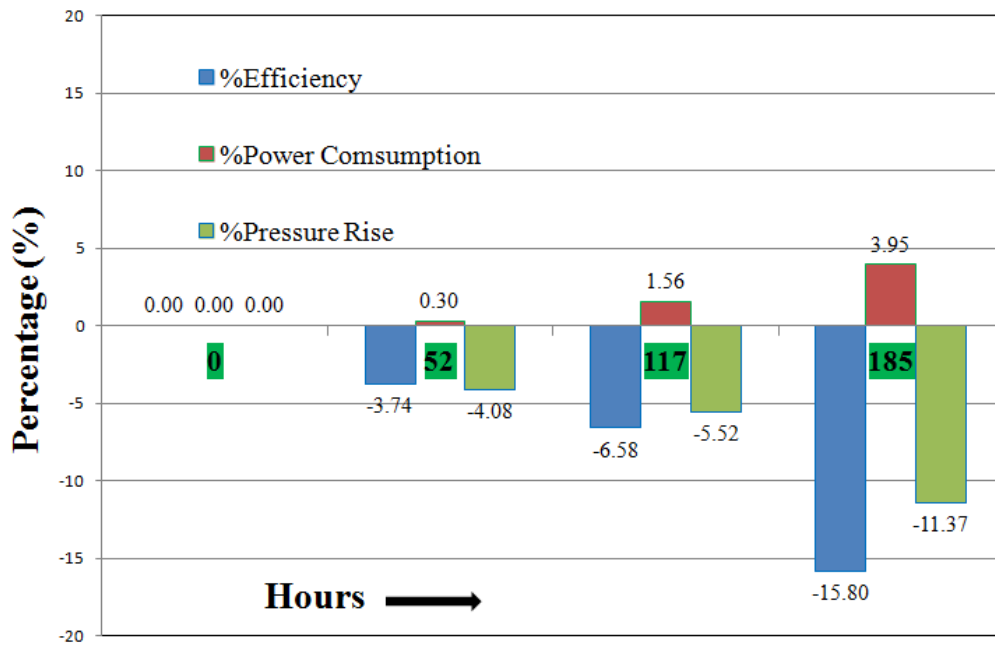


Figure 147. Pump Performance Degradation for 0% GVF

WJE 1000 at 3600 RPM and 15% GVF

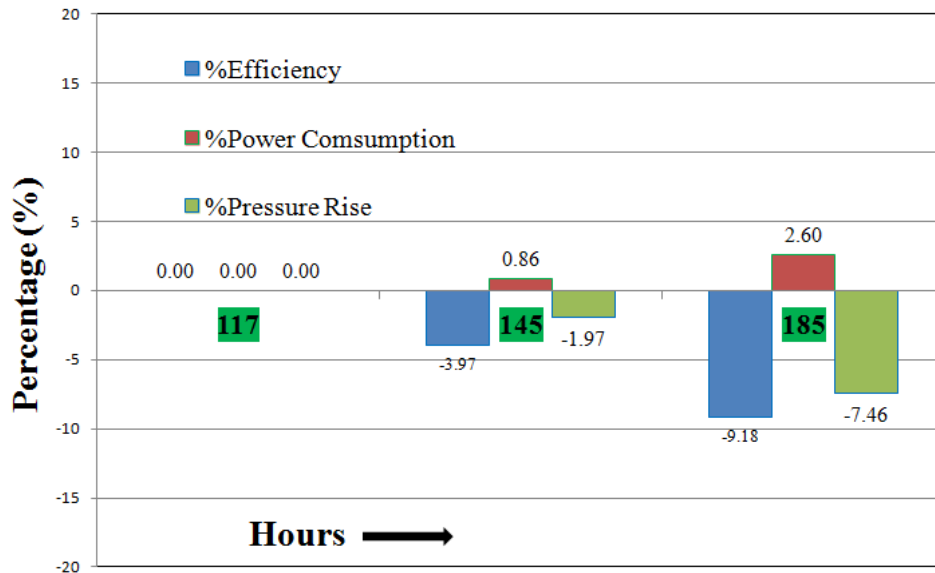


Figure 148. Pump Performance Degradation for 15% GVF

Table 10. Pump Degradation Track

Hour	%Efficiency	%Power Consumption	%Pressure Rise
0	0	0	0
16	-5.37	0.48	-6.14
24	-7.05	1.2	-6.27
32	-6.01	1.07	-4.88
40	-4.48	-0.67	-6.01
48	-3.35	-1.51	-5.68
56	-3.86	1.14	-2.95
72	-15.34	4.14	-10.06
104	-12.97	1.49	-11.52
117	-6.583	1.5636	-5.5153
185	-15.8	3.95	-11.37

APPENDIX C

PUMP COMPONENT WEAR MEASUREMENT

Table 11. Bushing ID Measurement

Bushing ID Measurement						
Hour	0 Hrs		8 Hrs		24 Hrs	
Location	Top	Bottom	Top	Bottom	Top	Bottom
Diffuser 3(B3/B4)	1.8830	1.8830	1.8840	1.8840	1.8880	1.8852
Diffuser 2(B10/B11)	1.8830	1.8830	1.8840	1.8840	1.8900	1.8851
Diffuser1(B16/B17)	1.8830	1.8830	1.8840	1.8840	1.8911	1.8890
Bottom Flange(B20/B21)	1.8830	1.8830	1.8840	1.8840	1.8860	1.8872
Hour	52 Hrs		117 Hrs		185 Hrs	
Location	Top	Bottom	Top	Bottom	Top	Bottom
Diffuser 3(B3/B4)	1.8889	1.8870	1.8937	1.8939	1.9139	1.9192
Diffuser 2(B10/B11)	1.8901	1.8887	1.8938	1.8924	1.9046	1.9091
Diffuser1(B16/B17)	1.8939	1.8907	1.9037	1.9012	1.9265	1.9235
Bottom Flange(B20/B21)	1.8901	1.8941	1.8964	1.9003	1.9101	1.9125

Table 12. Bearing OD Measurement

Journal Bearing OD Measurement						
Hour	0 Hrs		8 Hrs		24 Hrs	
Location	Top	Bottom	Top	Bottom	Top	Bottom
1	1.8710	1.8710	1.8710	1.8710	1.8699	1.8698
2	1.8710	1.8710	1.8710	1.8710	1.8701	1.8701
3	1.8710	1.8710	1.8710	1.8710	1.8631	1.8620
4	1.8710	1.8710	1.8710	1.8710	1.8620	1.8710
10	1.8710	1.8710	1.8710	1.8710	1.8697	1.8630
11	1.8710	1.8710	1.8710	1.8710	1.8625	1.8695
16	1.8710	1.8710	1.8710	1.8710		
17	1.8710	1.8710	1.8710	1.8710		
20	1.8710	1.8710	1.8710	1.8710	1.8710	1.8692
21	1.8710	1.8710	1.8710	1.8710	1.8653	1.8695
Hour	52 Hrs		117 Hrs		185 Hrs	
Location	Top	Bottom	Top	Bottom	Top	Bottom
1	1.8696	1.8696	1.8699	1.8695	1.8691	1.8449
2	1.8700	1.8704	1.8699	1.8700	1.8456	1.8702

Table 12. Continued

Journal Bearing OD Measurement						
3	1.8604	1.8601	1.8524	1.8522	1.8514	1.8381
4	1.8626	1.8671	1.8671	1.8559	1.8524	1.8560
10	1.8691	1.8586	1.8682	1.8500	1.8653	1.8390
11	1.8580	1.8610	1.8496	1.8675	1.8360	1.8650
16	1.8702	1.8647	1.8700	1.8563	1.8670	1.8439
17	1.8651	1.8711	1.8564	1.8709	1.8432	1.8709
20	1.8692	1.8609	1.8701	1.8514	1.8694	1.8426
21	1.8604	1.8692	1.8495	1.8691	1.8400	1.8693

Table 13. Journal Bearing Clearance

Journal Bearing Clearance					
Location	0 hr	8 hr	52 hr	117 hr	185 hr
Stuffing Box(1)	0.012	0.013	0.0205	0.0281	0.0701
Stuffing Box(2)	0.012	0.013	0.0241	0.0277	0.0774
Stage 3(3)	0.012	0.013	0.0288	0.0415	0.0758
Stage 3(4)	0.012	0.013	0.0251	0.0368	0.0668
Stage 2(10)	0.012	0.013	0.0315	0.0438	0.0656
Stage 2(11)	0.012	0.013	0.0307	0.0428	0.0731
Stage1(16)	0.012	0.013	0.0292	0.0474	0.0826
Stage1(17)	0.012	0.013	0.0256	0.0448	0.0803
Bottom Flange(20)	0.012	0.013	0.0292	0.0450	0.0675
Bottom Flange(21)	0.012	0.013	0.0337	0.0508	0.0725

Table 14. Sleeve Bearing Weight Track

(5) SLEEVE BEARING L=1.00"						
no.	0 hr	8 hr	52 hr	117 hr	185 hr	Location
1-A	0.52	0.52	0.52	0.52	0.49	Stuffing Box(1)
2-B	0.52	0.52	0.52	0.52	0.49	Stuffing Box(2)
3-C	0.52	0.52	0.51	0.50	0.47	Stage 3(3)
4-D	0.52	0.52	0.51	0.51	0.49	Stage 3(4)
10-E	0.52	0.52	0.51	0.50	0.48	Stage 2(10)
11-F	0.52	0.52	0.51	0.49	0.47	Stage 2(11)
16-G	0.52	0.52	⊗	⊗	⊗	Stage1(16)
17-H	0.52	0.52	⊗	⊗	⊗	Stage1(17)
20-I	0.52	0.52	0.51	0.50	0.48	Bottom Flange(20)
21-J	0.52	0.52	0.51	0.51	0.49	Bottom Flange(21)

Table 15. Spacer and Upthrust Plate Weight Track

(27) LONG SLEEVE L=2.313"					
no.	8.00	24.00	52.00	117.00	185.00
12-A	0.60	0.60	0.60	0.60	0.59
18-B	0.60				
no.	8.00	24.00	52.00	117.00	185.00
9-A	0.49	0.48	0.48	0.47	0.46
15-B	0.49				
(22) SHORT SLEEVE L=1.188"					
no.	8.00	24.00	52.00	117.00	185.00
8-A	0.31	0.31	0.31	0.31	0.30
14-B	0.31				
(25) TAPER LOCK BUSHING					
no.	8.00	24.00	52.00	117.00	185.00
7-A	1.45	1.46	1.46	1.46	1.45
13-B	1.46	1.45	1.45	1.45	1.44
19-C	1.45				1.45
(19) UPTHrust PLATE					
no.	8.00	24.00	52.00	117.00	185.00
6-A	0.82	0.82	0.82	0.82	0.81

Table 16. Impeller and Diffuser Weight Track

IMPELLER					
	0.00	8.00	52.00	117.00	185.00
3rd Stage Impeller	13.55	13.54	13.39	13.38	13.20
2nd Stage Impeller	13.35	13.32	13.18	13.16	13.00
1st Stage Impeller	13.35				13.20
DIFFUSER					
	8.00	24.00	52.00	117.00	185.00
3rd Stage Diffuser		58.20	58.10	58.00	57.80
2nd Stage Diffuser		57.40	57.30	57.20	56.80
1st Stage Diffuser		56.60	56.50	56.40	56.20

Table 17. Impeller Intake Labyrinth Diameter

Hours	0 hrs	8 hrs	24 hrs	52 hrs	117 hrs	185 hrs
3rd stage	5.296	5.289	5.285	5.2811	5.2785	5.2701
2nd stage	5.296	5.292	5.288	5.286	5.275	5.2599
1st stage	5.296	5.294	5.29	5.2839	5.2808	5.2631

Table 18. Impeller Discharge Labyrinth Diameter

Hours	0 hrs	8 hrs	24 hrs	52 hrs	117 hrs	185 hrs
3rd stage	4.484	4.477	4.472	4.4637	4.4595	4.4415
2nd stage	4.484	4.48	4.47	4.4649	4.458	4.4402
1st stage	4.484	4.477	4.476	4.473	4.465	4.4544

Table 19. Diffuser Suction Labyrinth Diameter

Hours	0 hrs	8 hrs	24 hrs	52 hrs	117 hrs	185 hrs
3rd stage	4.5	4.501	4.501	4.5029	4.4995	4.4972
2nd stage	4.499	4.5	4.502	4.5059	4.5	4.5
1st stage	4.501	4.501	4.503	4.5043	4.5028	4.5029

Table 20. Diffuser Discharge Labyrinth Diameter

Hours	0 hrs	8 hrs	24 hrs	52 hrs	117 hrs	185 hrs
3rd stage	5.308	×	5.309	5.3101	5.3105	5.3113
2nd stage	5.311	5.312	5.316	5.324	5.332	5.3508
1st stage	5.313	5.314	5.316	5.3199	5.338	5.3543
Bottom Flange	5.313	×	×	5.3219	5.345	5.358

Table 21. Impeller Intake Labyrinth Clearance

Hours	0 hrs	8 hrs	24 hrs	52 hrs	117 hrs	185 hrs
3rd stage	0.015	0.023	0.031	0.0429	0.0535	0.0807
2nd stage	0.017	0.022	0.028	0.0339	0.063	0.0944
1st stage	0.017	×	×	0.038	0.0642	0.0949

Table 22. Impeller Discharge Labyrinth Clearance

Hours	0 hrs	8 hrs	24 hrs	52 hrs	117 hrs	185 hrs
3rd stage	0.016	0.024	0.029	0.0392	0.04	0.0557
2nd stage	0.015	0.02	0.032	0.041	0.042	0.0598
1st stage	0.017	0.024	0.027	0.0313	0.0378	0.0485

APPENDIX D

VIBRATION SIGNATURE

D.1. 0 Hours

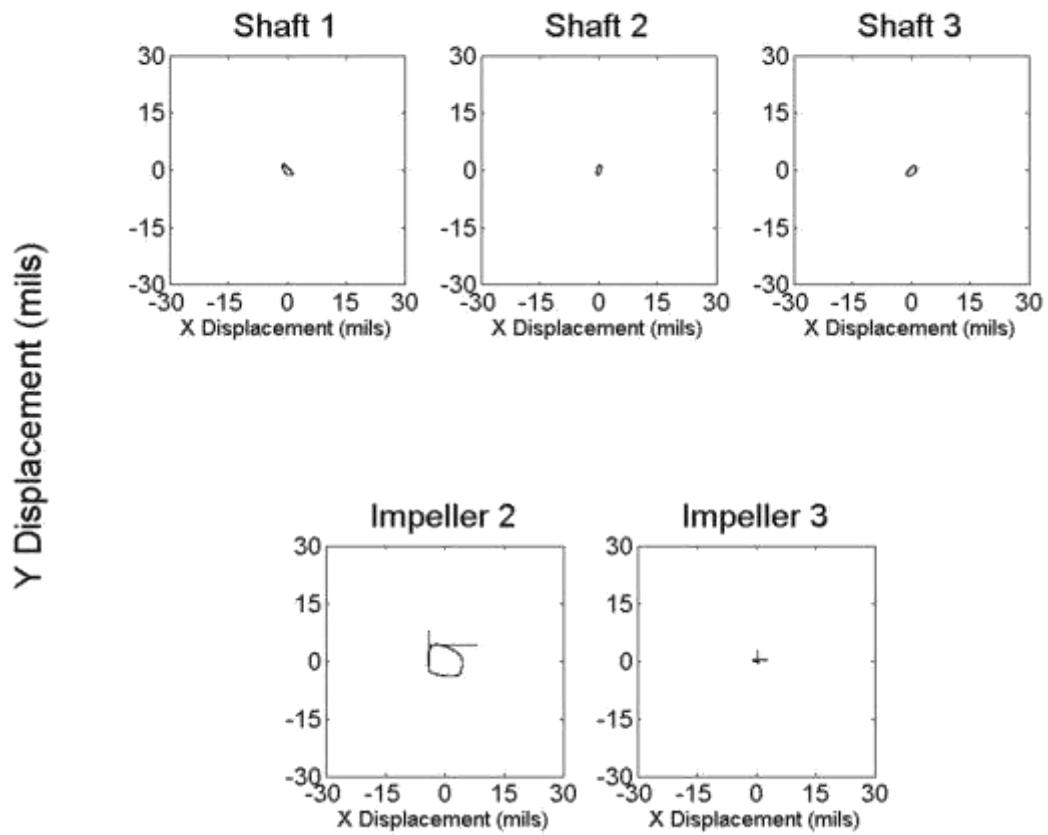


Figure 149. Orbit at 90 RPM – 0 Hours

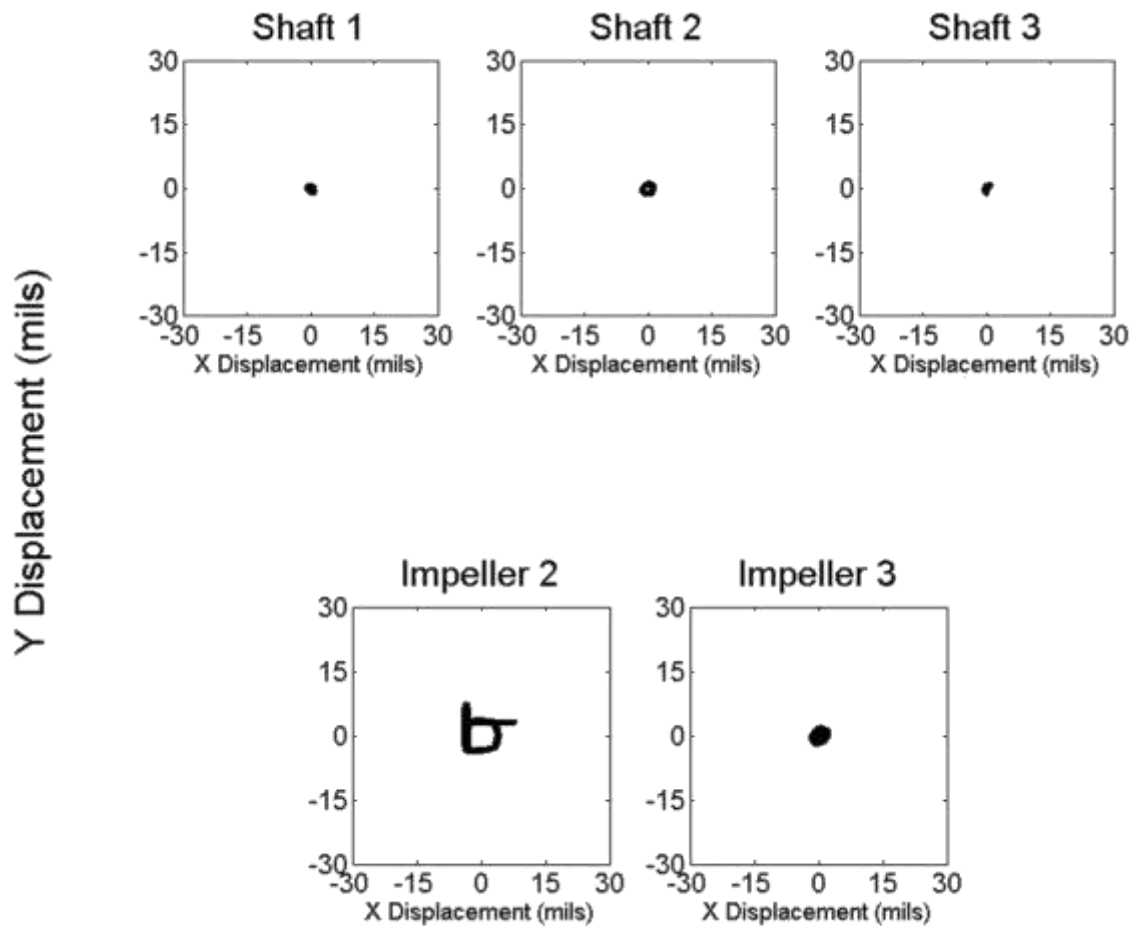


Figure 150. Orbit at 3600 RPM – 0 Hours

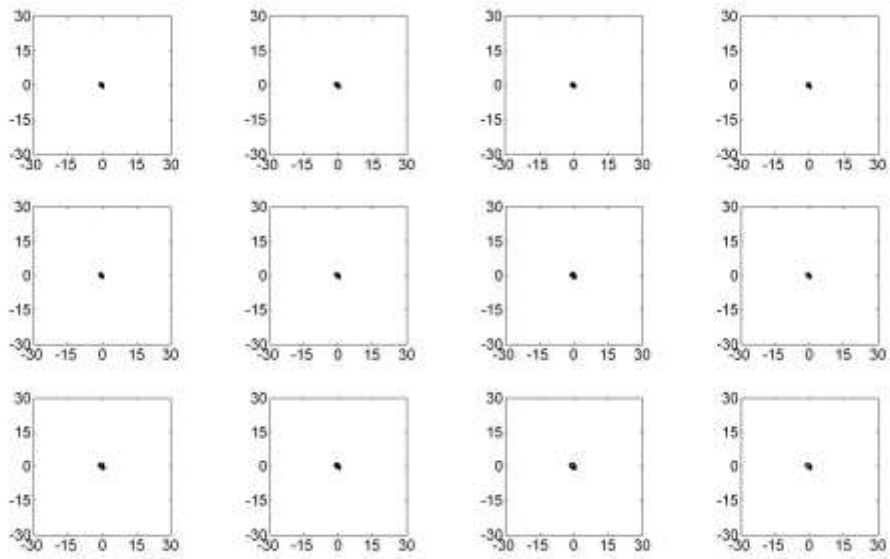


Figure 151. Shaft 1 Ramp Up Orbit – 0 Hours

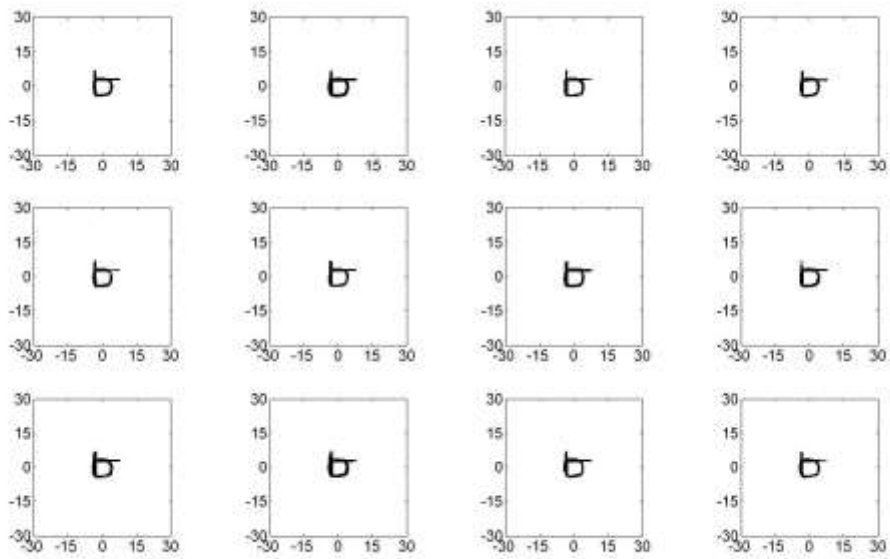


Figure 152. Impeller 2 Ramp Up Orbit – 0 Hours

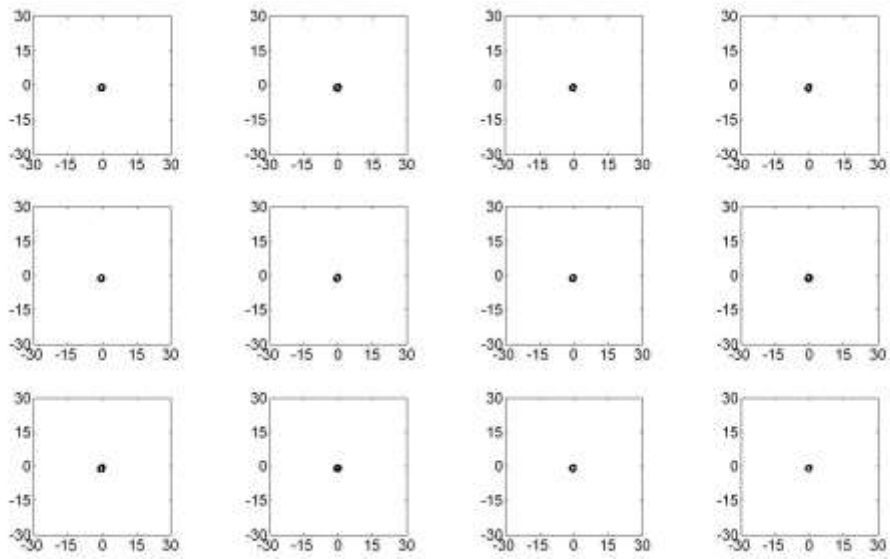


Figure 153. Shaft 2 Ramp Up Orbit – 0 Hours

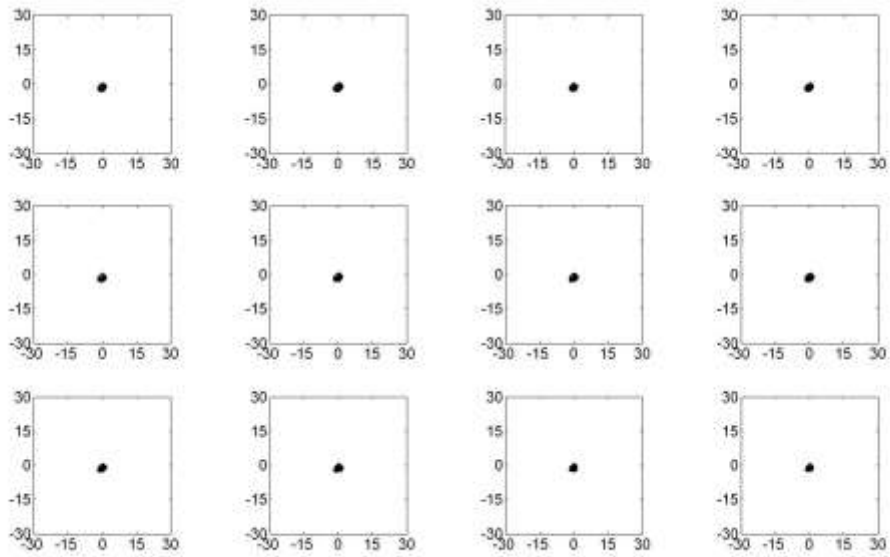


Figure 154. Impeller 3 Ramp Up Orbit – 0 Hours

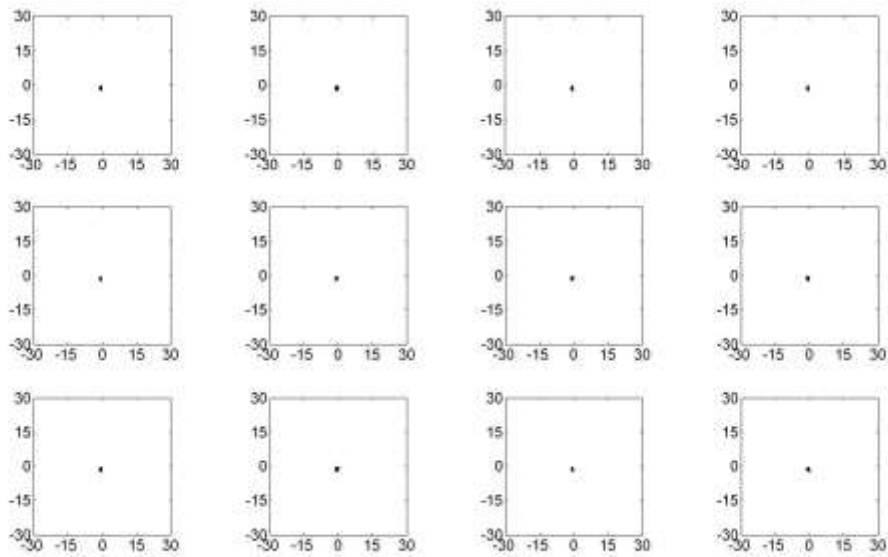


Figure 155. Shaft 3 Ramp Up Orbit – 0 Hours

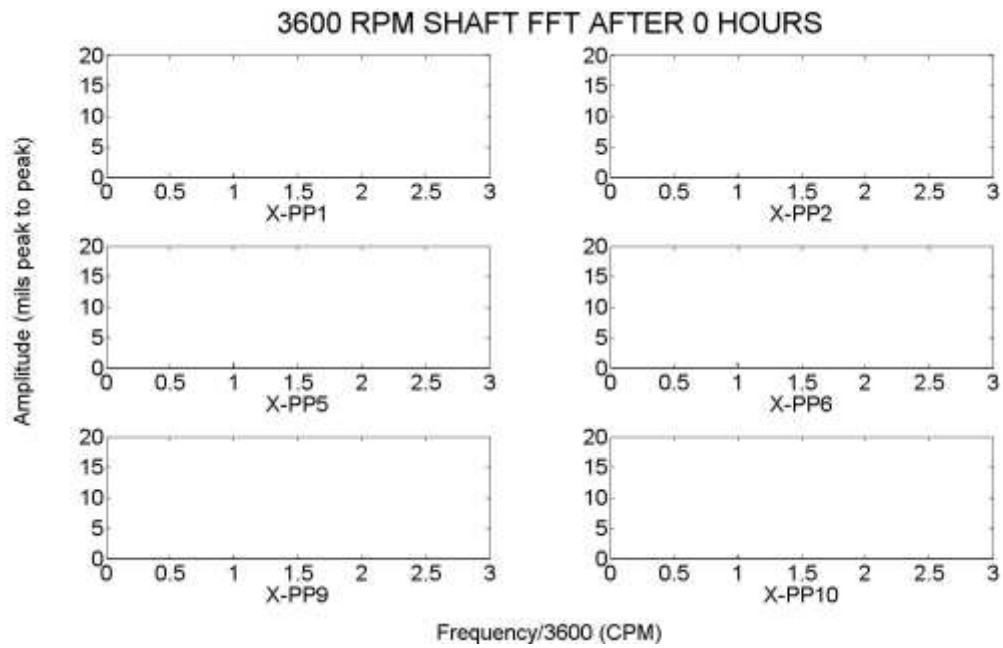


Figure 156. Shaft FFT – 0 Hours

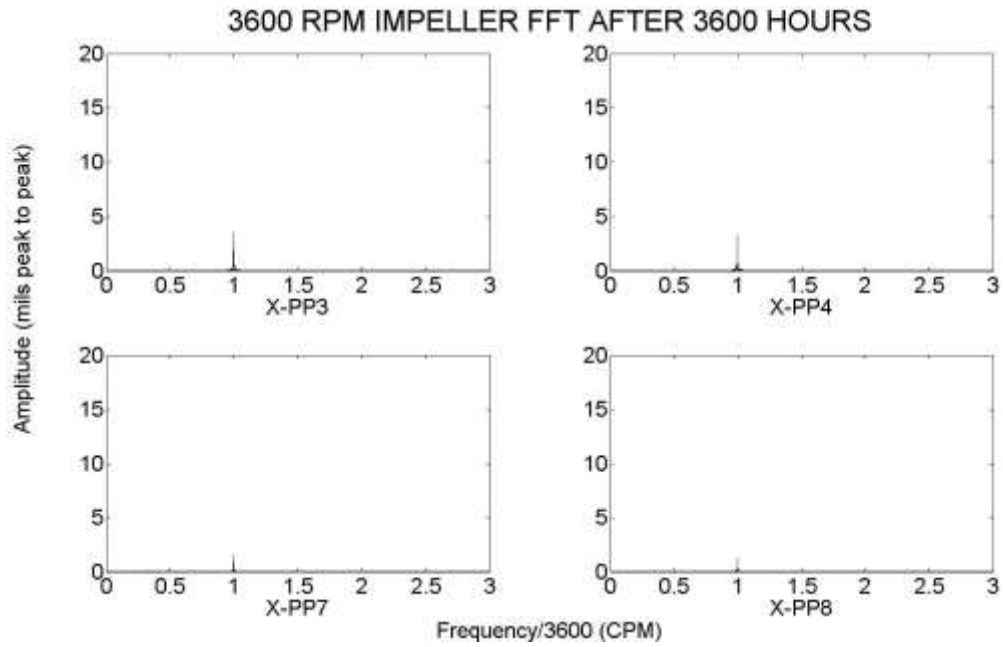


Figure 157. Impeller FFT – 0 Hours

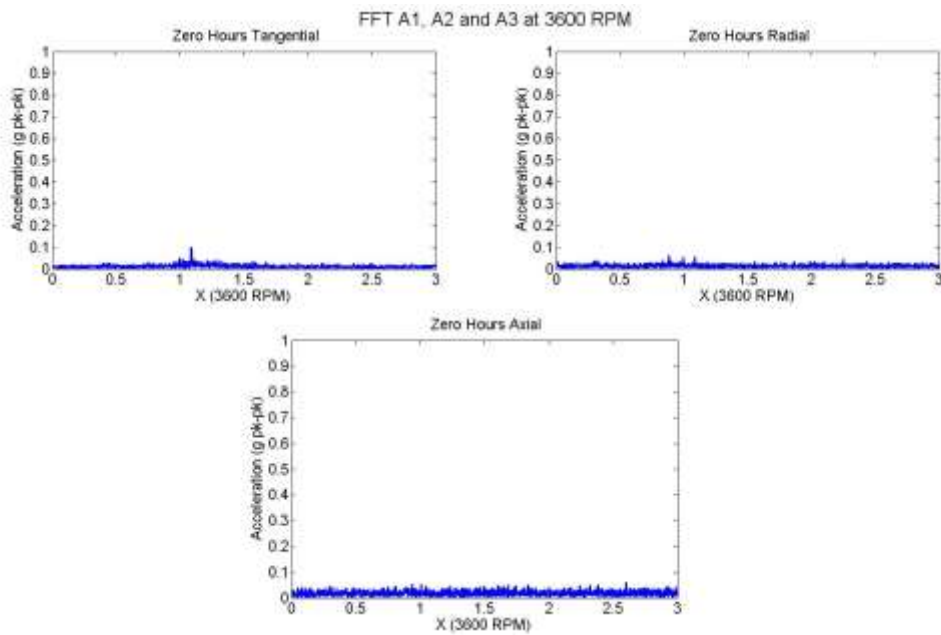


Figure 158. Inlet Accelerometer FFT – 0 Hours

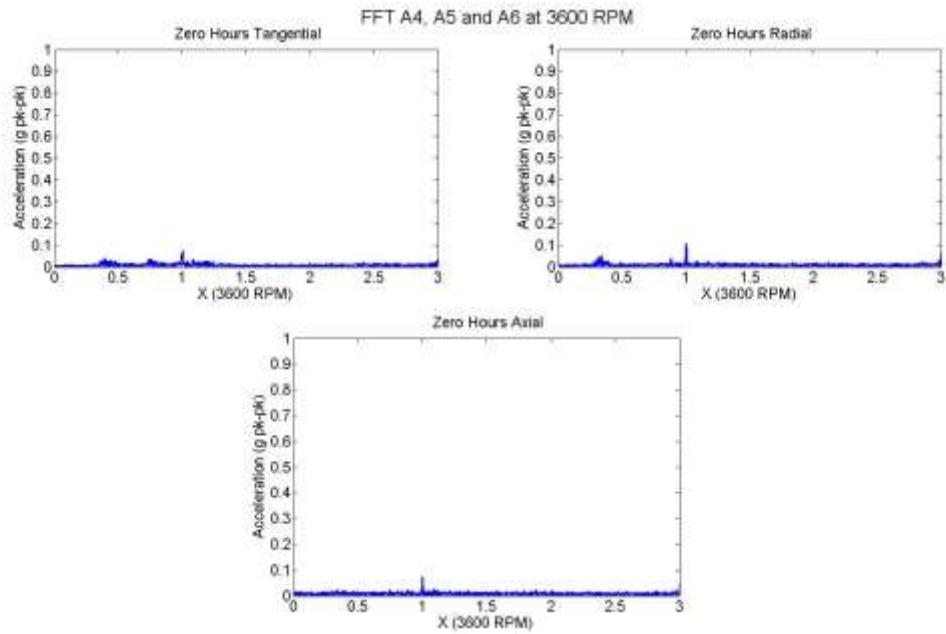


Figure 159. Outlet Accelerometer FFT – 0 Hours

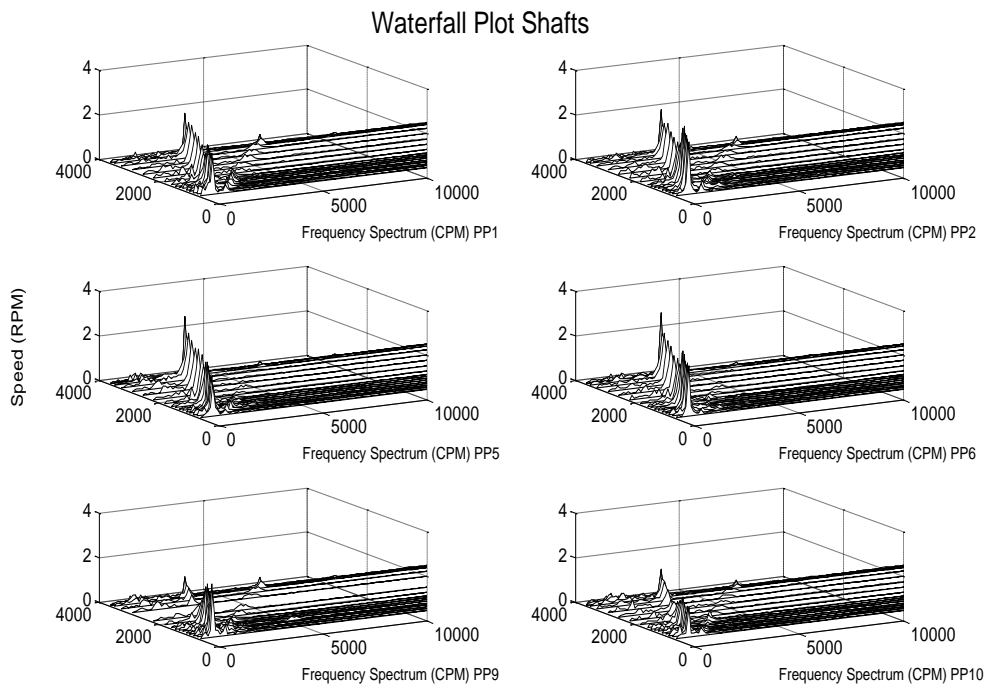


Figure 160. Shaft Waterfall Spectrum – 0 Hours

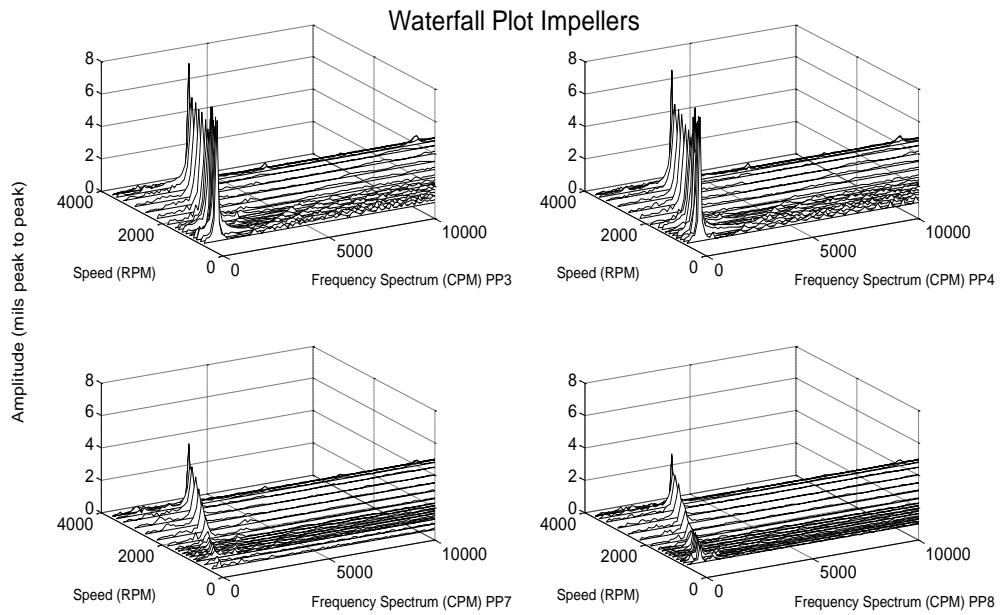


Figure 161. Impeller Waterfall Spectrum – 0 Hours

D.2. 8 Hours

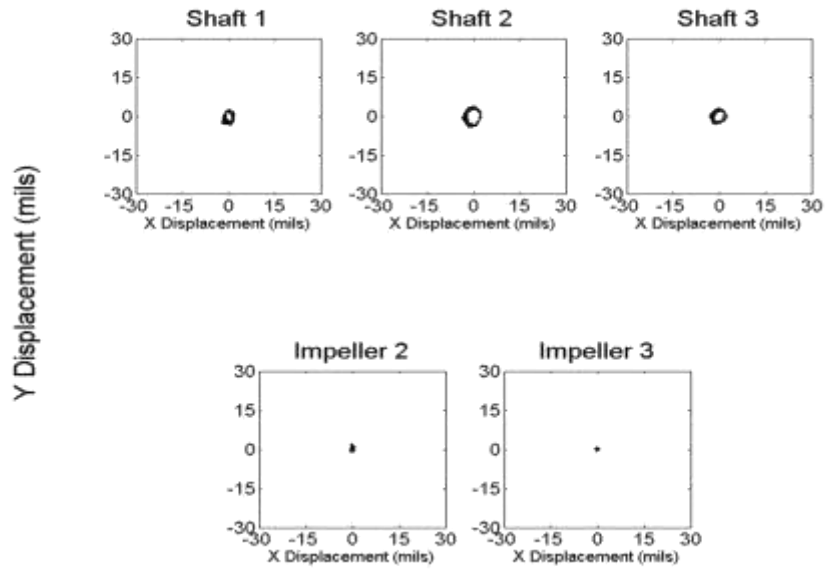


Figure 162. Orbit at 90 RPM – 8 Hours

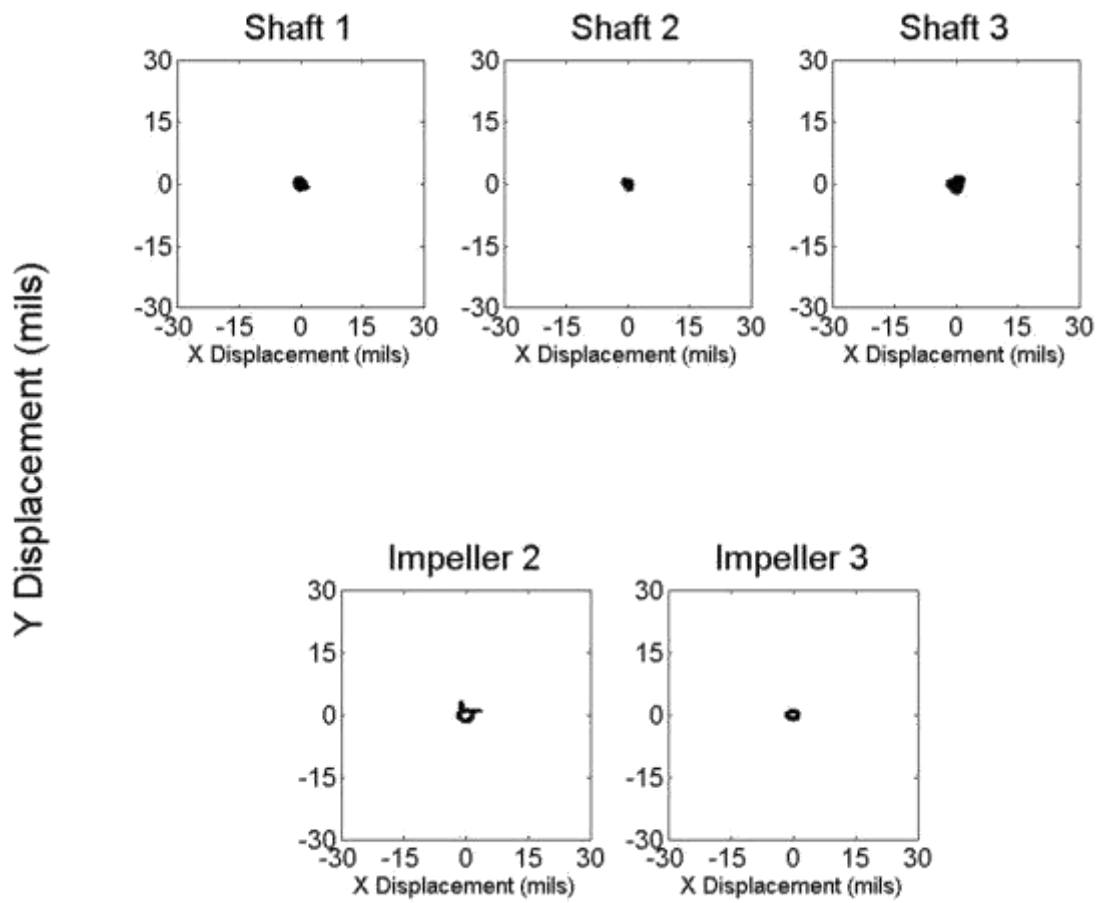


Figure 163. Orbit at 3600 RPM – 8 Hours

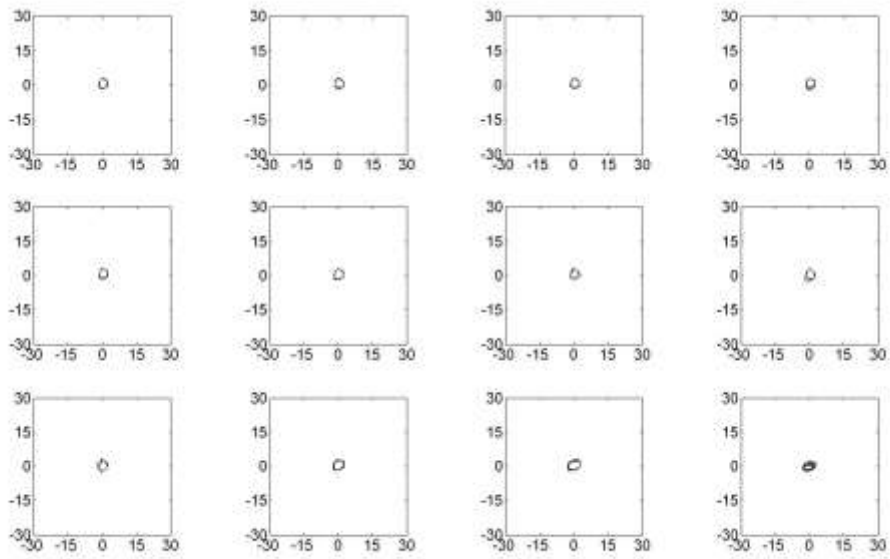


Figure 164. Shaft 1 Ramp Up Orbit – 8 Hours

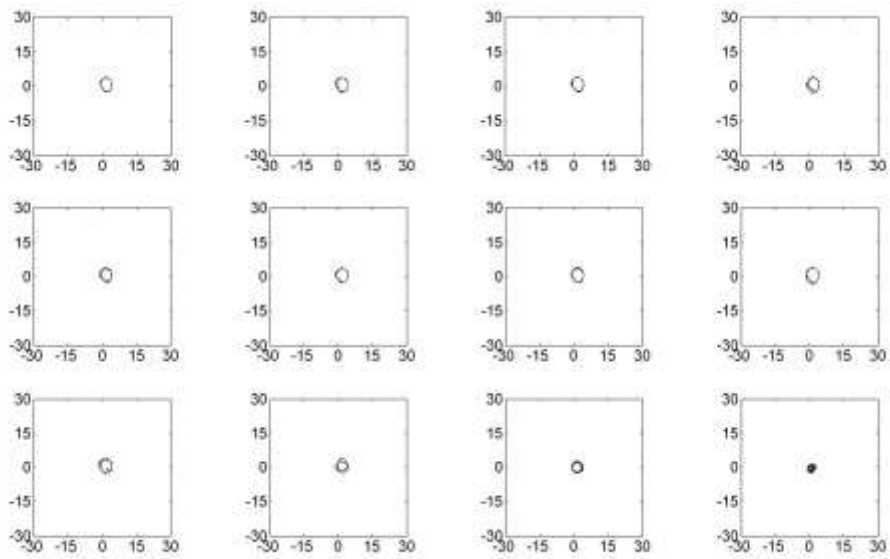


Figure 165. Shaft 2 Ramp Up Orbit – 8 Hours

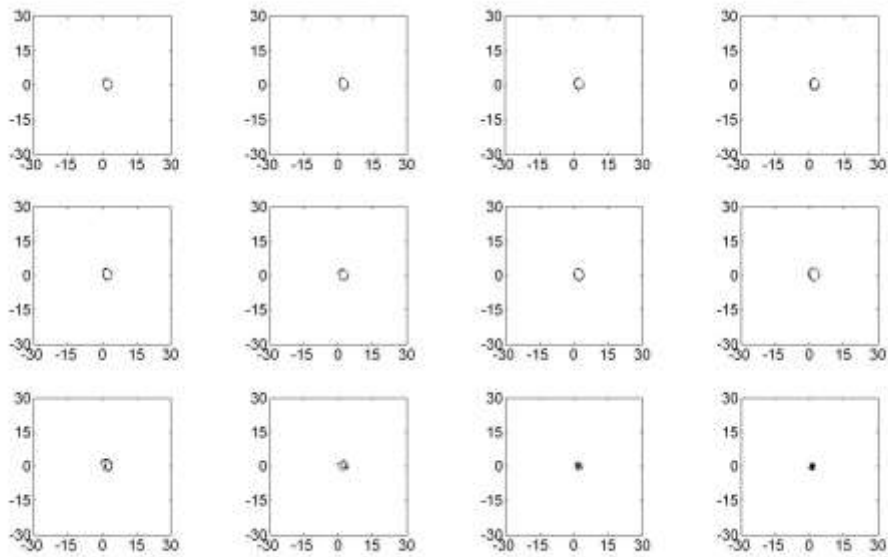


Figure 166. Shaft 3 Ramp Up Orbit – 8 Hours

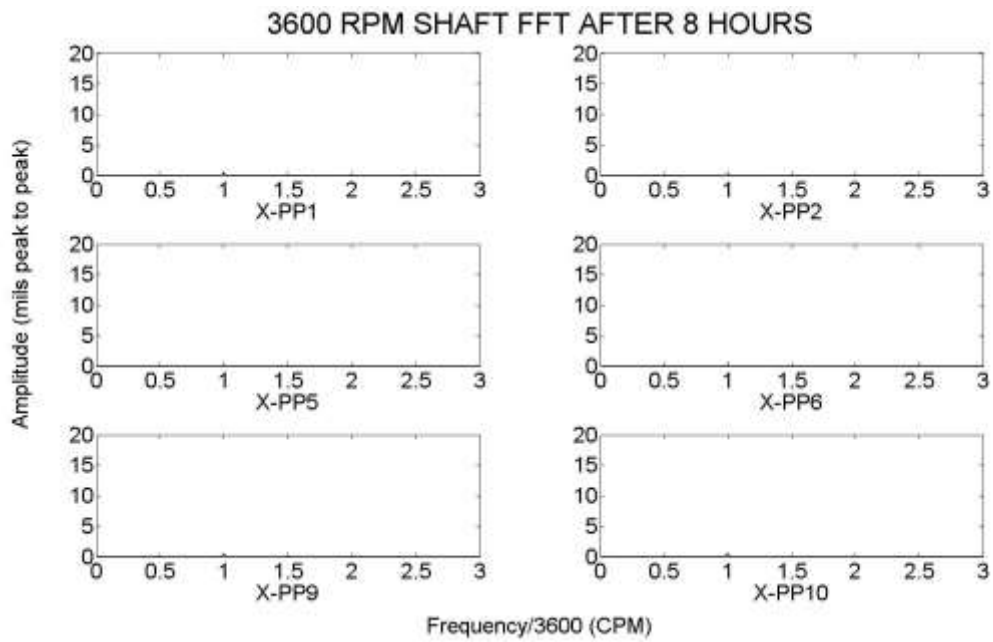


Figure 167. Shaft FFT – 8 Hours

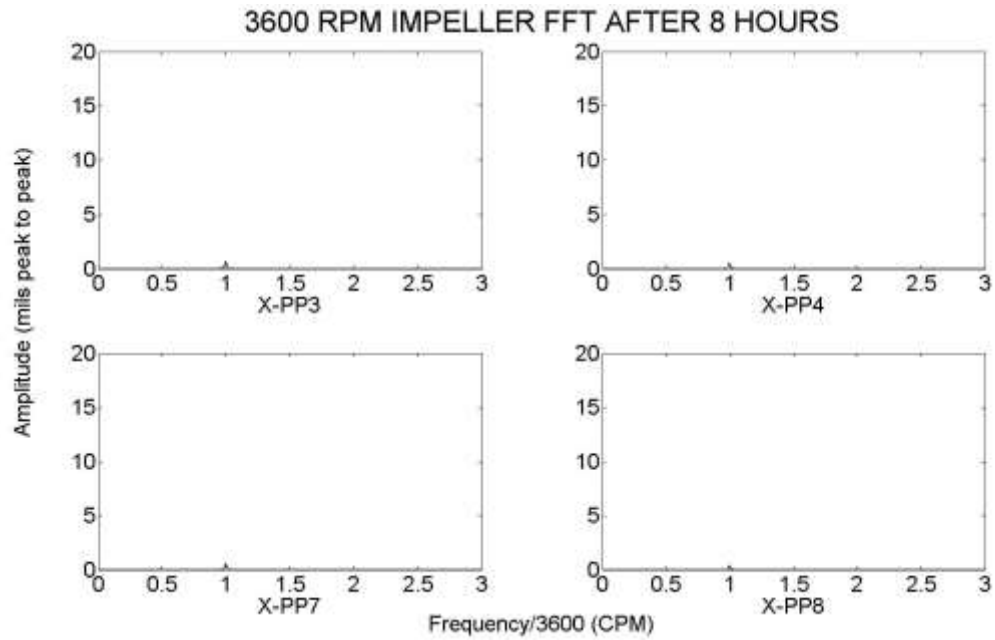


Figure 168. Impeller FFT – 8 Hours

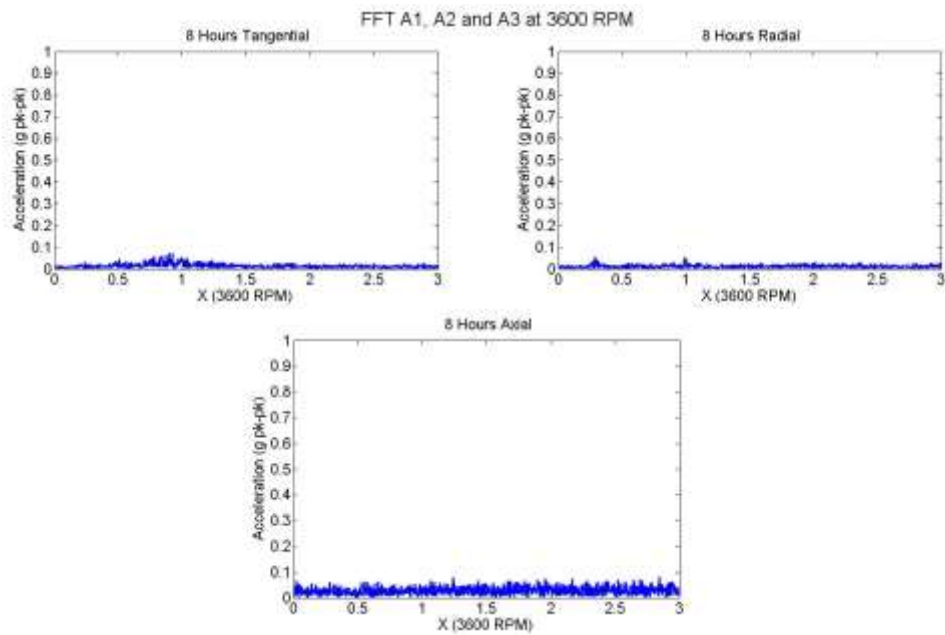


Figure 169. Inlet Accelerometer FFT – 8 Hours

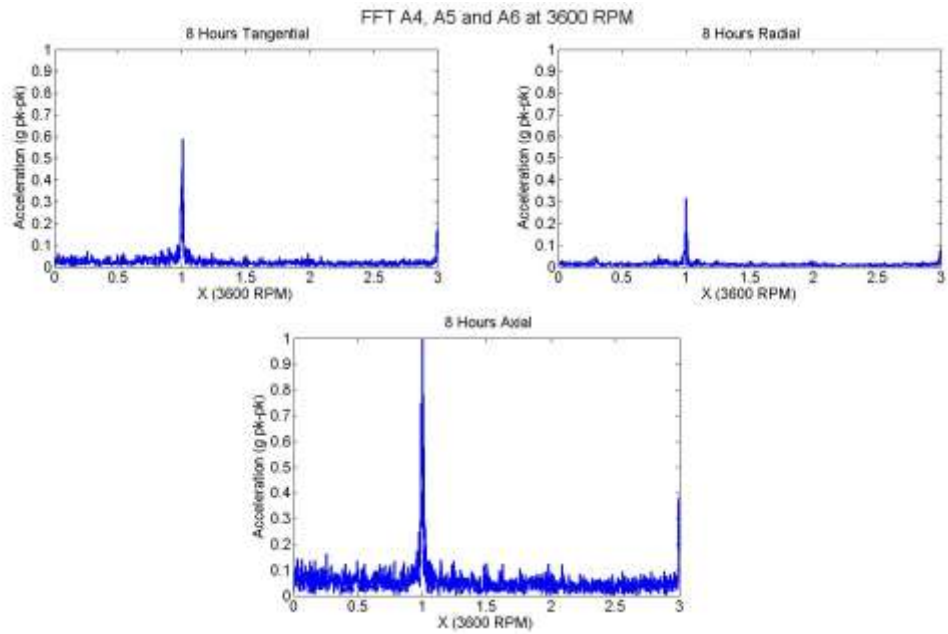


Figure 170. Outlet Accelerometer FFT – 8 Hours

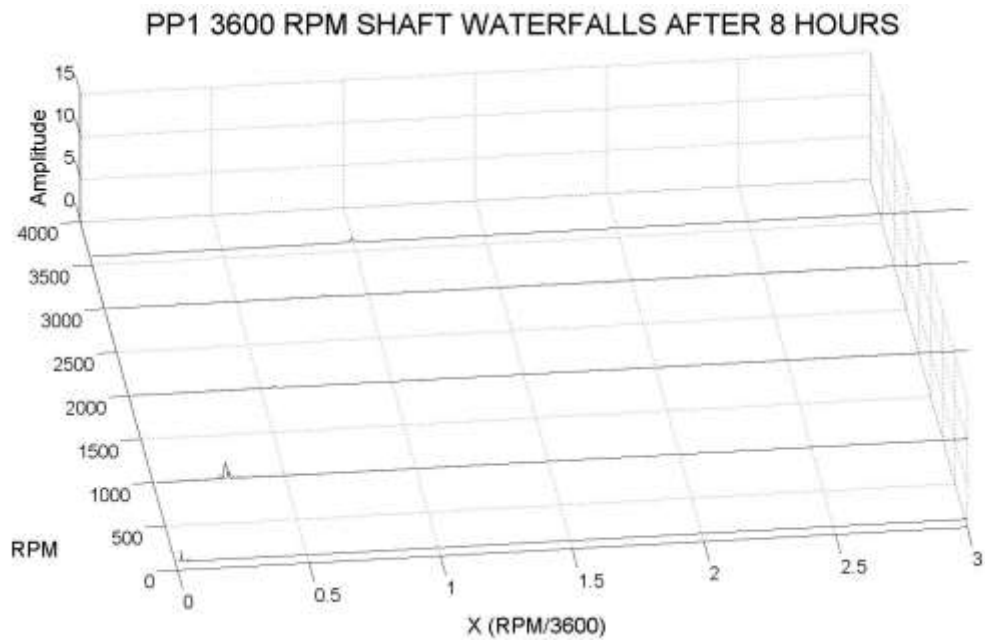


Figure 171. PP1 Waterfall Spectrum – 8 Hours

PP2 3600 RPM SHAFT WATERFALLS AFTER 8 HOURS

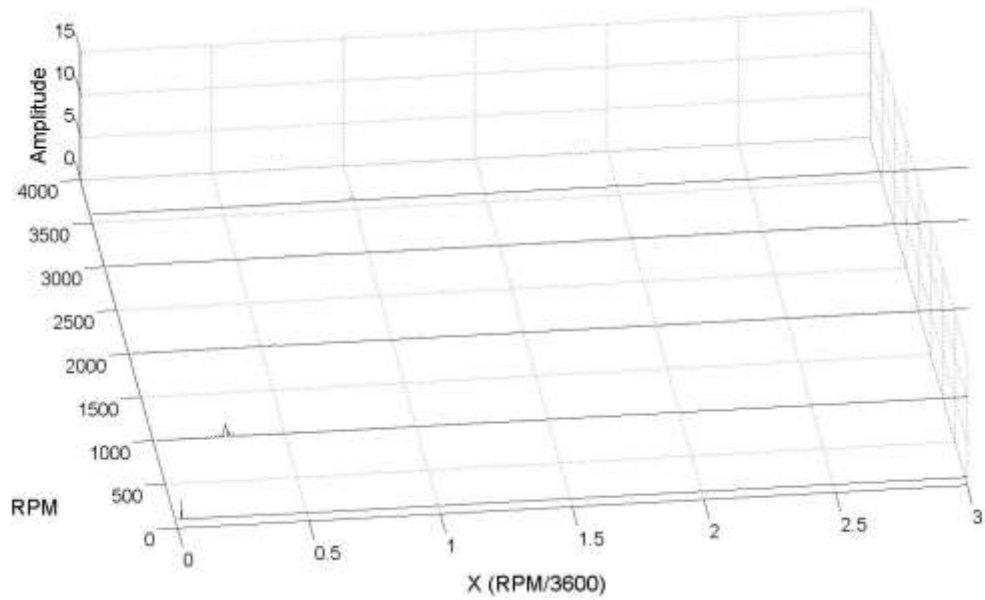


Figure 172. PP2 Waterfall Spectrum – 8 Hours

PP3 3600 RPM IMPELLER WATERFALLS AFTER 8 HOURS

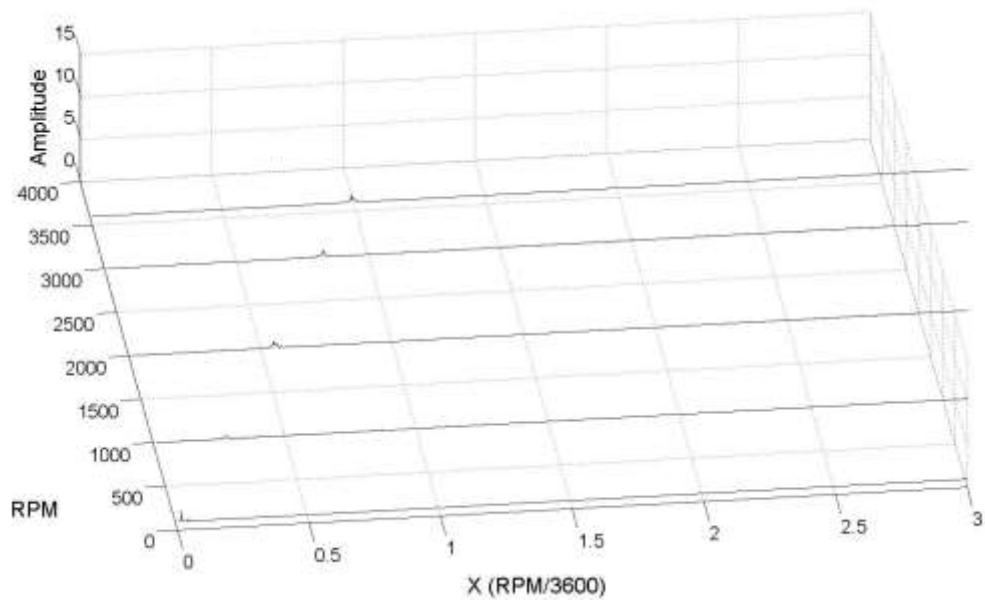


Figure 173. PP3 Waterfall Spectrum – 8 Hours

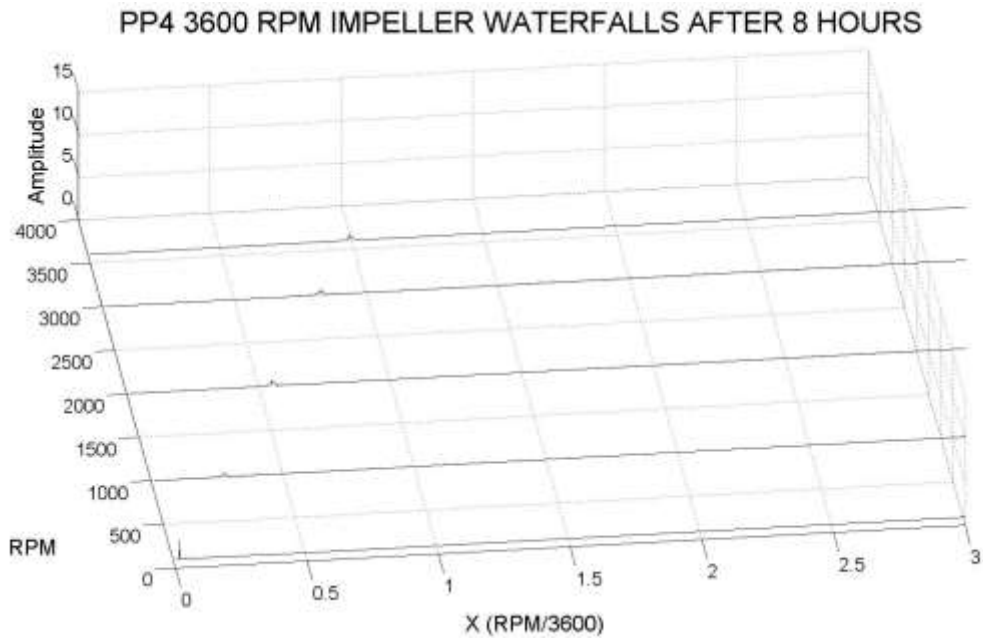


Figure 174. PP4 Waterfall Spectrum – 8 Hours

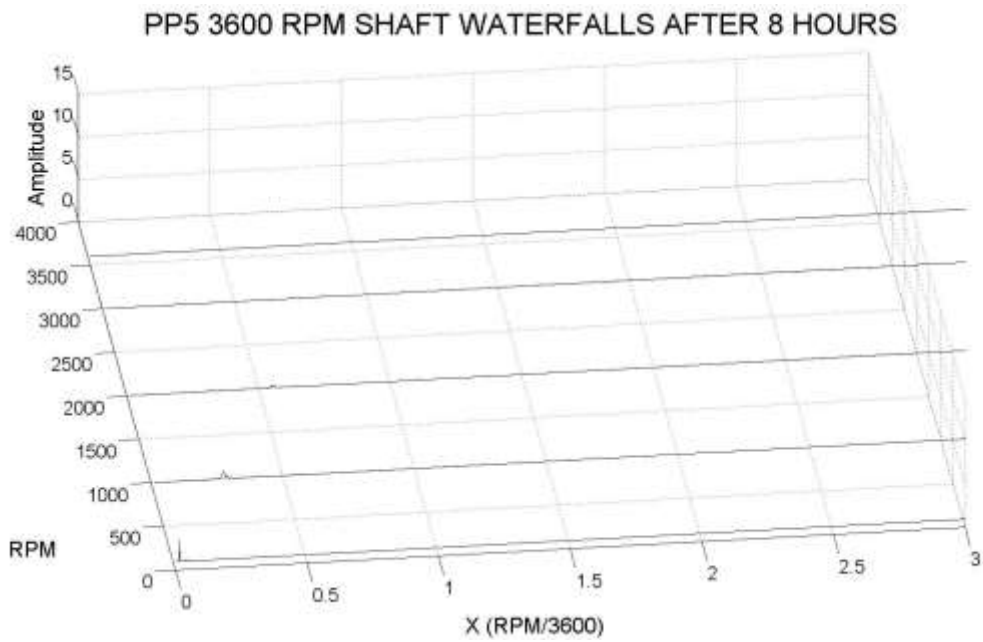


Figure 175. PP5 Waterfall Spectrum – 8 Hours

PP6 3600 RPM SHAFT WATERFALLS AFTER 8 HOURS

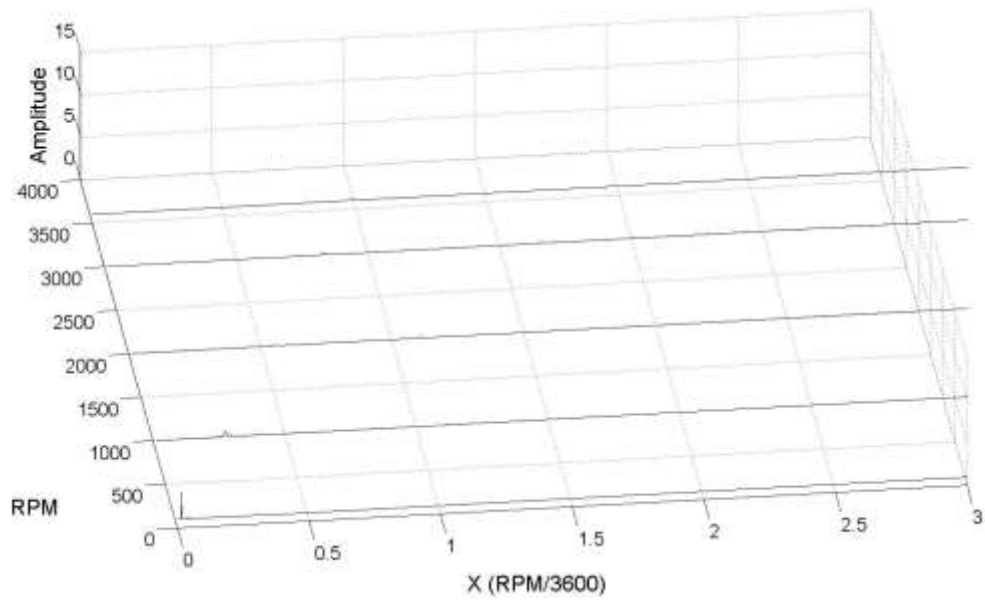


Figure 176. PP6 Waterfall Spectrum – 8 Hours

PP7 3600 RPM IMPELLER WATERFALLS AFTER 8 HOURS

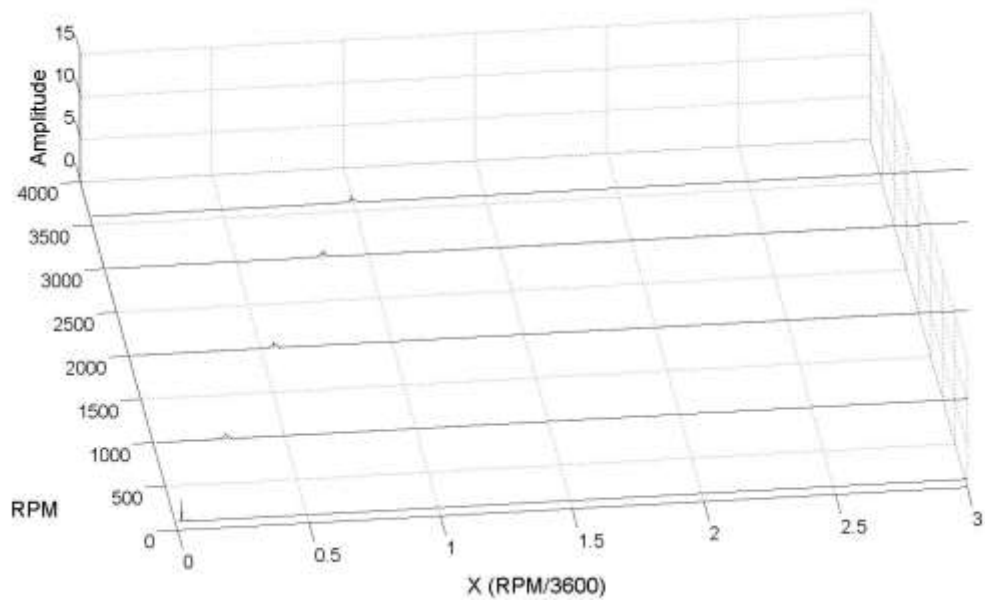


Figure 177. PP7 Waterfall Spectrum – 8 Hours

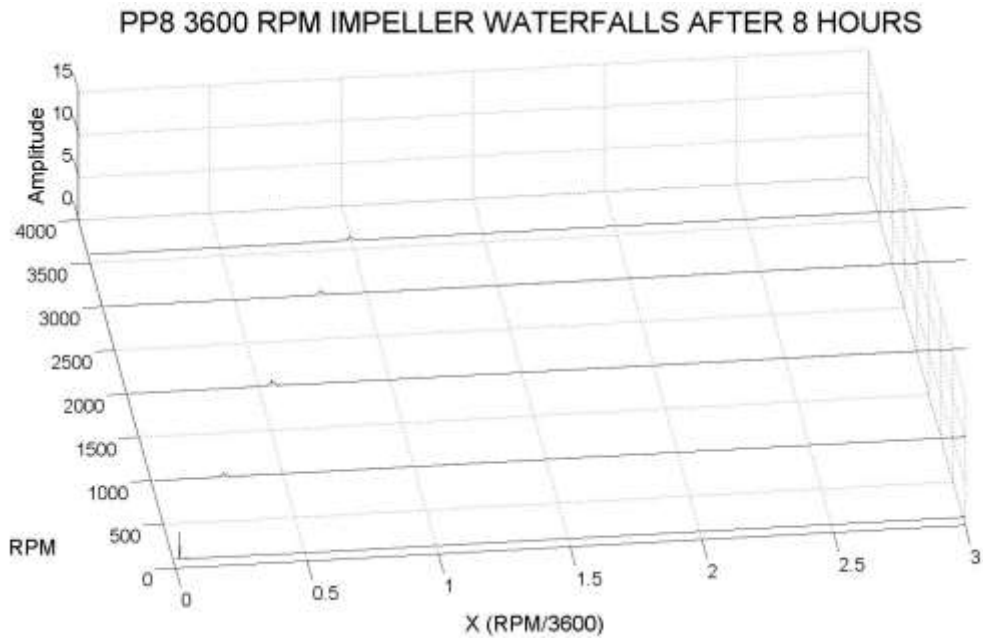


Figure 178. PP8 Waterfall Spectrum – 8 Hours

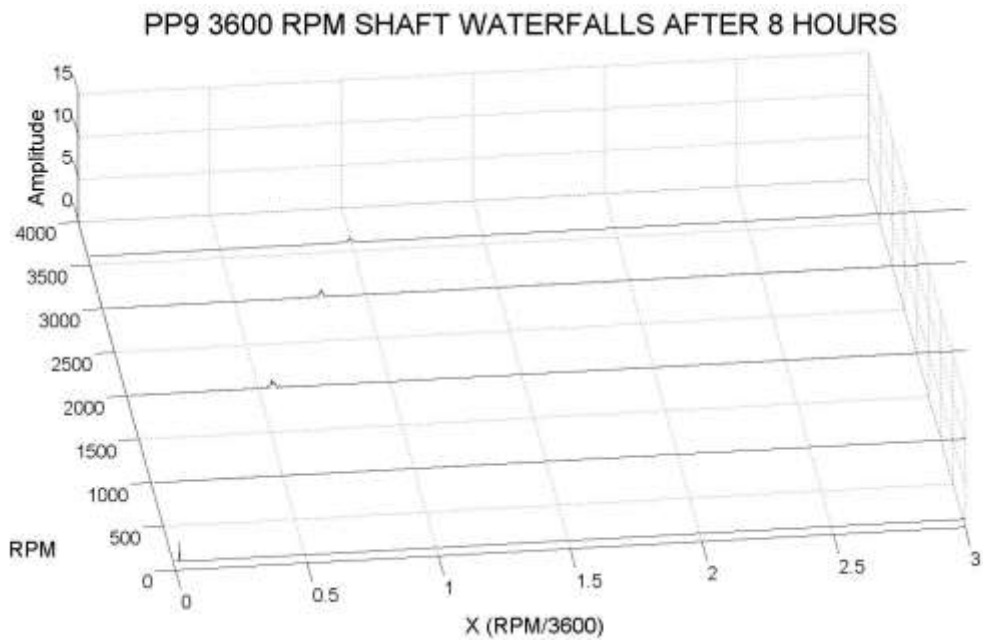


Figure 179. PP9 Waterfall Spectrum – 8 Hours

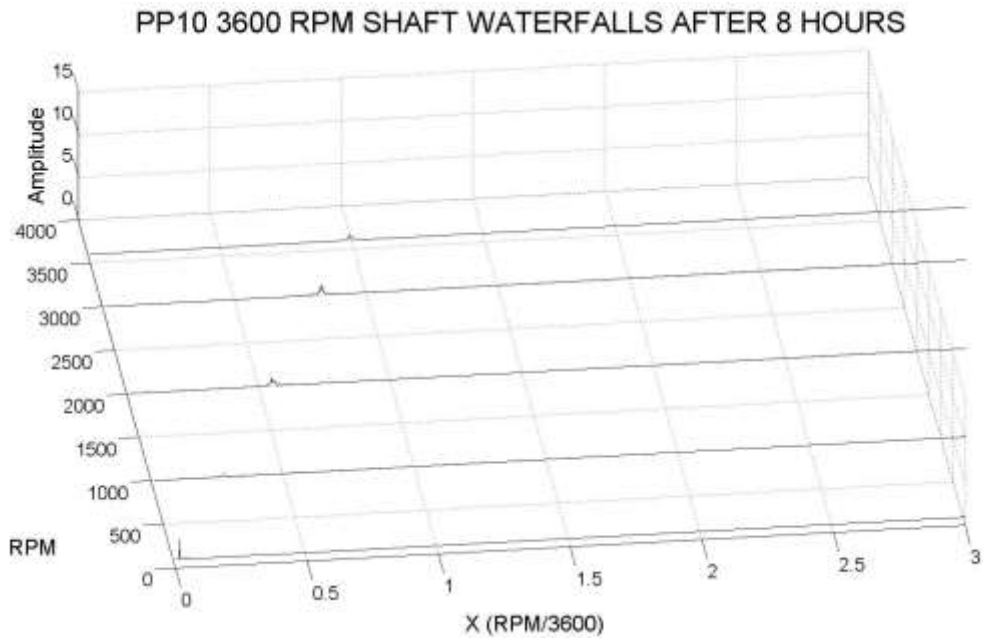


Figure 180. PP10 Waterfall Spectrum – 8 Hours

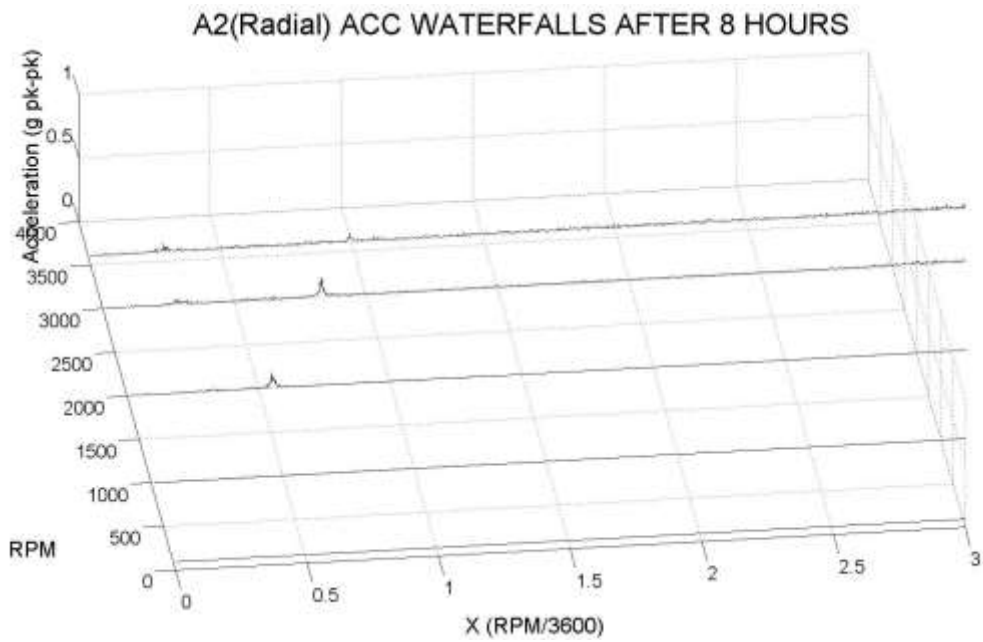


Figure 181. Inlet Accelerometer Radial Waterfall Spectrum – 8 Hours

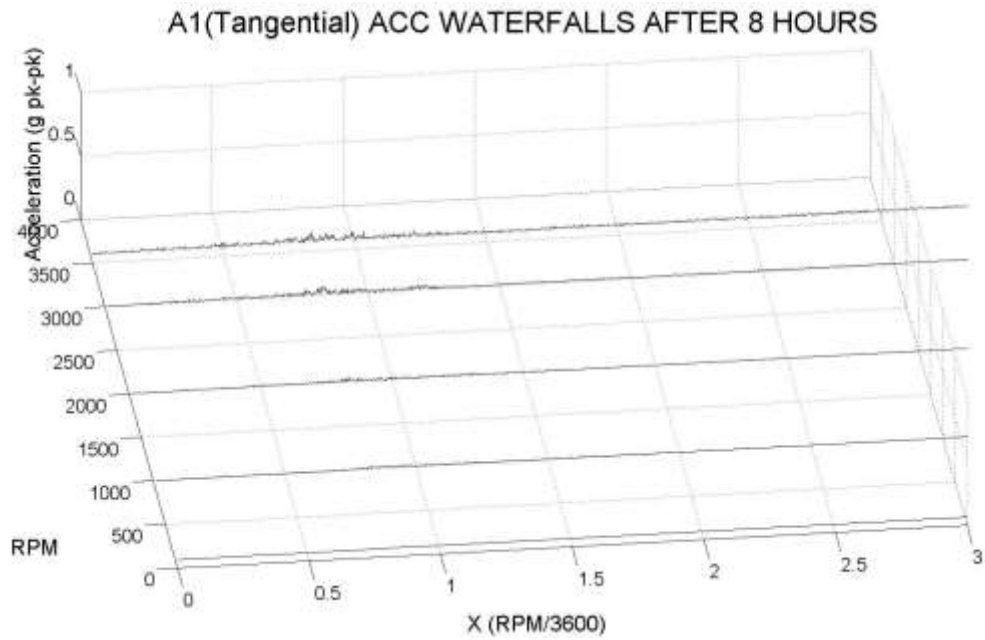


Figure 182. Inlet Accelerometer Tangential Waterfall Spectrum – 8 Hours

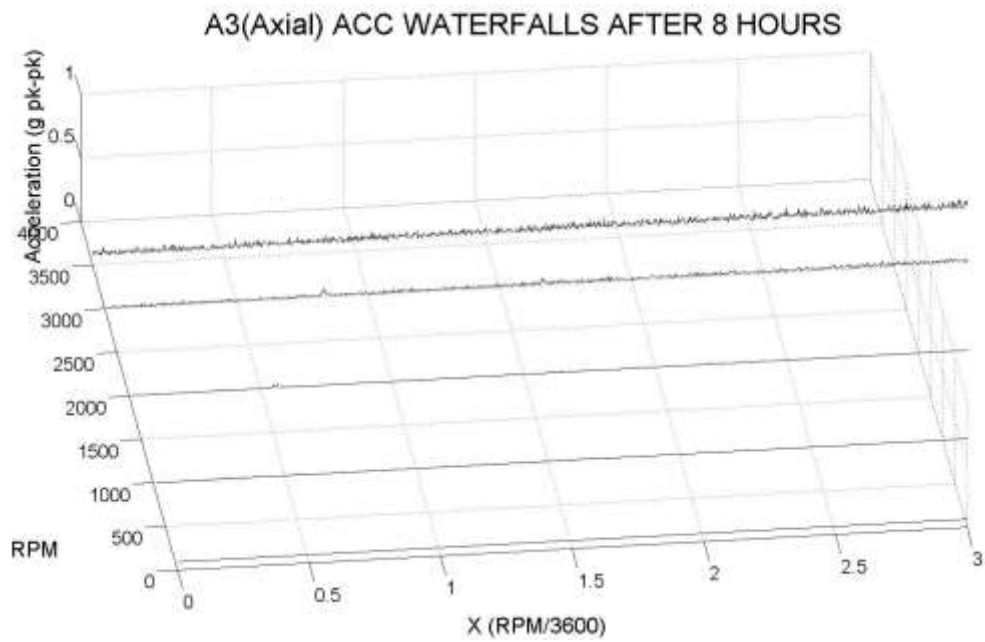


Figure 183. Inlet Accelerometer Axial Waterfall Spectrum – 8 Hours

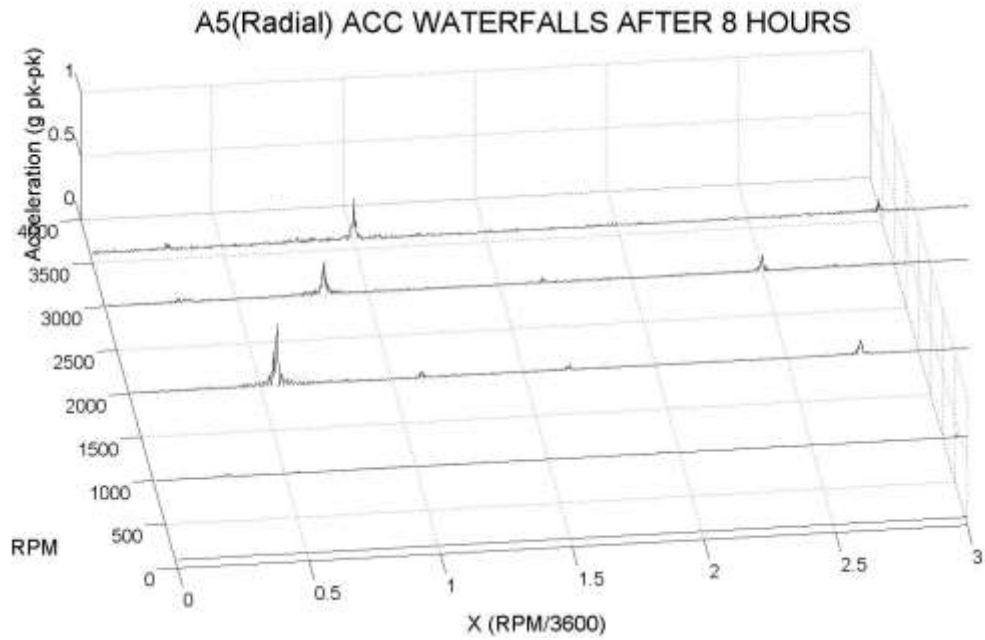


Figure 184. Outlet Accelerometer Radial Waterfall Spectrum – 8 Hours

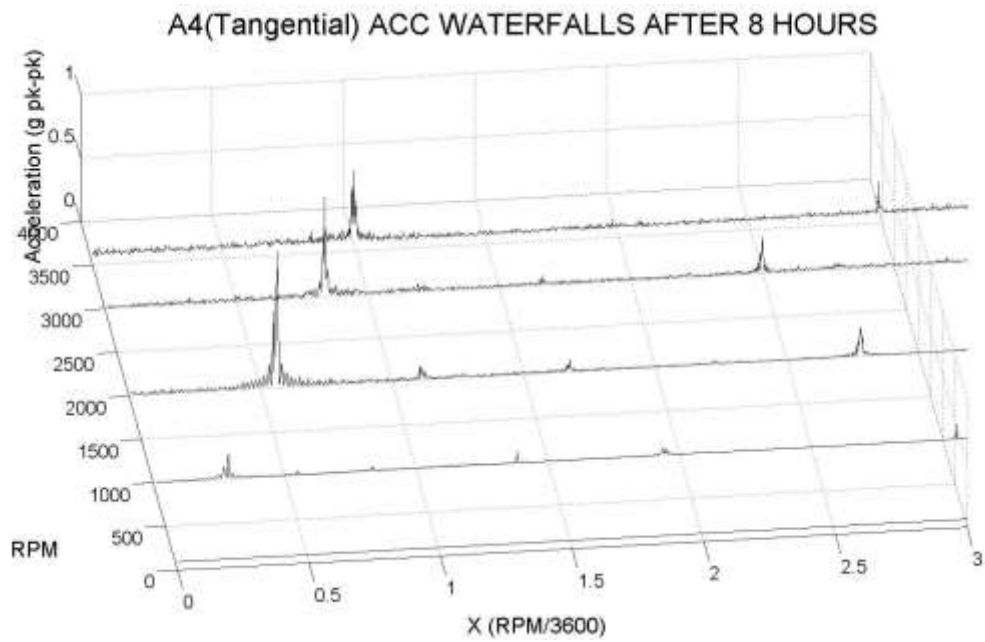


Figure 185. Outlet Accelerometer Tangential Waterfall Spectrum – 8 Hours

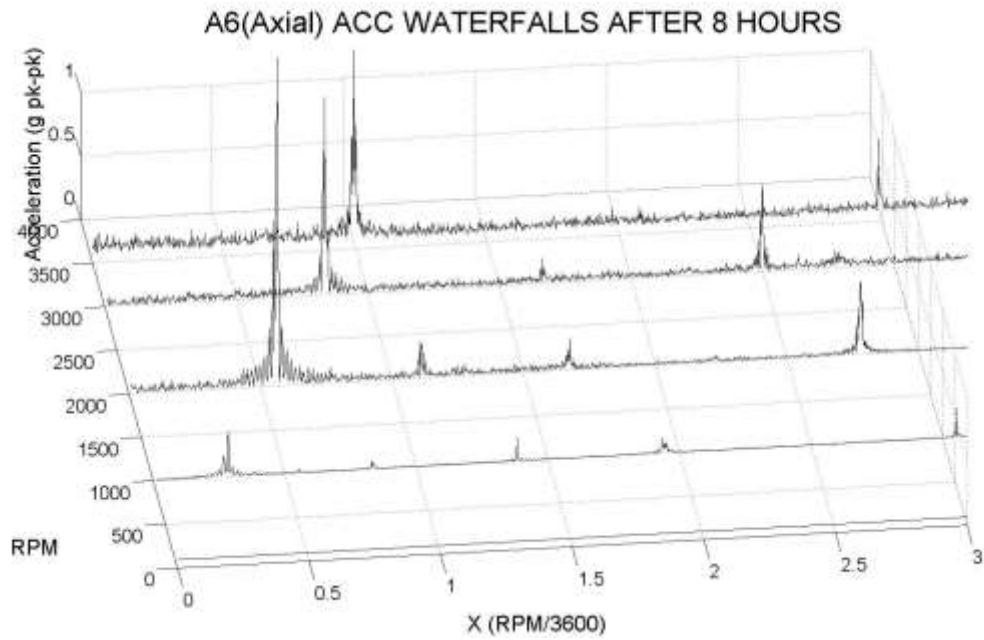


Figure 186. Outlet Accelerometer Axial Waterfall Spectrum – 8 Hours

D.3. 24 Hours

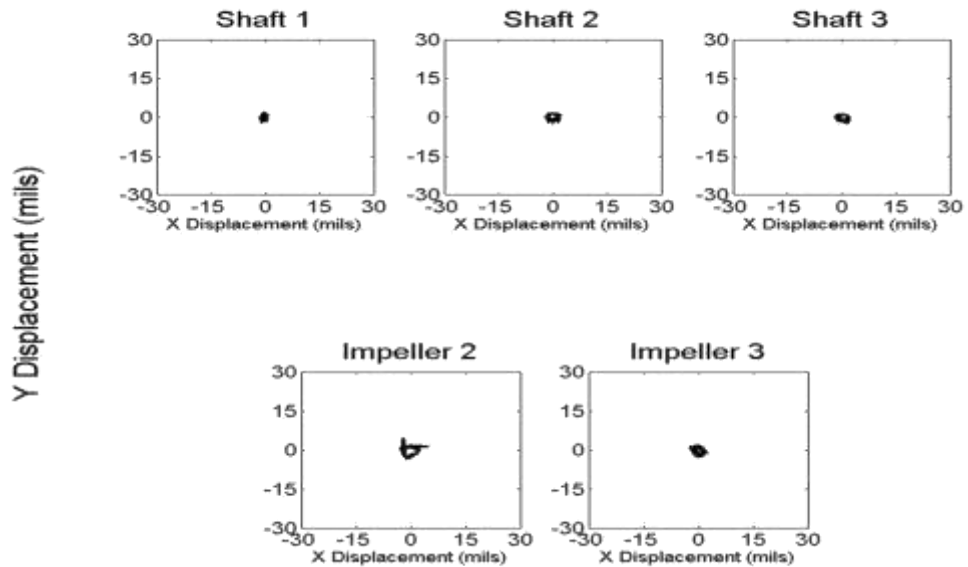
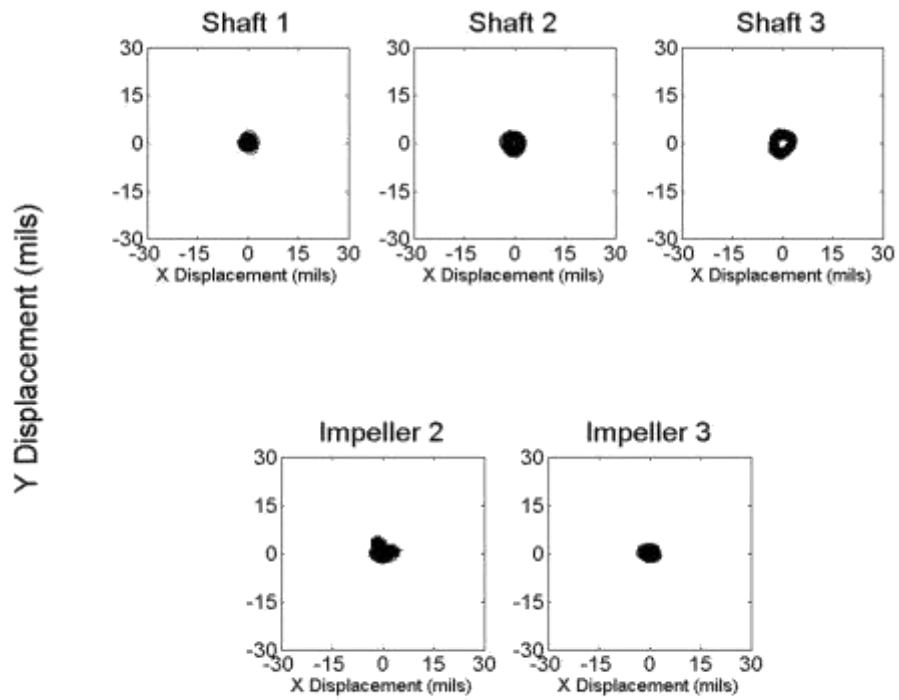


Figure 187. Orbit at 90 RPM – 24 Hours



24

Figure 188. Orbit at 3600 RPM – 24 Hours

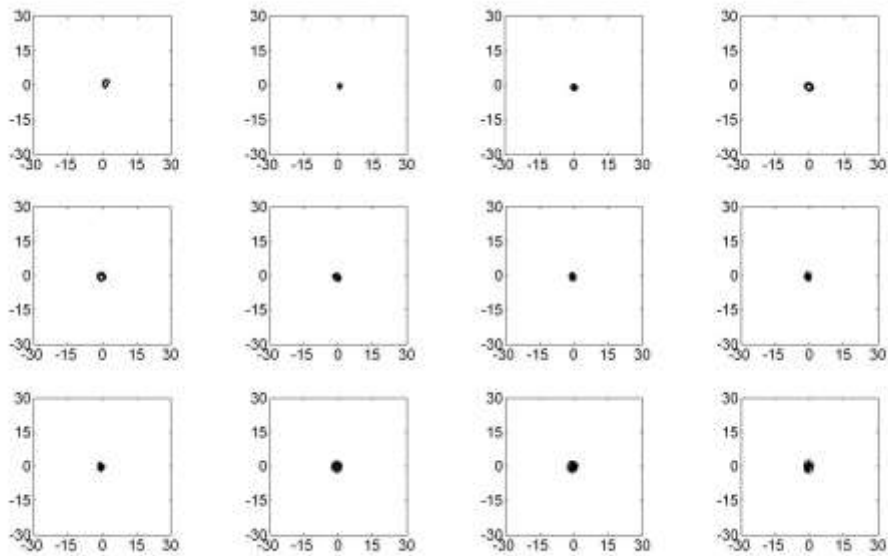


Figure 189. Shaft 1 Ramp Up Orbit – 24 Hours

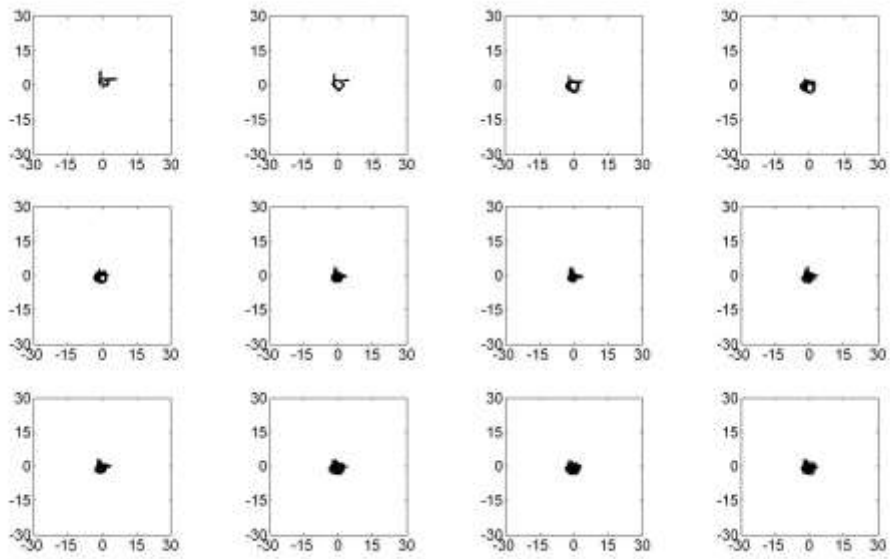


Figure 190. Impeller 2 Ramp Up Orbit – 24 Hours

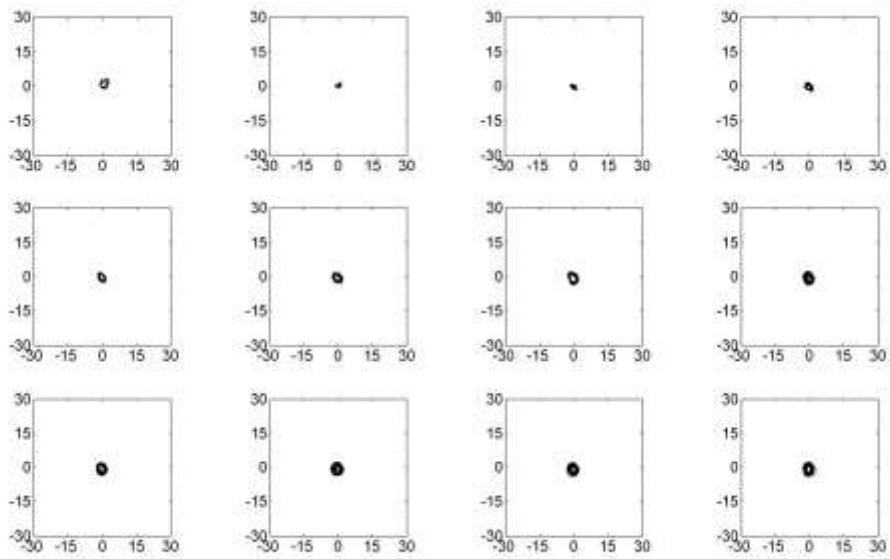


Figure 191. Shaft 2 Ramp Up Orbit – 24 Hours

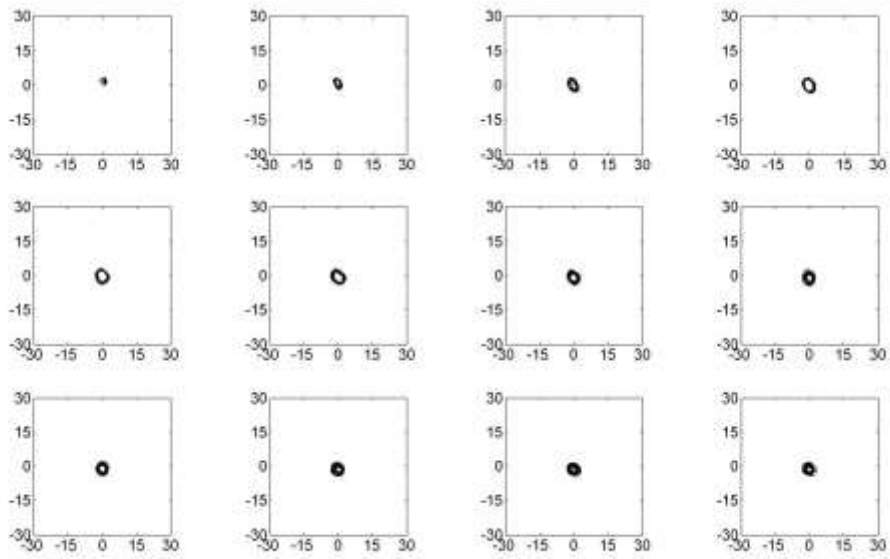


Figure 192. Impeller 2 Ramp Up Orbit – 24 Hours

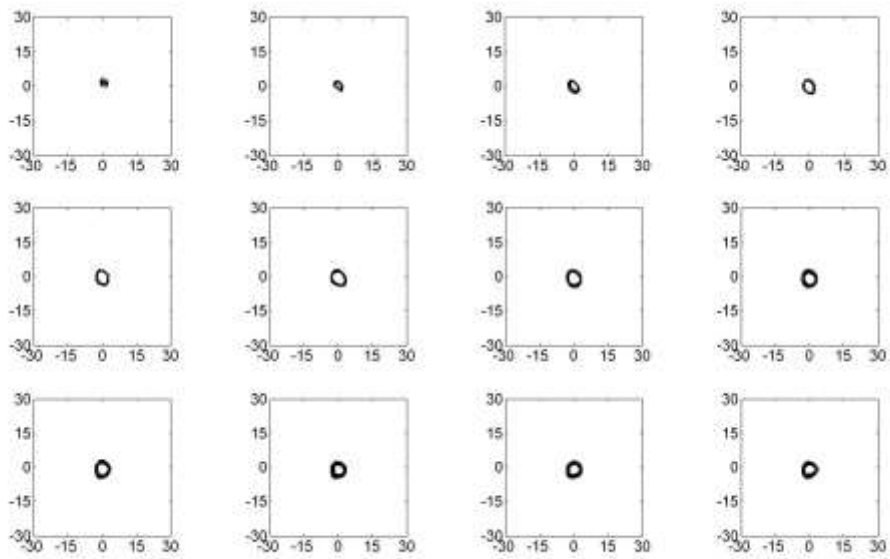


Figure 193. Shaft 3 Ramp Up Orbit – 24 Hours

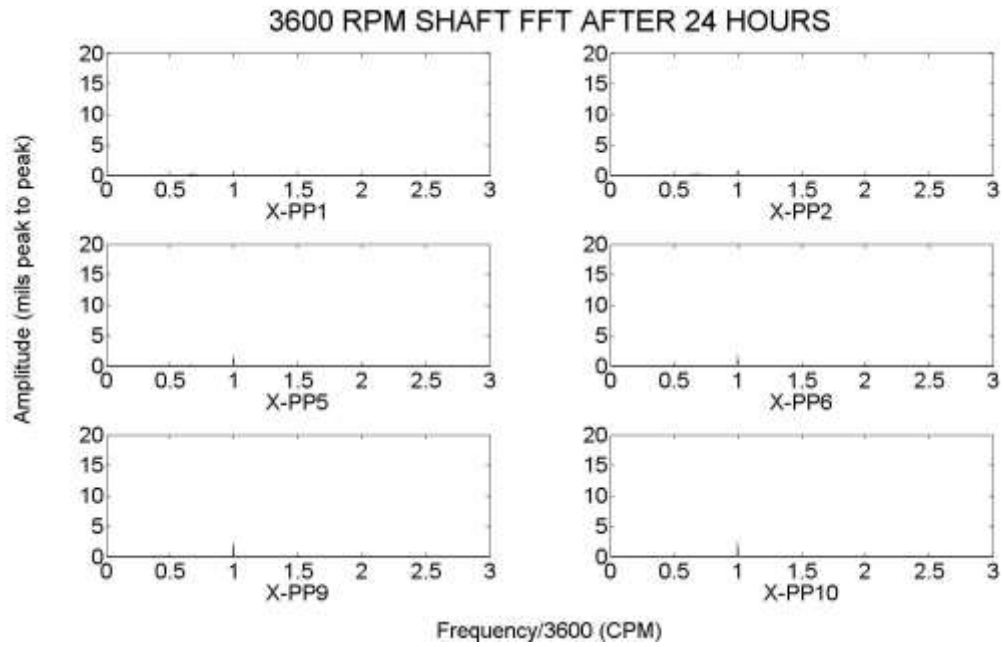


Figure 194. Shaft FFT – 24 Hours

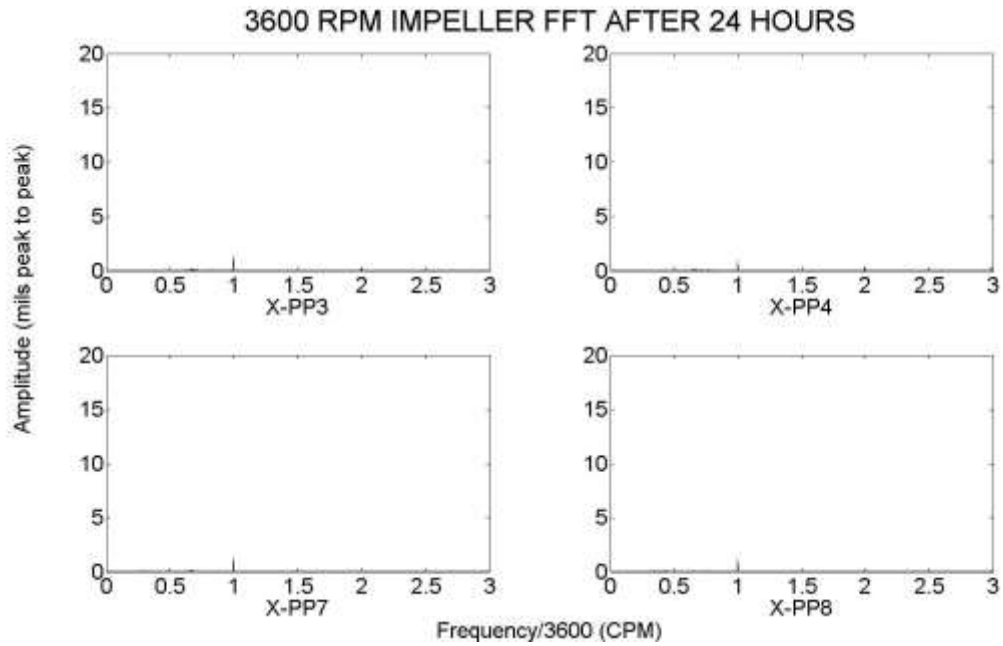


Figure 195. Impeller FFT – 24 Hours

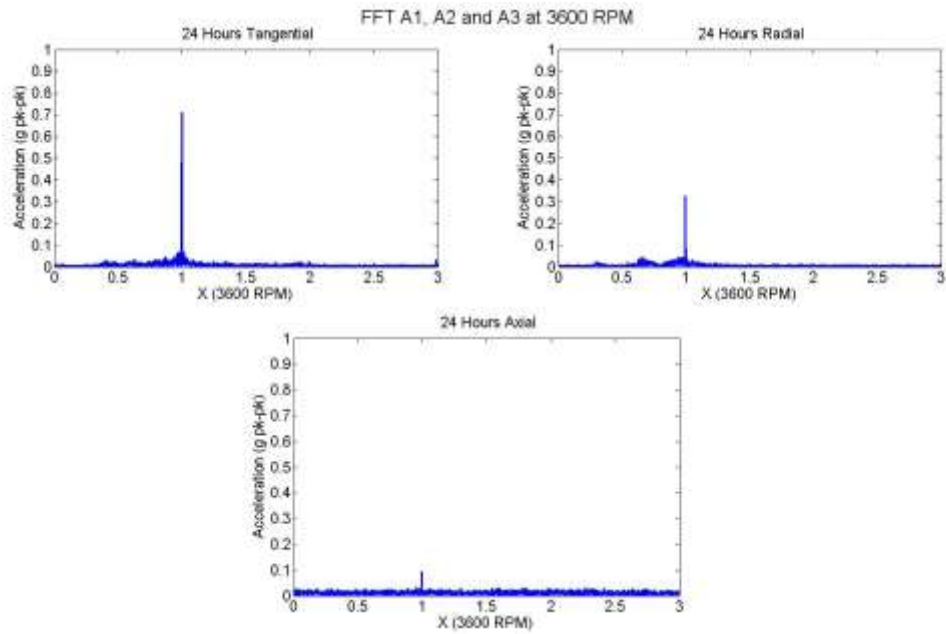


Figure 196. Inlet Accelerometer FFT – 24 Hours

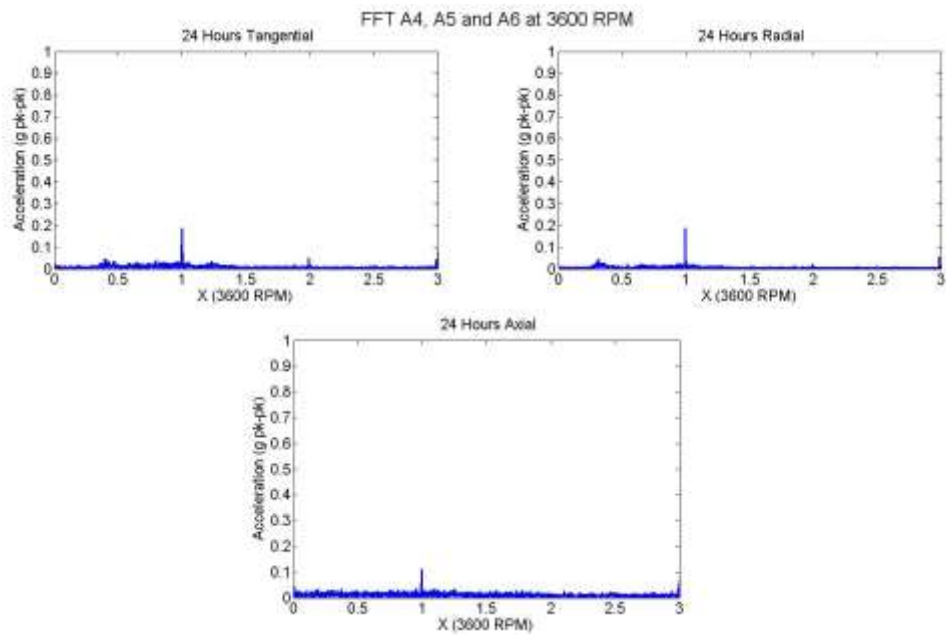


Figure 197. Outlet Accelerometer FFT – 24 Hours

PP1 3600 RPM SHAFT WATERFALLS AFTER 24 HOURS

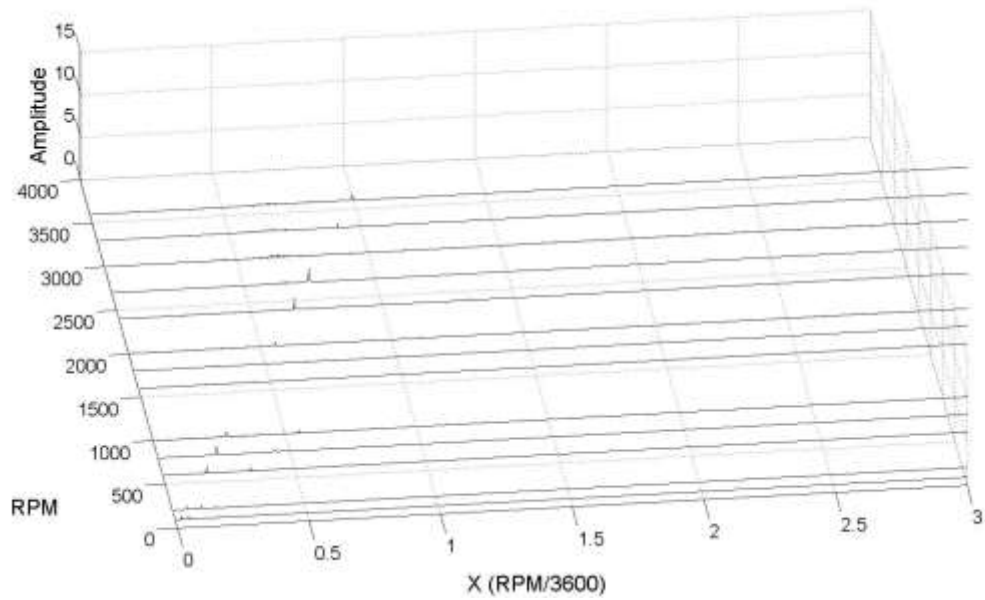


Figure 198. PP1 Waterfall Spectrum – 24 Hours

PP2 3600 RPM SHAFT WATERFALLS AFTER 24 HOURS

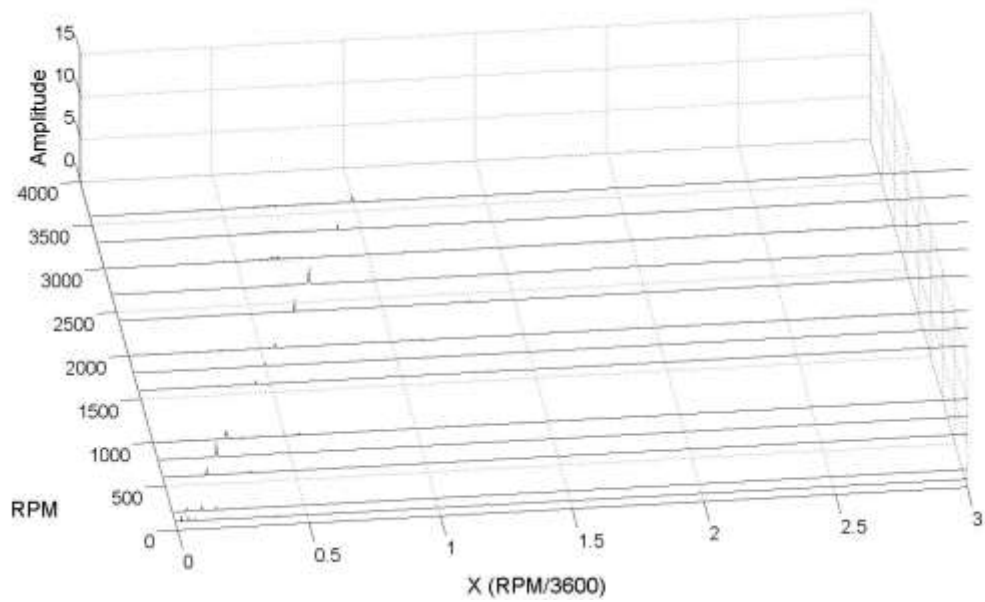


Figure 199. PP2 Waterfall Spectrum – 24 Hours

PP3 3600 RPM IMPELLER WATERFALLS AFTER 24 HOURS

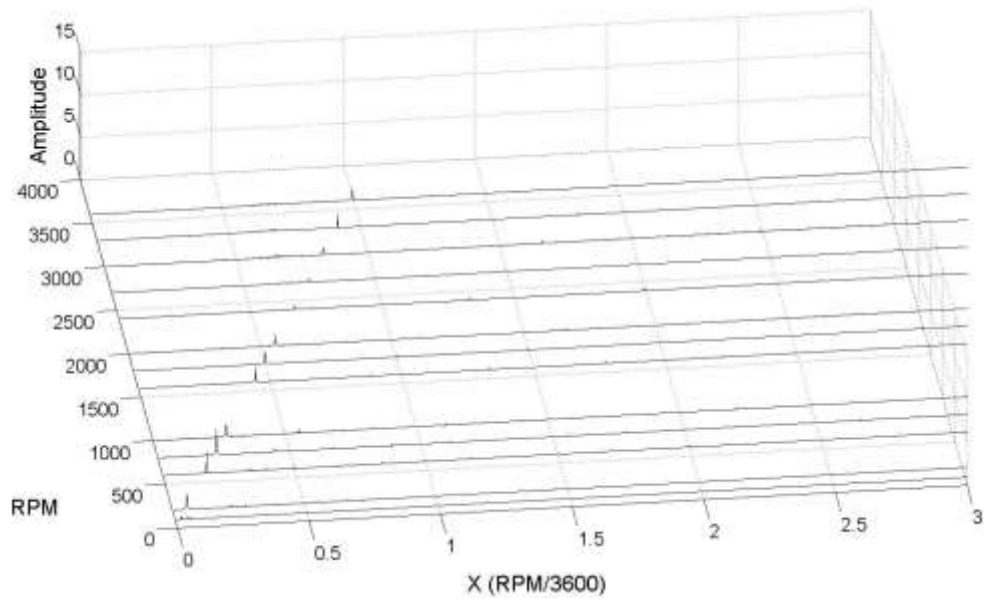


Figure 200. PP3 Waterfall Spectrum – 24 Hours

PP4 3600 RPM IMPELLER WATERFALLS AFTER 24 HOURS

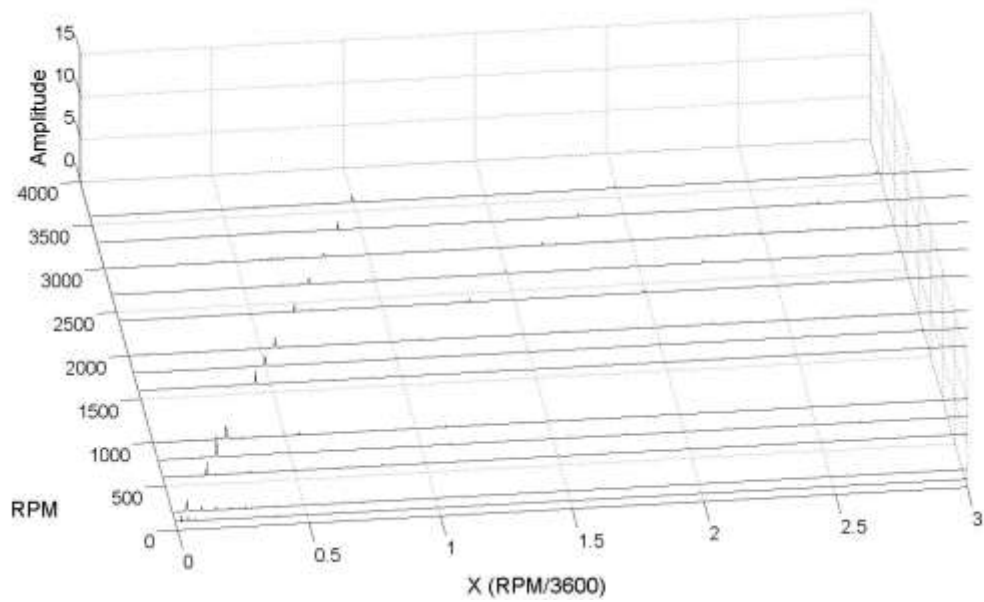


Figure 201. PP4 Waterfall Spectrum – 24 Hours

PP5 3600 RPM SHAFT WATERFALLS AFTER 24 HOURS

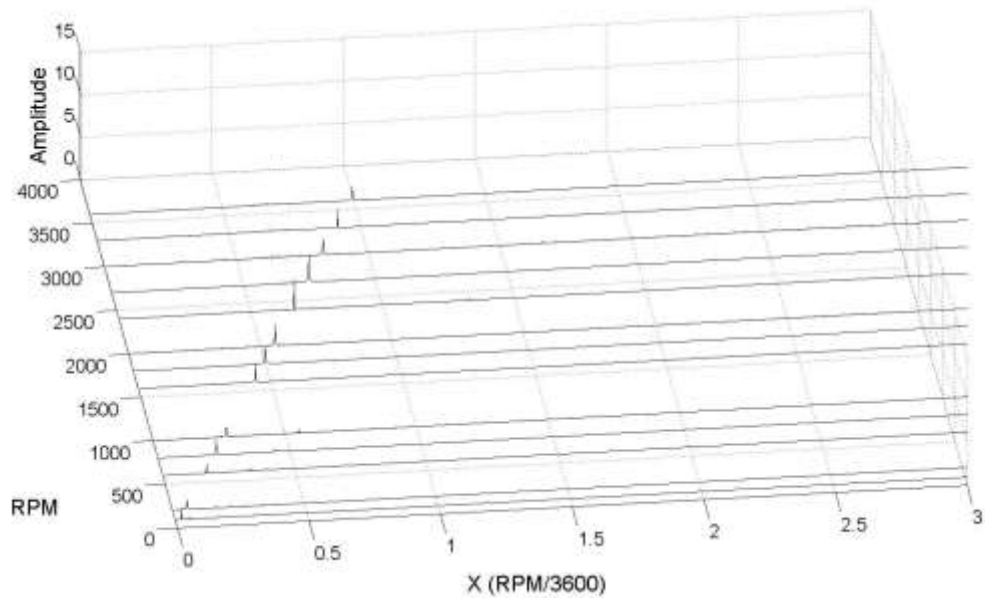


Figure 202. PP5 Waterfall Spectrum – 24 Hours

PP6 3600 RPM SHAFT WATERFALLS AFTER 24 HOURS

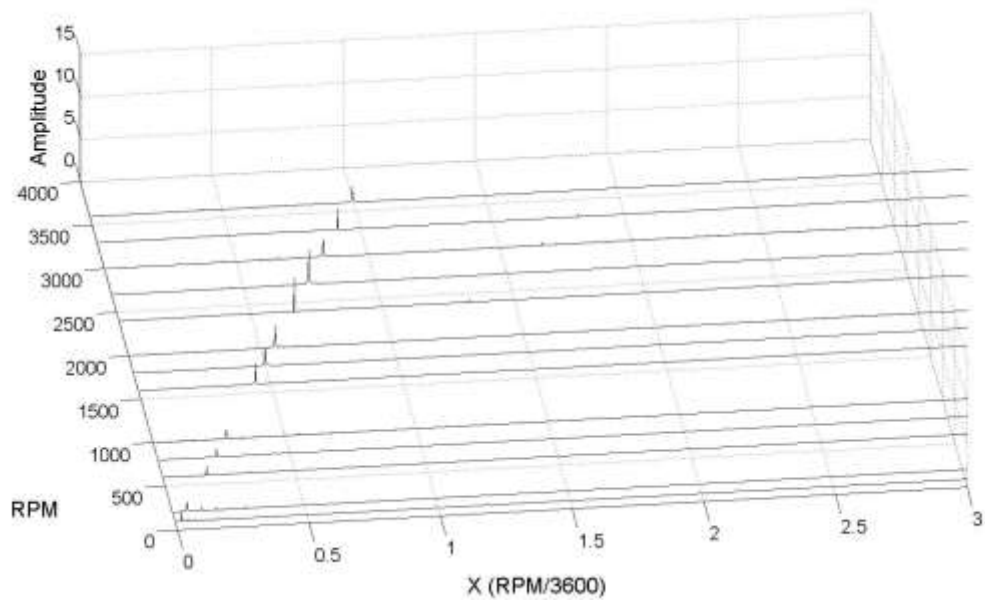


Figure 203. PP6 Waterfall Spectrum – 24 Hours

PP7 3600 RPM IMPELLER WATERFALLS AFTER 24 HOURS

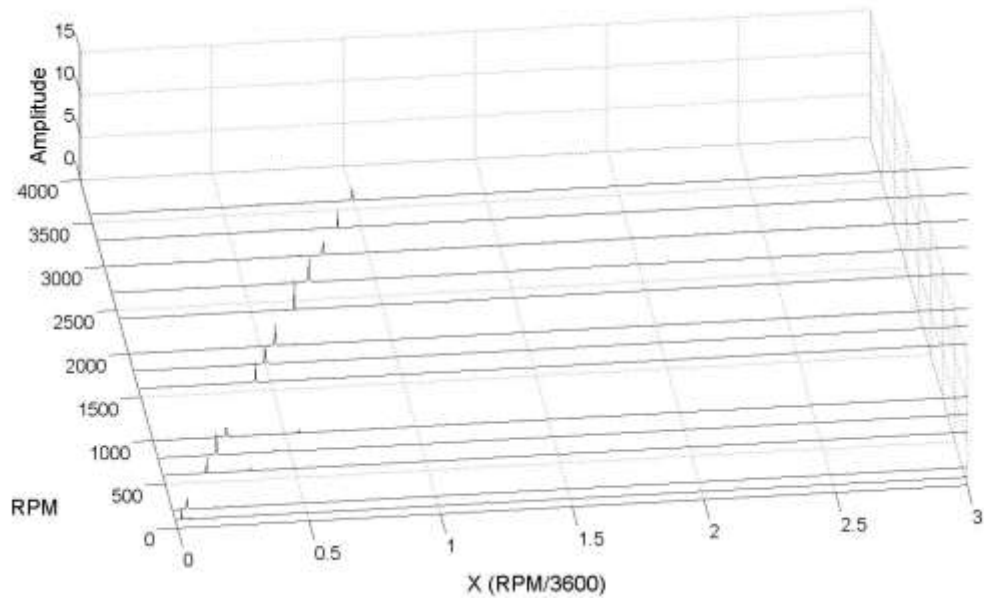


Figure 204. PP7 Waterfall Spectrum – 24 Hours

PP8 3600 RPM IMPELLER WATERFALLS AFTER 24 HOURS

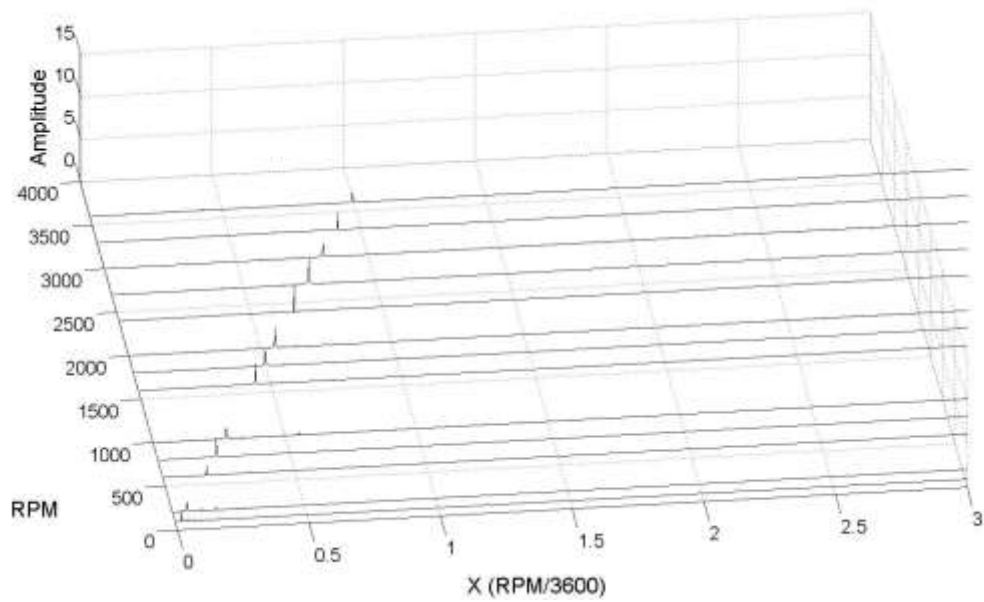


Figure 205. PP8 Waterfall Spectrum – 24 Hours

PP9 3600 RPM SHAFT WATERFALLS AFTER 24 HOURS

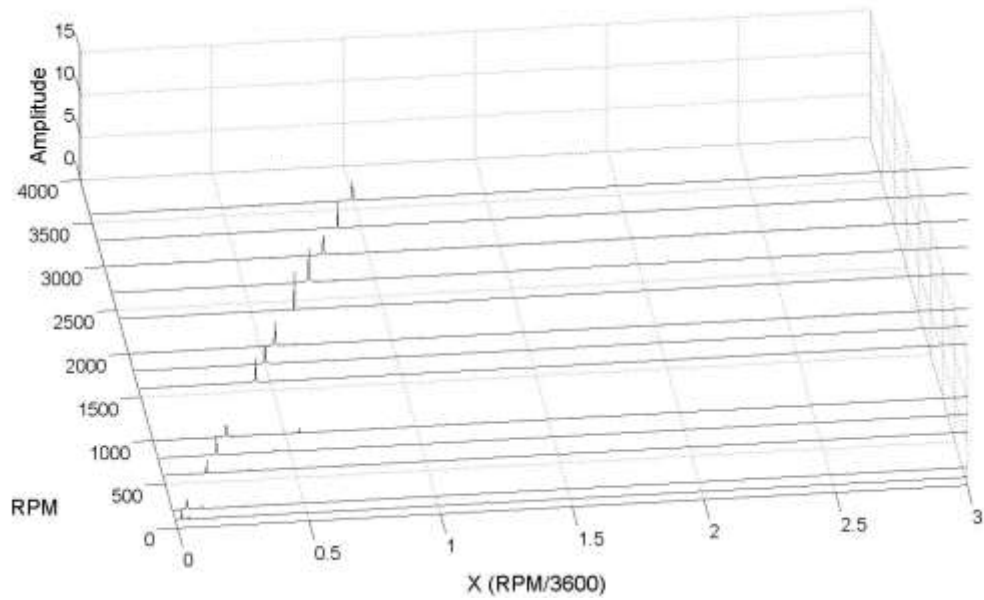


Figure 206. PP9 Waterfall Spectrum – 24 Hours

PP10 3600 RPM SHAFT WATERFALLS AFTER 24 HOURS

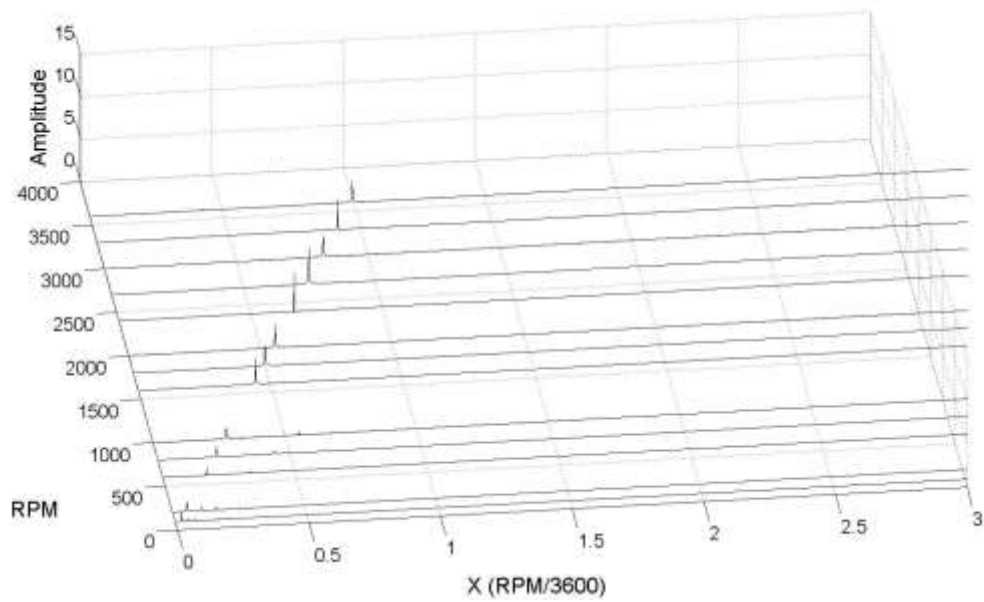


Figure 207. PP10 Waterfall Spectrum – 24 Hours

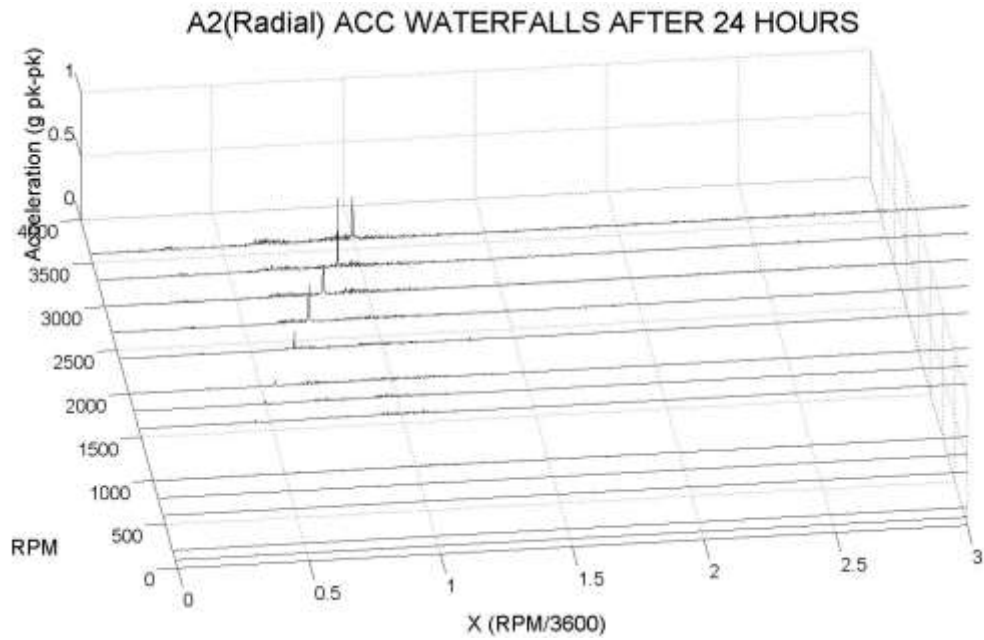


Figure 208. Inlet Accelerometer Radial Waterfall Spectrum – 24 Hours

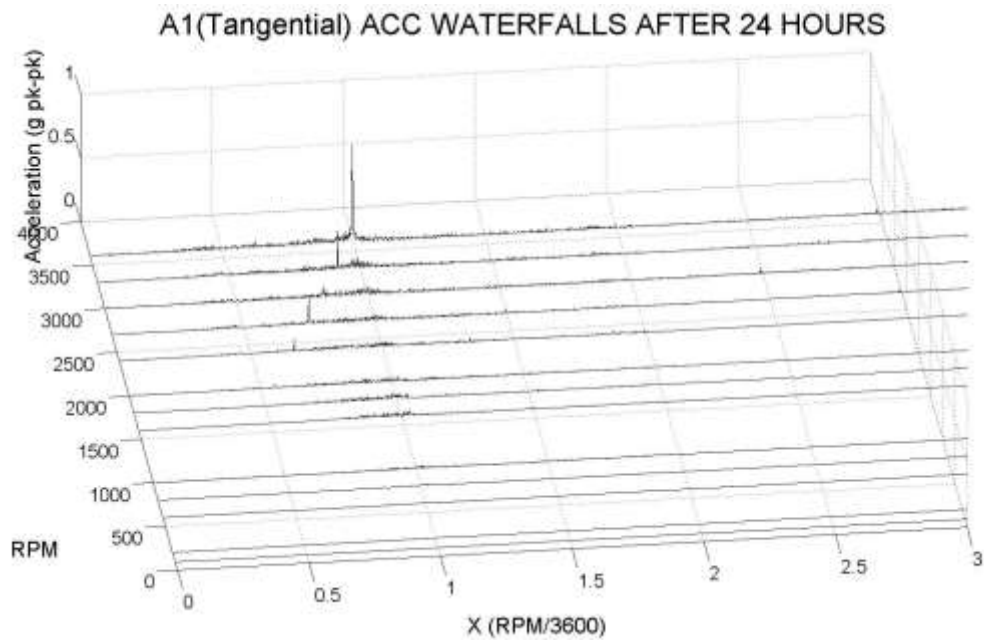


Figure 209. Inlet Accelerometer Tangential Waterfall Spectrum – 24 Hours

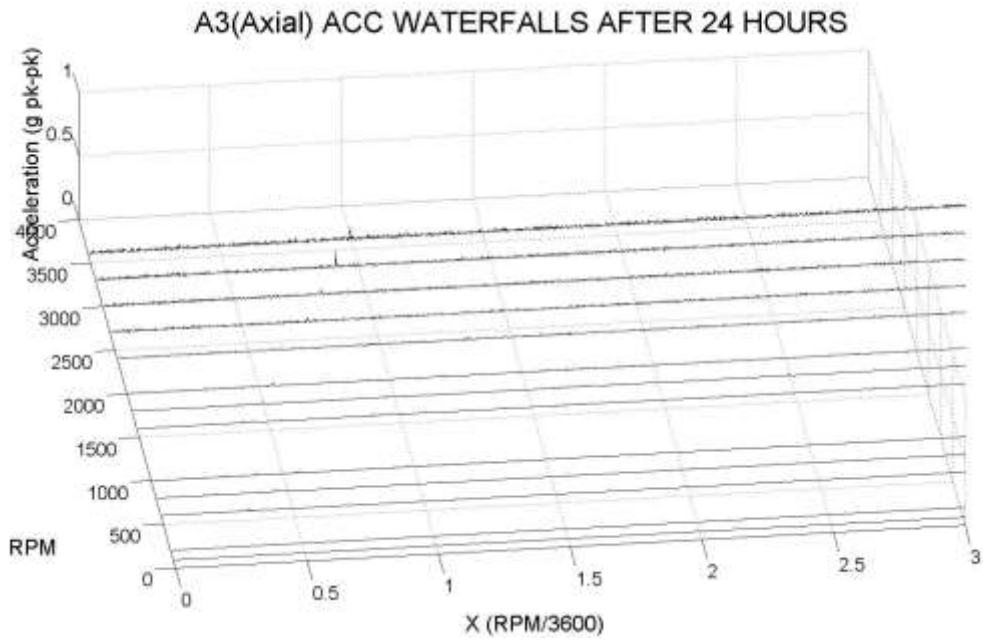


Figure 210. Inlet Accelerometer Axial Waterfall Spectrum – 24 Hours

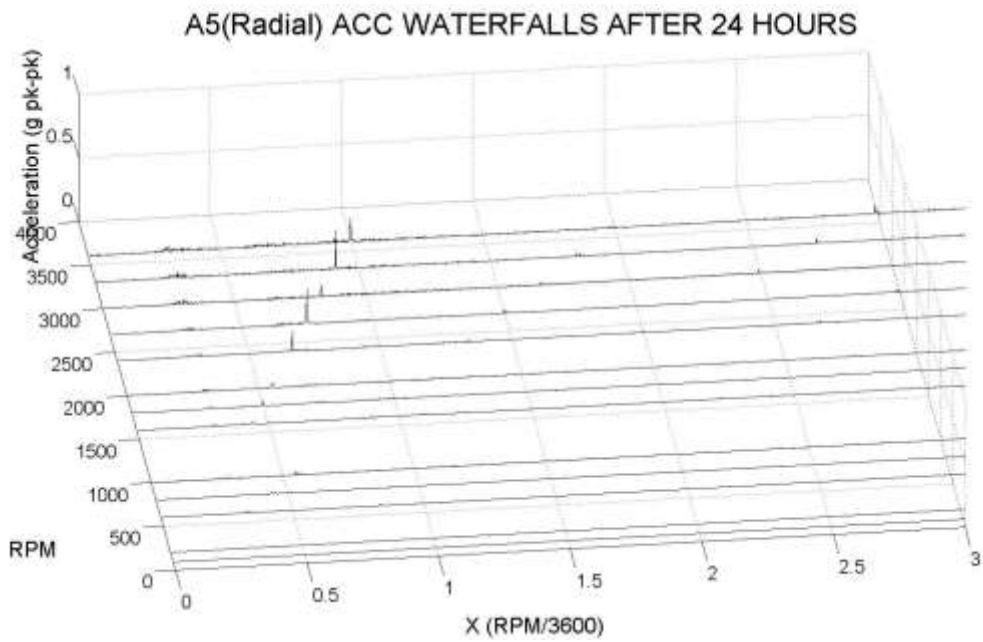


Figure 211. Outlet Accelerometer Radial Waterfall Spectrum – 24 Hours

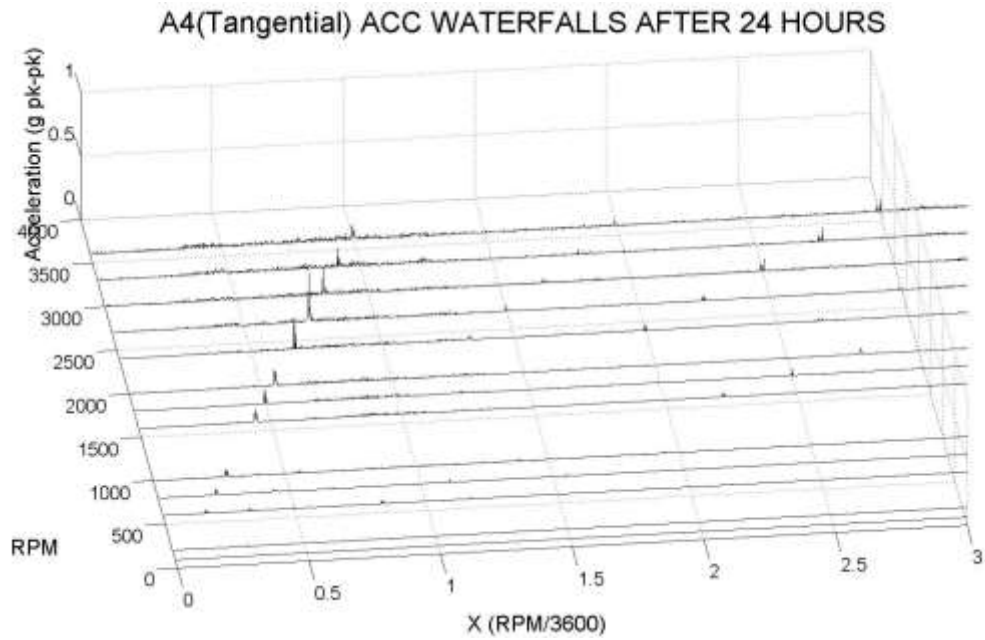


Figure 212. Outlet Accelerometer Tangential Waterfall Spectrum – 24 Hours

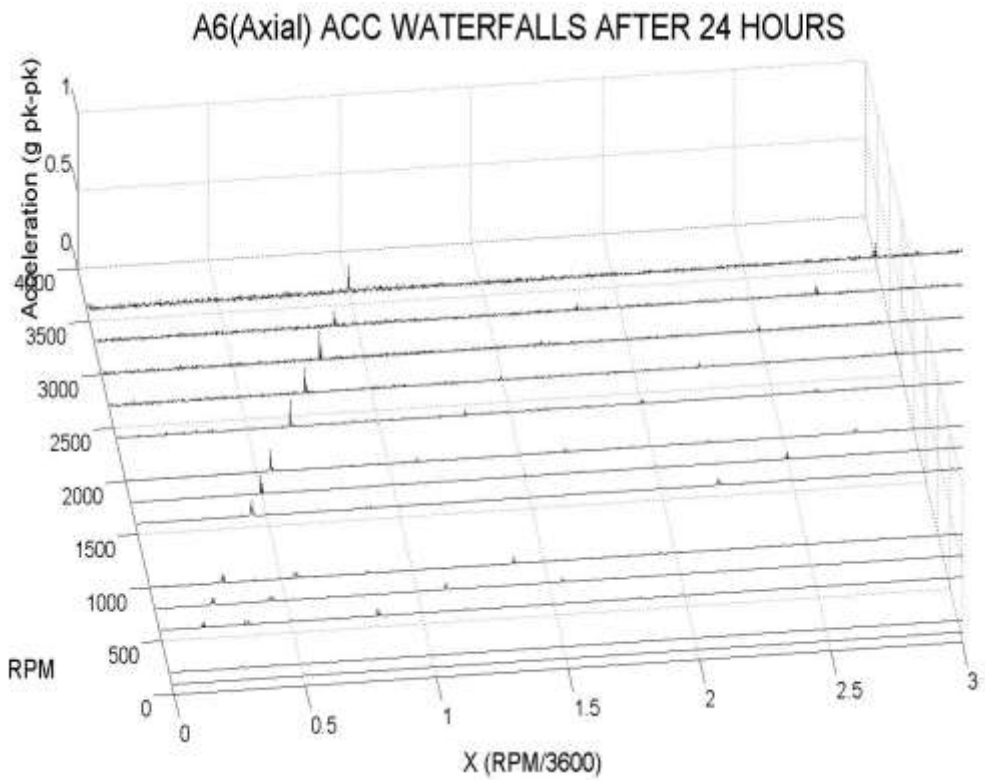


Figure 213. Outlet Accelerometer Axial Waterfall Spectrum – 24 Hours

D.4. 52 Hours

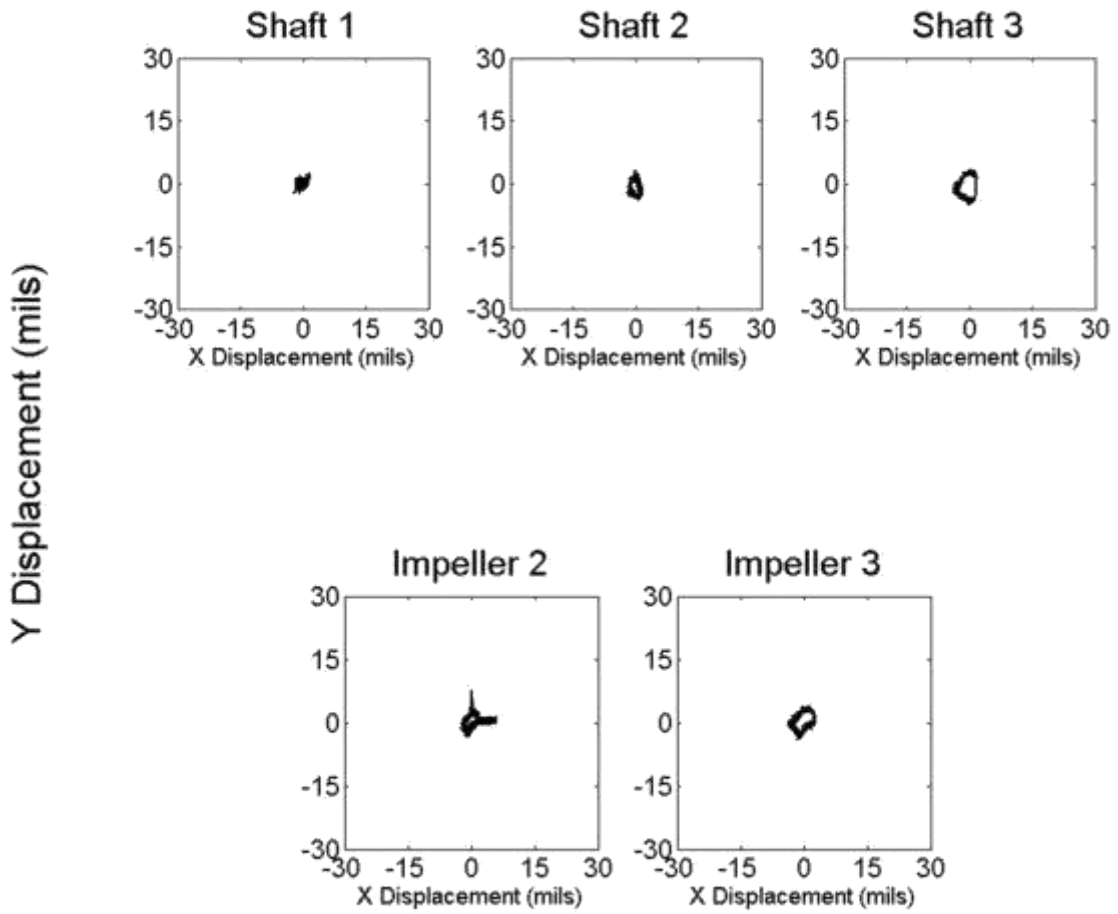


Figure 214. Orbit at 90 RPM – 52 Hours

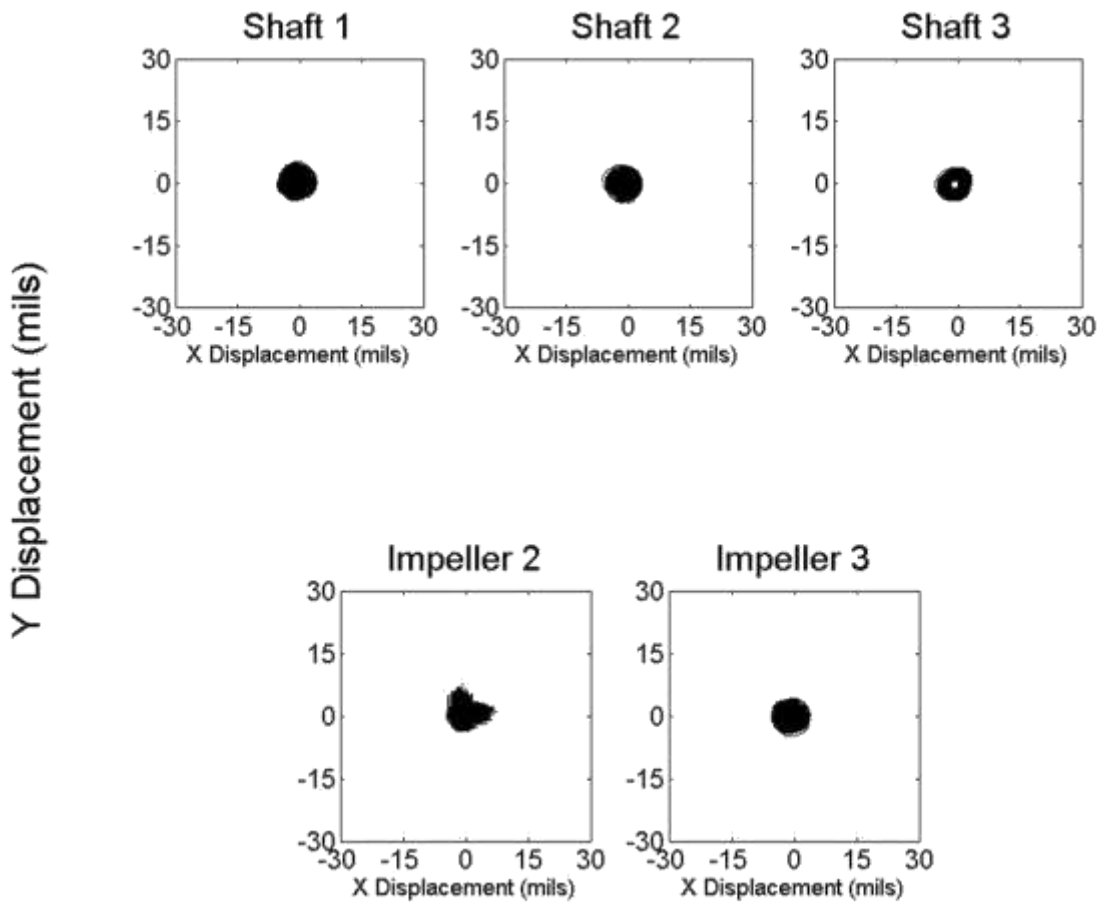


Figure 215. Orbit at 3600 RPM – 52 Hours

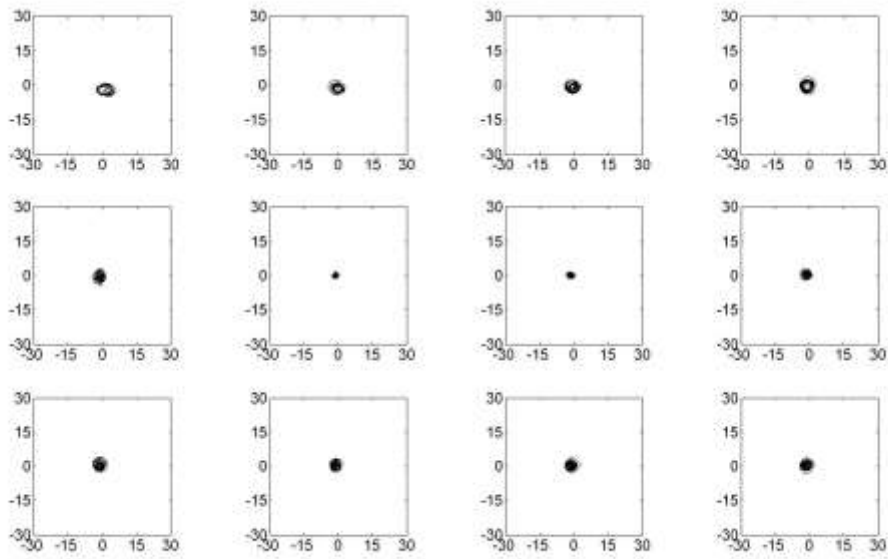


Figure 216. Shaft 1 Ramp Up Orbit – 52 Hours

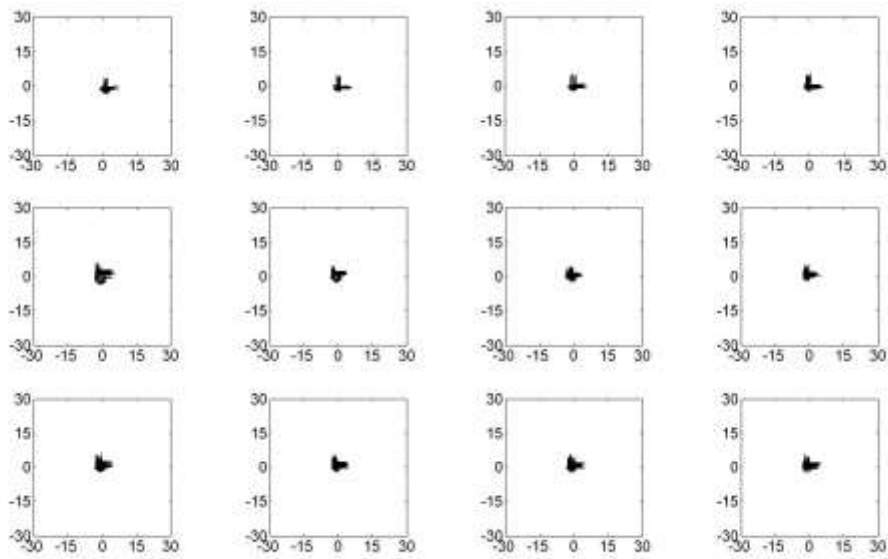


Figure 217. Impeller 2 Ramp Up Orbit – 52 Hours

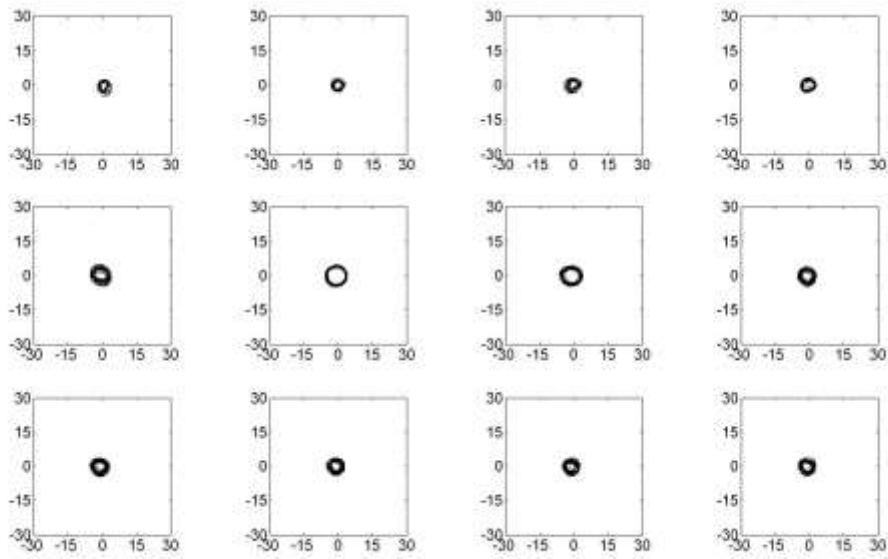


Figure 218. Shaft 2 Ramp Up Orbit – 52 Hours

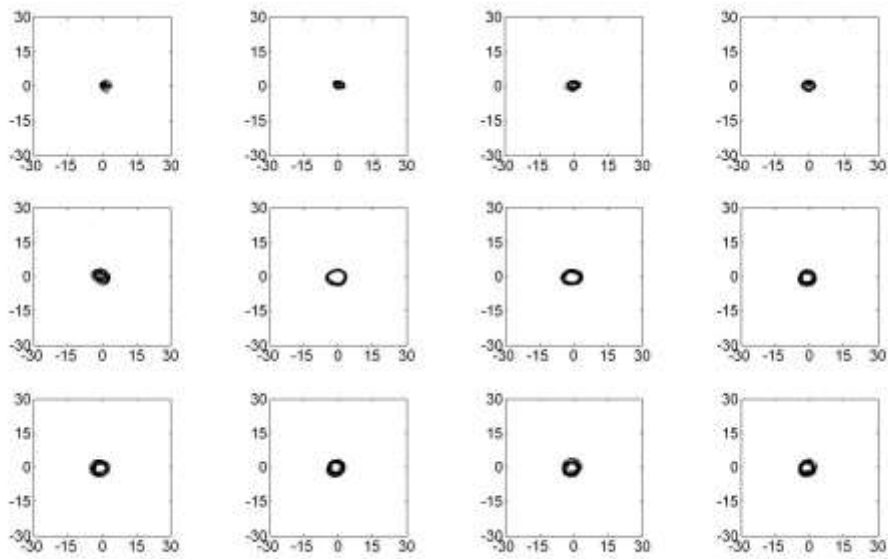


Figure 219. Impeller 3 Ramp Up Orbit – 52 Hours

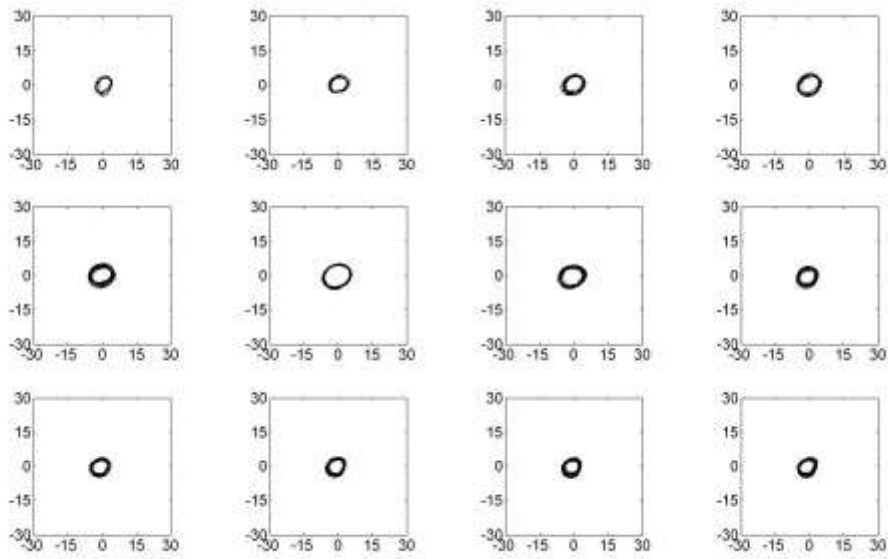


Figure 220. Shaft 3 Ramp Up Orbit – 52 Hours

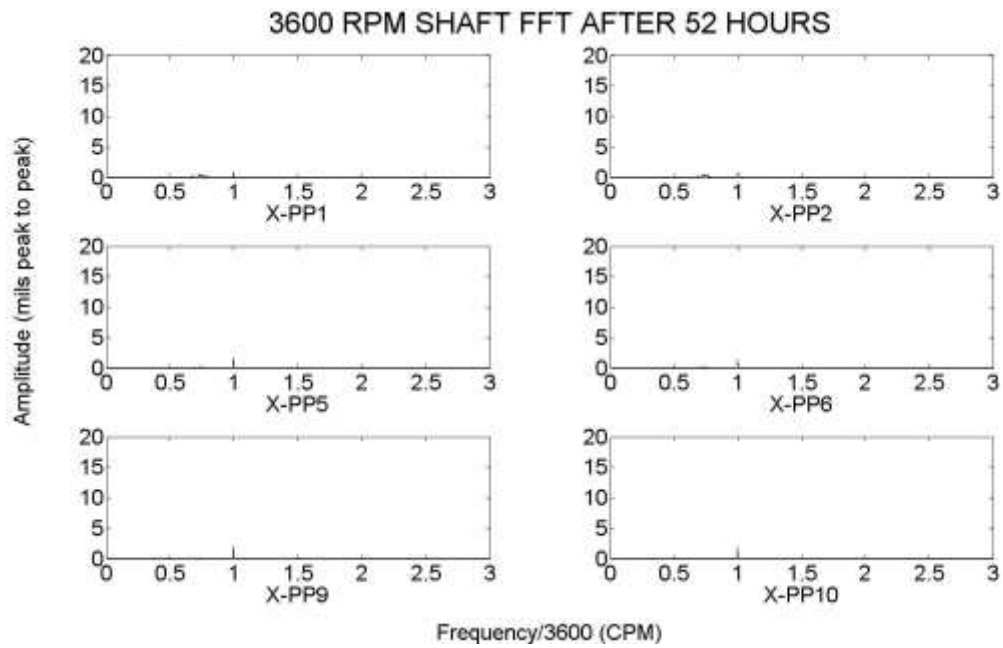


Figure 221. Shaft FFT – 52 Hours

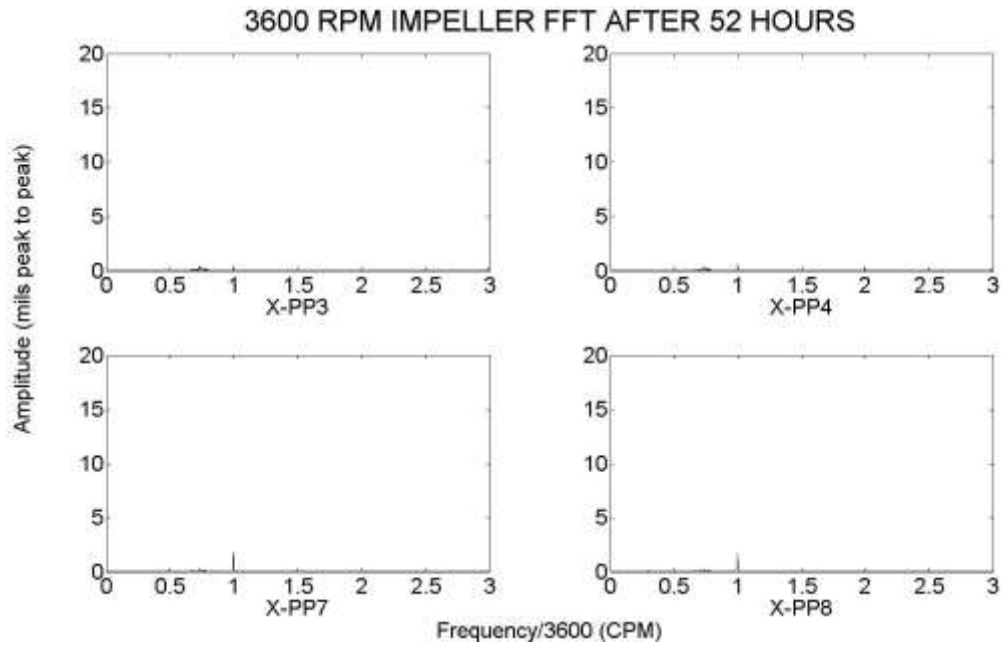


Figure 222. Impeller FFT – 52 Hours

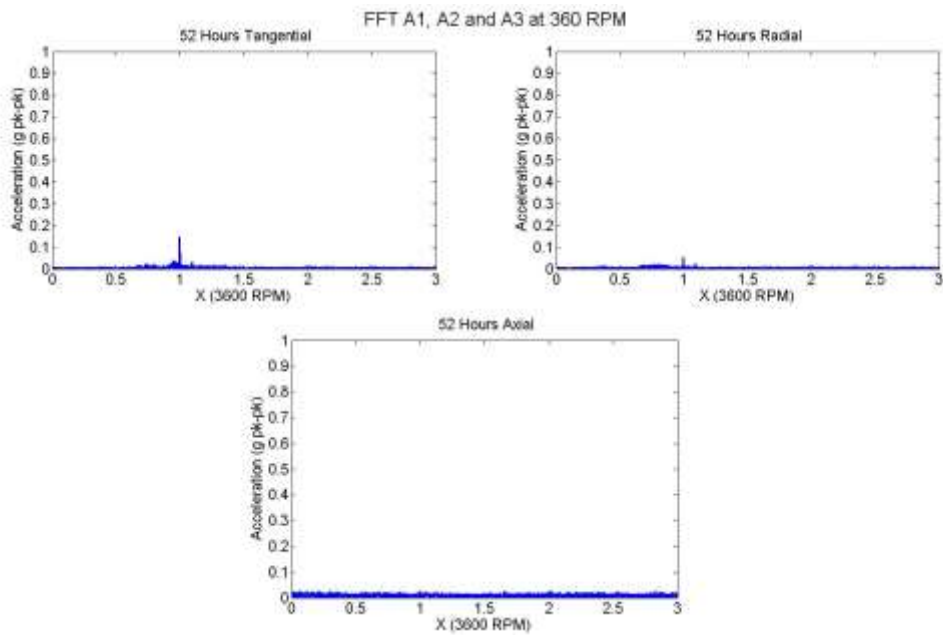


Figure 223. Inlet Accelerometer FFT – 52 Hours

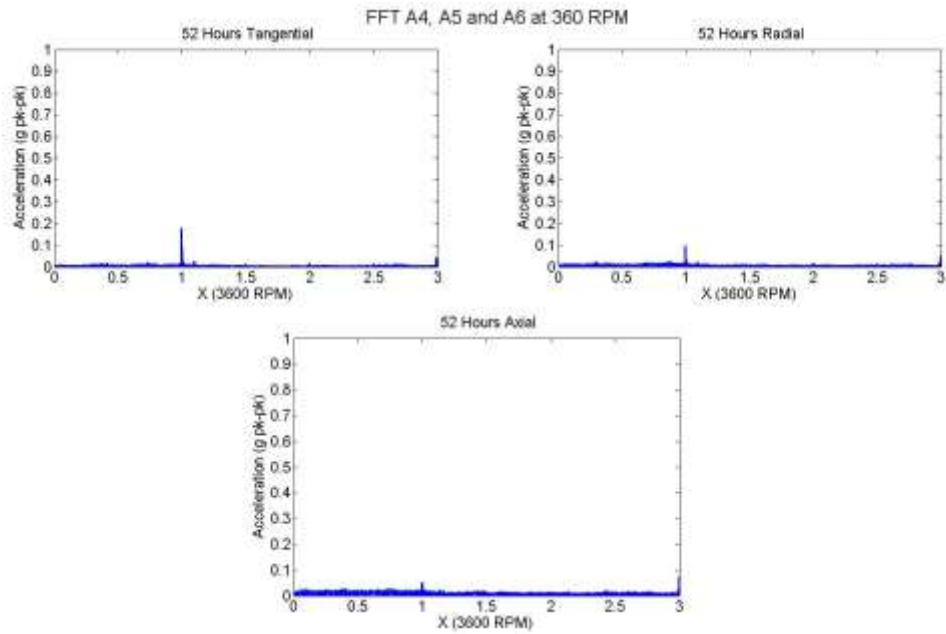


Figure 224. Outlet Accelerometer FFT – 52 Hours

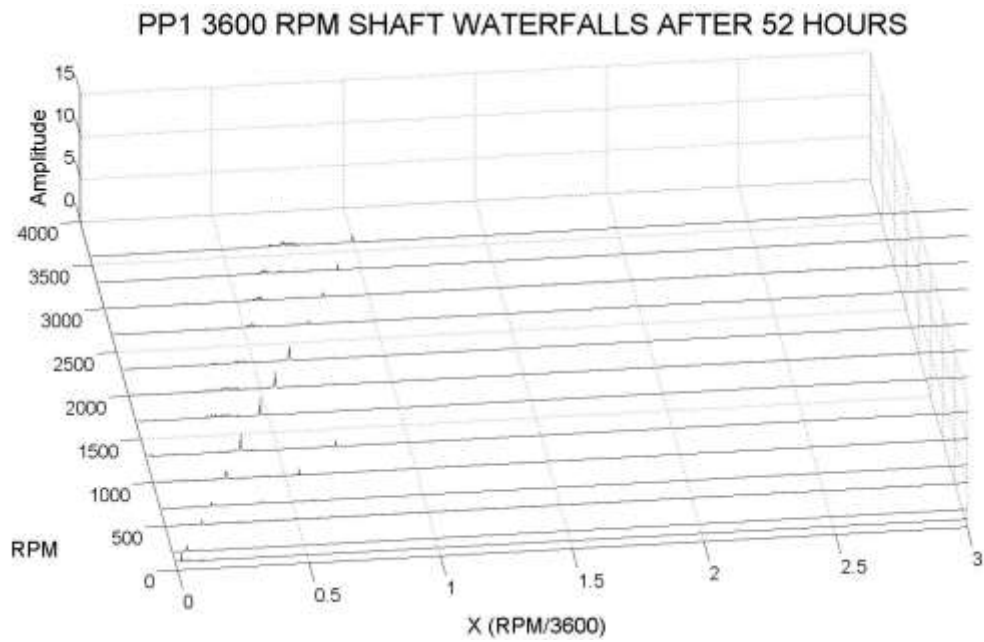


Figure 225. PP1 Waterfall Spectrum – 52 Hours

PP2 3600 RPM SHAFT WATERFALLS AFTER 52 HOURS

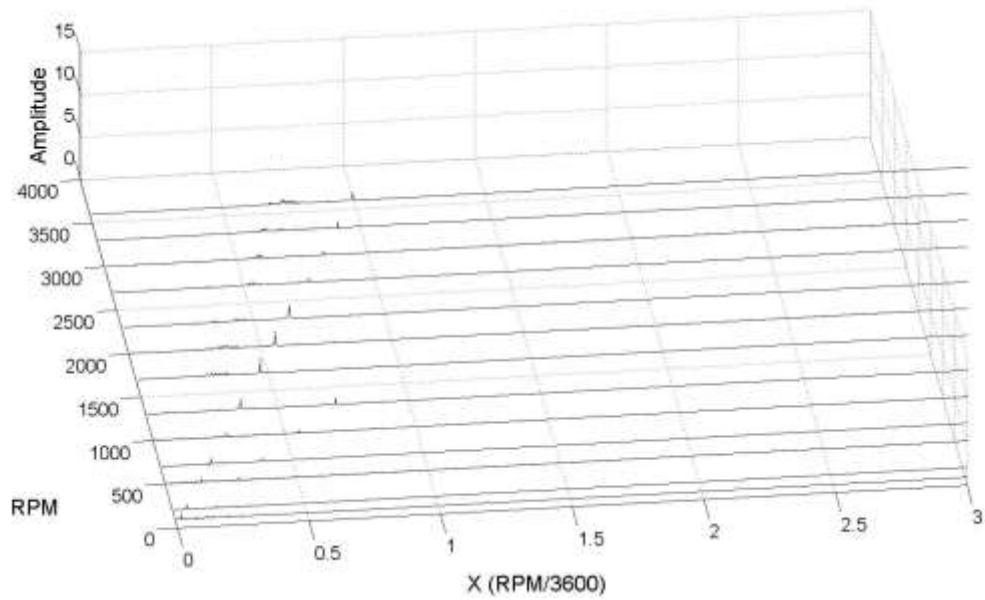


Figure 226. PP2 Waterfall Spectrum – 52 Hours

PP3 3600 RPM IMPELLER WATERFALLS AFTER 52 HOURS

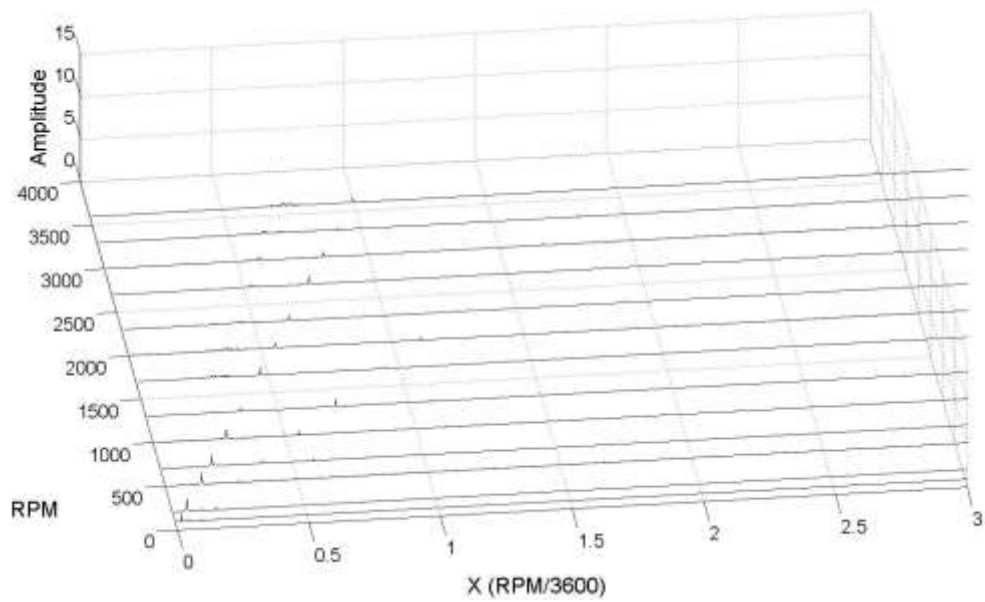


Figure 227. PP3 Waterfall Spectrum – 52 Hours

PP4 3600 RPM IMPELLER WATERFALLS AFTER 52 HOURS

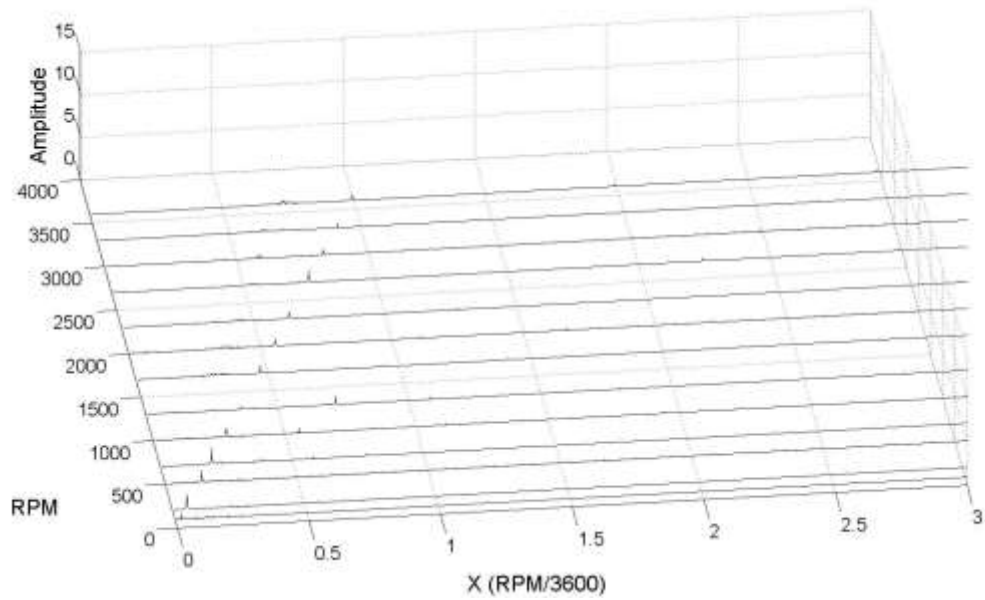


Figure 228. PP4 Waterfall Spectrum – 52 Hours

PP5 3600 RPM SHAFT WATERFALLS AFTER 52 HOURS

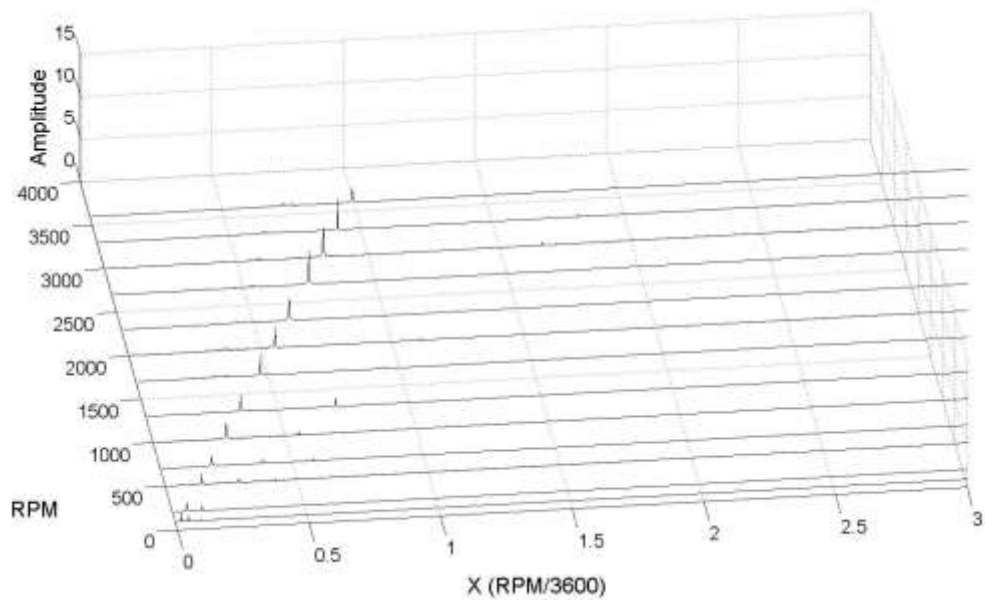


Figure 229. PP5 Waterfall Spectrum – 52 Hours

PP6 3600 RPM SHAFT WATERFALLS AFTER 52 HOURS

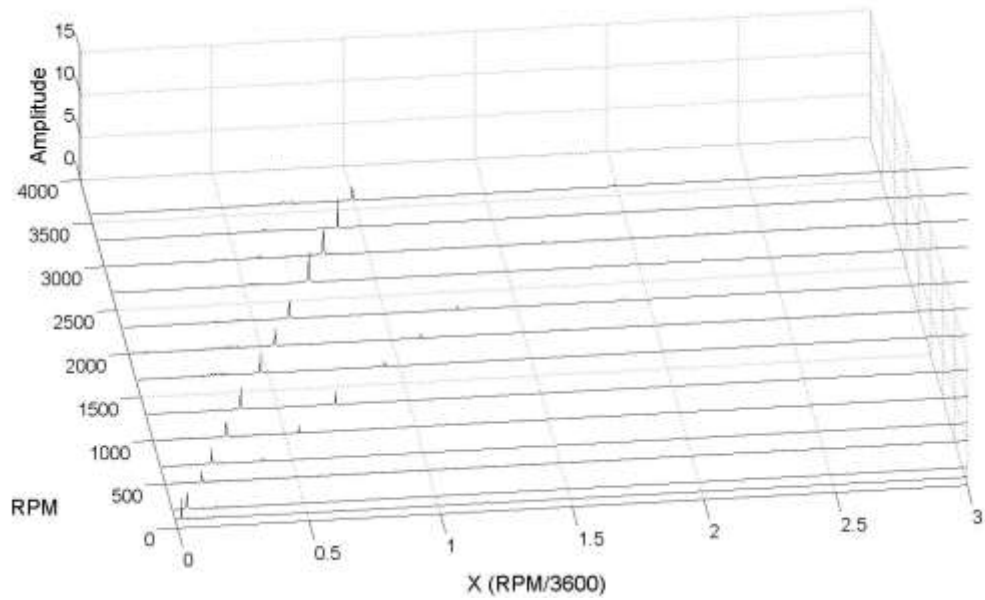


Figure 230. PP6 Waterfall Spectrum – 52 Hours

PP7 3600 RPM IMPELLER WATERFALLS AFTER 52 HOURS

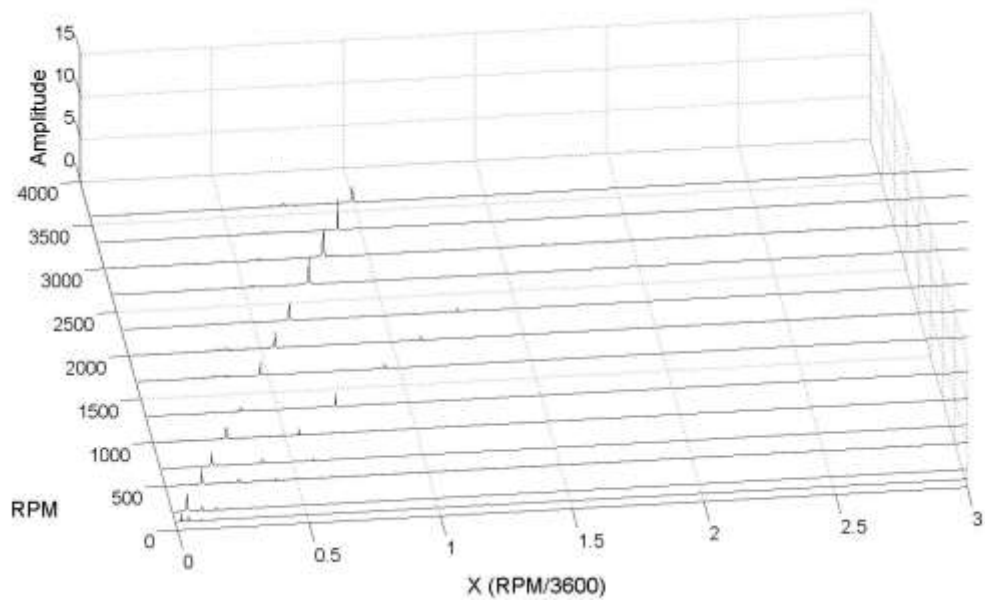


Figure 231. PP7 Waterfall Spectrum – 52 Hours

PP8 3600 RPM IMPELLER WATERFALLS AFTER 52 HOURS

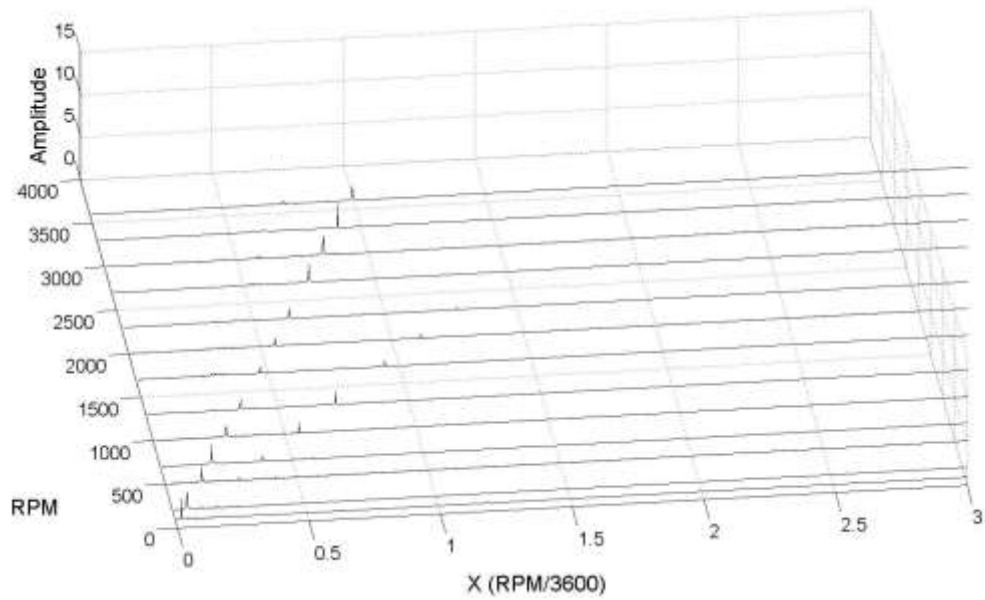


Figure 232. PP8 Waterfall Spectrum – 52 Hours

PP9 3600 RPM SHAFT WATERFALLS AFTER 52 HOURS

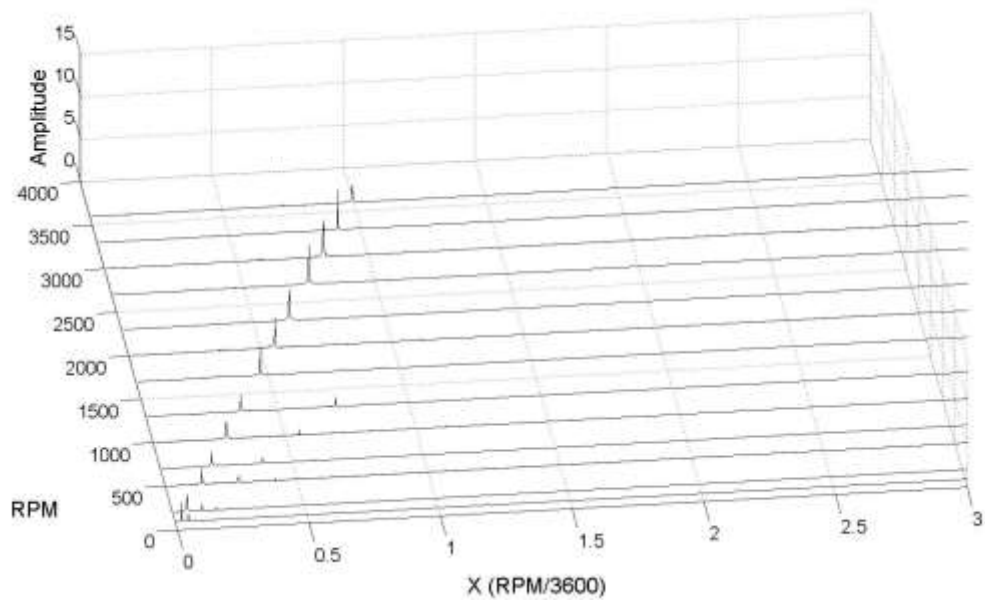


Figure 233. PP9 Waterfall Spectrum – 52 Hours

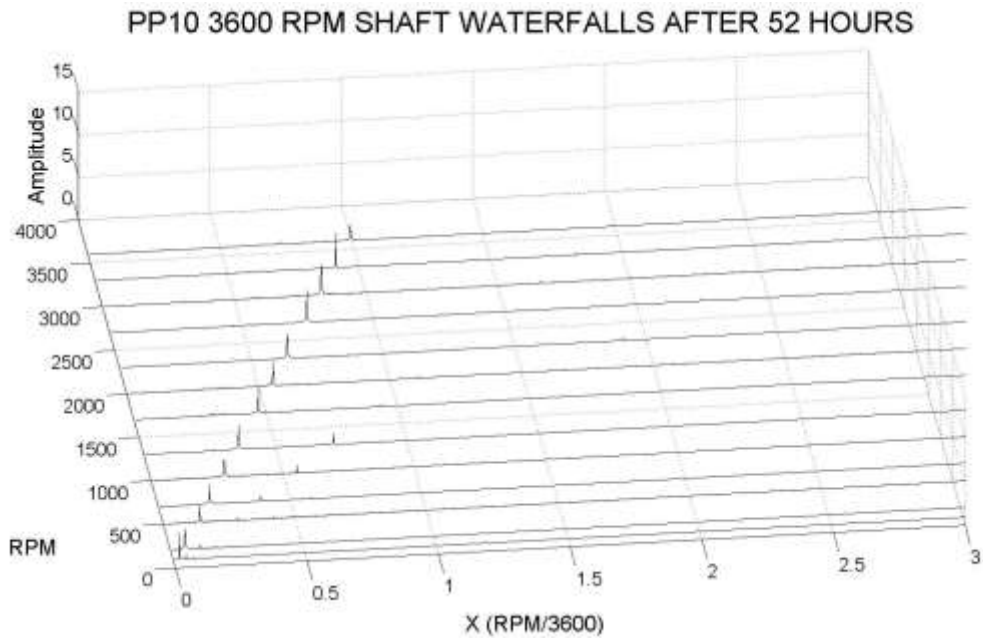


Figure 234. PP10 Waterfall Spectrum – 52 Hours

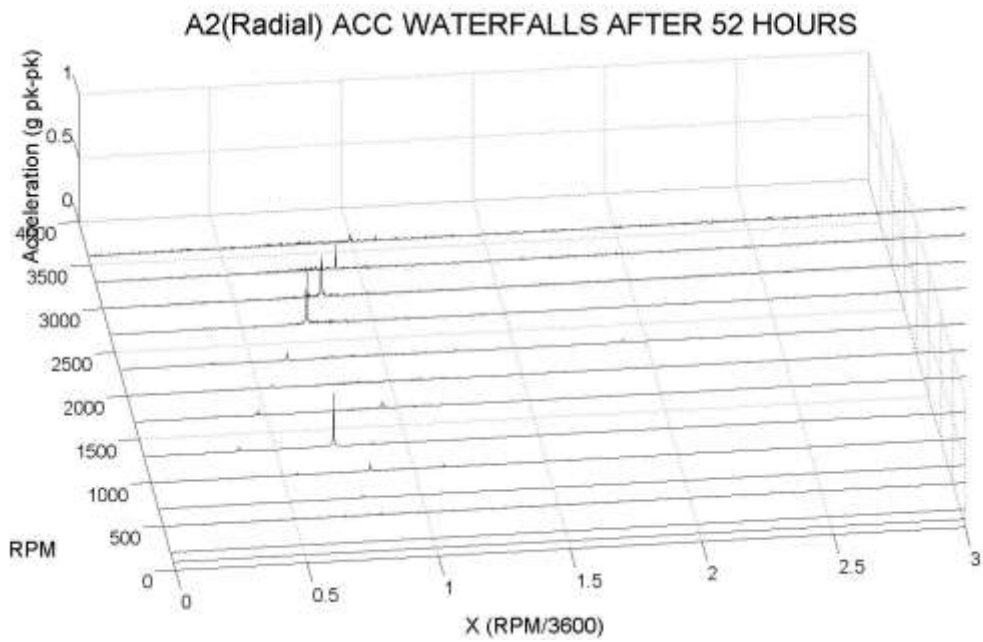


Figure 235. Inlet Accelerometer Radial Waterfall Spectrum – 52 Hours

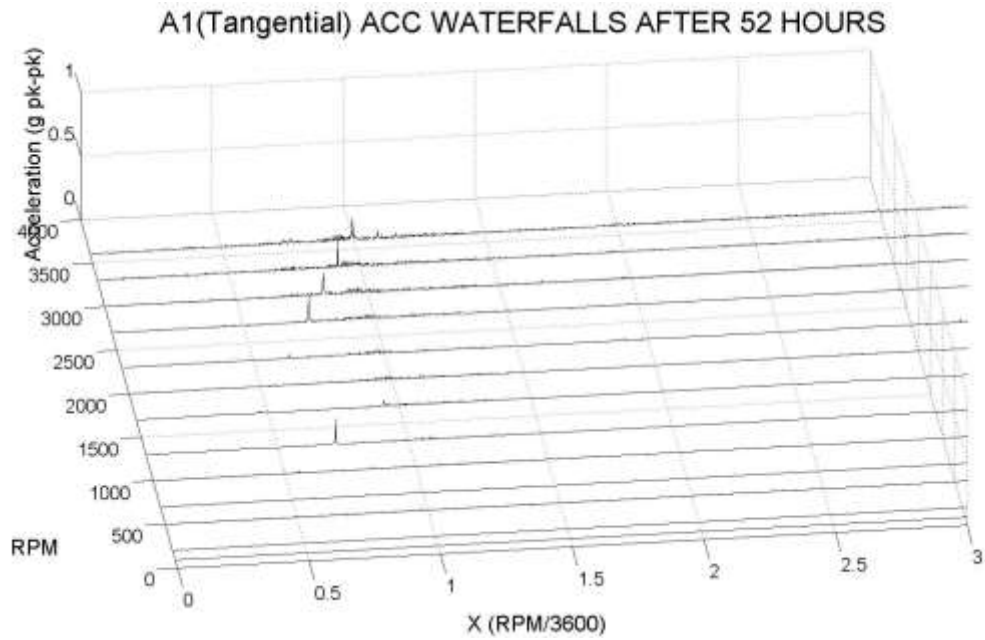


Figure 236. Inlet Accelerometer Tangential Waterfall Spectrum – 52 Hours

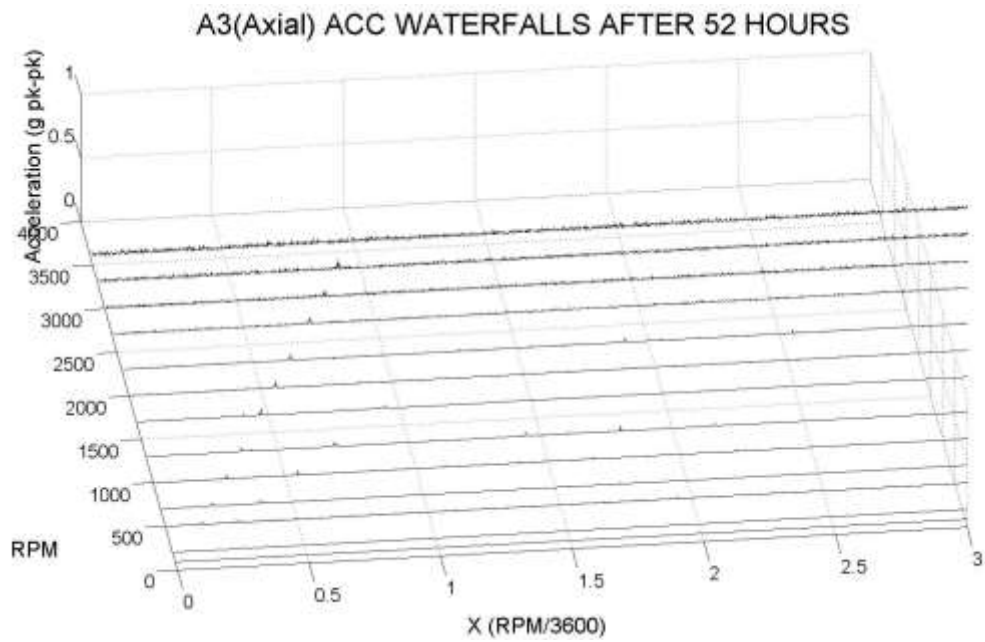


Figure 237. Inlet Accelerometer Axial Waterfall Spectrum – 52 Hours

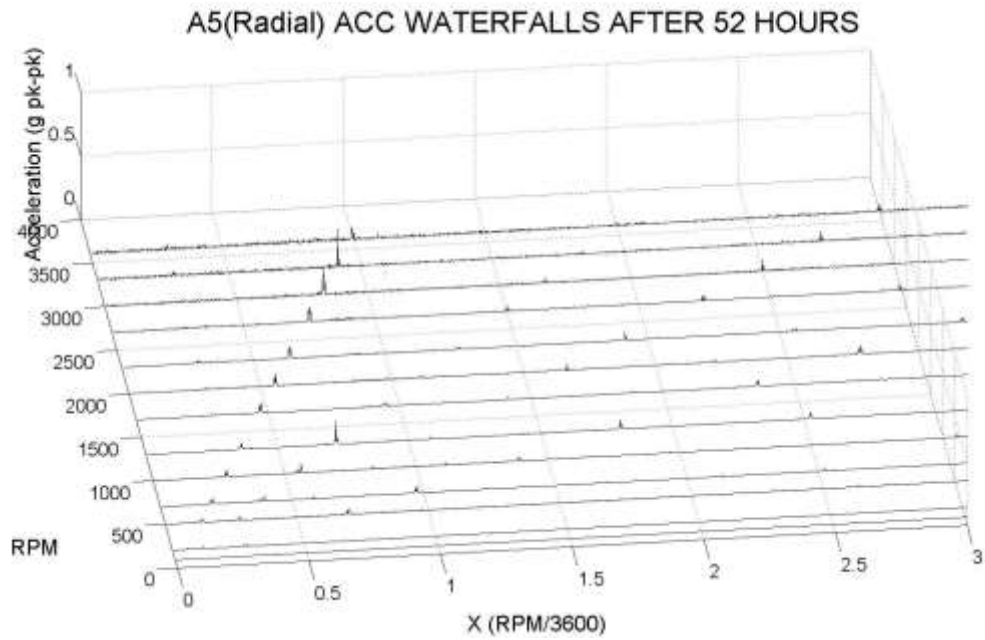


Figure 238. Outlet Accelerometer Radial Waterfall Spectrum – 52 Hours

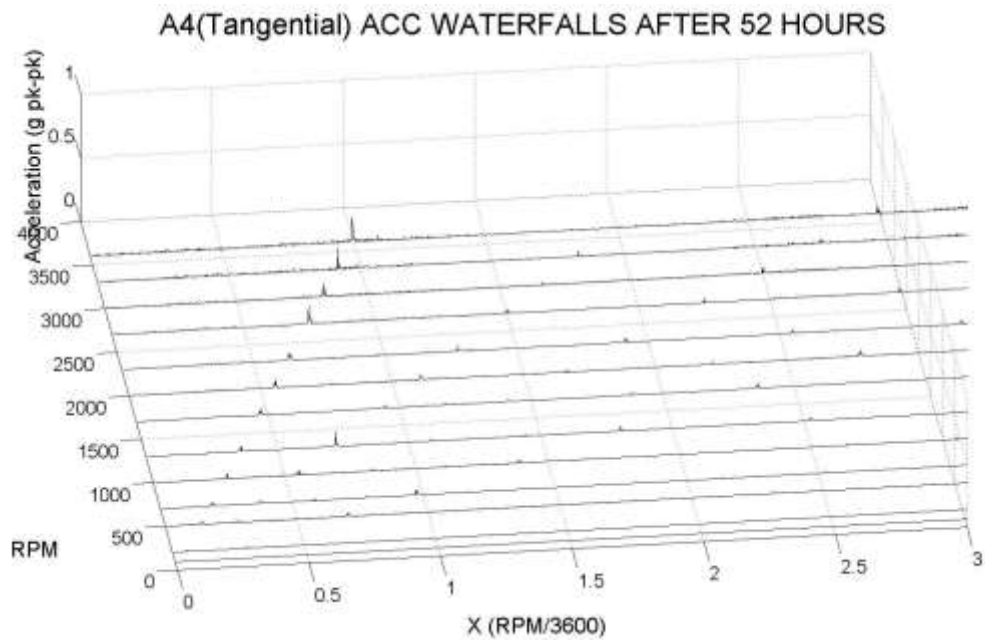


Figure 239. Outlet Accelerometer Tangential Waterfall Spectrum – 52 Hours

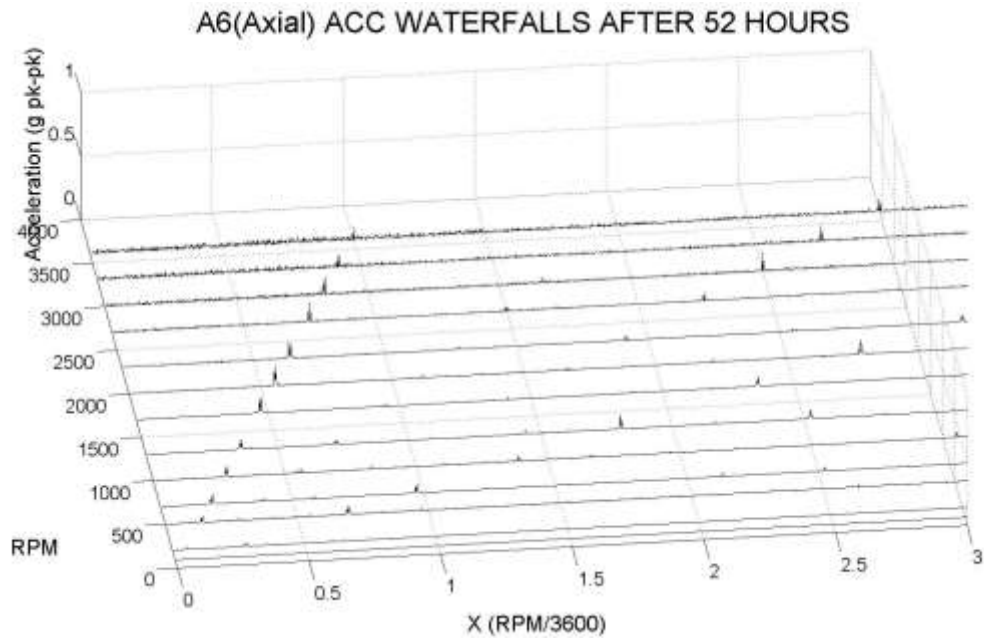


Figure 240. Outlet Accelerometer Axial Waterfall Spectrum – 52 Hours

D.5. 117 Hours

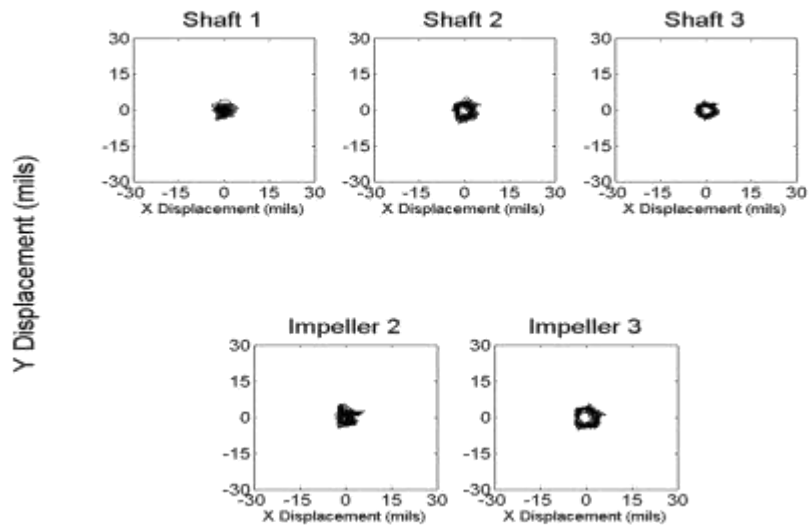


Figure 241. Orbit at 90 RPM – 117 Hours

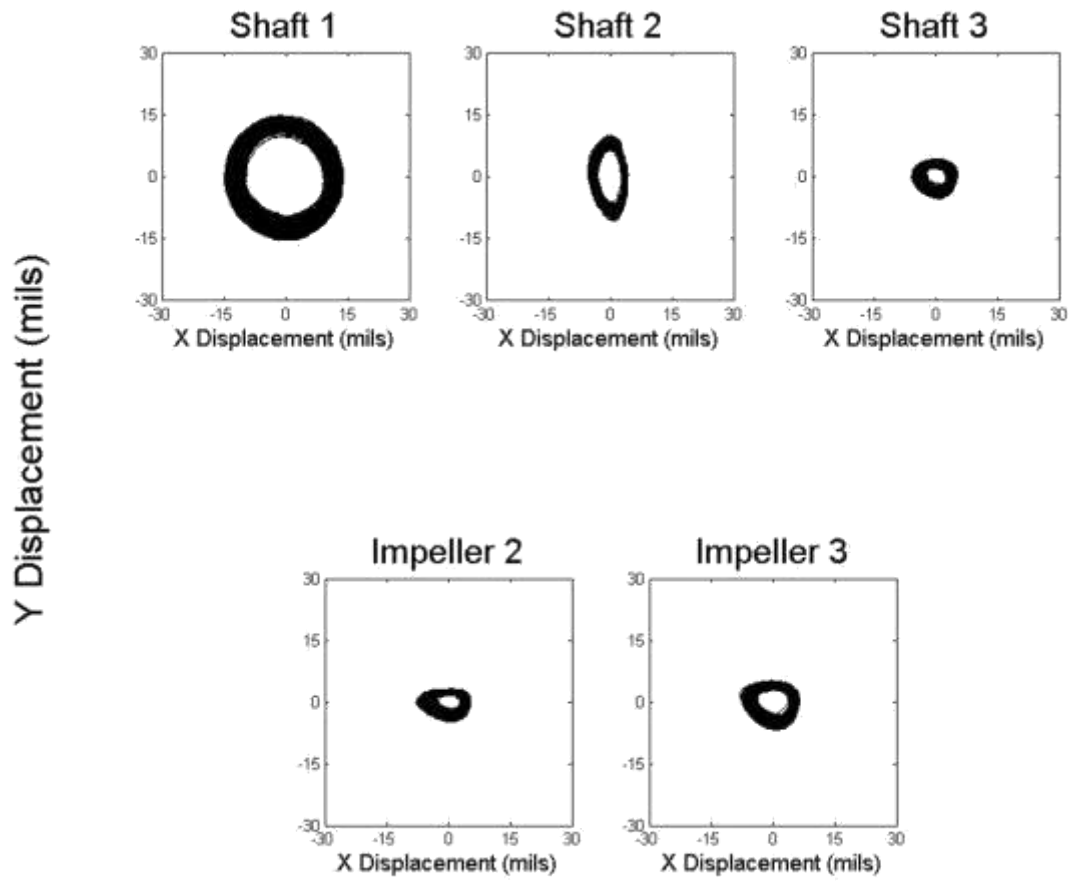


Figure 242. Orbit at 3600 RPM – 117 Hours

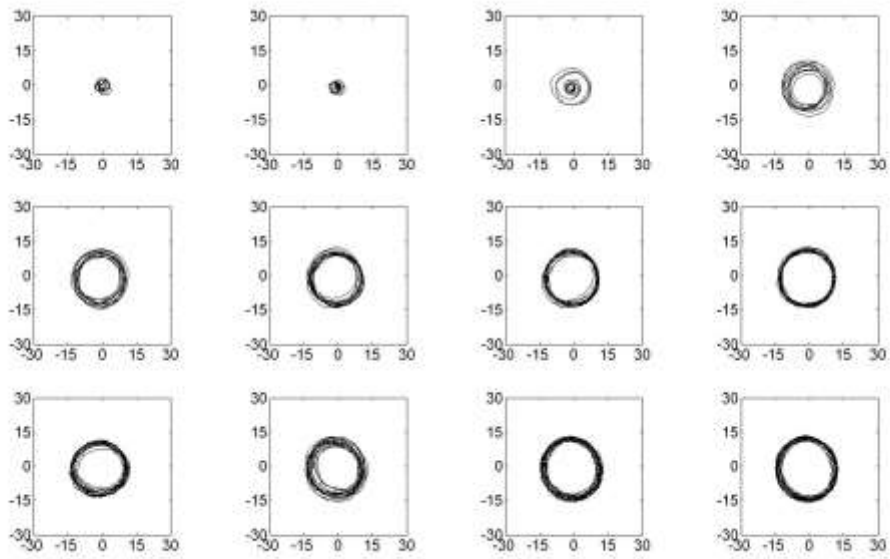


Figure 243. Shaft 1 Ramp Up Orbit – 117 Hours

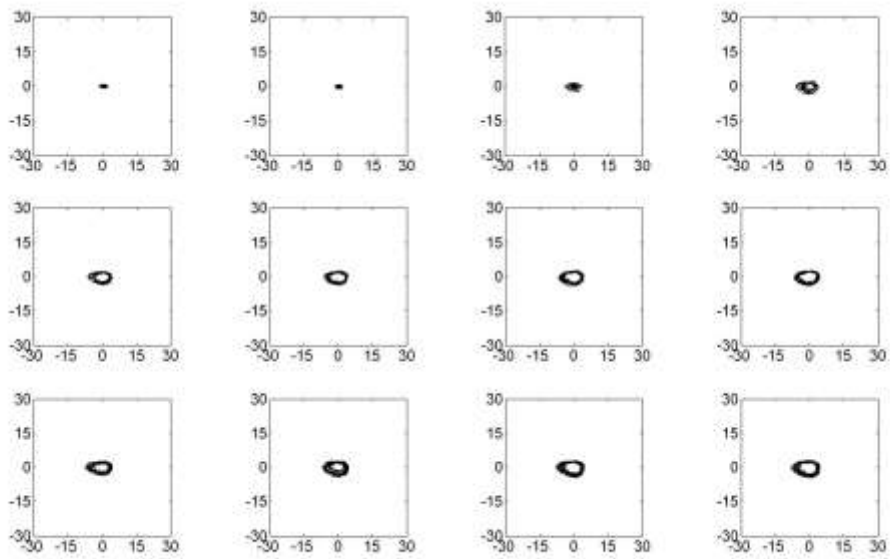


Figure 244. Impeller 2 Ramp Up Orbit – 117 Hours

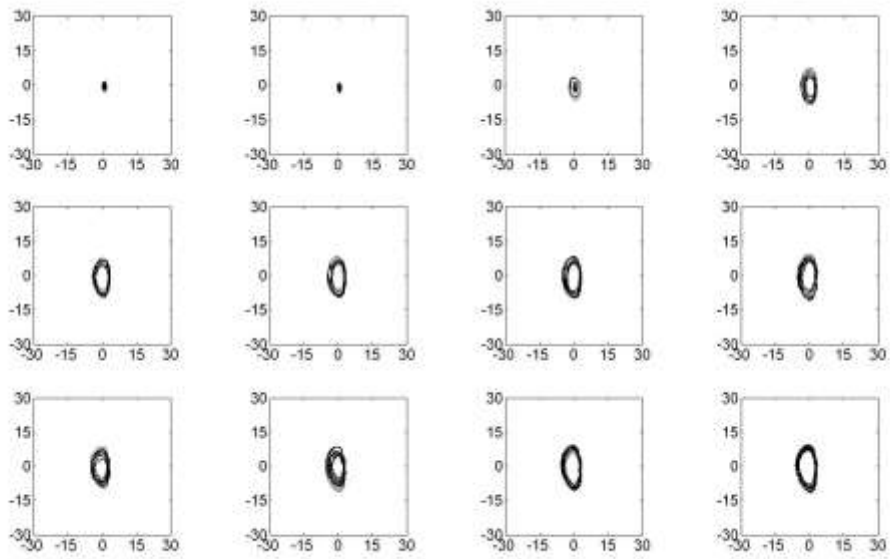


Figure 245. Shaft 2 Ramp Up Orbit – 117 Hours

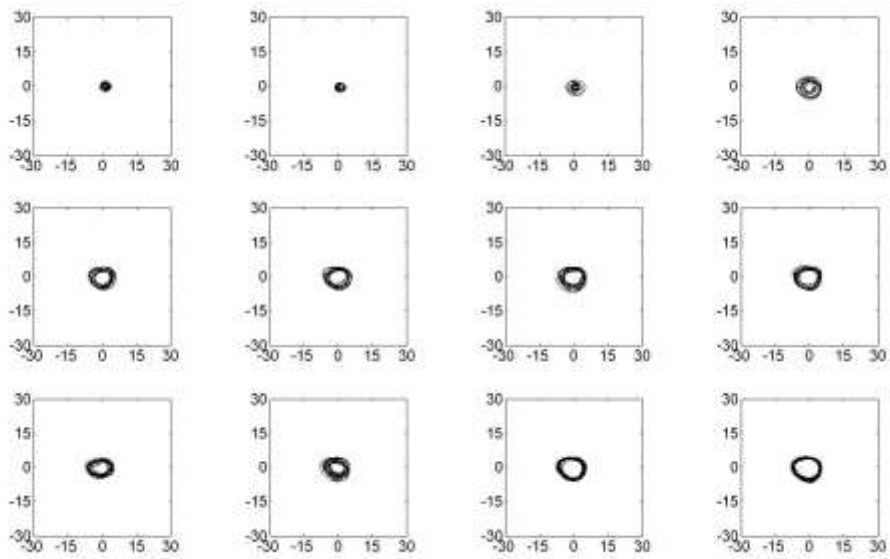


Figure 246. Impeller 3 Ramp Up Orbit – 117 Hours

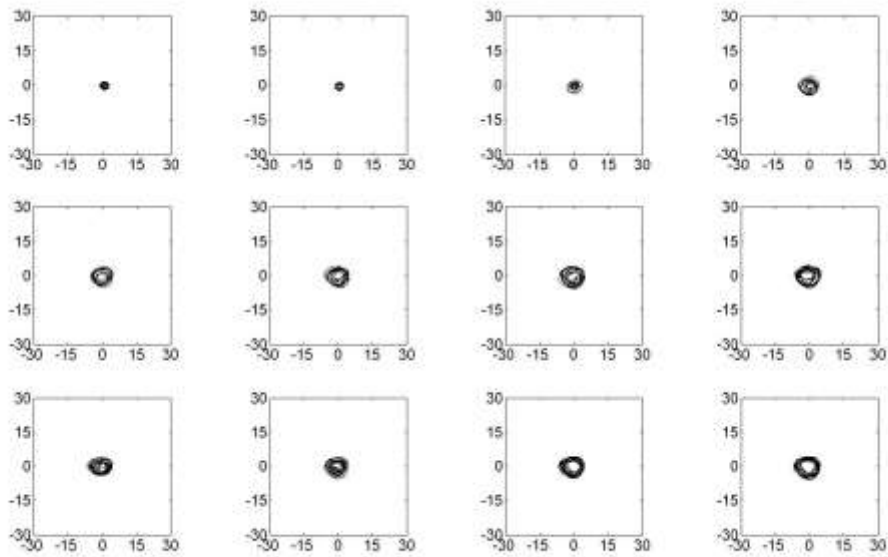


Figure 247. Shaft 3 Ramp Up Orbit – 117 Hours

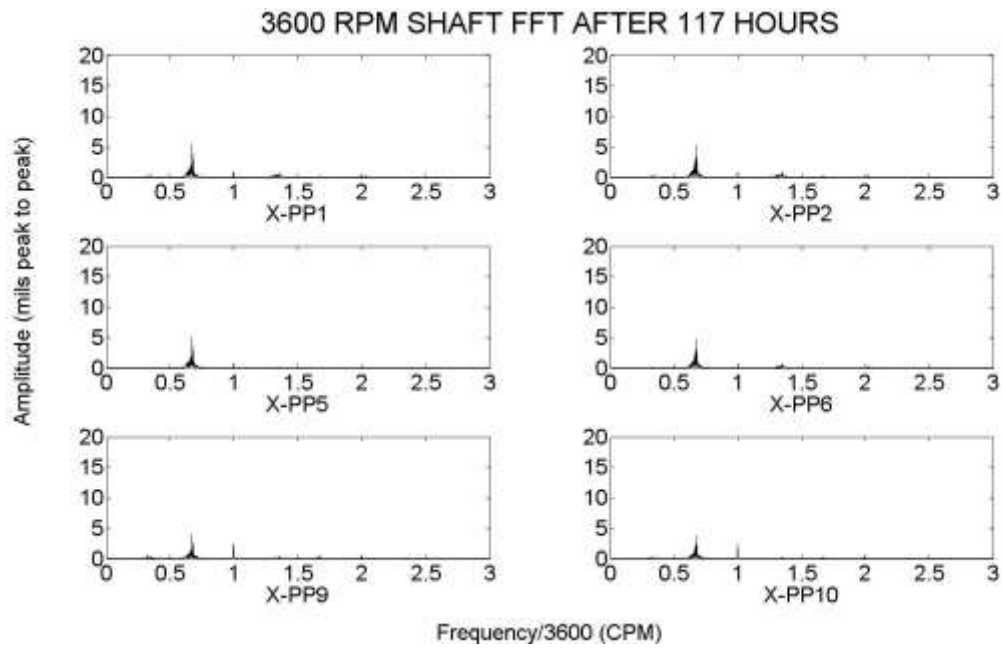


Figure 248. Shaft FFT – 117 Hours

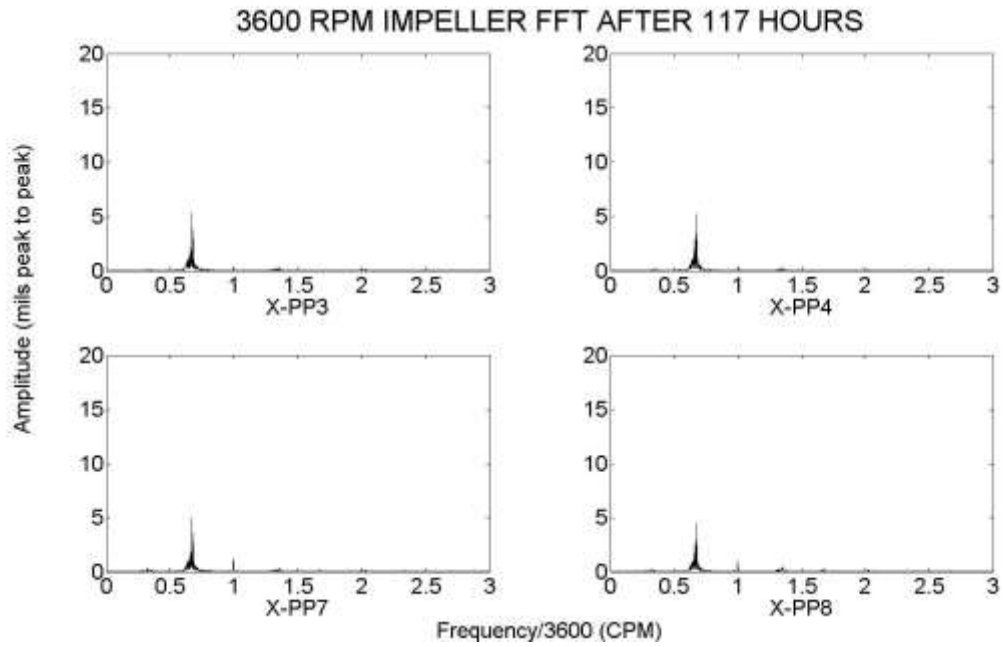


Figure 249. Impeller FFT – 117 Hours

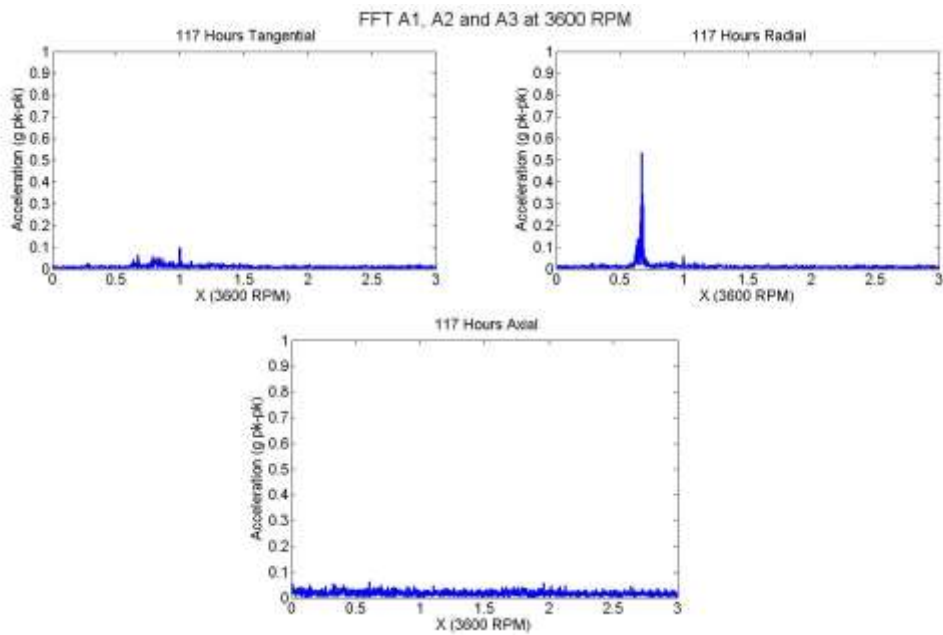


Figure 250. Inlet Accelerometer FFT – 117 Hours

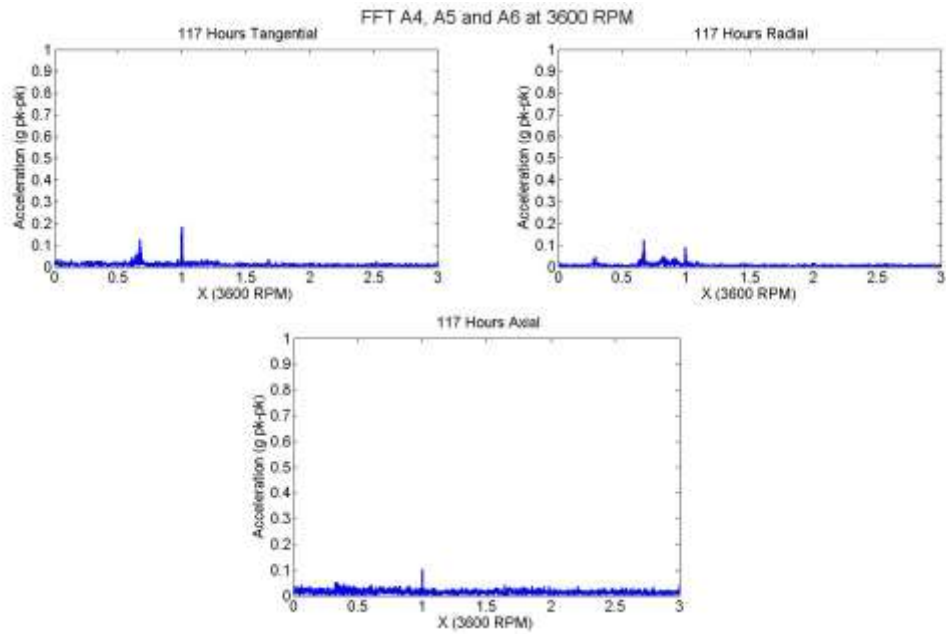


Figure 251. Outlet Accelerometer FFT – 117 Hours

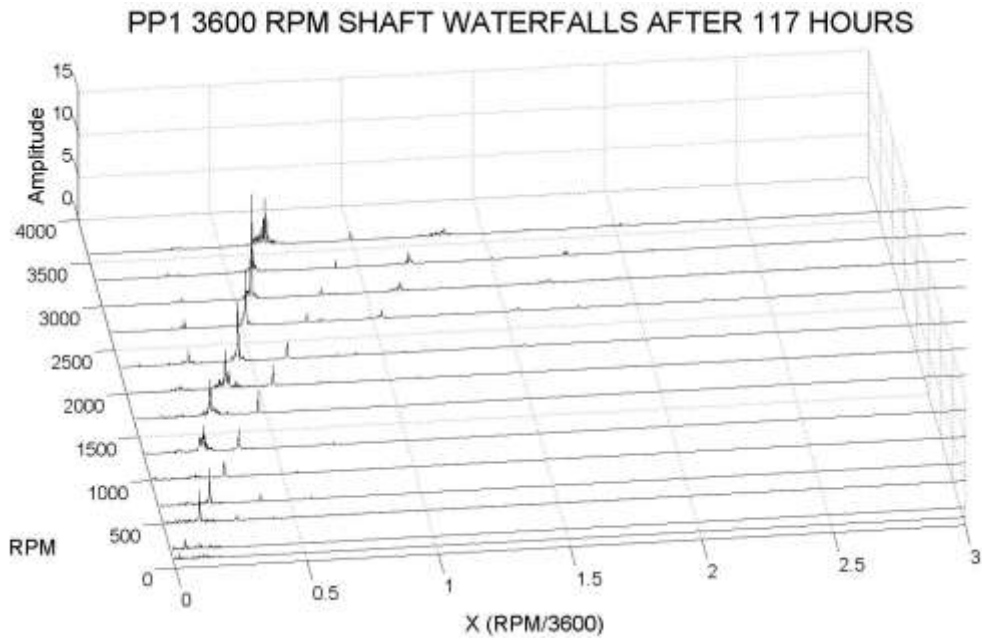


Figure 252. PP1 Waterfall Spectrum – 117 Hours

PP2 3600 RPM SHAFT WATERFALLS AFTER 117 HOURS

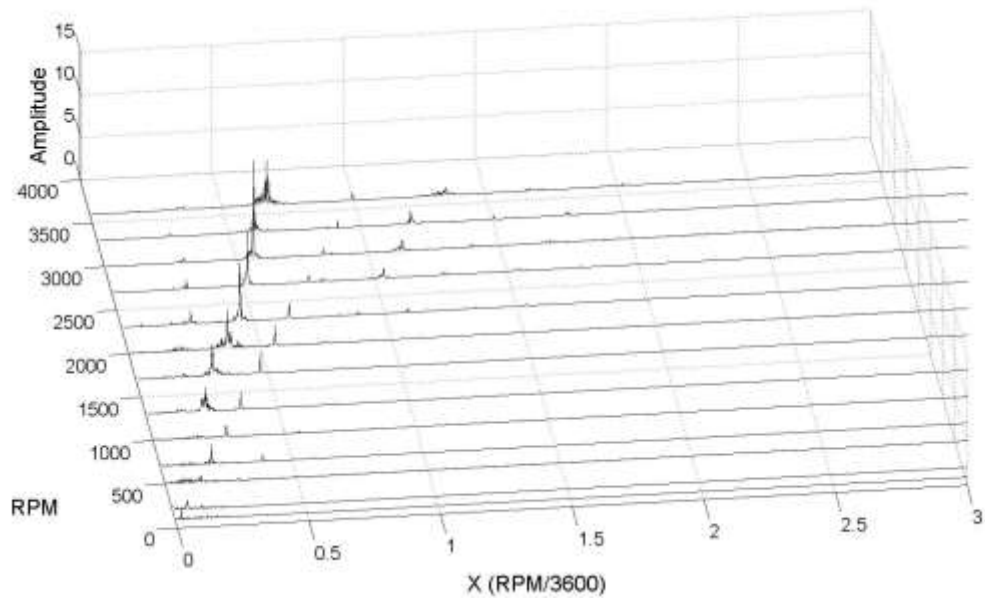


Figure 253. PP2 Waterfall Spectrum – 117 Hours

PP3 3600 RPM IMPELLER WATERFALLS AFTER 117 HOURS

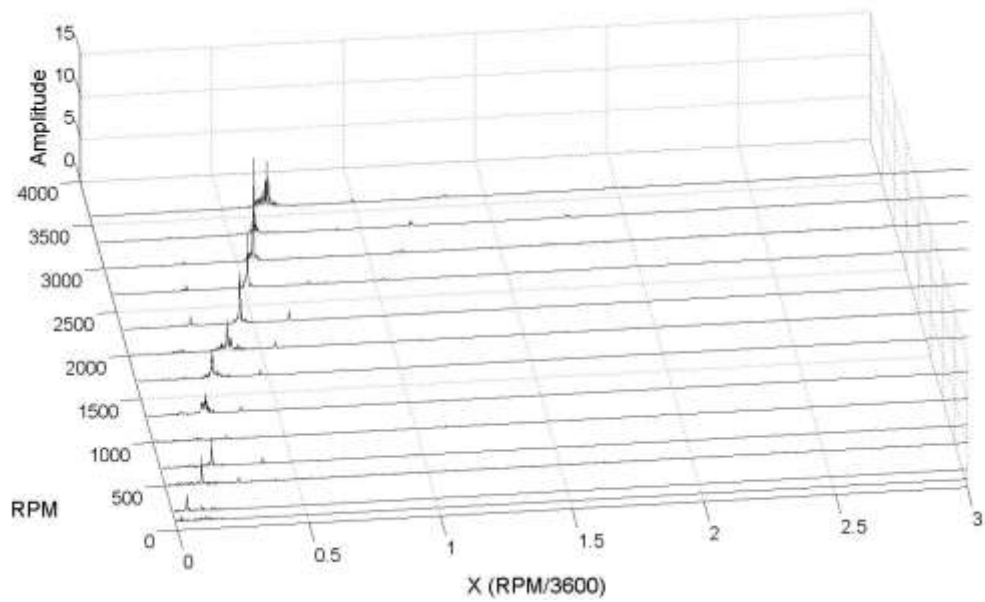


Figure 254. PP3 Waterfall Spectrum – 117 Hours

PP4 3600 RPM IMPELLER WATERFALLS AFTER 117 HOURS

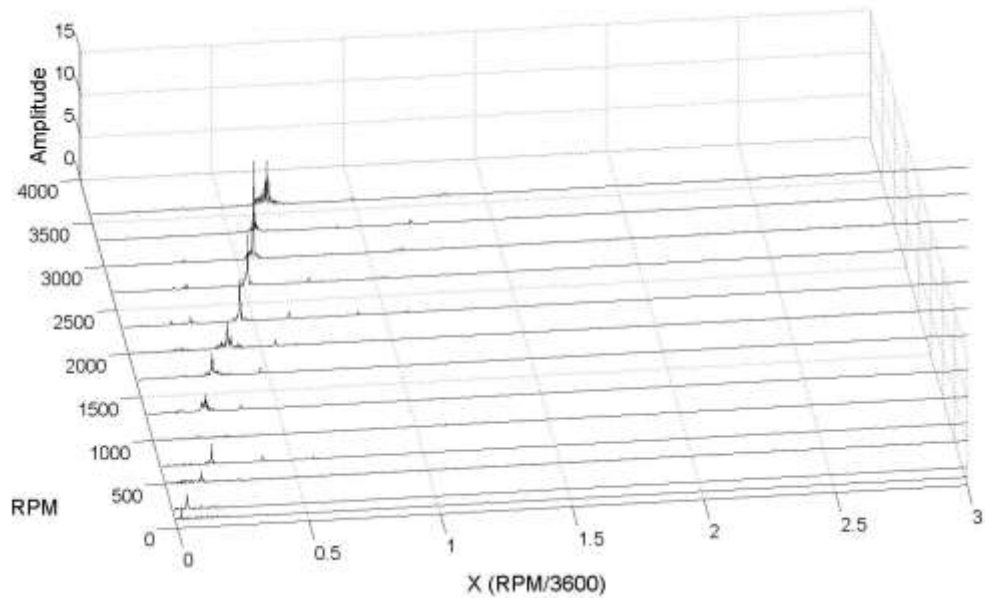


Figure 255. PP4 Waterfall Spectrum – 117 Hours

PP5 3600 RPM SHAFT WATERFALLS AFTER 117 HOURS

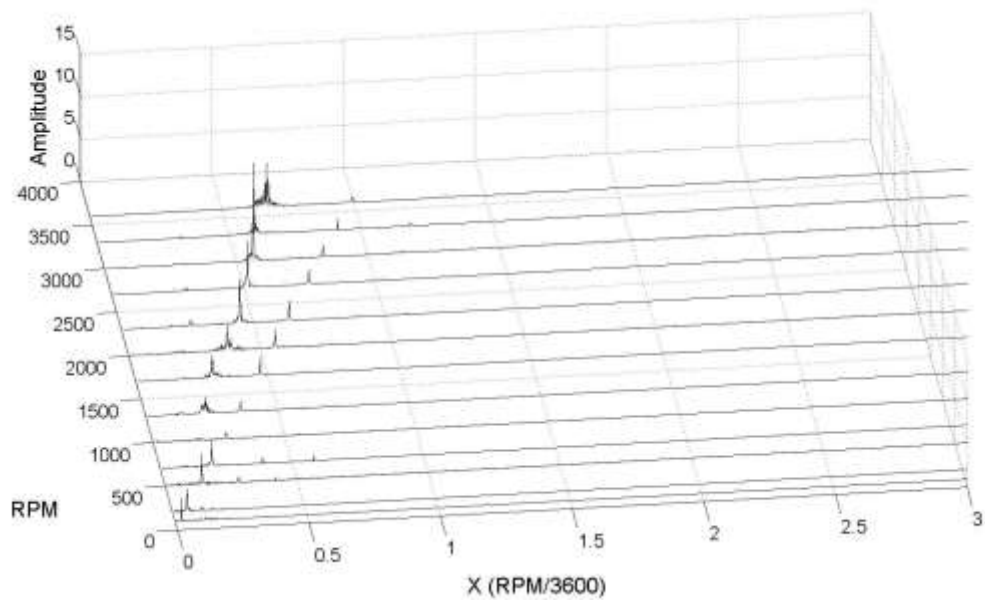


Figure 256. PP5 Waterfall Spectrum – 117 Hours

PP6 3600 RPM SHAFT WATERFALLS AFTER 117 HOURS

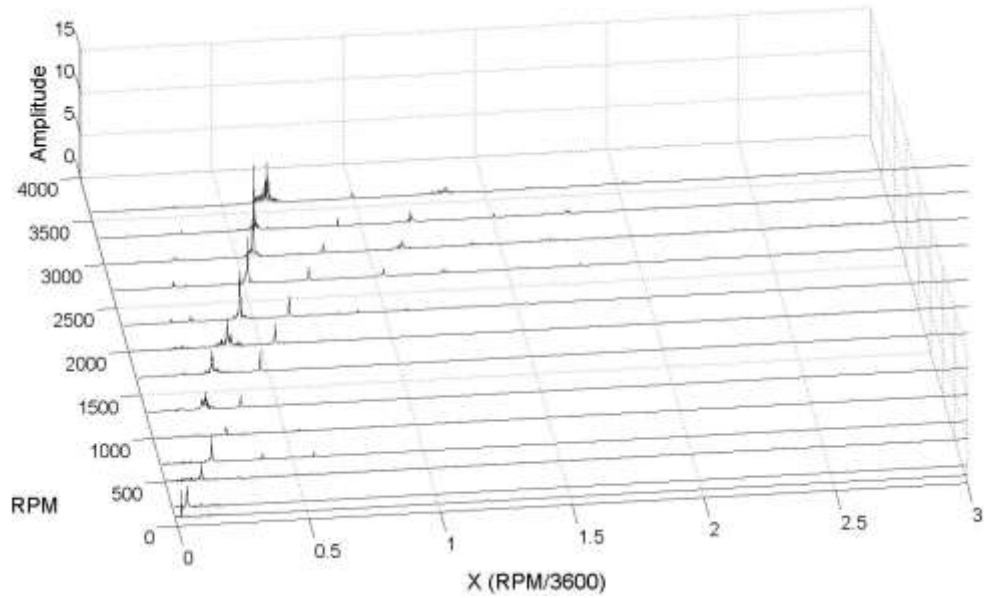


Figure 257. PP6 Waterfall Spectrum – 117 Hours

PP7 3600 RPM IMPELLER WATERFALLS AFTER 117 HOURS

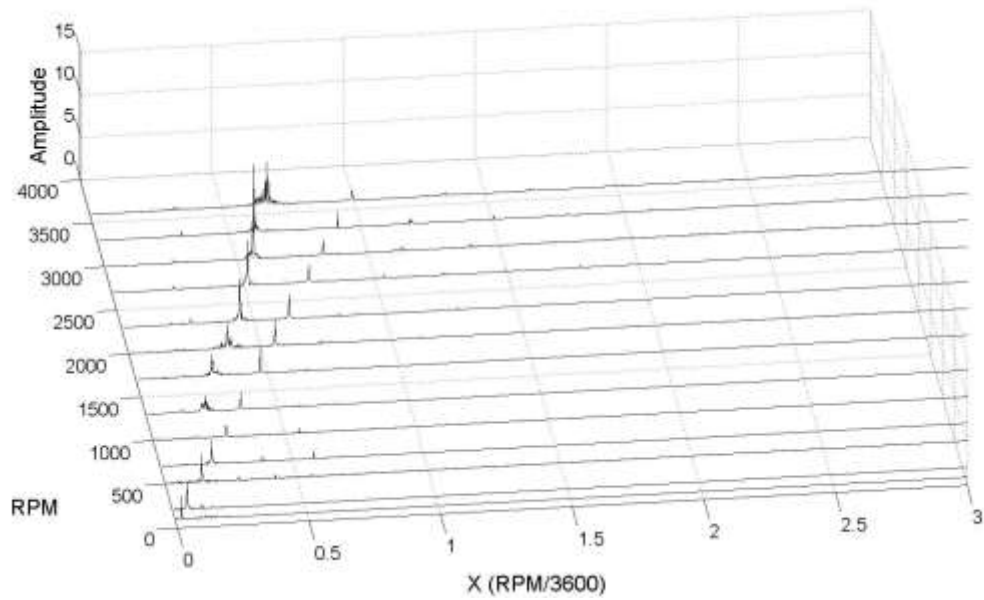


Figure 258. PP7 Waterfall Spectrum – 117 Hours

PP8 3600 RPM IMPELLER WATERFALLS AFTER 117 HOURS

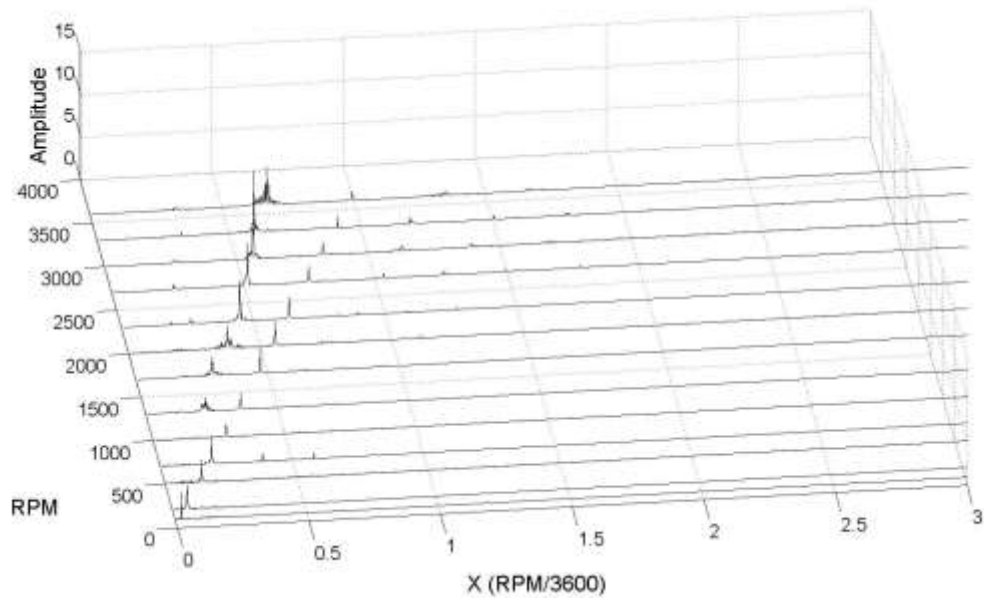


Figure 259. PP8 Waterfall Spectrum – 117 Hours

PP9 3600 RPM SHAFT WATERFALLS AFTER 117 HOURS

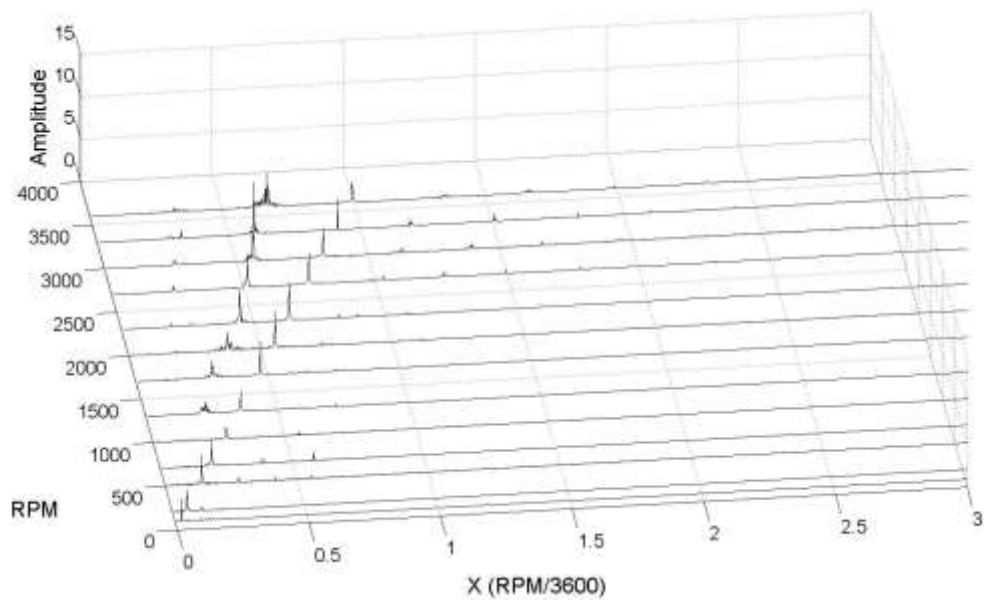


Figure 260. PP9 Waterfall Spectrum – 117 Hours

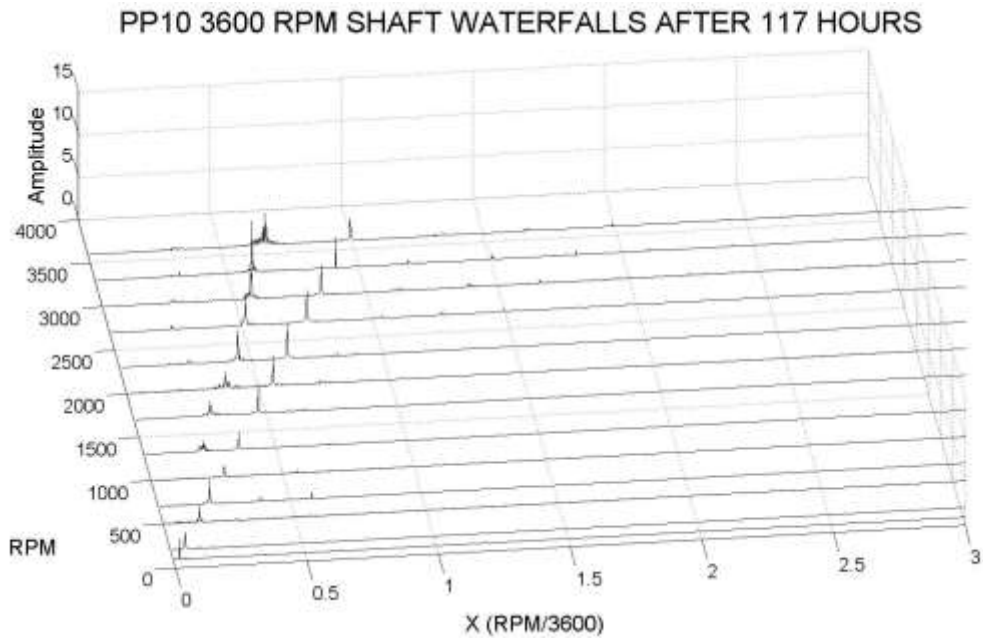


Figure 261. PP10 Waterfall Spectrum – 117 Hours

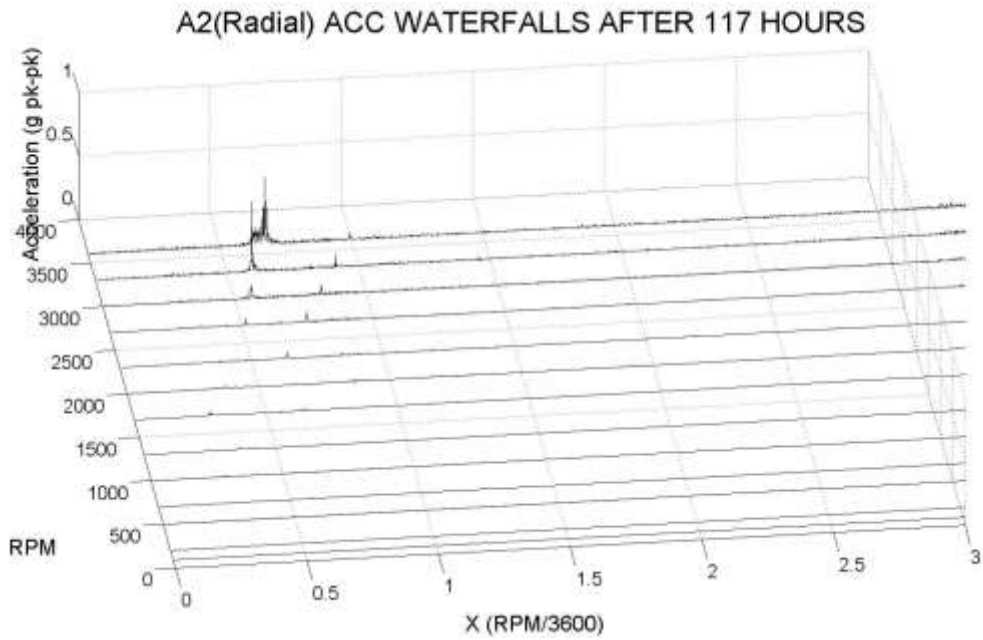


Figure 262. Inlet Accelerometer Radial Waterfall Spectrum – 117 Hours

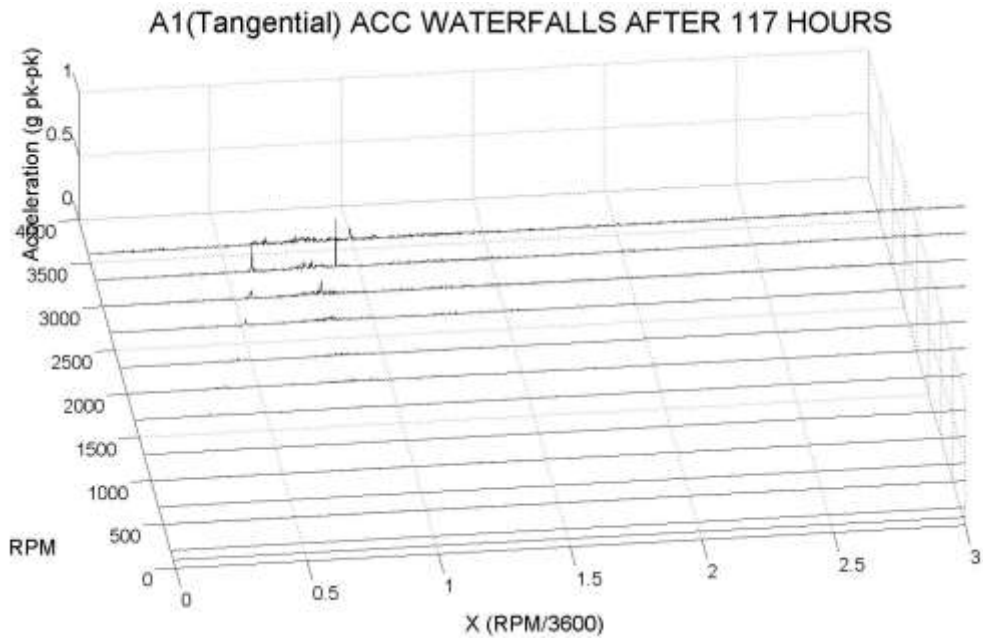


Figure 263. Inlet Accelerometer Tangential Waterfall Spectrum – 117 Hours

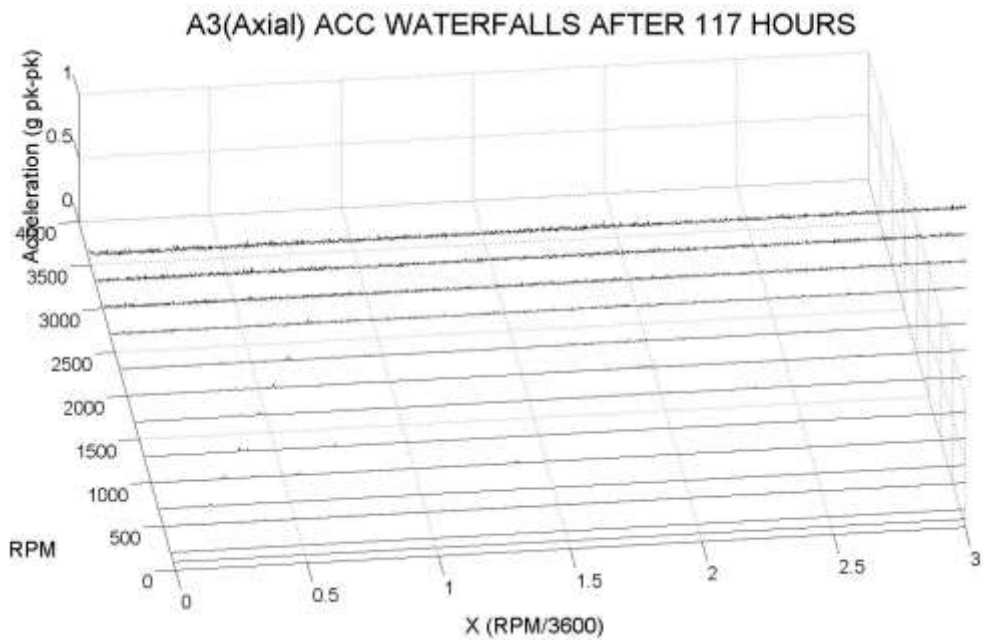


Figure 264. Inlet Accelerometer Axial Waterfall Spectrum – 117 Hours

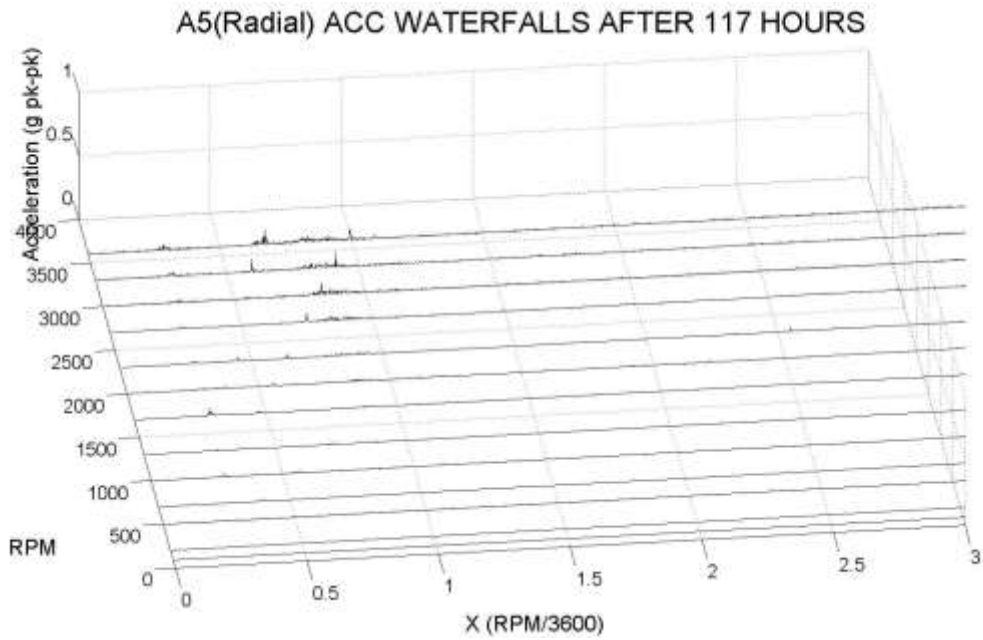


Figure 265. Outlet Accelerometer Radial Waterfall Spectrum – 117 Hours

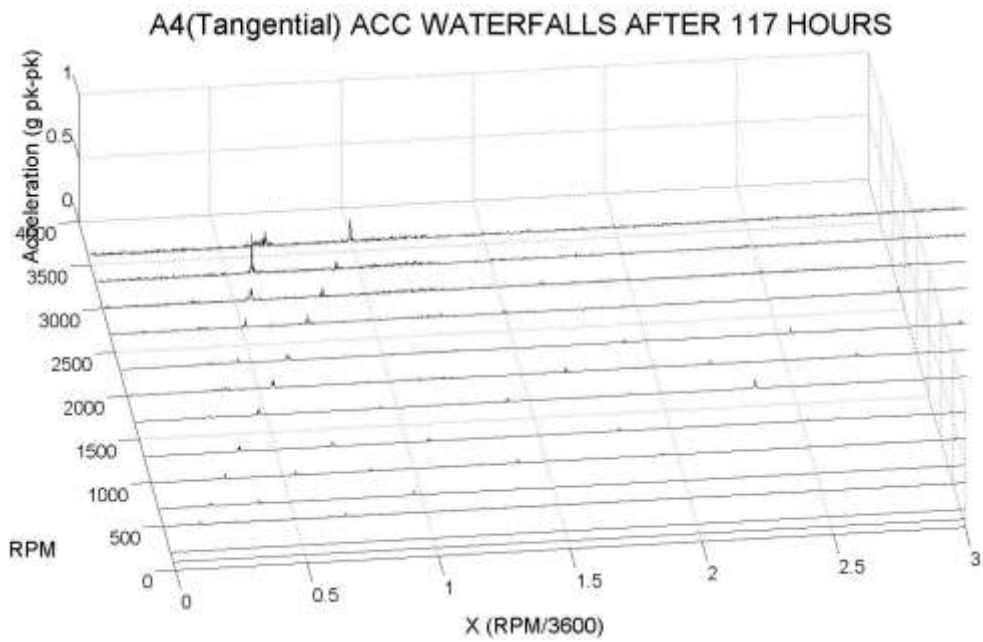


Figure 266. Outlet Accelerometer Tangential Waterfall Spectrum – 117 Hours

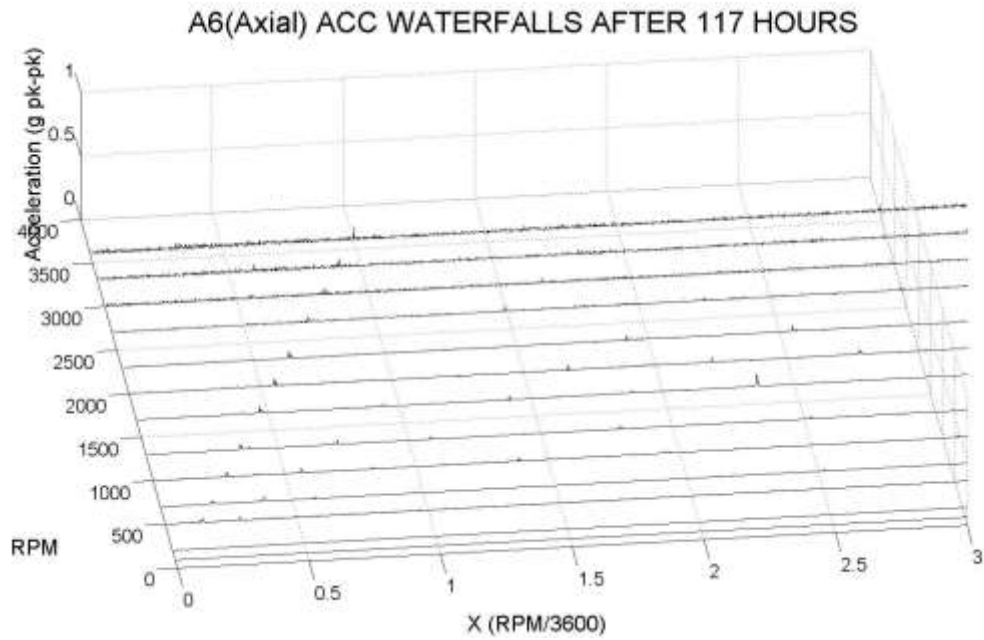


Figure 267. Outlet Accelerometer Axial Waterfall Spectrum – 117 Hours

D.6. 185 Hours

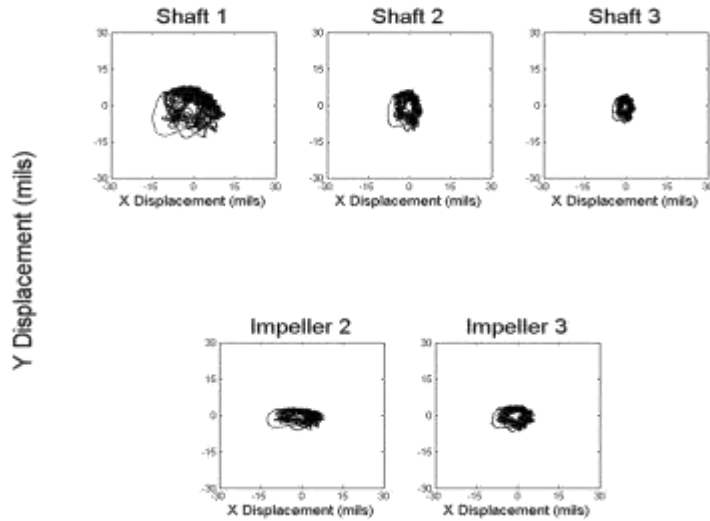


Figure 268. Orbit at 90 RPM – 185 Hours

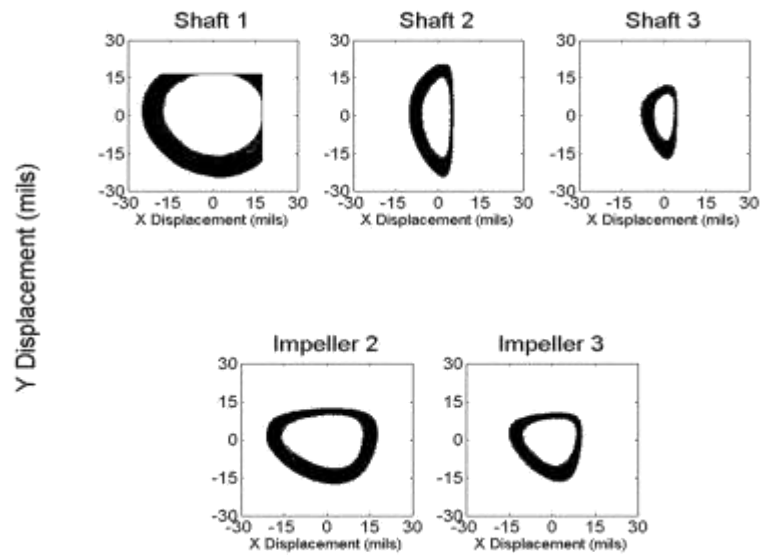


Figure 269. Orbit at 3600 RPM – 185 Hours

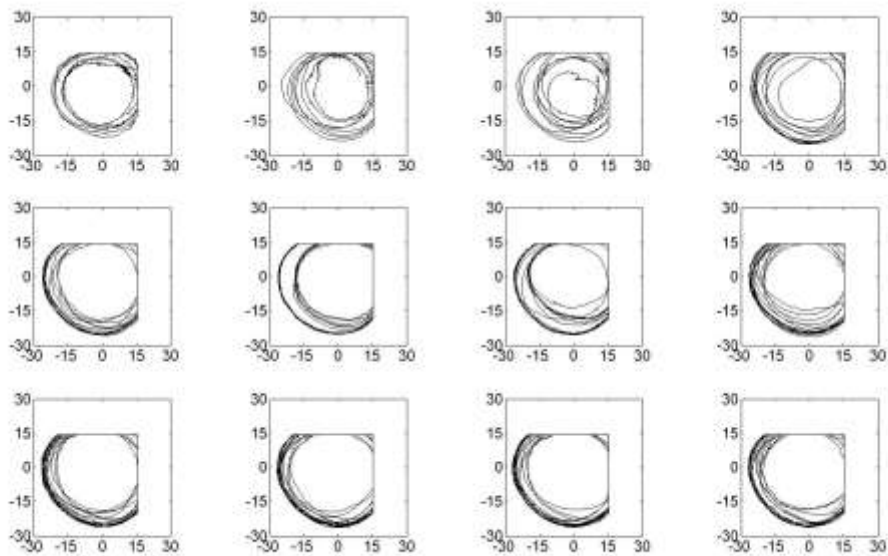


Figure 270. Shaft 1 Ramp Up Orbit – 185 Hours

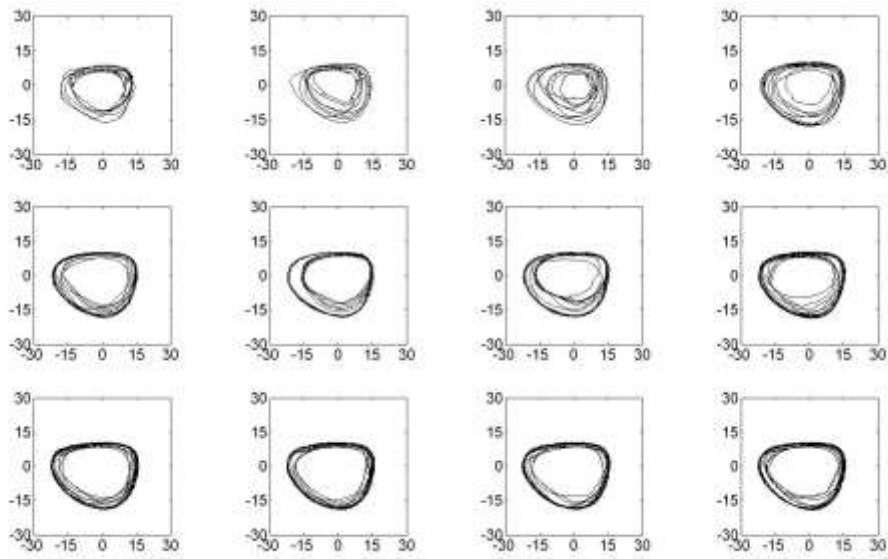


Figure 271. Impeller 2 Ramp Up Orbit – 185 Hours

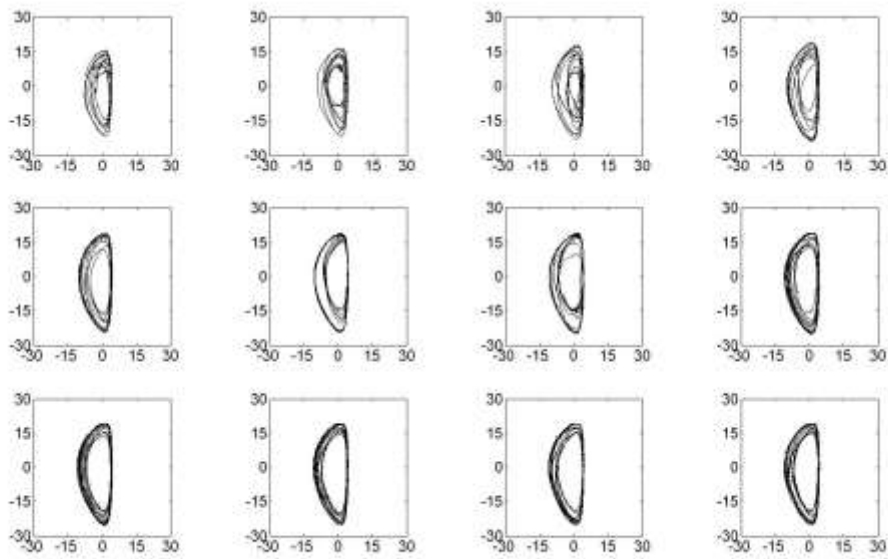


Figure 272. Shaft 2 Ramp Up Orbit – 185 Hours

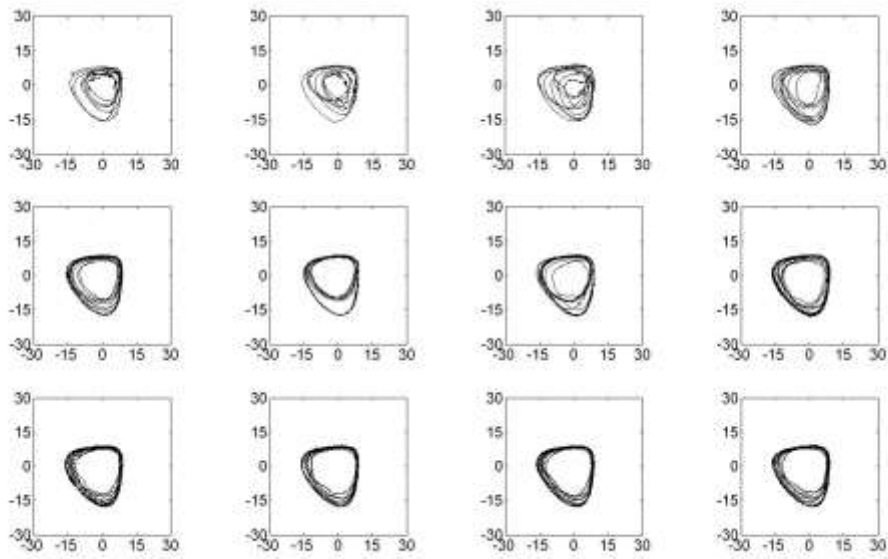


Figure 273. Impeller 3 Ramp Up Orbit – 185 Hours

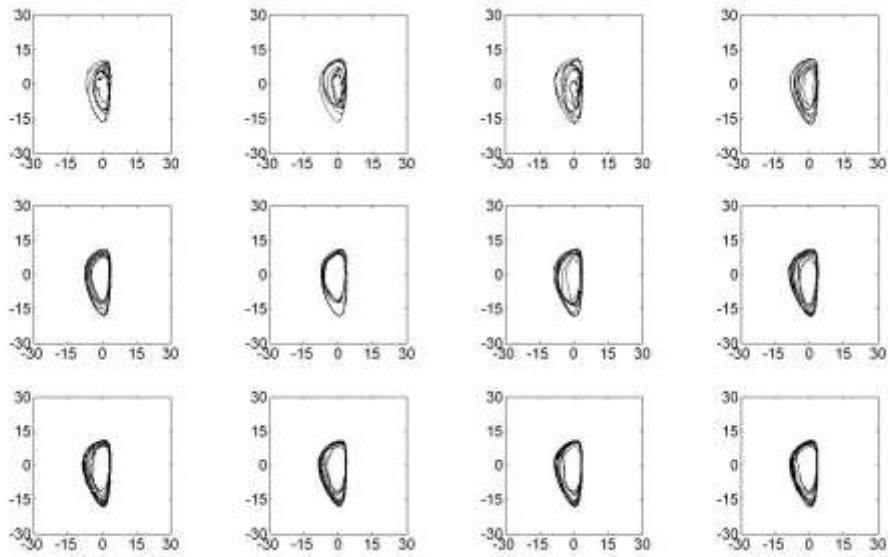


Figure 274. Shaft 3 Ramp Up Orbit – 185 Hours

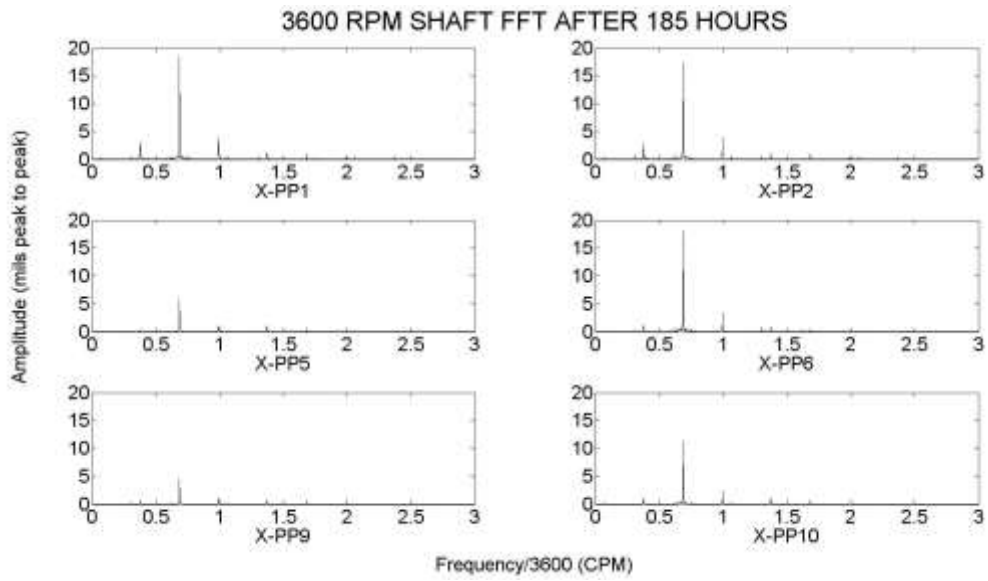


Figure 275. Shaft FFT – 185 Hours

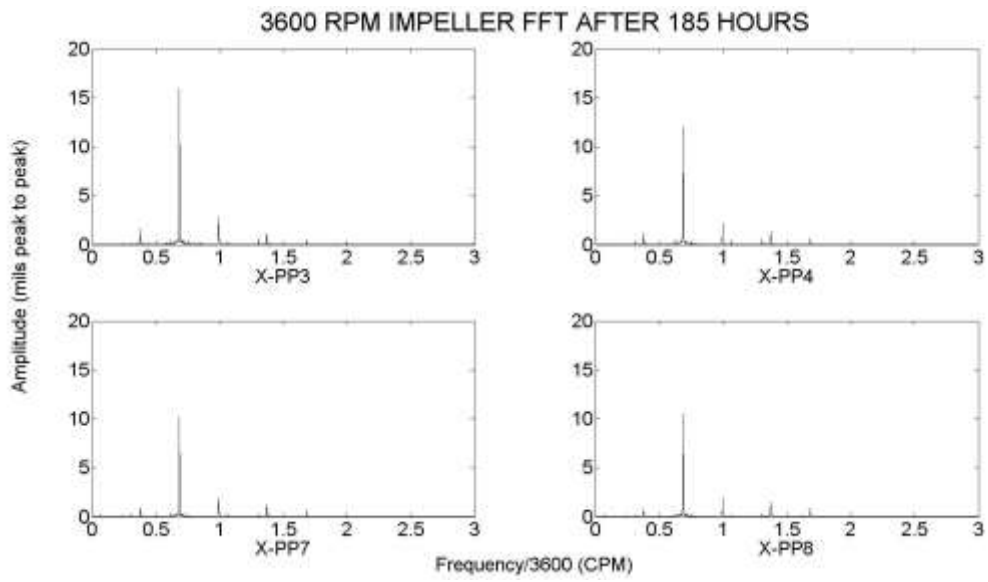


Figure 276. Impeller FFT – 185 Hours

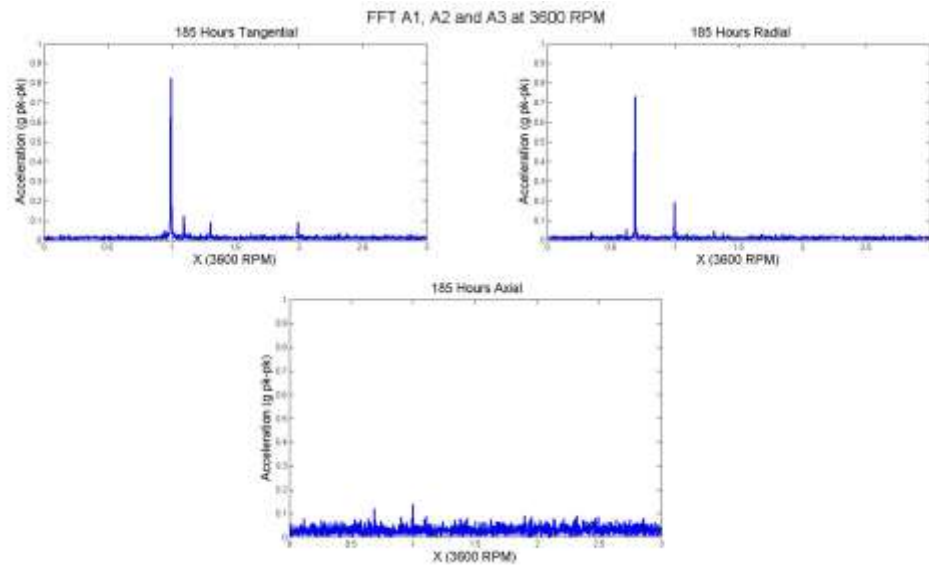


Figure 277. Inlet Accelerometer FFT – 185 Hours

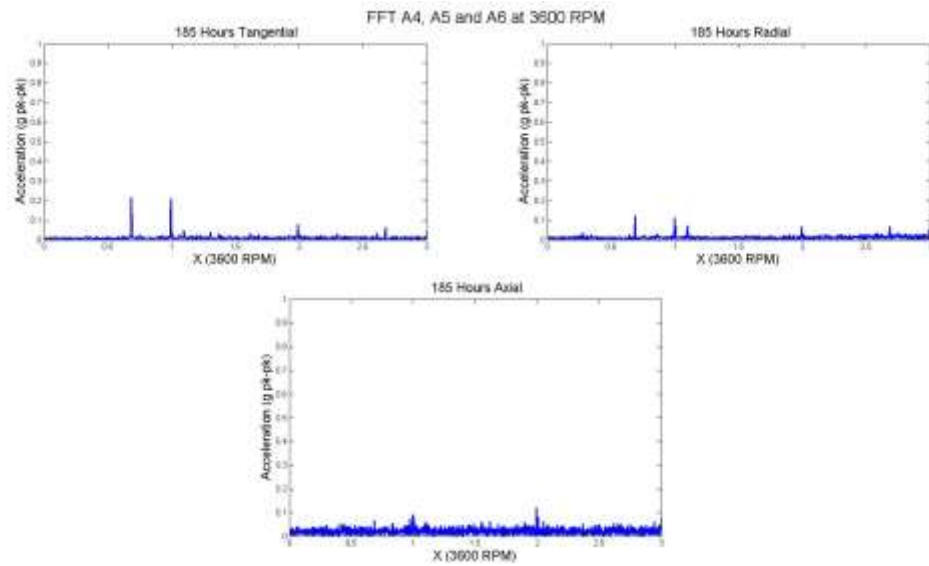


Figure 278. Outlet Accelerometer FFT – 185 Hours

PP1 3600 RPM SHAFT WATERFALLS AFTER 185 HOURS

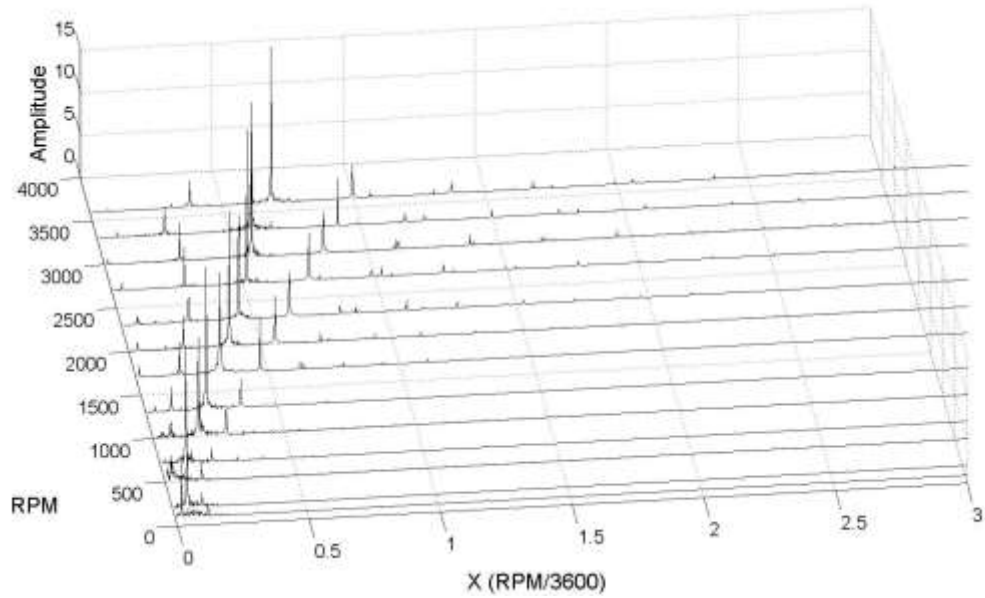


Figure 279. PP1 Waterfall Spectrum – 185 Hours

PP2 3600 RPM SHAFT WATERFALLS AFTER 185 HOURS

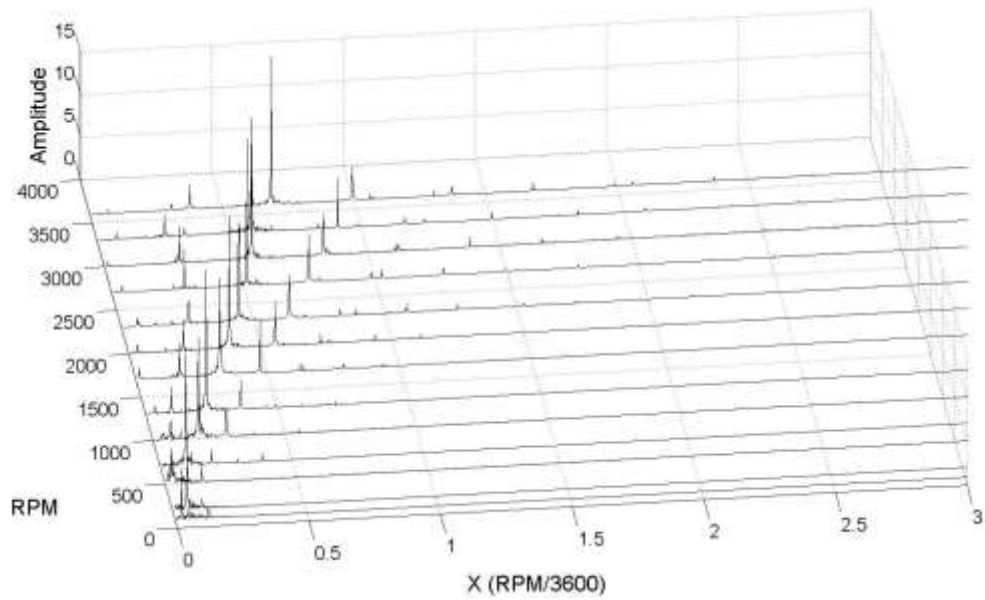


Figure 280. PP2 Waterfall Spectrum – 185 Hours

PP3 3600 RPM IMPELLER WATERFALLS AFTER 185 HOURS

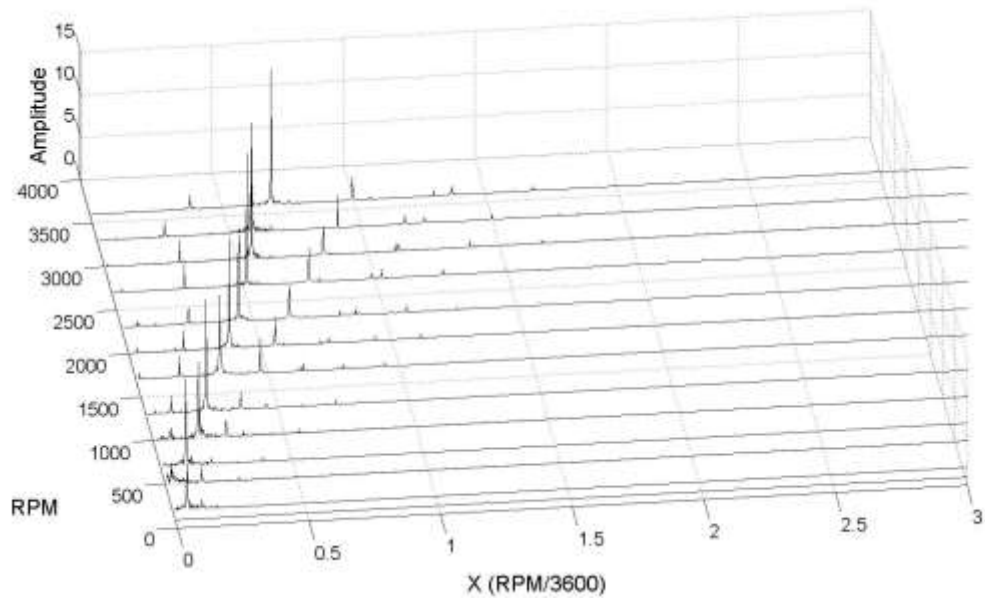


Figure 281. PP3 Waterfall Spectrum – 185 Hours

PP4 3600 RPM IMPELLER WATERFALLS AFTER 185 HOURS

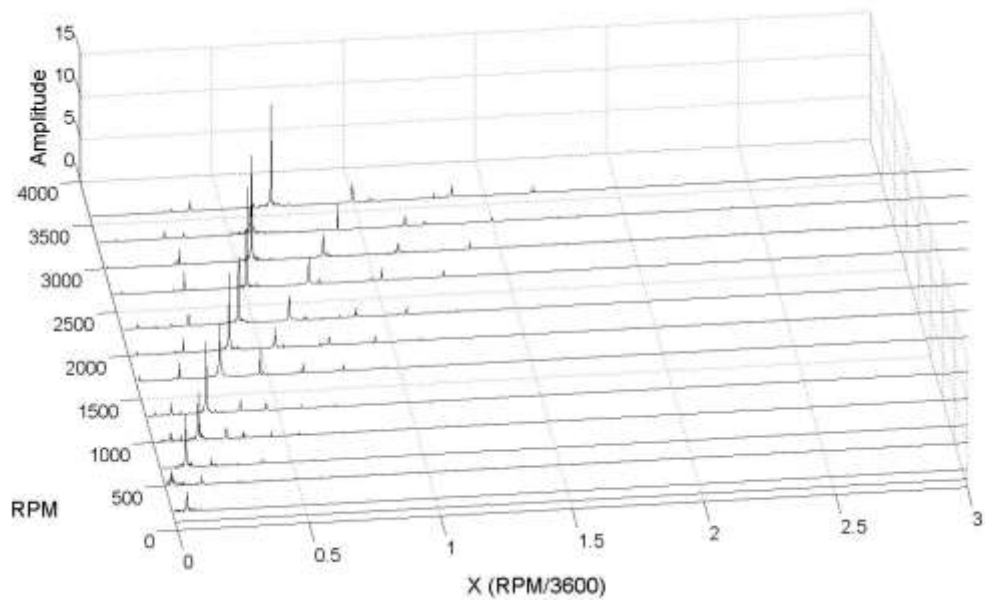


Figure 282. PP4 Waterfall Spectrum – 185 Hours

PP5 3600 RPM SHAFT WATERFALLS AFTER 185 HOURS

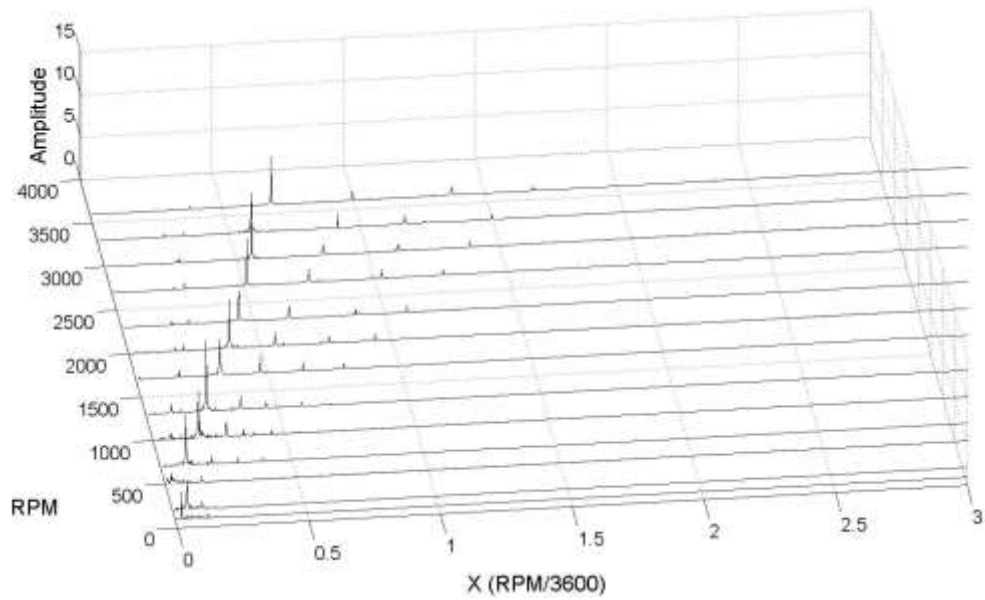


Figure 283. PP5 Waterfall Spectrum – 185 Hours

PP6 3600 RPM SHAFT WATERFALLS AFTER 185 HOURS

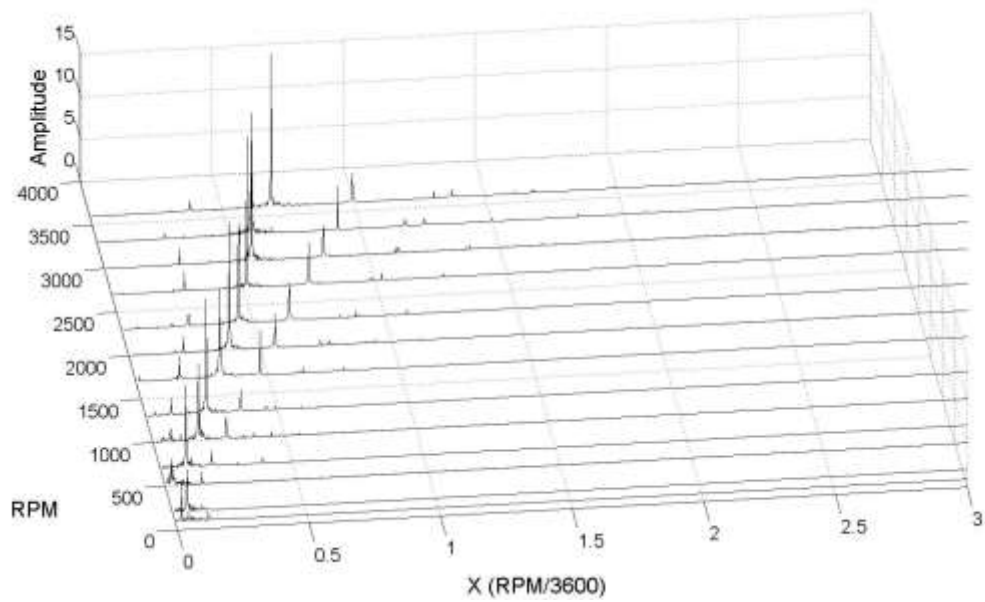


Figure 284. PP6 Waterfall Spectrum – 185 Hours

PP7 3600 RPM IMPELLER WATERFALLS AFTER 185 HOURS

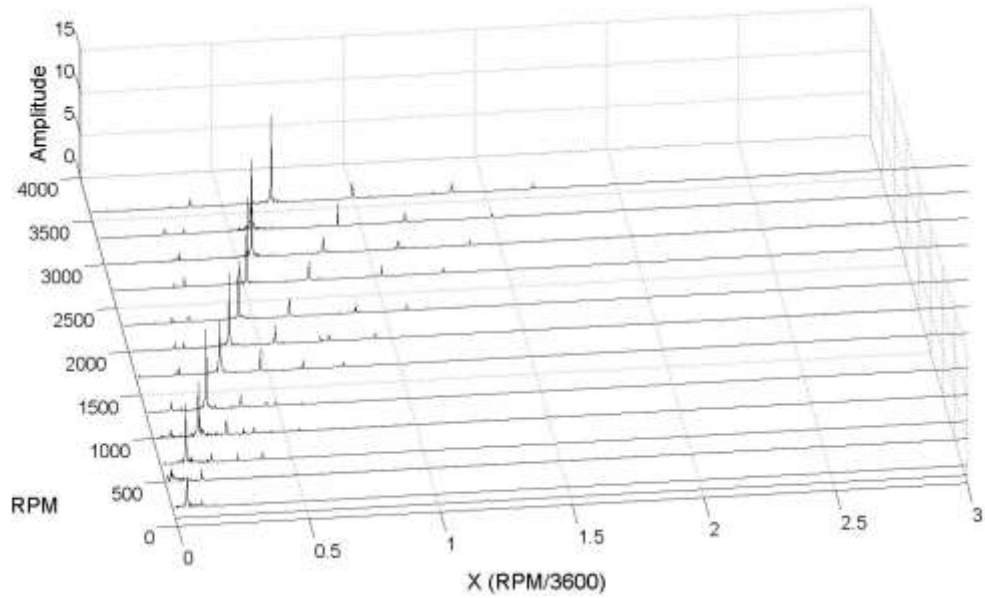


Figure 285. PP7 Waterfall Spectrum – 185 Hours

PP8 3600 RPM IMPELLER WATERFALLS AFTER 185 HOURS

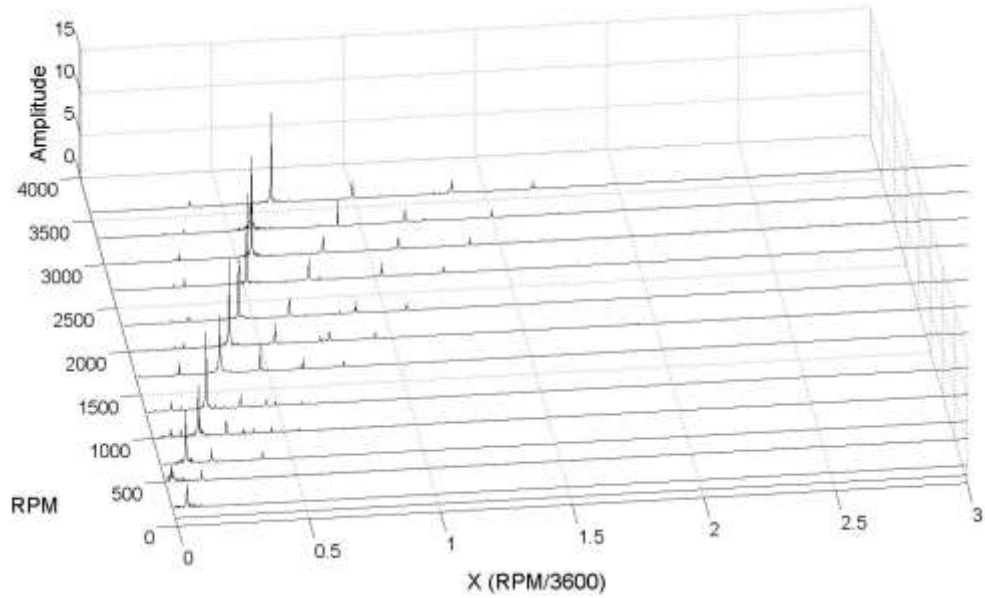


Figure 286. PP8 Waterfall Spectrum – 185 Hours

PP9 3600 RPM SHAFT WATERFALLS AFTER 185 HOURS

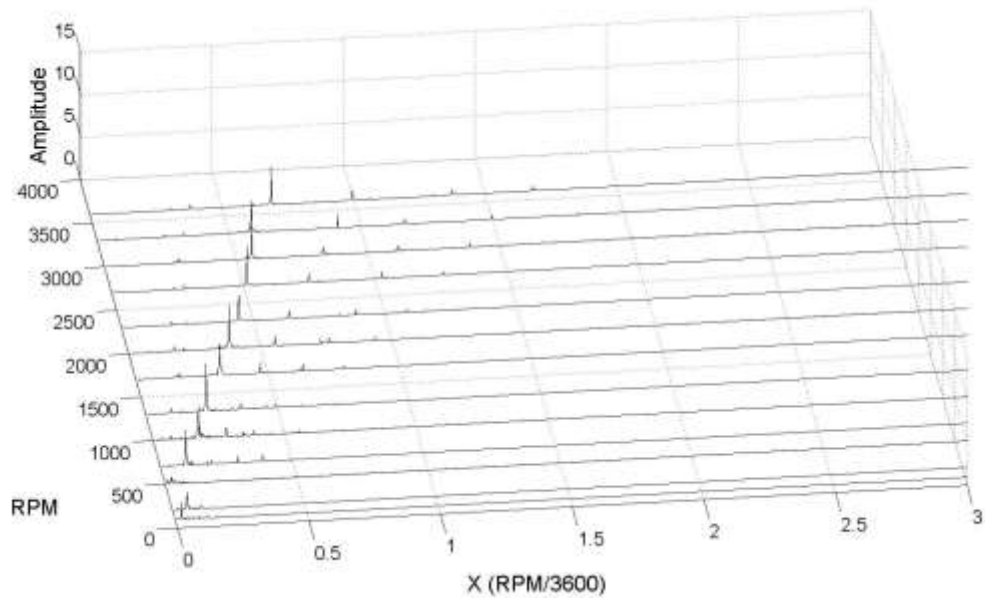


Figure 287. PP9 Waterfall Spectrum – 185 Hours

PP10 3600 RPM SHAFT WATERFALLS AFTER 185 HOURS

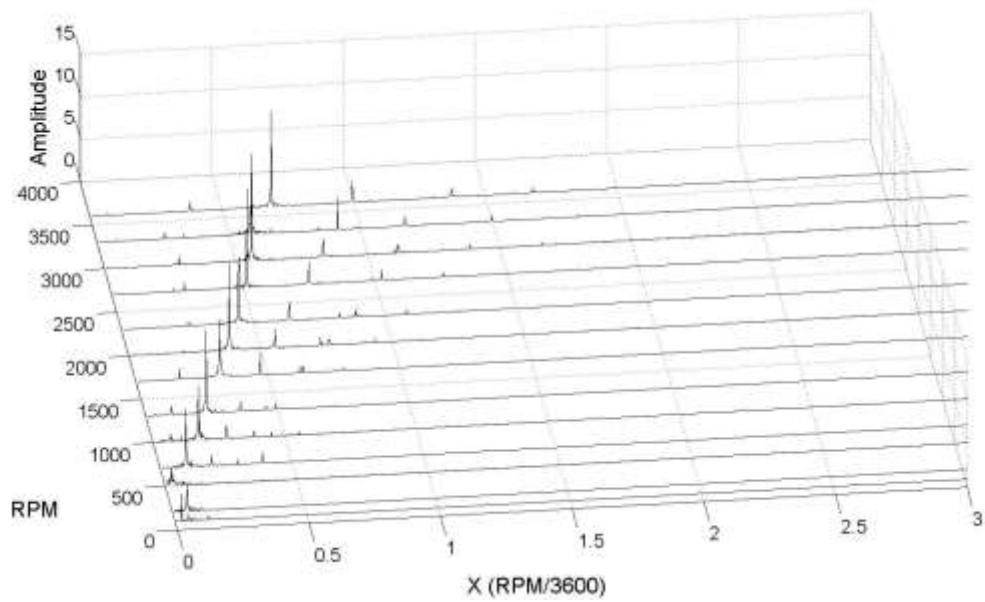


Figure 288. PP10 Waterfall Spectrum – 185 Hours

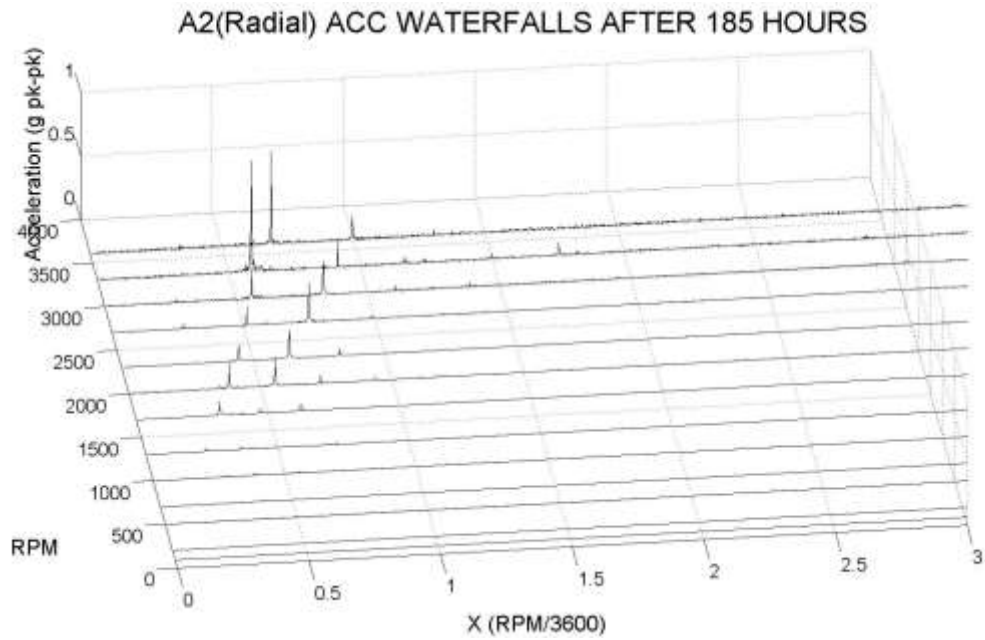


Figure 289. Inlet Accelerometer Radial Waterfall Spectrum – 185 Hours

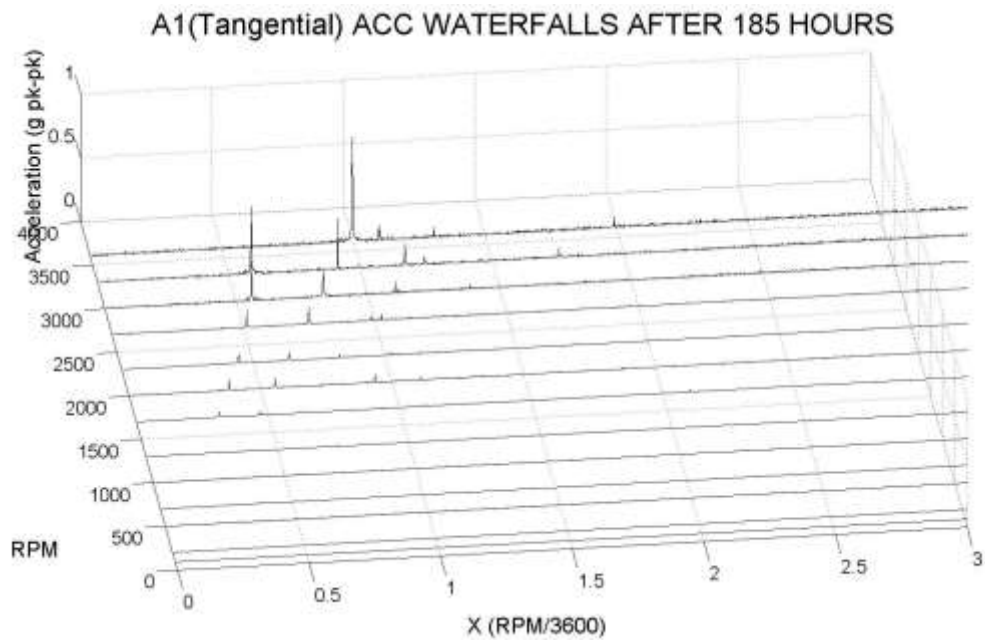


Figure 290. Inlet Accelerometer Tangential Waterfall Spectrum – 185 Hours

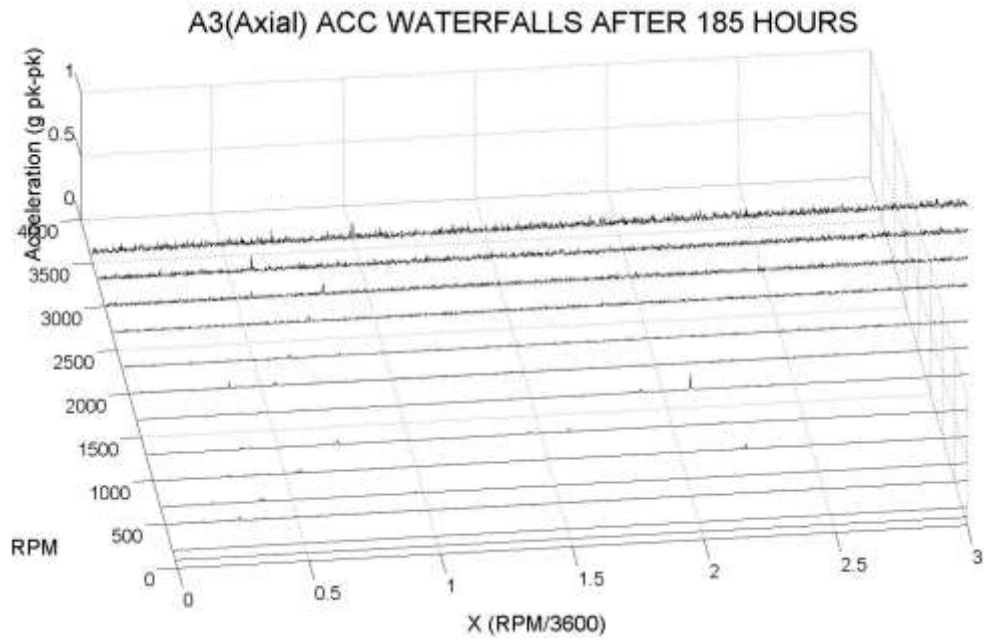


Figure 291. Inlet Accelerometer Axial Waterfall Spectrum – 185 Hours

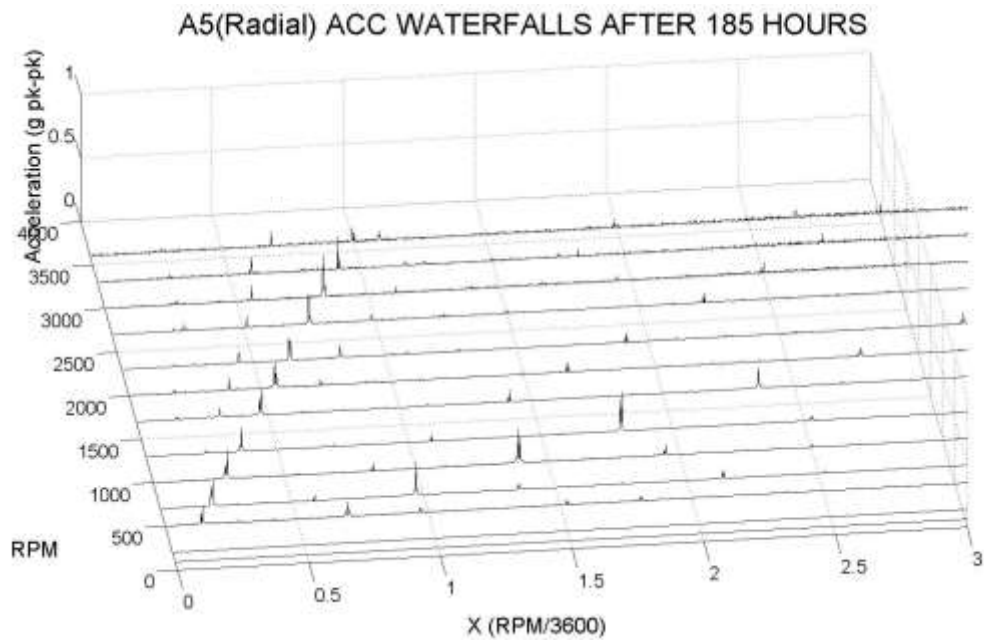


Figure 292. Outlet Accelerometer Radial Waterfall Spectrum – 185 Hours

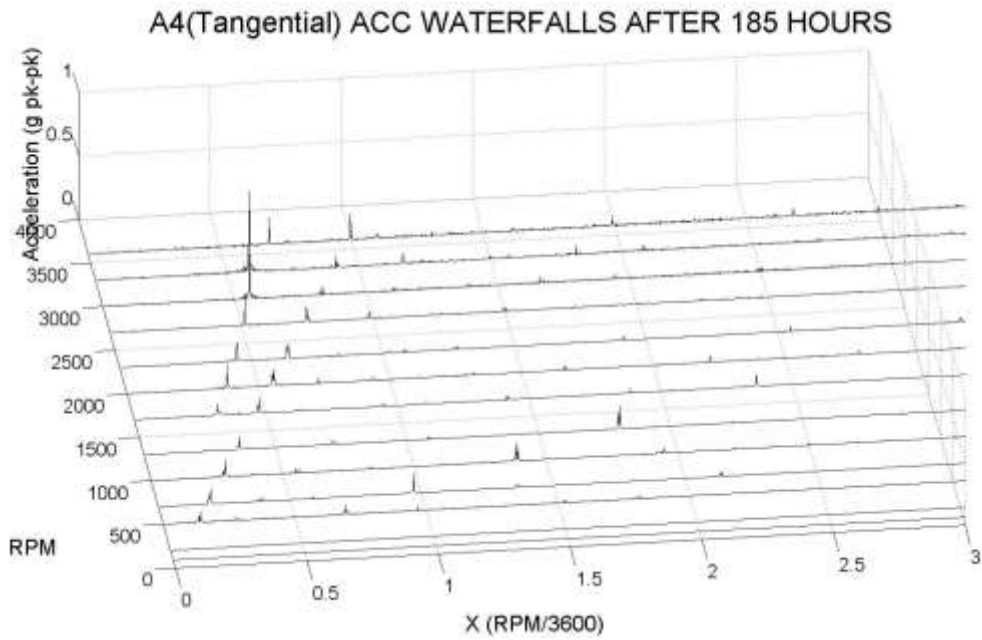


Figure 293. Outlet Accelerometer Tangential Waterfall Spectrum – 185 Hours

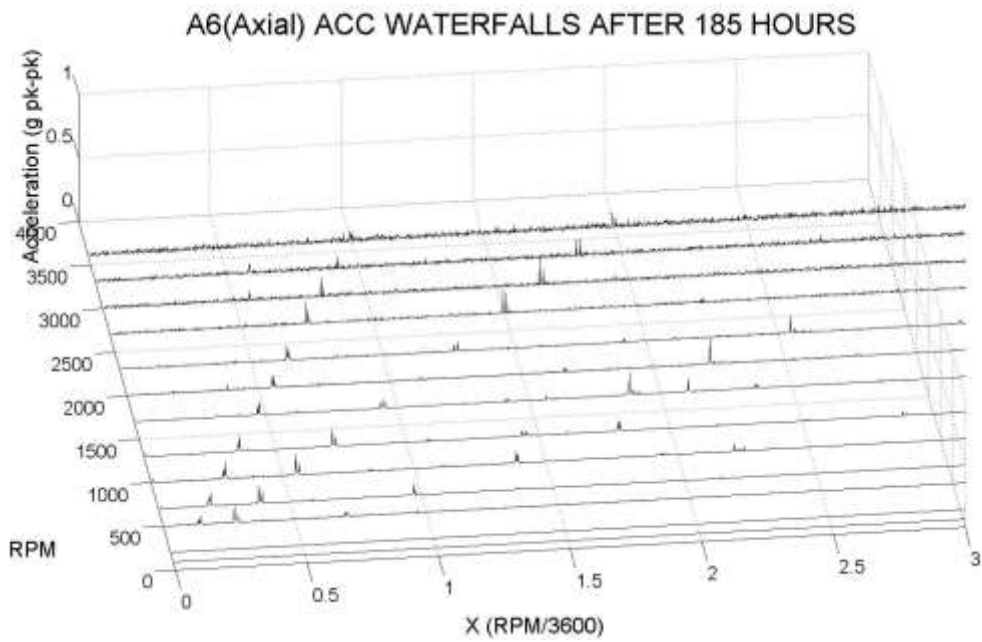


Figure 294. Outlet Accelerometer Axial Waterfall Spectrum – 185 Hours

D.7. FFT vs Time

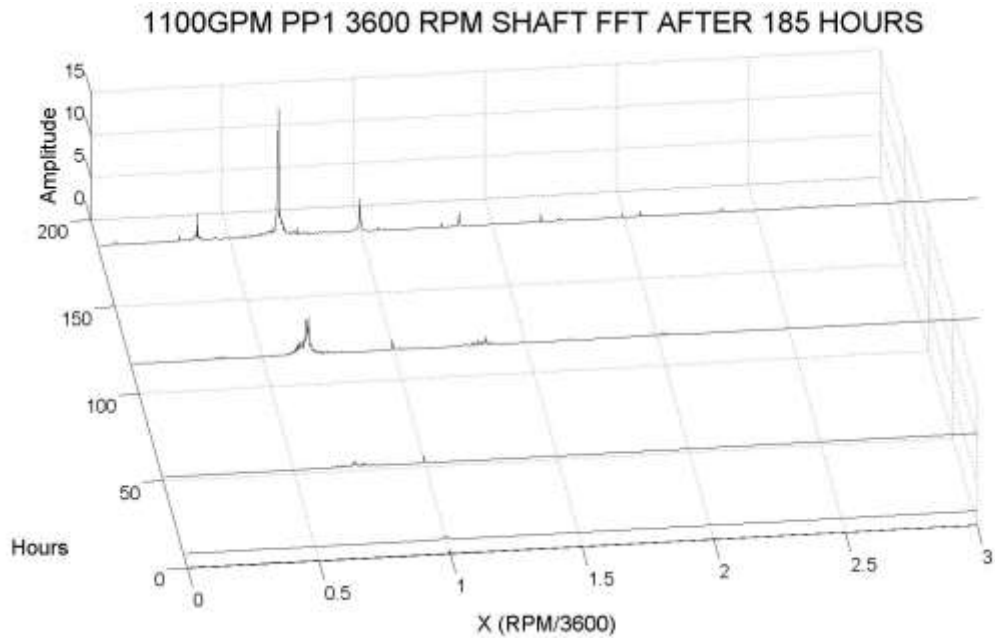


Figure 295. PP1 FFT vs Time Spectrum

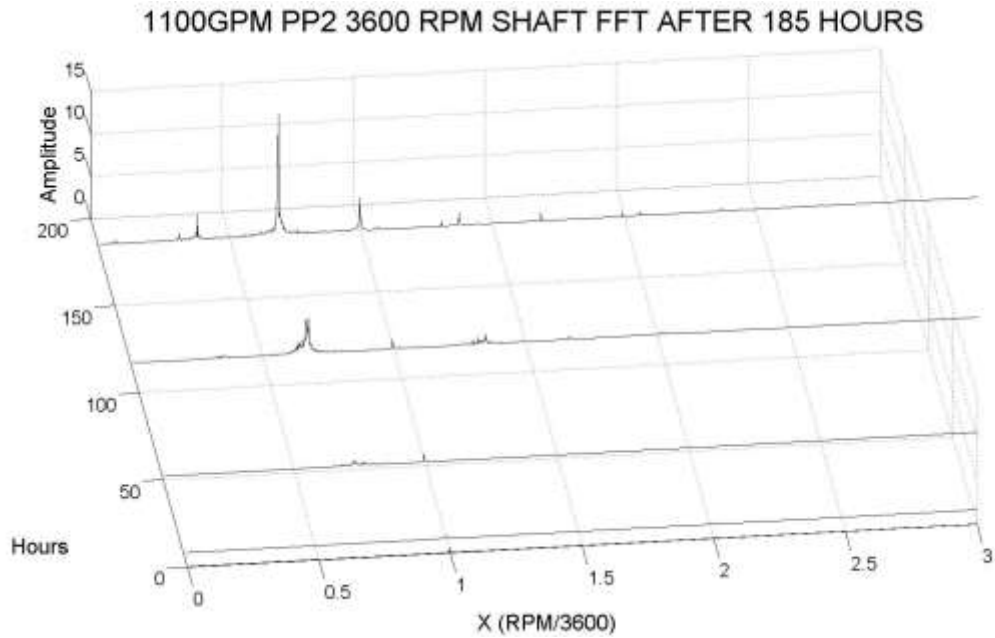


Figure 296. PP2 FFT vs Time Spectrum

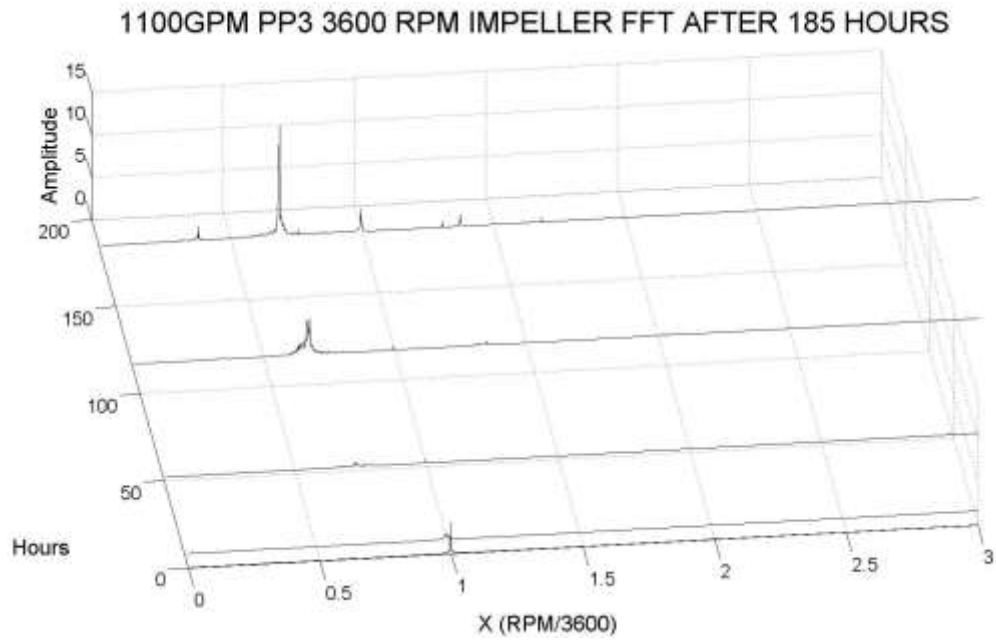


Figure 297. PP3 FFT vs Time Spectrum

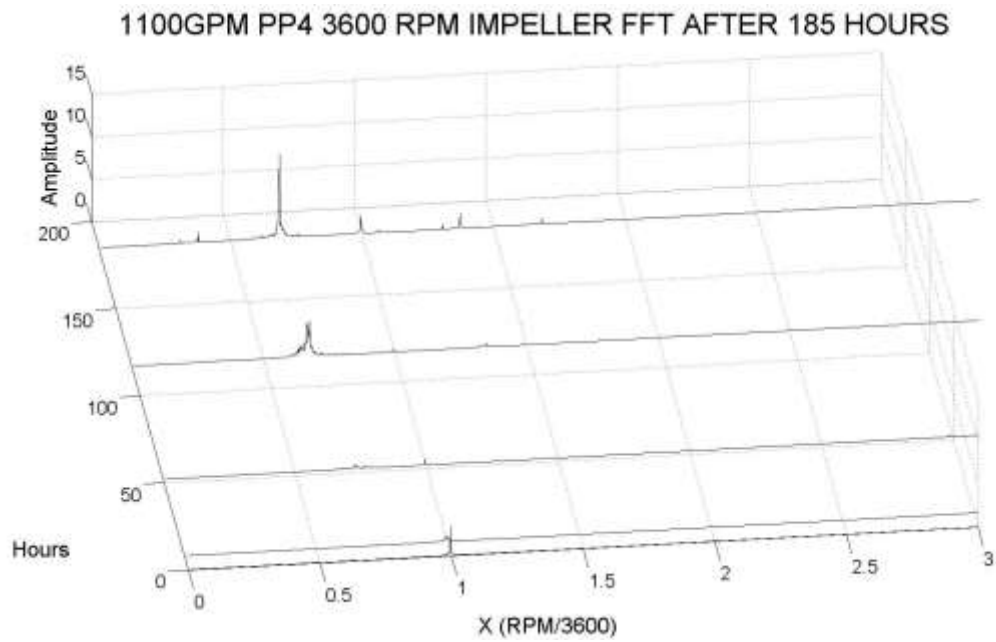


Figure 298. PP4 FFT vs Time Spectrum

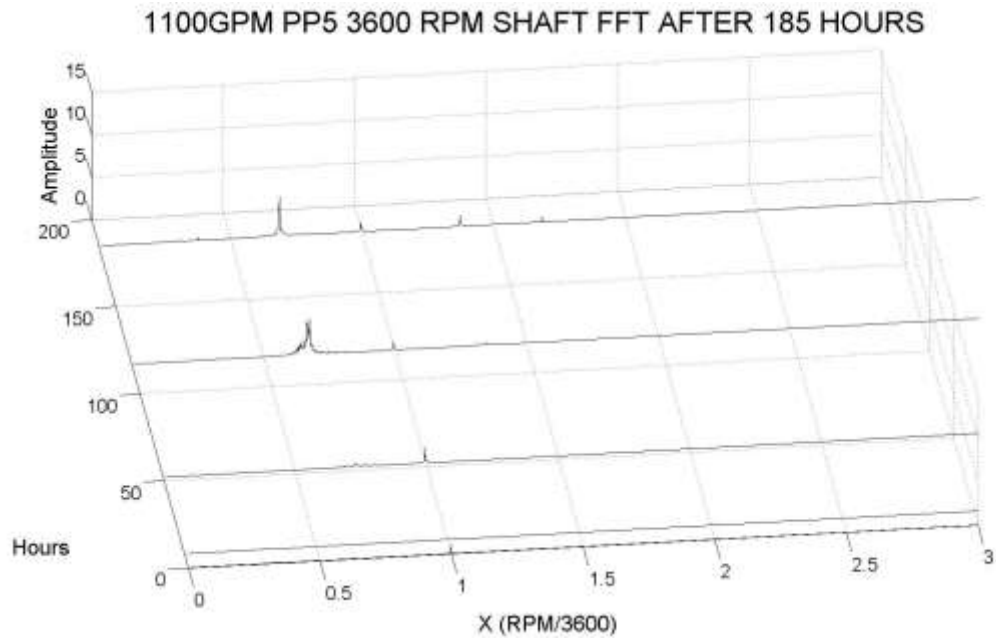


Figure 299. PP5 FFT vs Time Spectrum

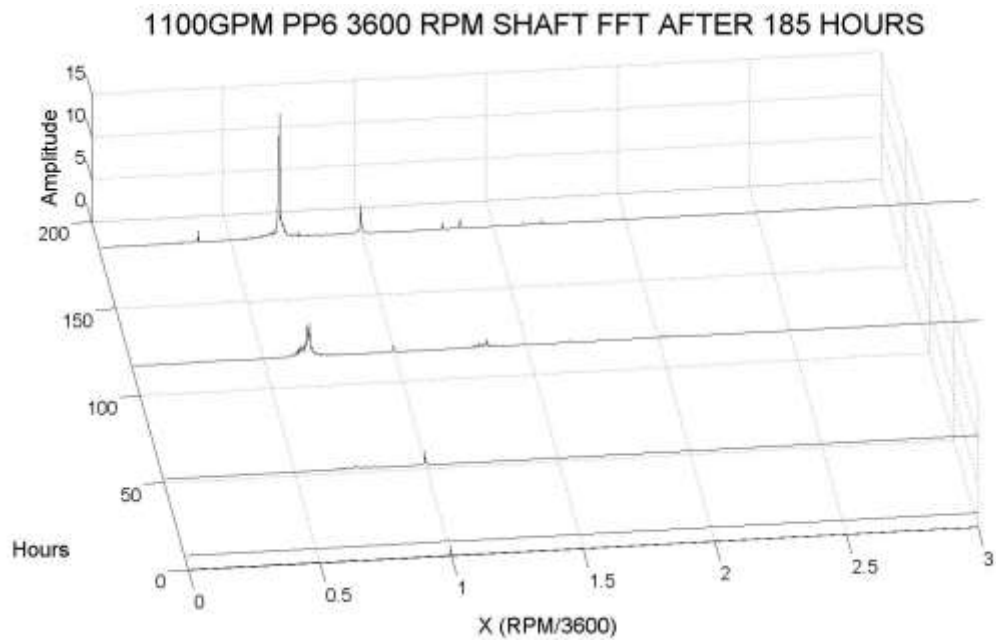


Figure 300. PP6 FFT vs Time Spectrum

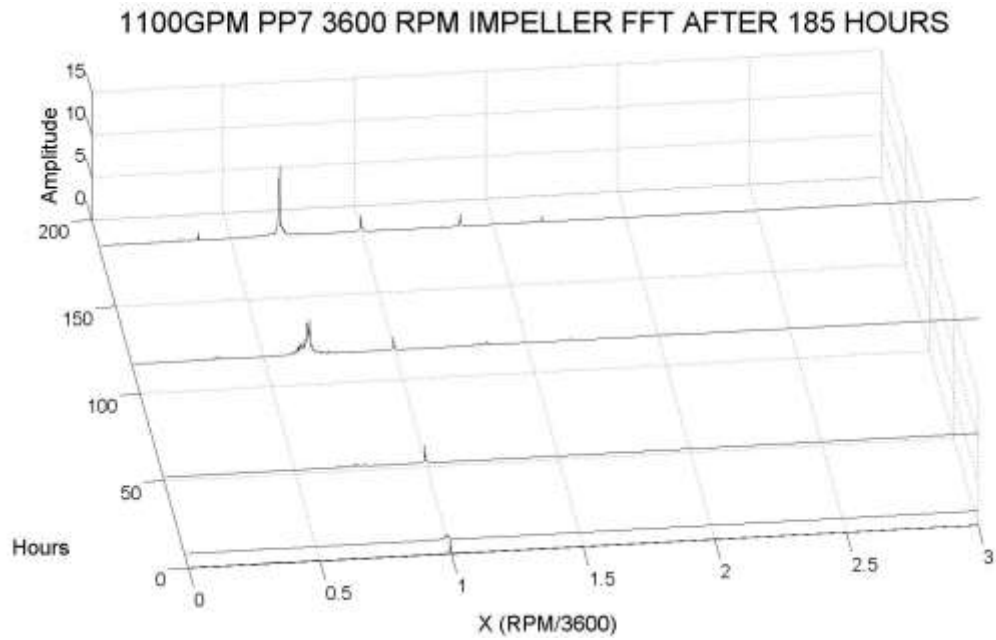


Figure 301. PP7 FFT vs Time Spectrum

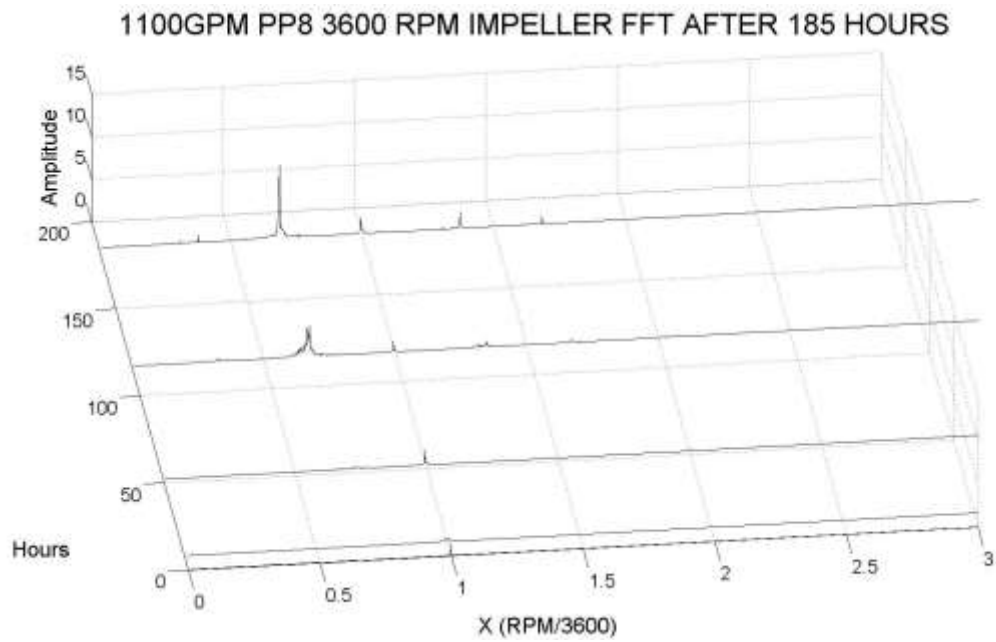


Figure 302. PP8 FFT vs Time Spectrum

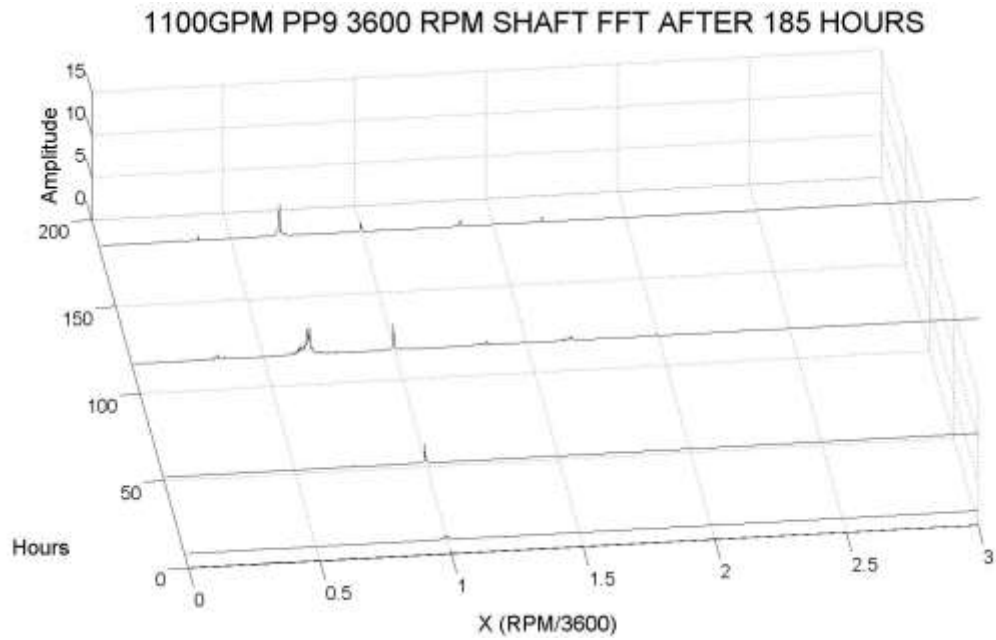


Figure 303. PP9 FFT vs Time Spectrum

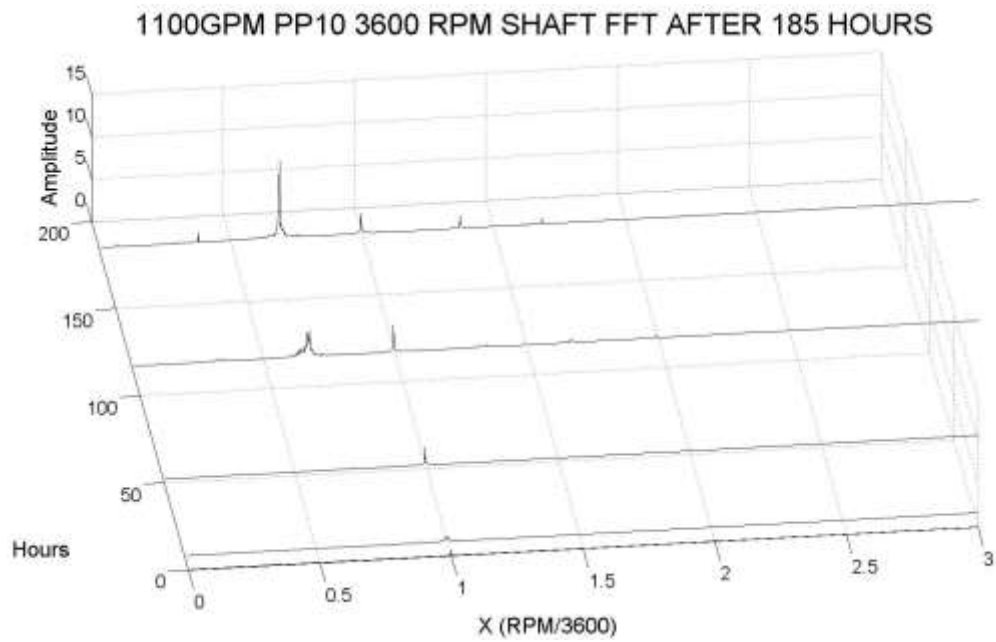


Figure 304. PP10 FFT vs Time Spectrum

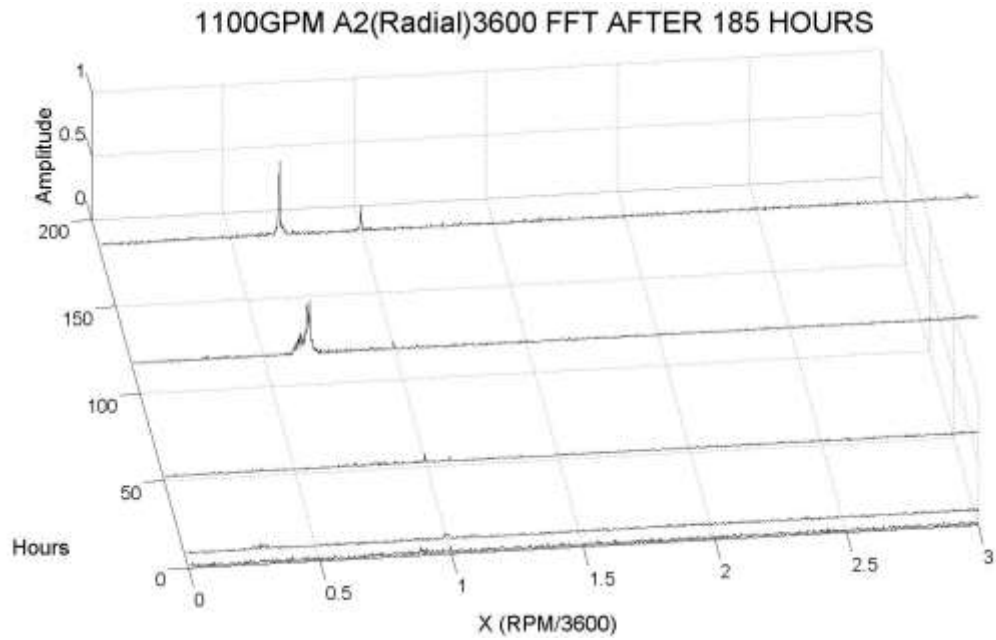


Figure 305. Inlet Radial FFT vs Time Spectrum

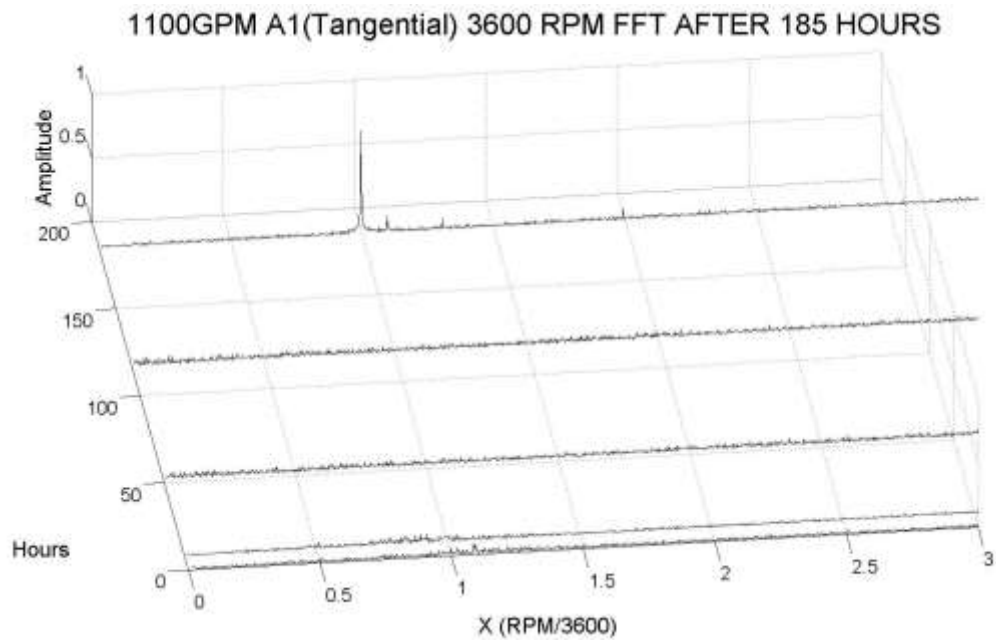


Figure 306. Inlet Tangential FFT vs Time Spectrum

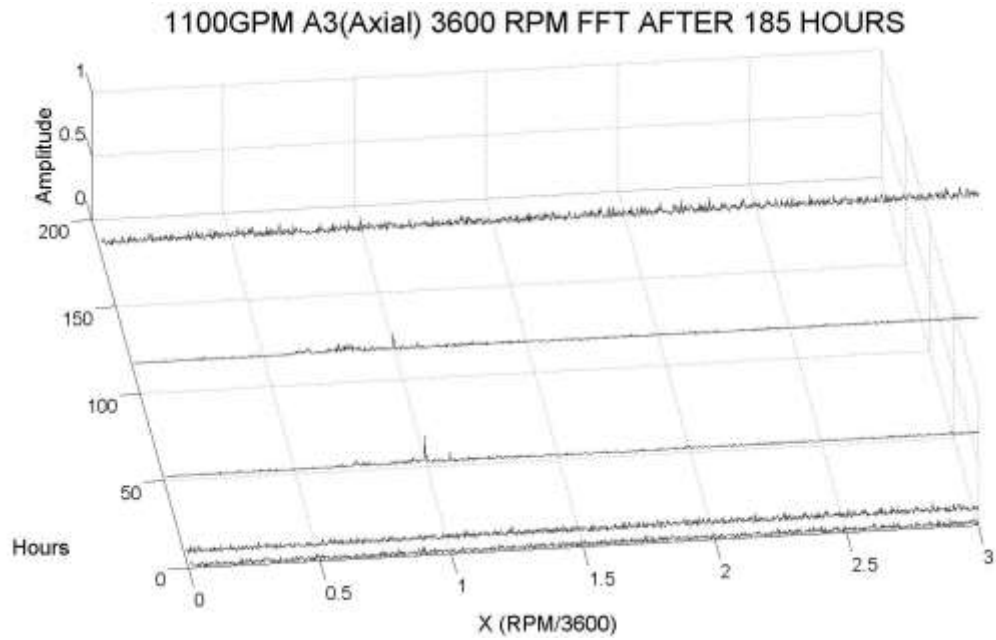


Figure 307. Inlet Axial FFT vs Time Spectrum

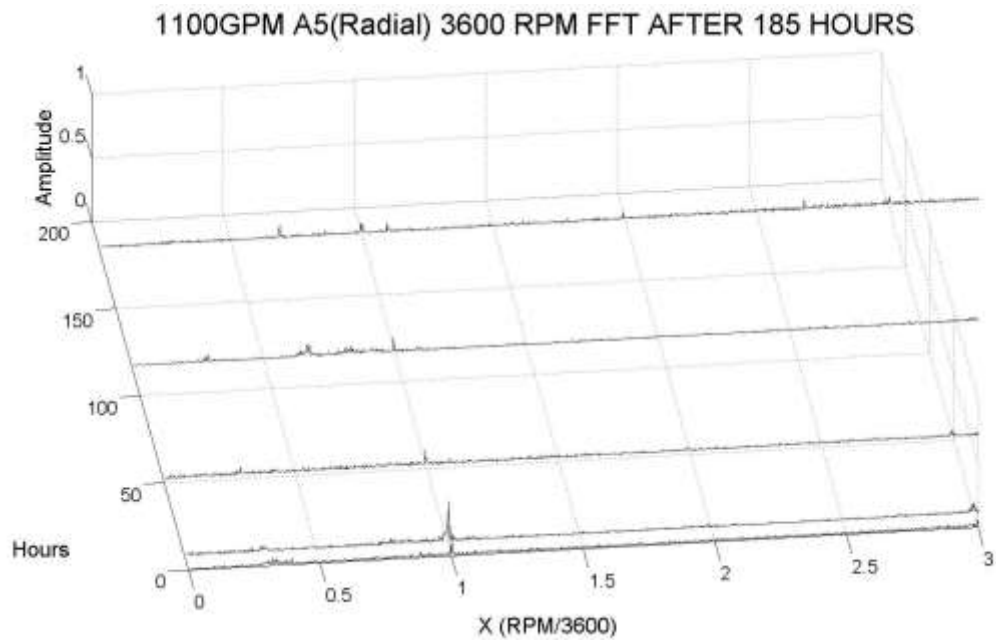


Figure 308. Outlet Radial FFT vs Time Spectrum

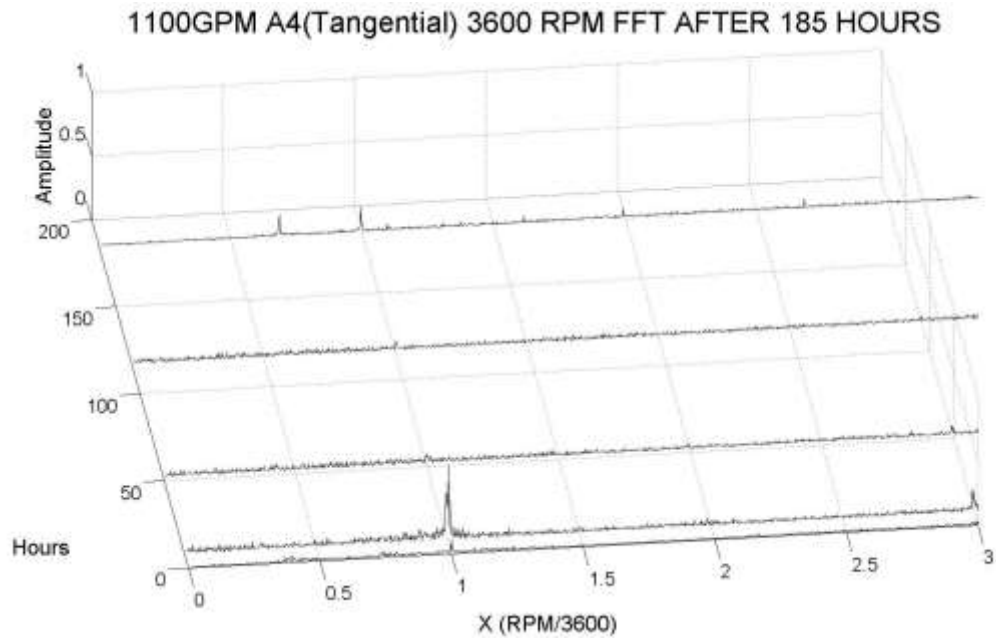


Figure 309. Outlet Tangential FFT vs Time Spectrum

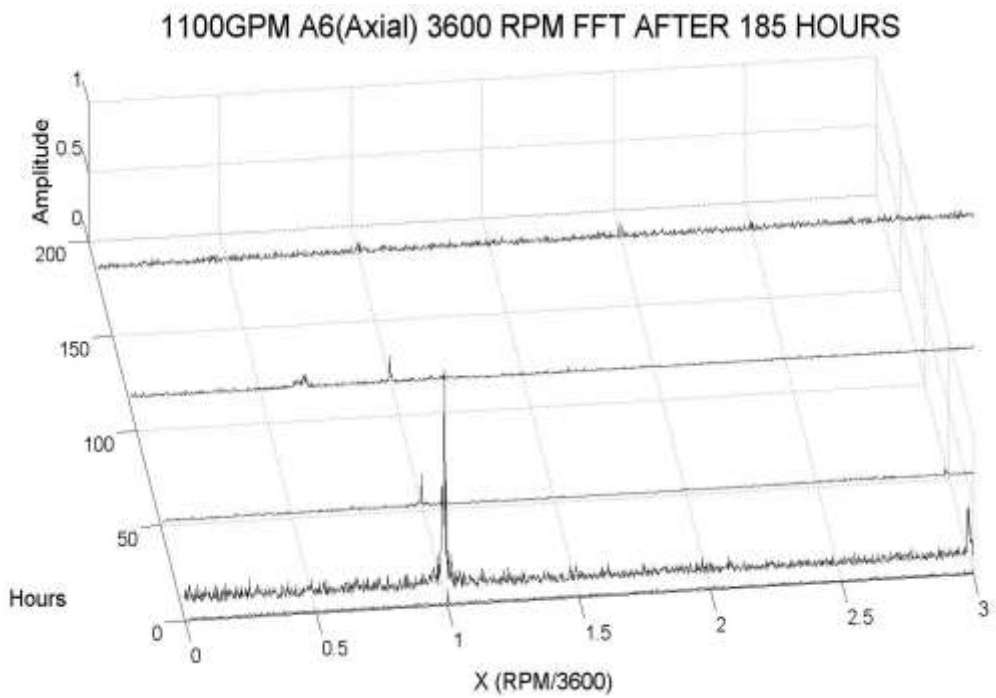
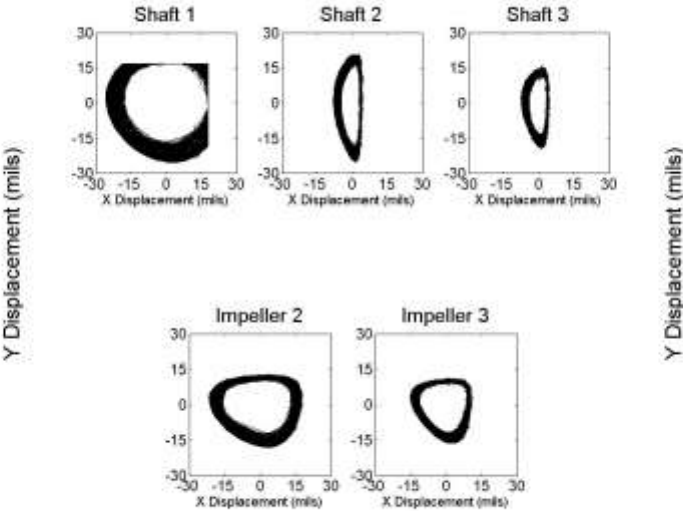


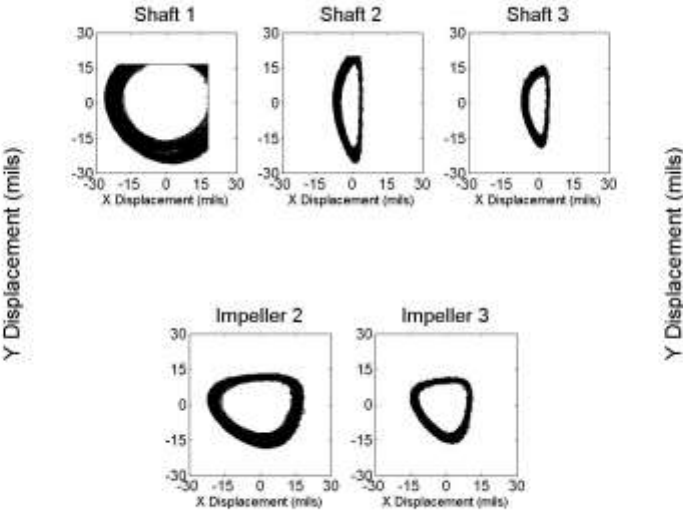
Figure 310. Outlet Axial FFT vs Time Spectrum

D.8. Vibration Signature vs GVF



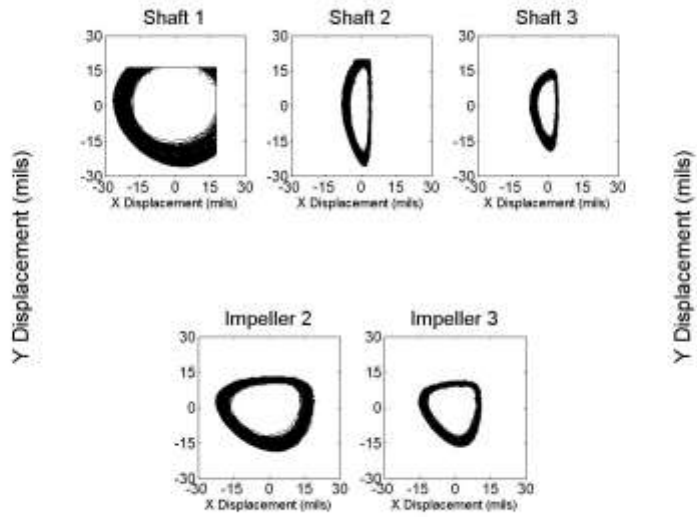
185

Figure 311. 0% GVF Orbit



185

Figure 312. 10% GVF Orbit



185

Figure 313. 15% GVF Orbit

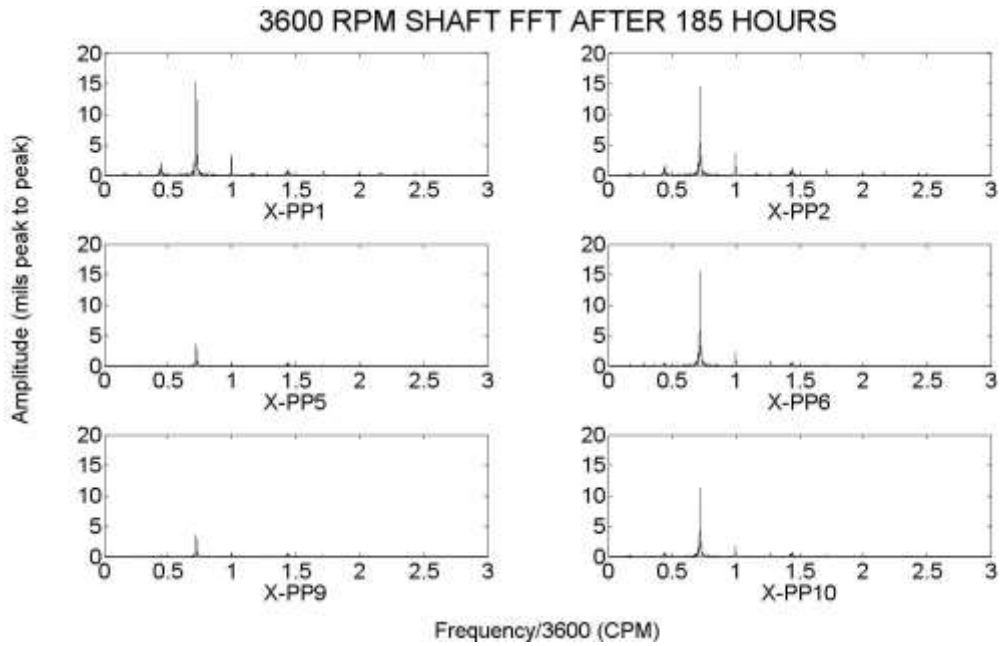


Figure 314. Shaft FFT at 15% GVF

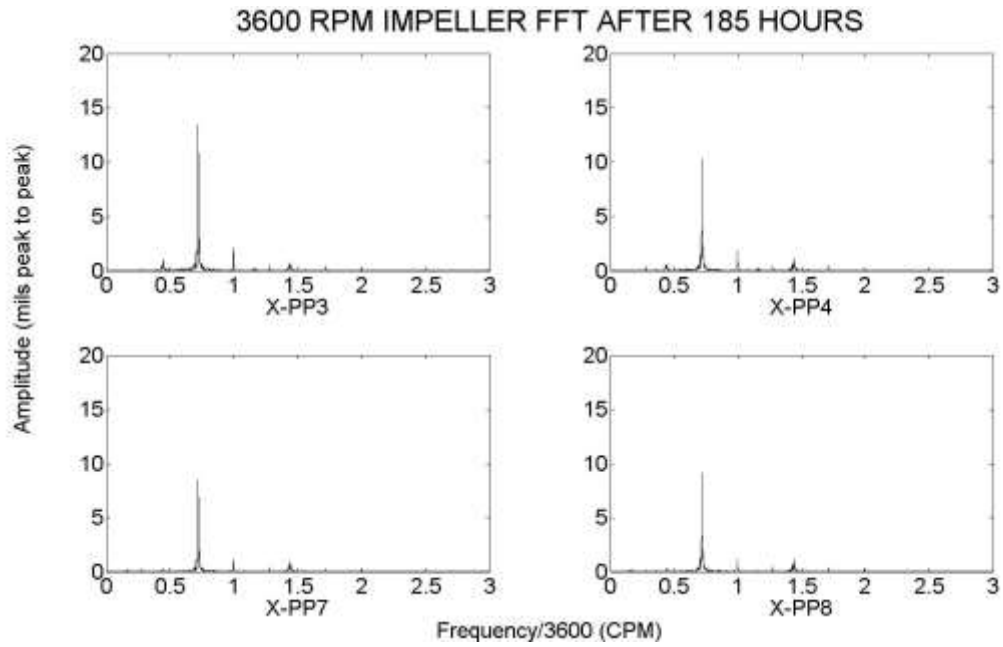


Figure 315. Impeller FFT at 15% GVF

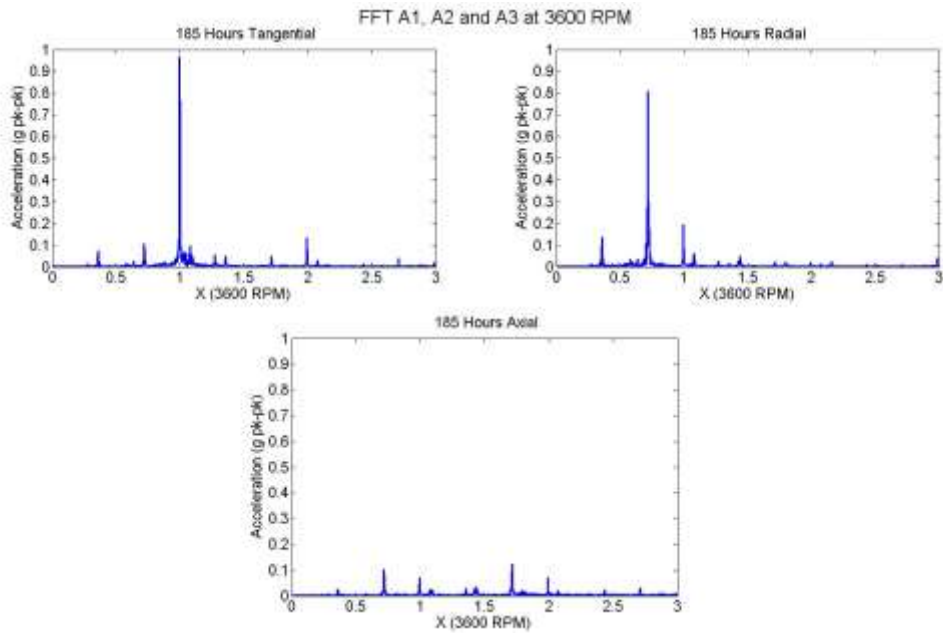


Figure 316. Inlet Accelerometer FFT at 15% GVF

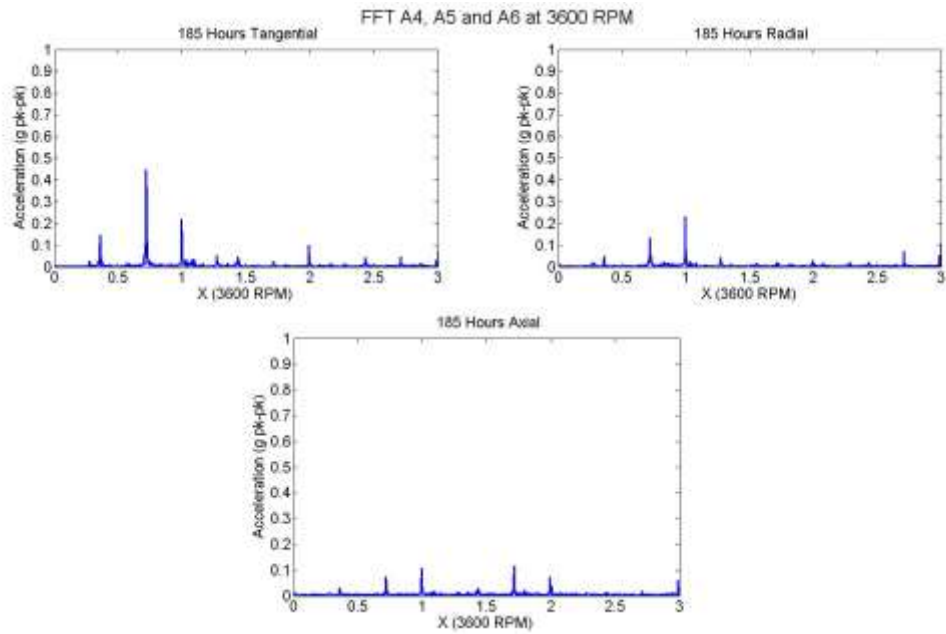


Figure 317. Outlet Accelerometer FFT at 15% GVF

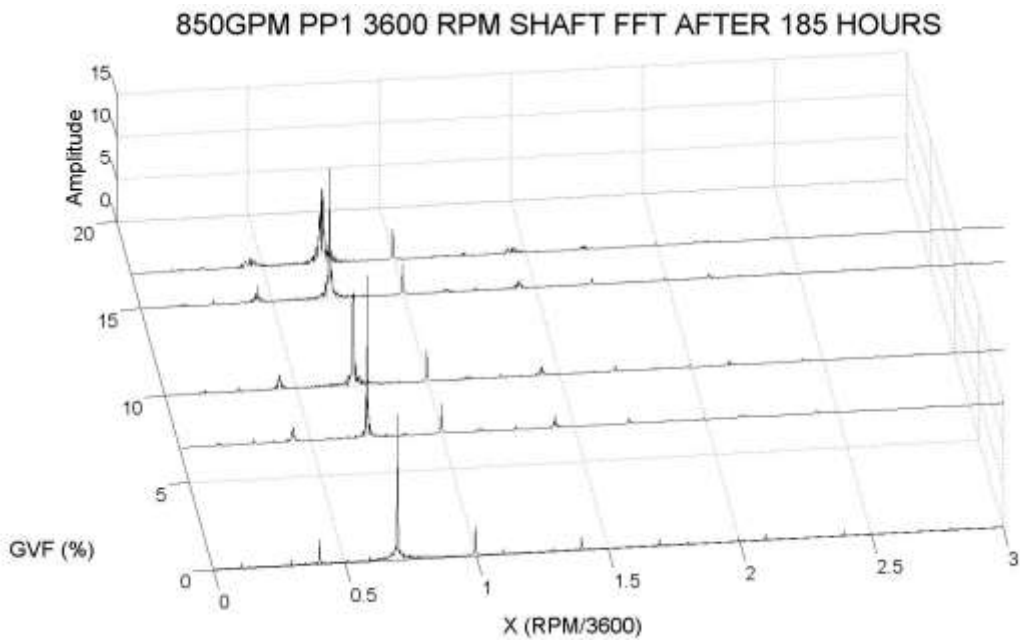


Figure 318. PP1 FFT vs GVF Spectrum

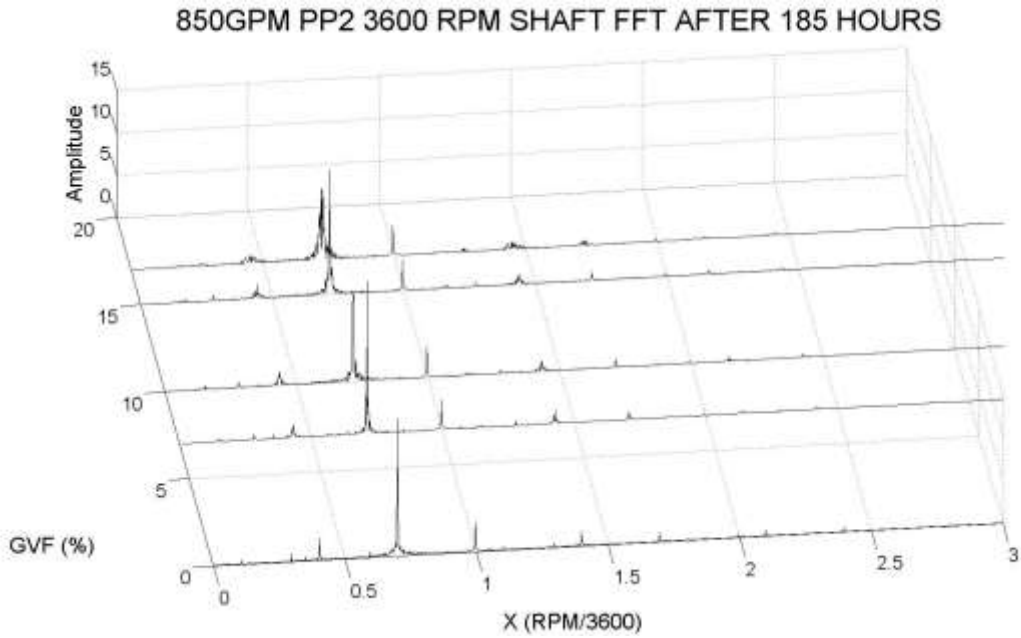


Figure 319. PP2 FFT vs GVF Spectrum

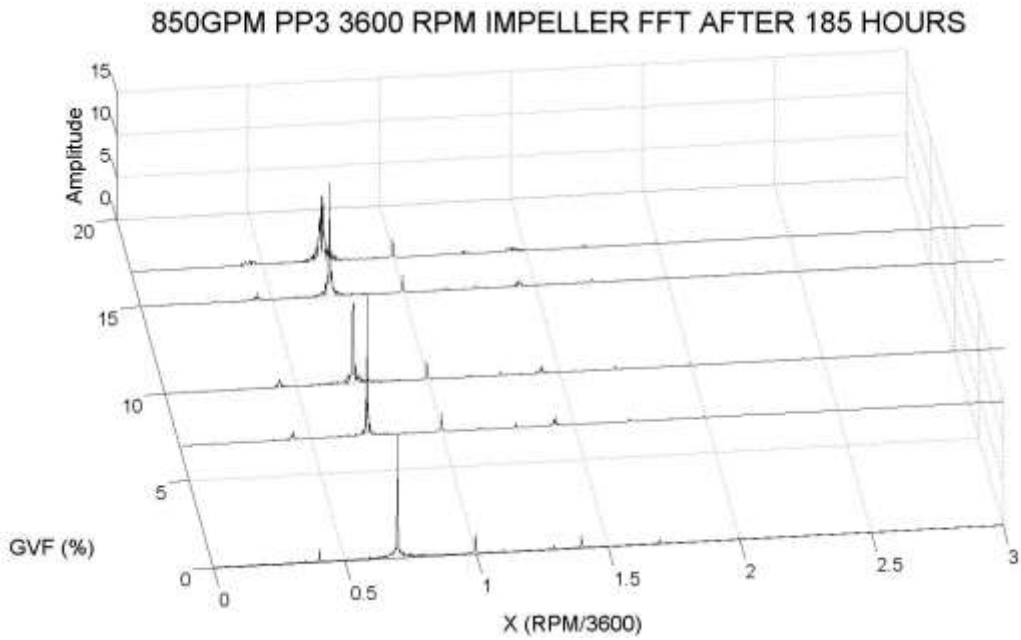


Figure 320. PP3 FFT vs GVF Spectrum

850GPM PP4 3600 RPM IMPELLER FFT AFTER 185 HOURS

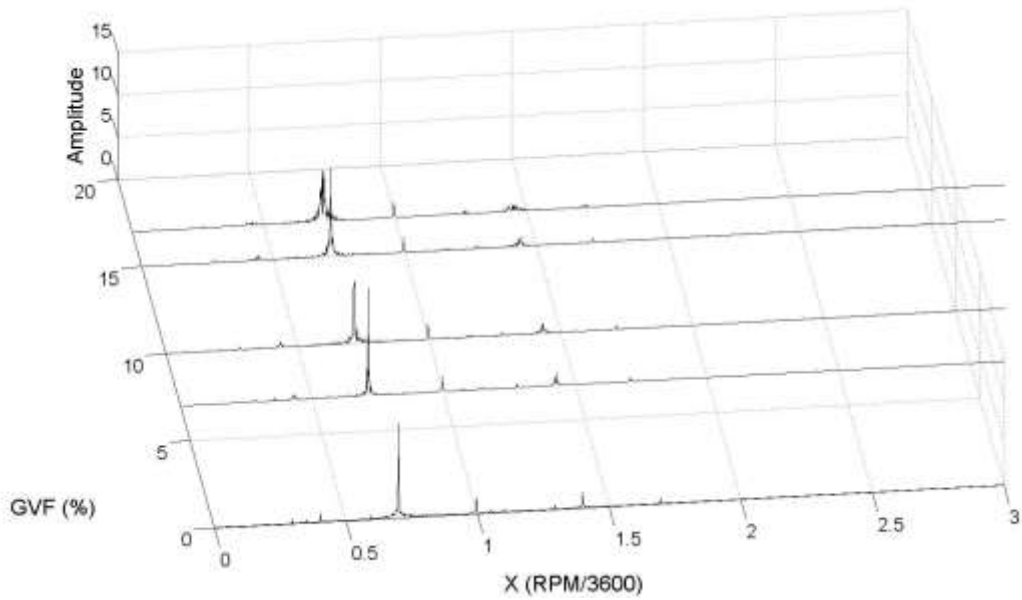


Figure 321. PP4 FFT vs GVF Spectrum

850GPM PP5 3600 RPM SHAFT FFT AFTER 185 HOURS

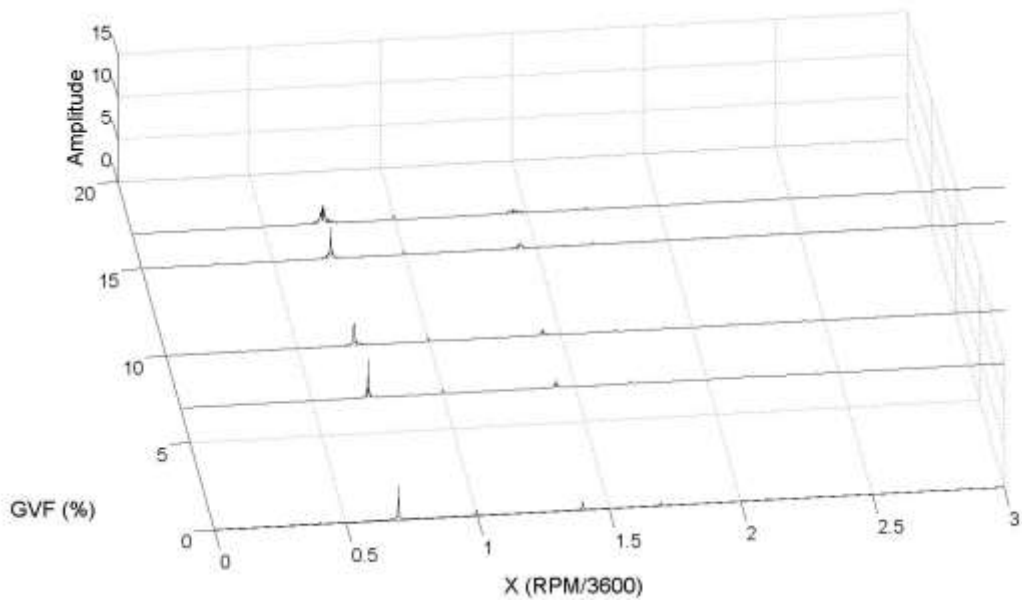


Figure 322. PP5 FFT vs GVF Spectrum

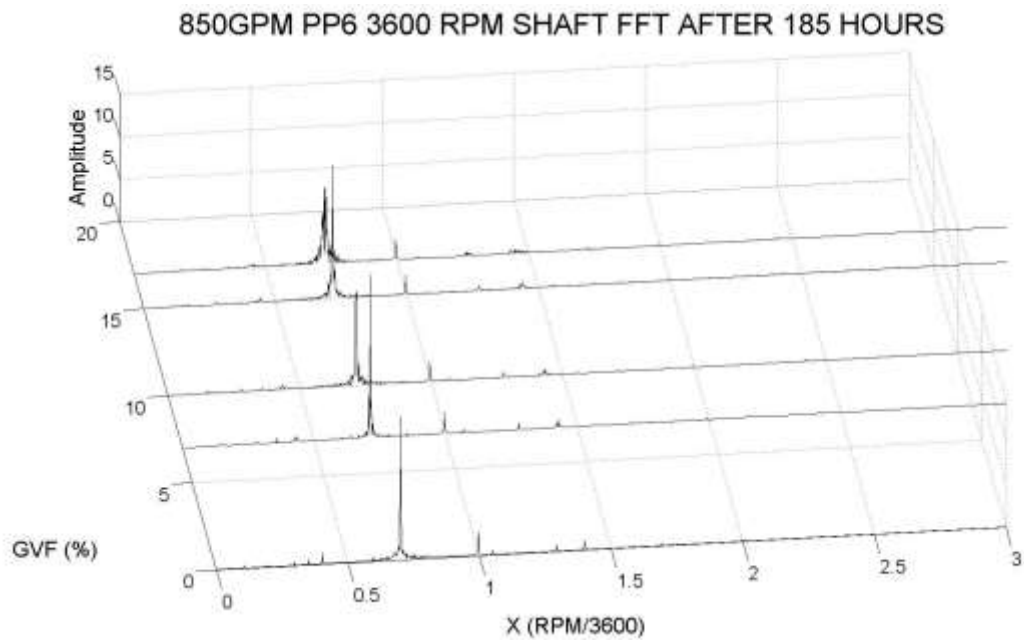


Figure 323. PP6 FFT vs GVF Spectrum

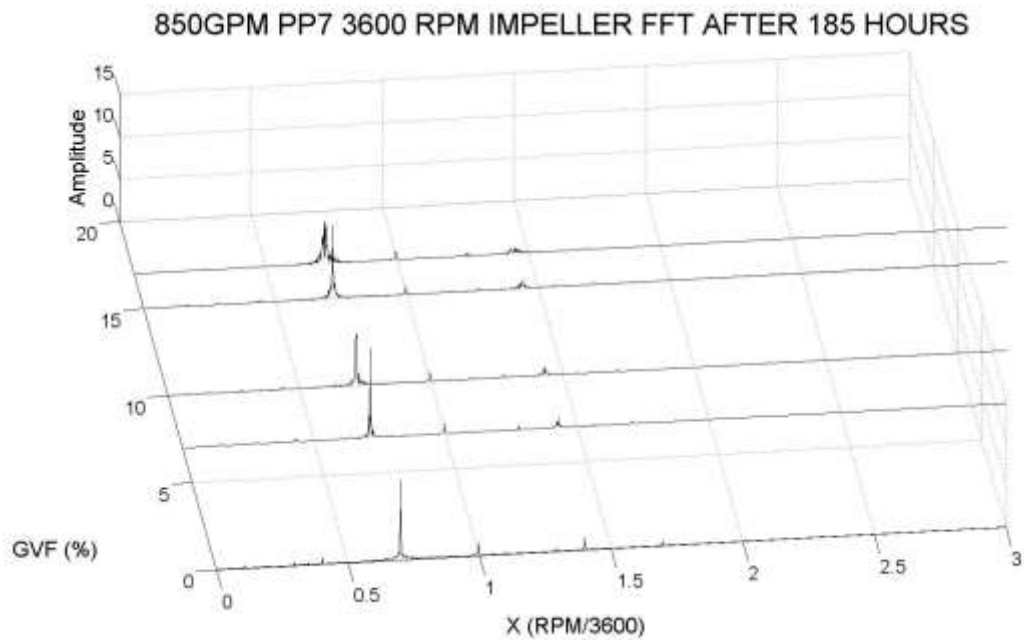


Figure 324. PP7 FFT vs GVF Spectrum

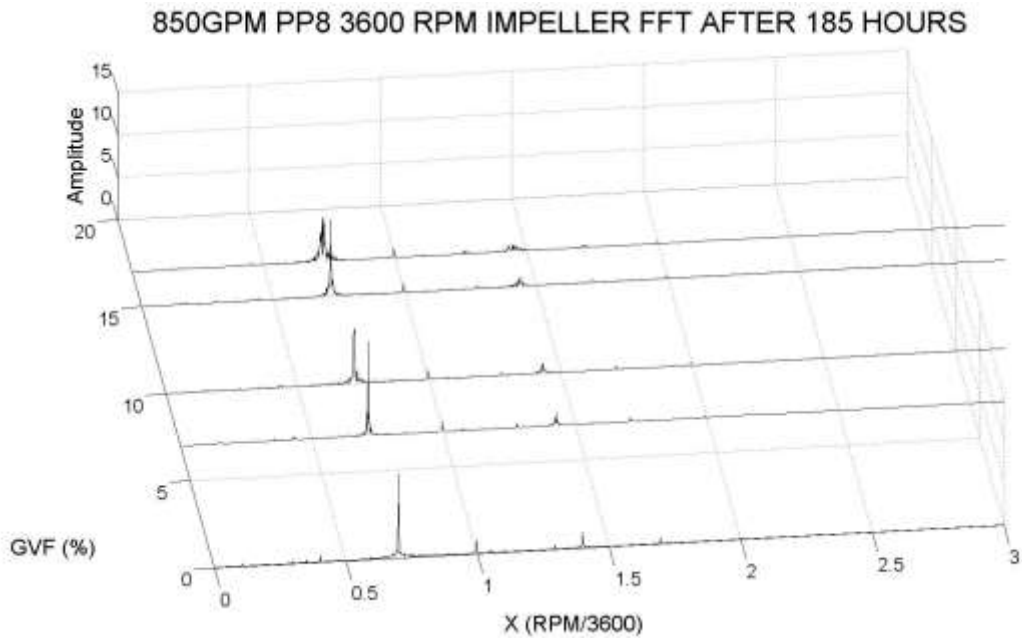


Figure 325. PP8 FFT vs GVF Spectrum

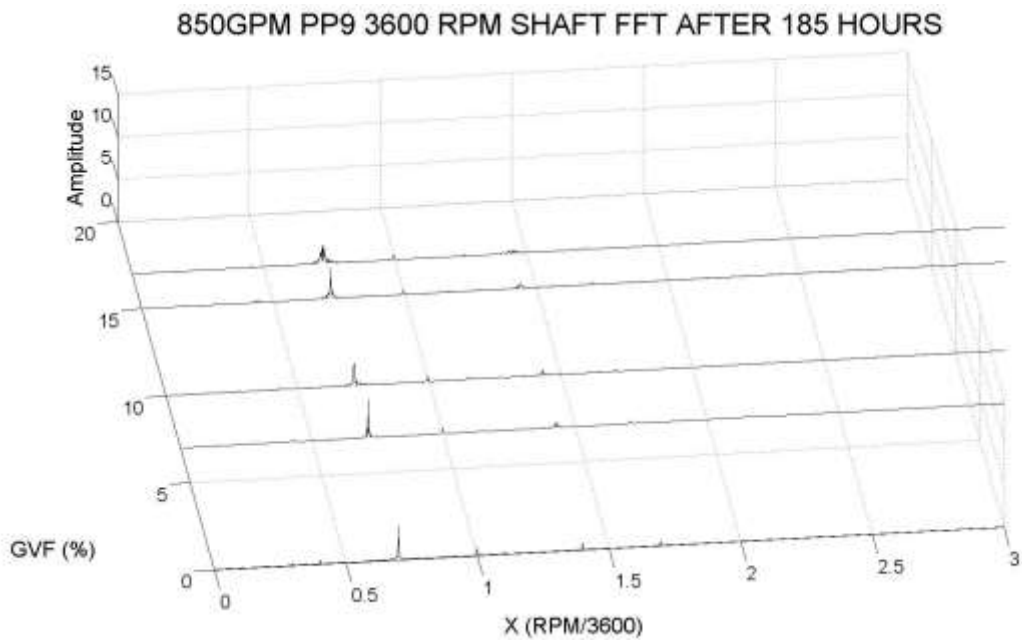


Figure 326. PP9 FFT vs GVF Spectrum

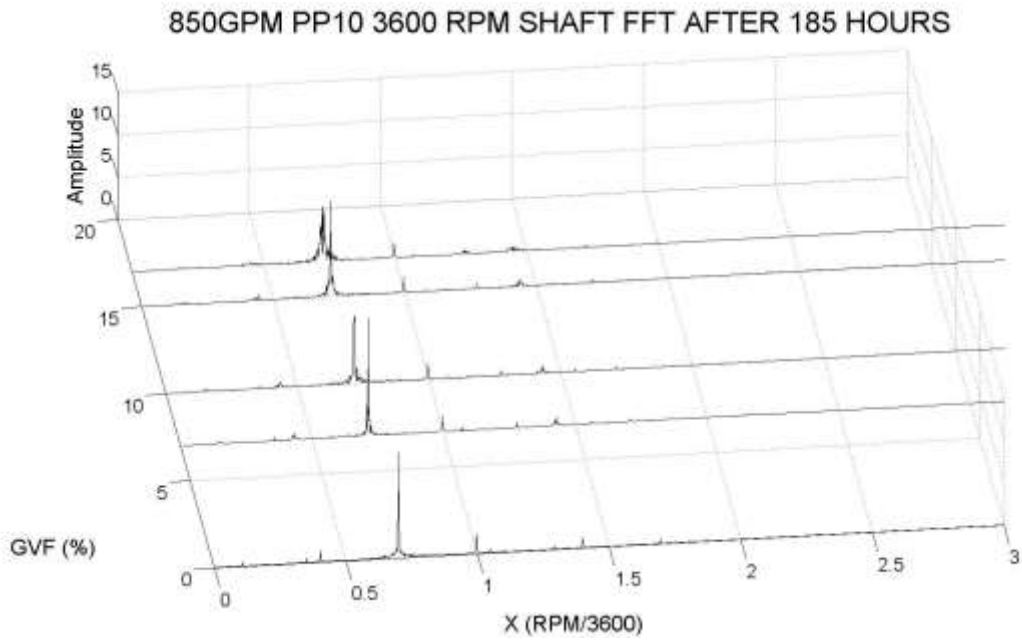


Figure 327. PP10 FFT vs GVF Spectrum

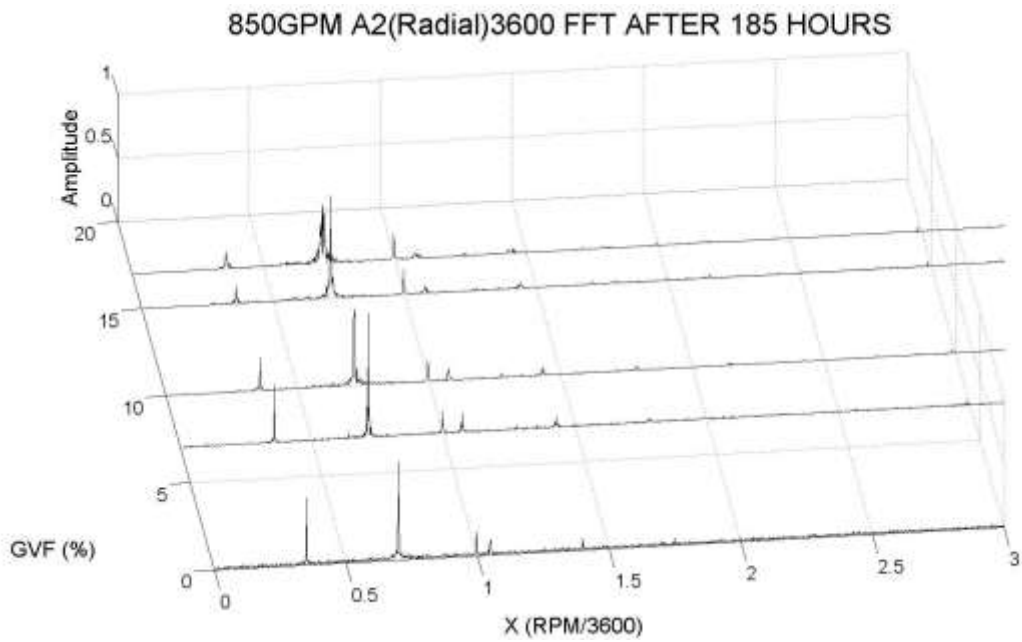


Figure 328. Inlet Radial FFT vs GVF Spectrum

850GPM A1(Tangential) 3600 RPM FFT AFTER 185 HOURS

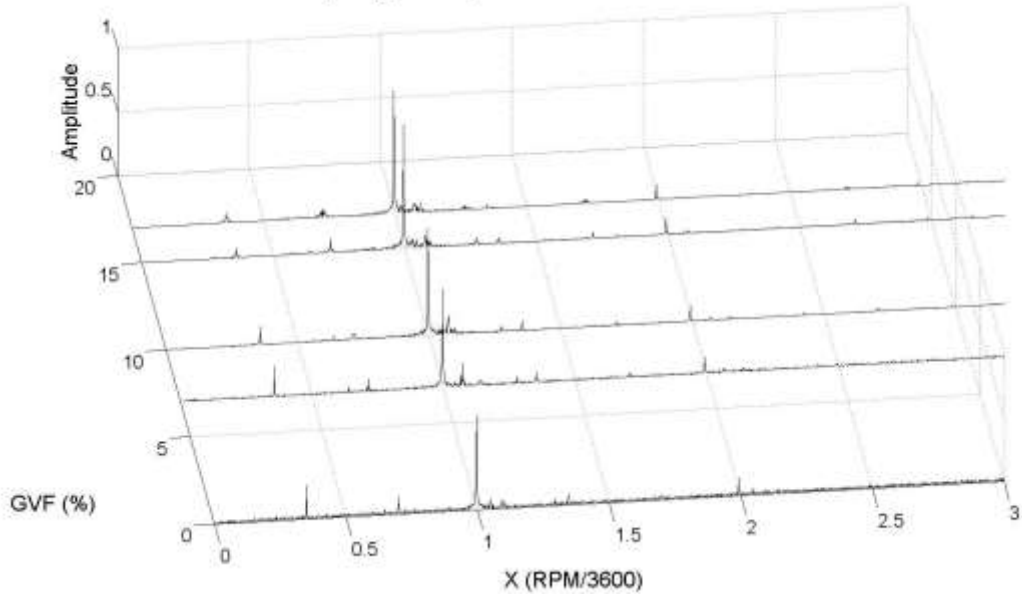


Figure 329. Inlet Tangential FFT vs GVF Spectrum

850GPM A3(Axial) 3600 RPM FFT AFTER 185 HOURS

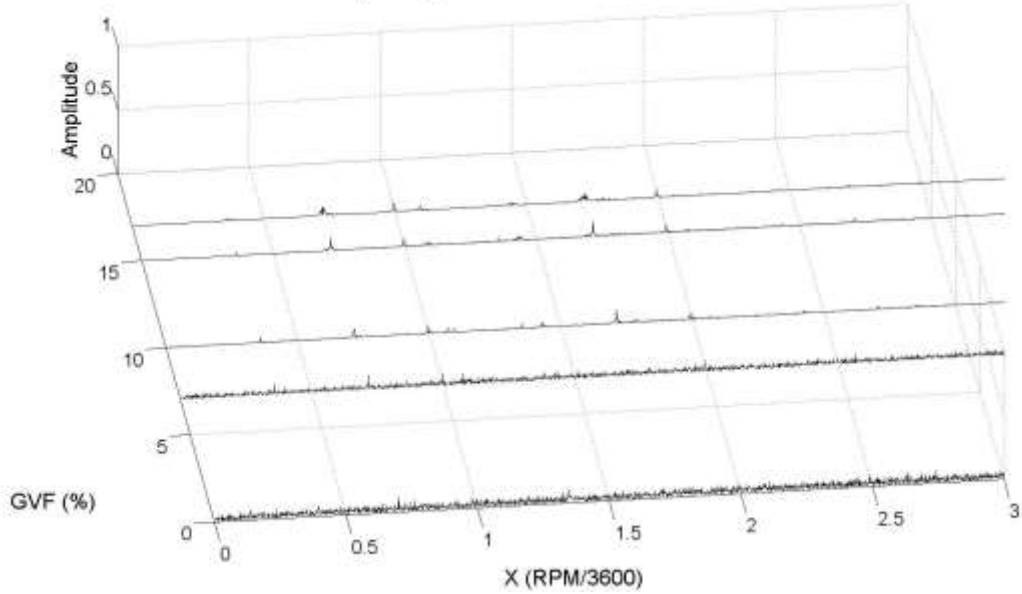


Figure 330. Inlet Axial FFT vs GVF Spectrum

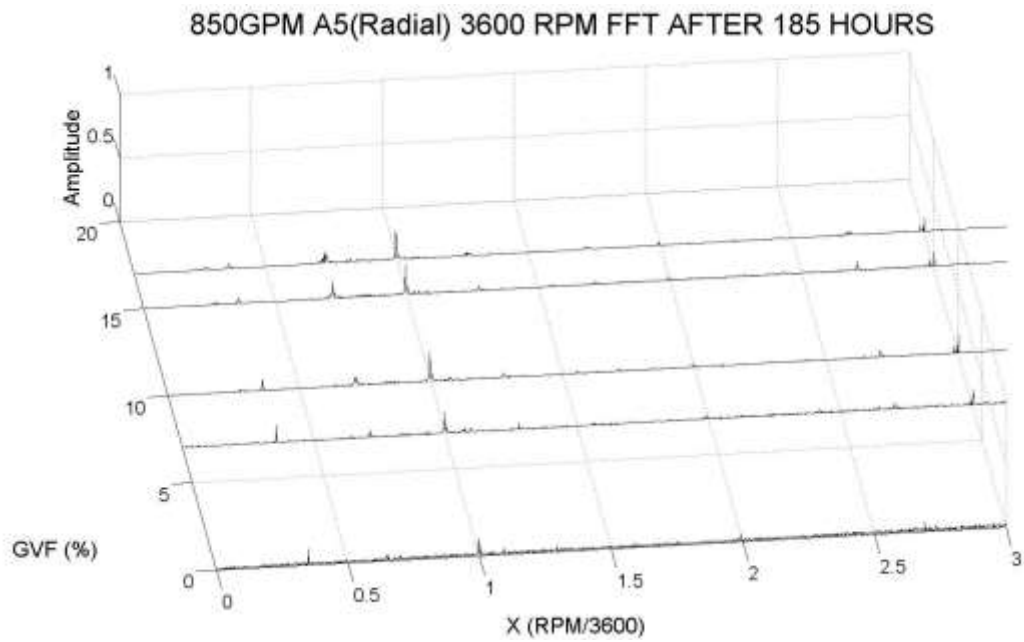


Figure 331. Outlet Radial FFT vs GVF Spectrum

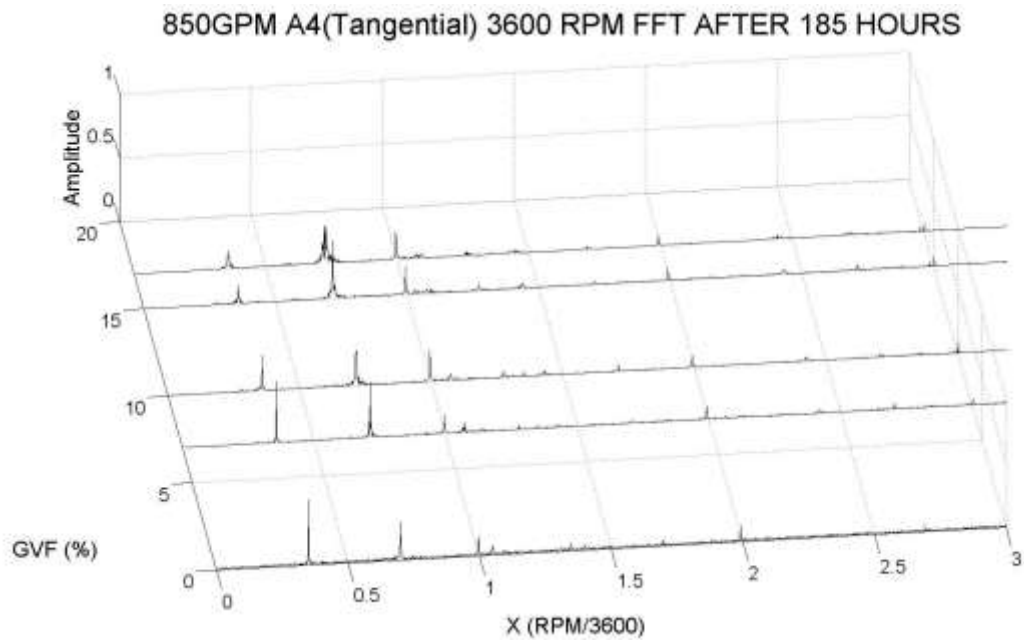


Figure 332. Outlet Tangential FFT vs GVF Spectrum

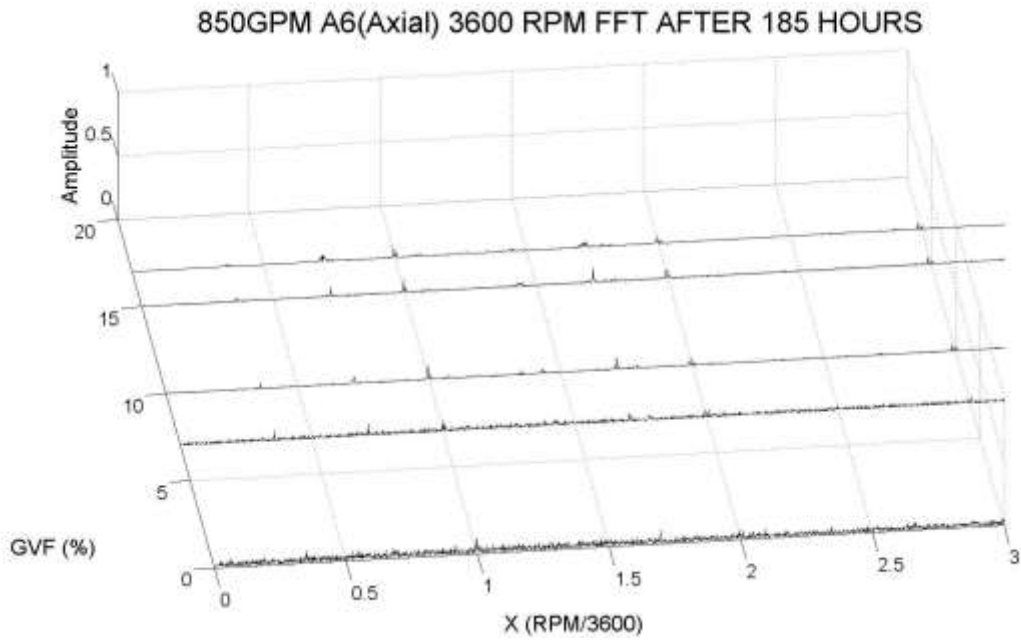


Figure 333. Outlet Axial FFT vs GVF Spectrum

D.9. Vibration Signature vs Flow Rate Spectrum at 15% GVF

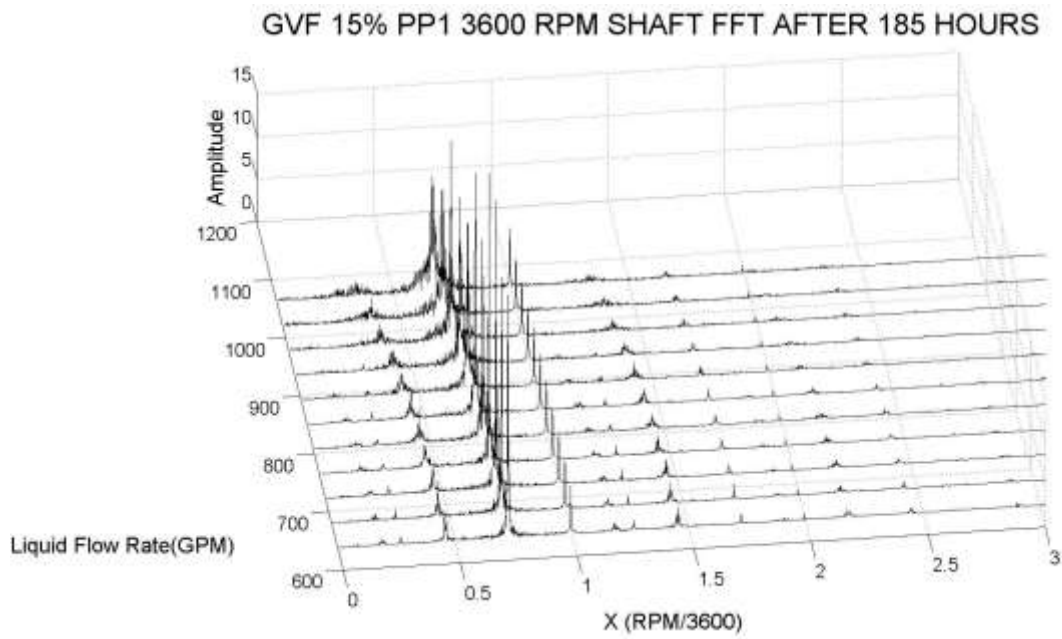


Figure 334. PP1 FFT vs Flow Rate Spectrum

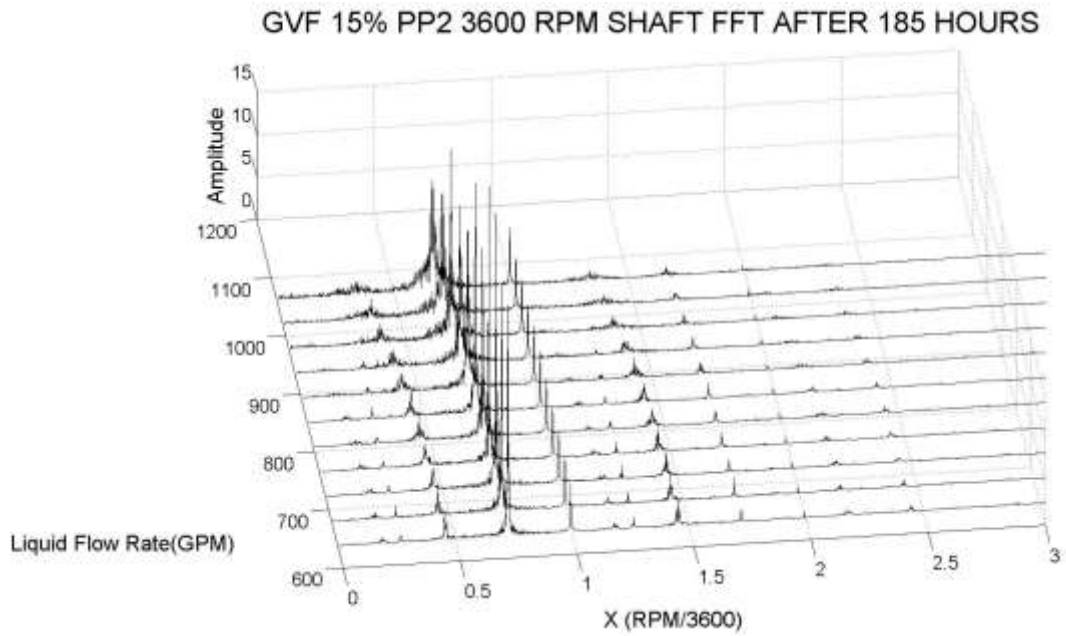


Figure 335. PP2 FFT vs Flow Rate Spectrum

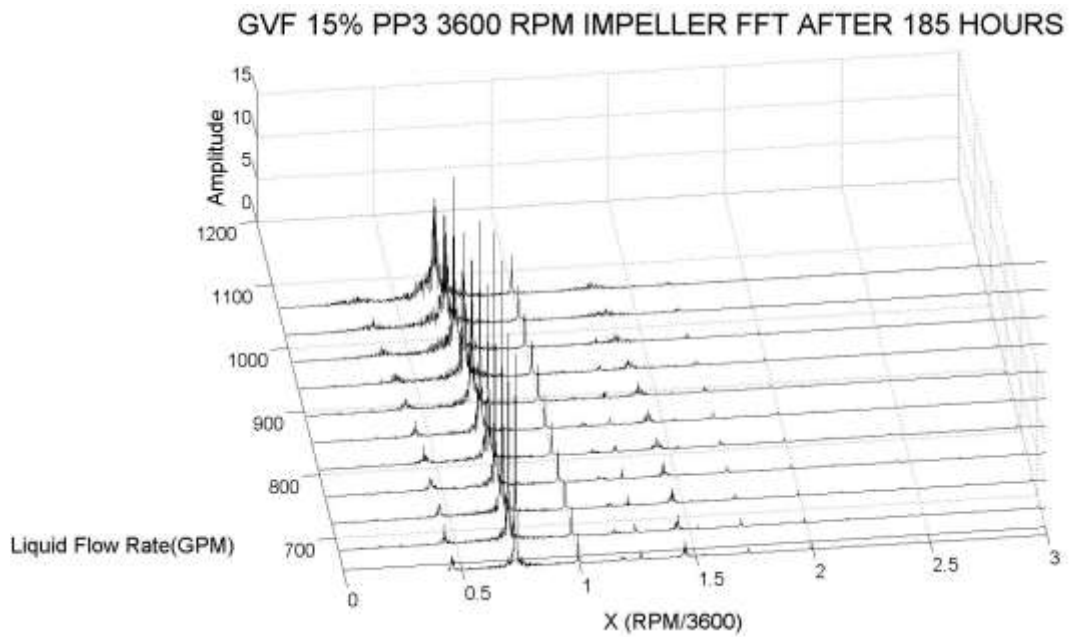
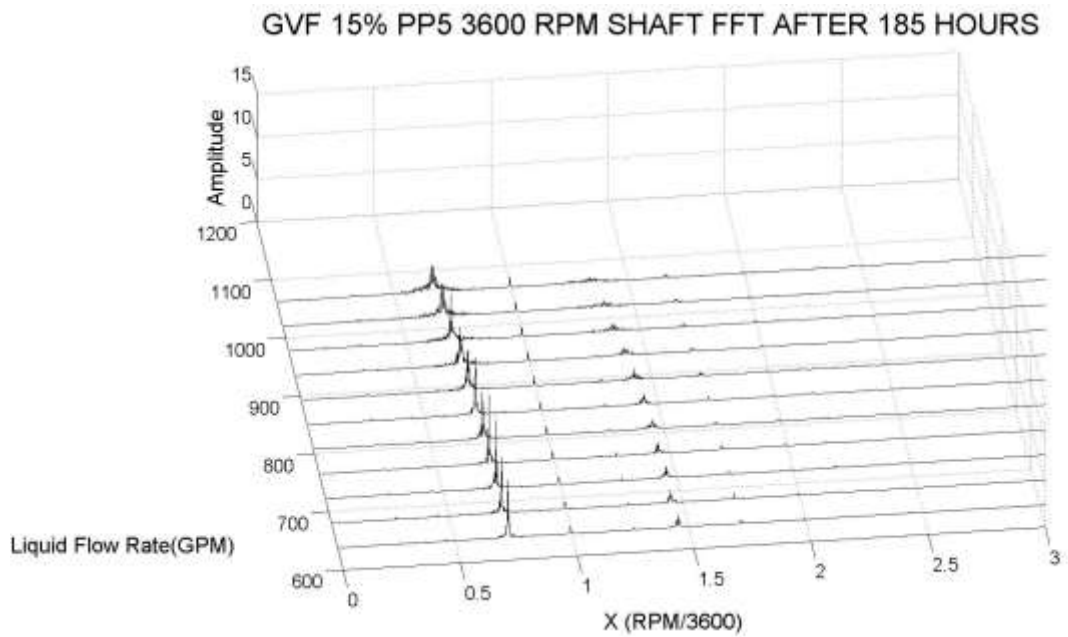
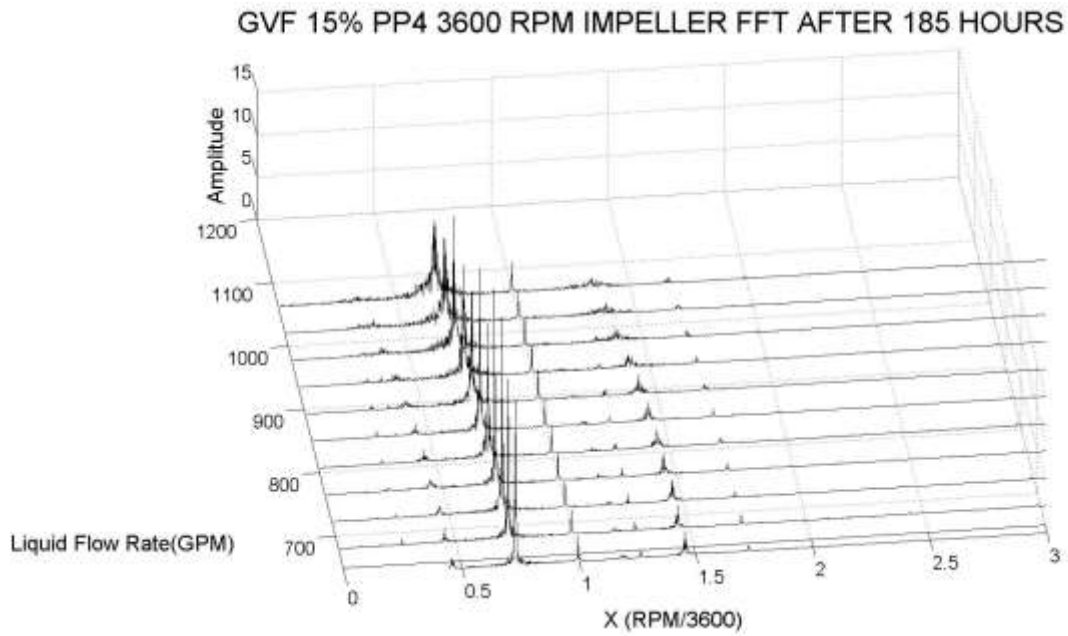


Figure 336. PP3 FFT vs Flow Rate Spectrum



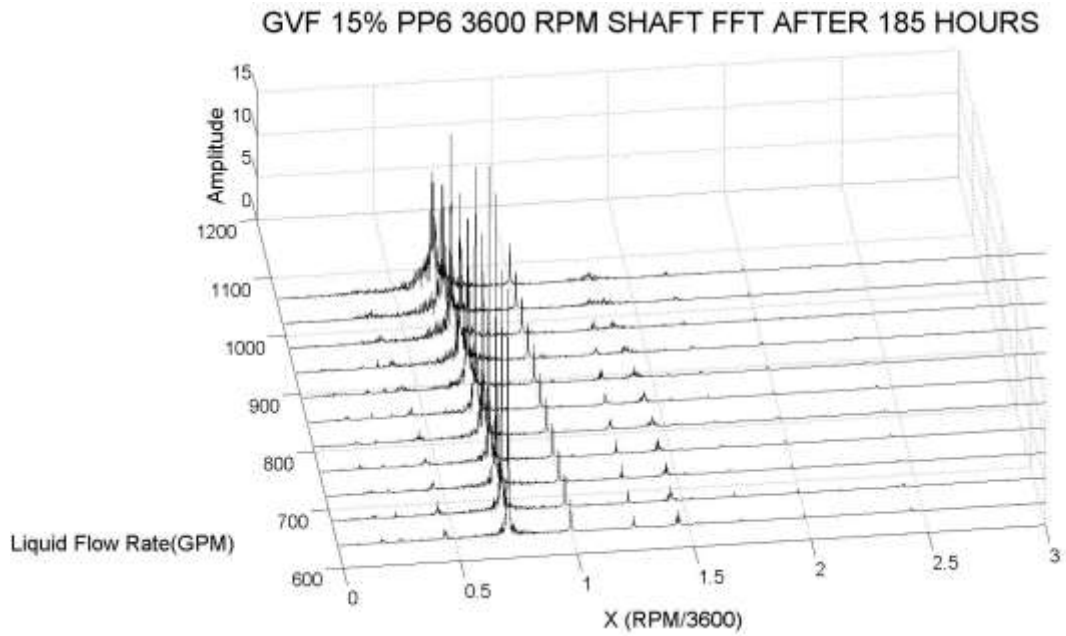


Figure 339. PP6 FFT vs Flow Rate Spectrum

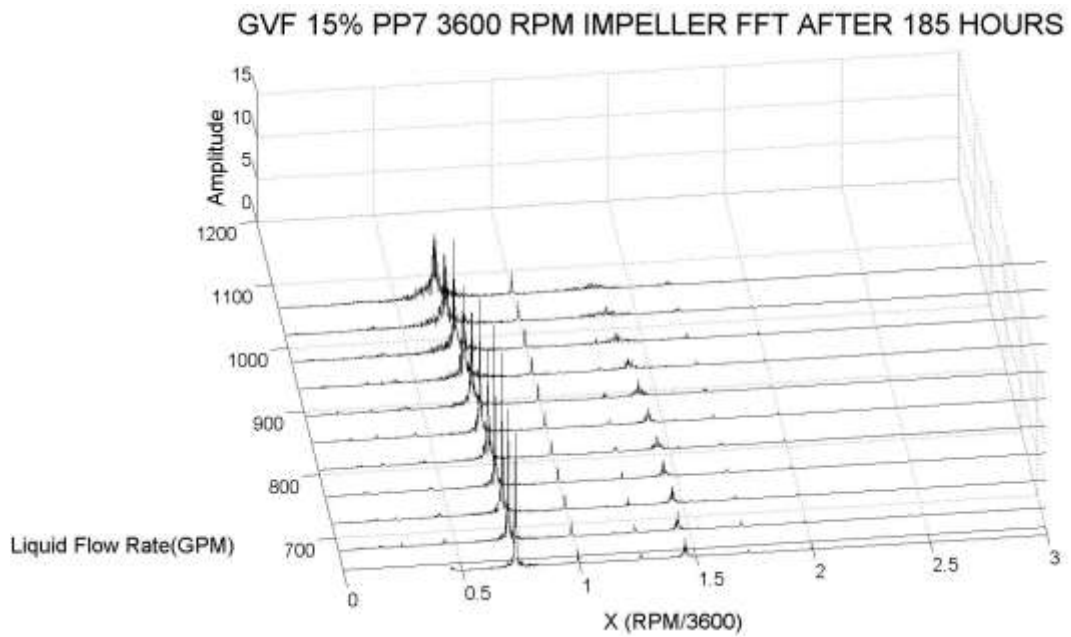
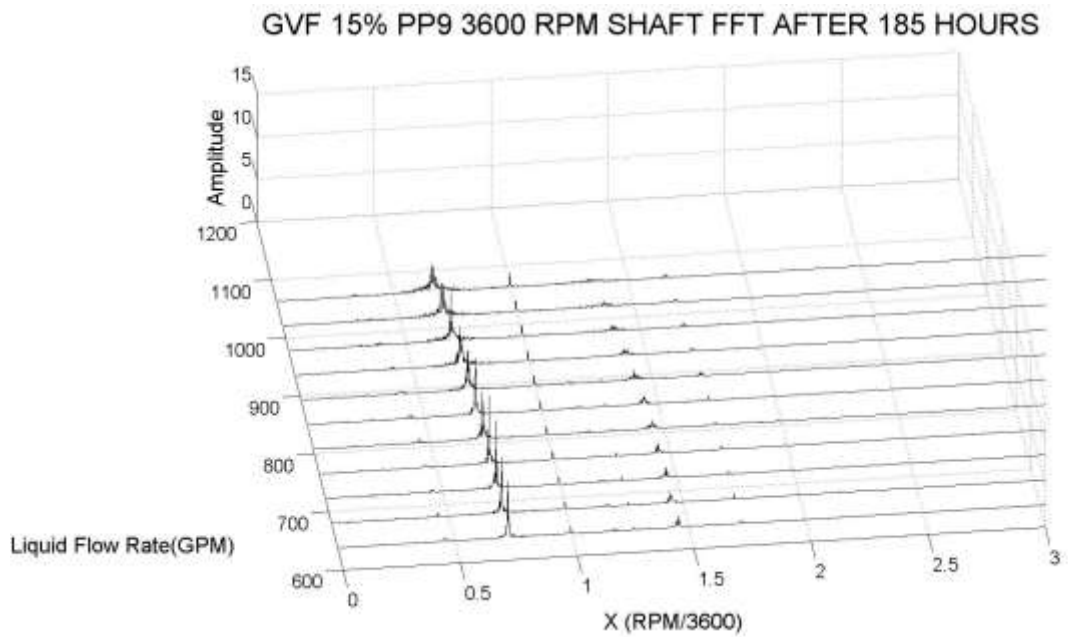
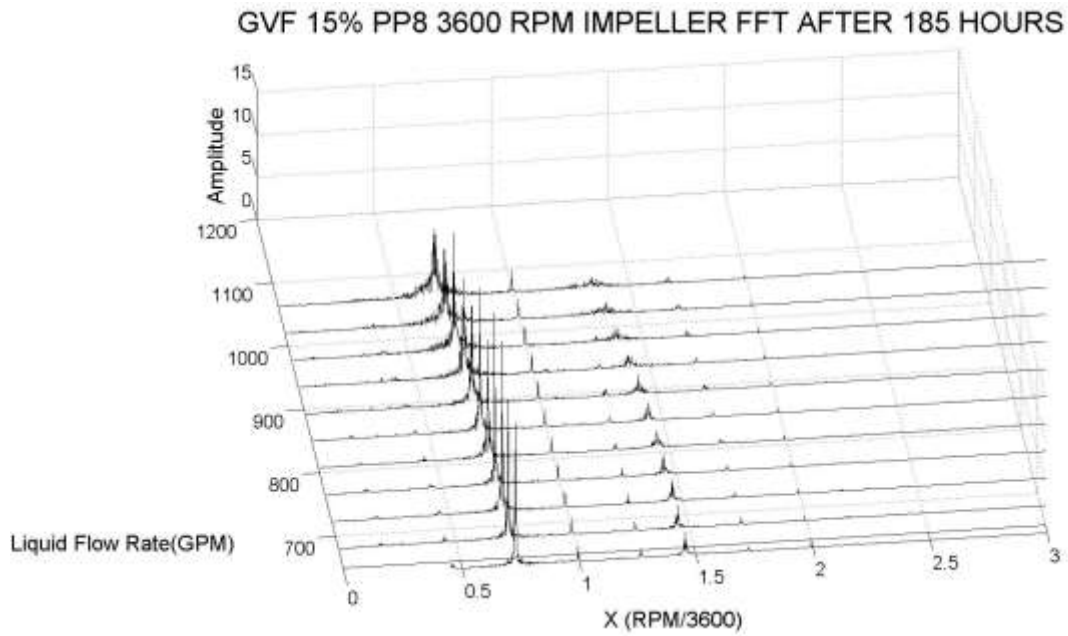


Figure 340. PP7 FFT vs Flow Rate Spectrum



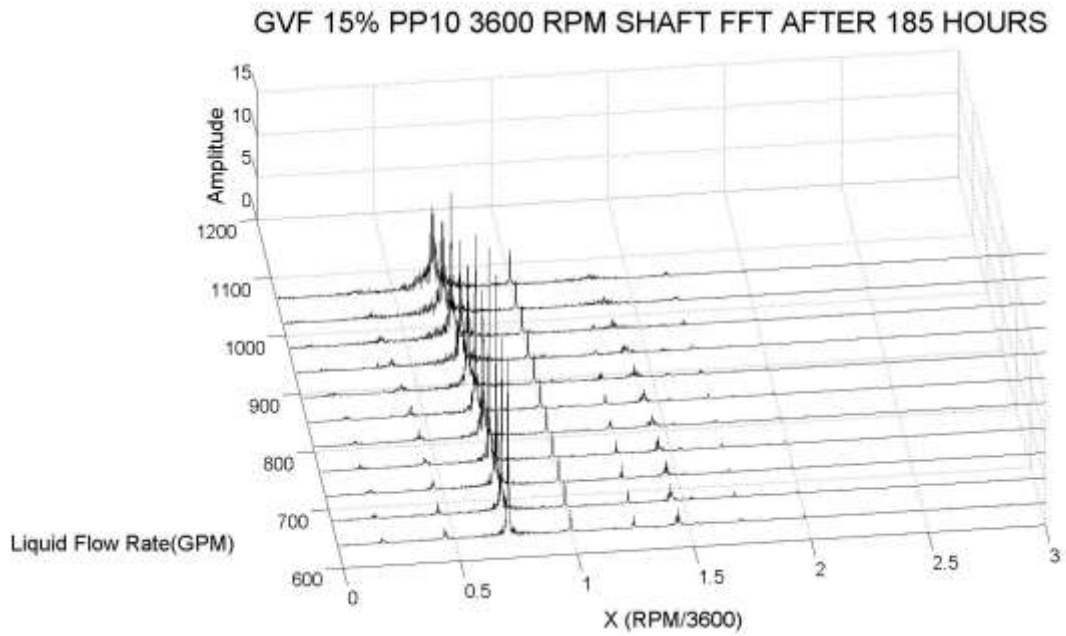


Figure 343. PP10 FFT vs Flow Rate Spectrum

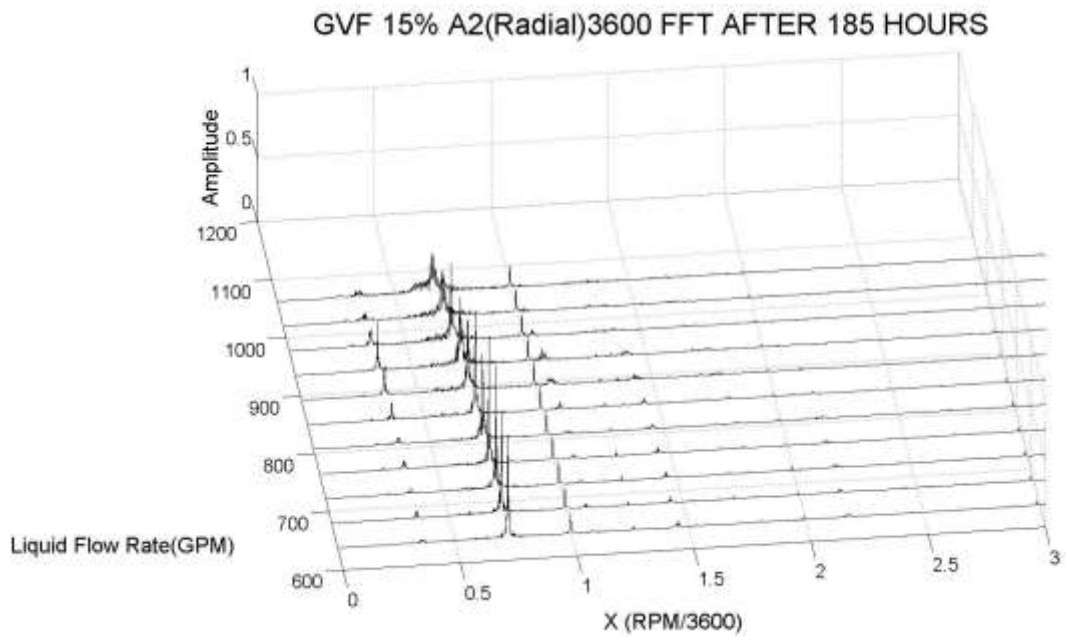


Figure 344. Inlet Accelerometer Radial FFT vs Flow Rate Spectrum

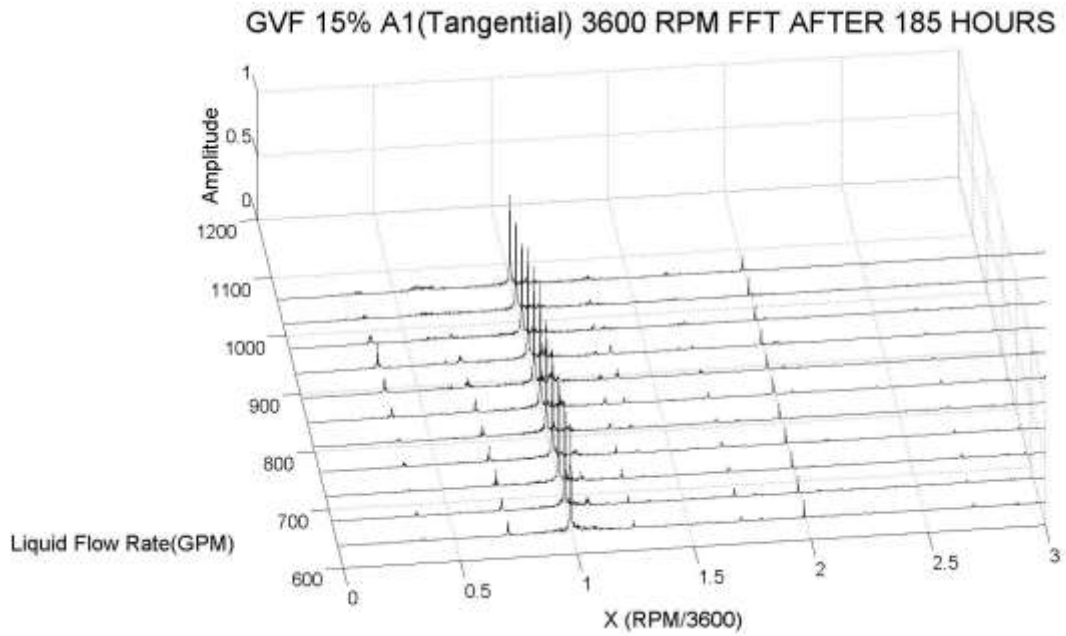


Figure 345. Inlet Accelerometer Tangential FFT vs Flow Rate Spectrum

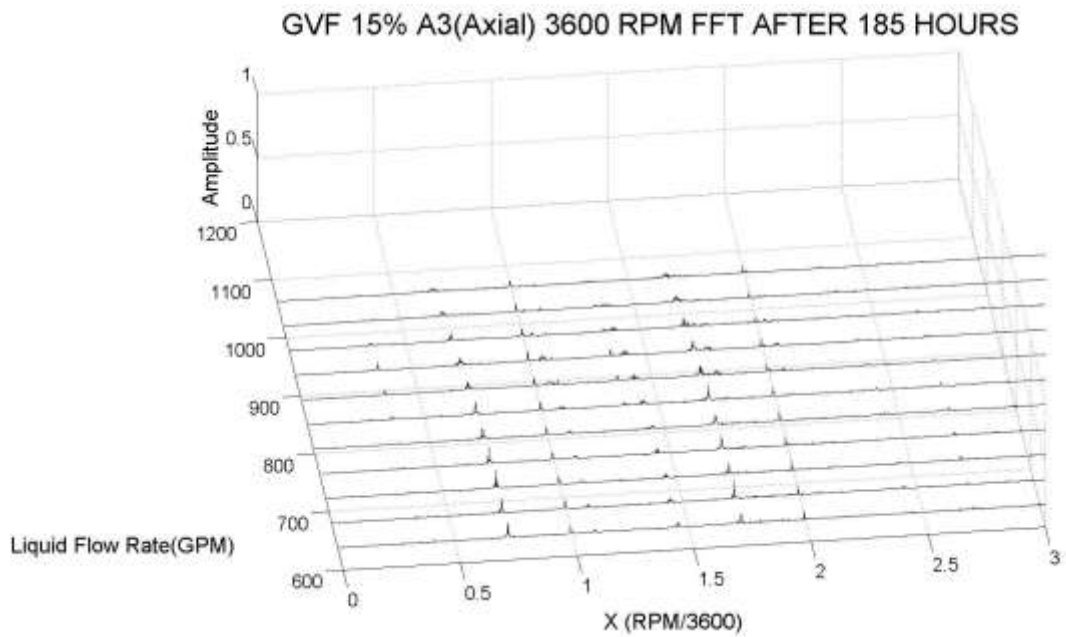


Figure 346. Inlet Accelerometer Axial FFT vs Flow Rate Spectrum

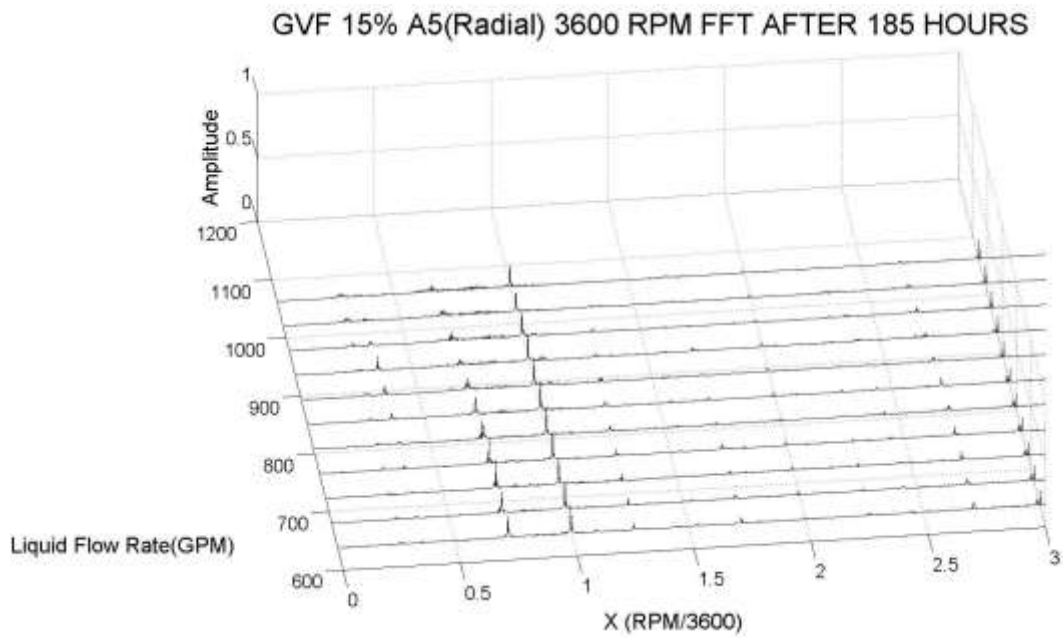


Figure 347. Outlet Accelerometer Radial FFT vs Flow Rate Spectrum

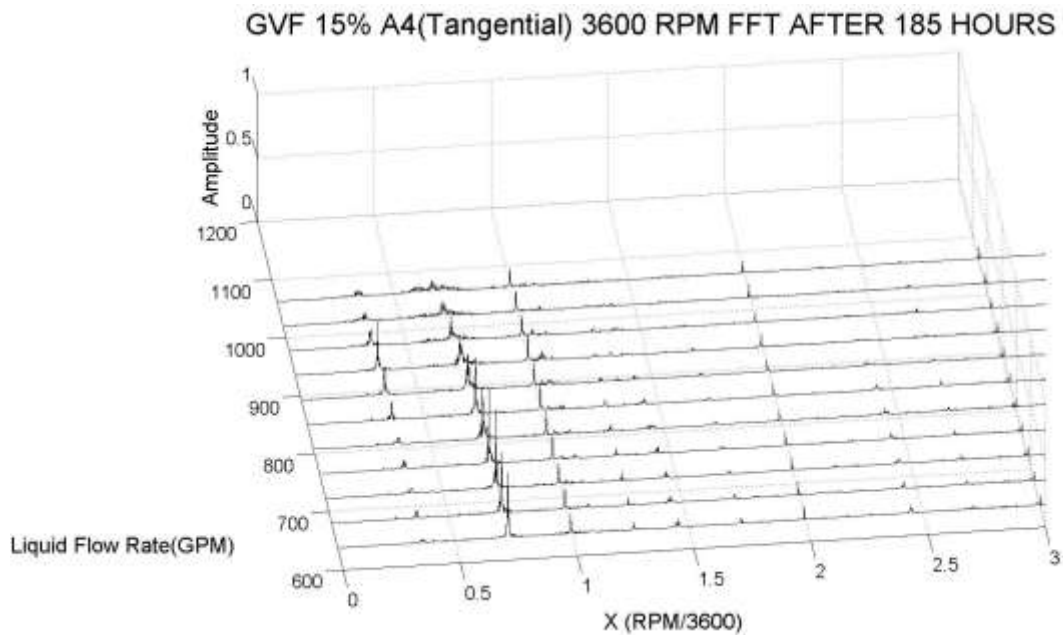


Figure 348. Outlet Accelerometer Tangential FFT vs Flow Rate Spectrum

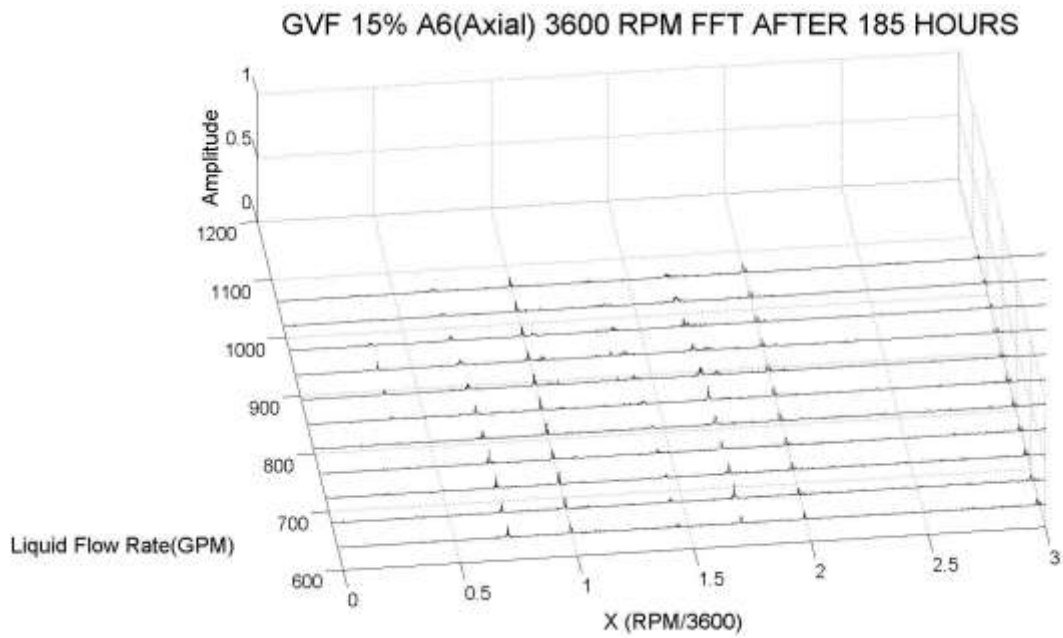


Figure 349. Outlet Accelerometer Axial FFT vs Flow Rate Spectrum